Dynamics and Heat Transfer Enhancement of MHD Flows past a Circular Cylinder in a Duct at High Hartmann Number

by

Wisam K. Hussam Alsaadi

A Thesis submitted to Monash University

for the degree of

Doctor of Philosophy

November 2012

Department of Mechanical and Aerospace Engineering

Monash University

I dedicate this dissertation to my wonderful family who have helped me through this journey every step of the way. Thank you to my wife who was my greatest supporter and would not let me give up when the task seemed impossible. Thank you to my daughters and son who understood me when I had to do my work instead of play. Thank you to my parents who instilled in me the importance of education and perseverance to always give my best effort.

Copyright Notices

Notice 1

Under the Copyright Act 1968, this thesis must be used only under the normal conditions of scholarly fair dealing. In particular no results or conclusions should be extracted from it, nor should it be copied or closely paraphrased in whole or in part without the written consent of the author. Proper written acknowledgement should be made for any assistance obtained from this thesis.

Notice 2

I certify that I have made all reasonable efforts to secure copyright permissions for third-party content included in this thesis and have not knowingly added copyright content to my work without the owner's permission.

Statement of Originality

This thesis contains no material that has been accepted for the award of a degree or diploma in this or any other university. To the best of the candidate's knowledge and belief, this thesis contains no material previously published or written by another person except where due reference is made in the text of this thesis.

Candidate: Wisam K. Hussam

November 2012

Supervisor Certificate

This is to certify that preparation of the thesis entitled **Dynamics and Heat Transfer Enhancement of MHD Flows past a Circular Cylinder in a Duct at High Hartmann Number** and submitted by *Wisam K. Hussam Al-saadi* was made under my supervision at the Mechanical and Aerospace Engineering Department, Monash University in partial fulfillment of the requirements for the degree of Doctor of Philosophy in fluid dynamics and heat transfer for fusion applications.

Signature:

Principal Supervisor: Dr. Gregory J. Sheard

Signature:

Co Supervisor: Prof. Mark C. Thompson

Abstract

A numerical study of magnetohydrodynamic flows and heat transfer past a circular cylinder in a duct under a strong magnetic field parallel to the cylinder axis is presented. In this configuration, the flow is quasi-two-dimensional and the modified Navier–Stokes equations are solved in a two–dimensional domain. The numerical simulations have been performed over a range of parameters including the Reynolds number $50 \leq Re \leq 3000$, modified Hartmann number $50 \leq Ha^\star \lesssim 500$, blockage ratio $0.1 \leq \beta \leq 0.5$, offset ratio $0.25 \leq \gamma \leq 1$, velocity amplitude $0 \leq A \leq 3$ and forcing frequency $0 \leq St_e \leq 10$. The primary aim of this study is to understand the fundamental mechanism that governs transition to unsteady flow in this system and exploit this for further improvements in heat transfer for MHD cooling duct flows.

With this aim in mind, a spectral-element method is employed to compute the MHD flow and heat transfer past a confined circular cylinder in a rectangular duct. Meshes have been constructed to deal with the significant number of geometric flow parameters combinations. Thorough validation and grid resolution studies have been performed to ensure adequate domain sizes, and spatial and temporal resolutions to accurately resolve all flow and thermal features for the reported flow variable ranges. Studies show that the reported flow parameters are converged to better than 0.3% in terms of spatial and temporal accuracy and 1% with respect to the domain size. For the optimal growth studies, the dependence of energy growth on upstream domain length is also considered through the calculation of the energy growth over a fixed time span. This verifies that the effect of truncating the upstream length from $32d$ to $8d$ causes an error of less than 3% in the growth rate prediction.

The critical Reynolds number Re_c for the transition from steady to periodic flow is determined as a function of $Ha^\star$ and β, and this is found to increase with increasing $Ha^\star$ and β. In addition, the variation of the wake recirculation length in the steady flow regime is determined as a function of Reynolds number, Hartman number and blockage ratio, and a universal expression is proposed.

The characteristics of heat transfer depend strongly on the proximity of the cylinder to the heated wall. For small blockage ratios, it increases significantly as the gap ratio decreases from 1 to 0.25. However, there is a substantial drop in heat transfer for high blockage ratio. Downstream cross-stream mixing induced by the cylinder wake is found to increase the heat transfer augmentation by more than a factor of two in some cases. The maximum gain in heat transfer generated by placing the cylinder in the channel near to the wall with that at the centerline was obtained for the lowest blockage ratio $\beta = 0.1$, as the cylinder is further approached the heated wall.

For all β, a very significant transient energy growth is found in the subcritical regime below the onset of vortex shedding. This suggests a potential for the design of an actuation mechanism to invoke vortex shedding and then enhance heat transfer in these ducts. The energy amplification of the disturbances is found to decrease significantly with increasing Hartmann number and the peak growth shifts towards smaller times while it increases significantly with increasing blockage ratio.

The structure of the optimal initial disturbance is found to be consistent across the all blockage ratios being tested. In line with similar problems, it convects along the separating region being amplified to the peak growth state downstream of the recirculation bubble. The maximum time for maximum energy growth $\tau_{\max}$ is found to increase significantly as recirculation length increases which demonstrates the amplifying nature of the separated shear layers in the wake.

The critical Reynolds number for the onset of positive growth at different Hartmann numbers and blockage ratios is determined. It is found that it increases rapidly with increasing Hartmann number and blockage ratio. For all β, the peak energy amplification grows exponentially with Re from low Hartmann numbers.

Direct numerical simulation studies in which the inflow is perturbed by random white noise confirms the predictions arising from the transient growth analysis: that is, the perturbation excites and feeds energy into the global mode.

A considerable increase in heat transfer from the heated channel wall occurs from rotational oscillation of the cylinder, with a maximum enhancement of approximately 22% observed at higher amplitude over that for steady flow. The oscillation frequency range for effective enhancement is widened in both directions, while the frequency at which the peak of the Nusselt number occurs is shifted slightly to a lower frequency as A is increased. It is found that as the amplitude was reduced, the forcing frequency approaches the global frequency mode.

Acknowledgments

First and foremost, this thesis would not have been possible without God almighty, to whom I am evermore grateful.

I would like to thank my supervisors, Dr. Gregory Sheard and Professor Mark Thompson, for all the assistance and guidance they have provided over the duration of my candidature. They have provided continuous enthusiasm, direction and support without which this work would not have been possible. In particular I would like to extend my sincere thanks to Dr. Gregory Sheard, whose ideas contributed greatly to the material presented in this thesis. I would also like to extend my thanks to Dr. Justin Leontini for the insight he has offered into this research.

I am grateful to the Department of Mechanical and Aerospace Engineering, Monash University, for providing the post-graduate office and resources necessary for the completion of this study. Furthermore, I wish to acknowledge the Monash e-Research Centre (MeRC) through the use of Monash Sun Grid (MSG) cluster, and the National Computational Infrastructure (NCI) for providing the computational facilities which were essential to this work. A special thank you must be given to Mr. Philip Chan from (MeRC) for his great help on the post-processing of data, and introducing me to basic Linux.

I would like to express my gratitude for the financial support provided through the Ministry of Higher Education and Scientific Research scholarship from the Iraqi Government.

I would like to thank all of my fellow post-graduate students in the Department of Mechanical and Aerospace Engineering. In particular many thanks go to Mr. Nicholas Bousted, Christopher Ellis, Anirudh Rao, Christopher Butler, Muhammed Musaher and Gazy Faissal for sharing lots of useful thoughts and discussions.

To my family, I would like thank my mother, my brothers and sisters, my daughters and son for the help and support that they offered throughout this time. Finally, I would like to thank my wife, Tagreed, for love and support

during the most critical time of my candidature, thank you.

Publication Arising from Thesis

Hussam, W.K., Thompson, M.C. & Sheard, G.J. 2012 Optimal transient disturbances behind a circular cylinder in a quasi two-dimensional magnetohydrodynamic duct flow. *Physics of Fluids.* **24** (2), 8–14.

Hussam, W.K., Thompson, M.C. & Sheard, G.J. 2011 Dynamics and heat transfer in a quasi-two-dimensional MHD flow past a circular cylinder in a duct at high Hartmann number. *International Journal of Heat and Mass Transfer.* **54**(5), 1091–1100.

Hussam, W.K., Thompson, M.C. & Sheard, G.J. 2011 Optimal transient disturbances preceding vortex shedding in magneto-hydrodynamic flow past a circular cylinder in a duct. *In Mechanical, Industrial, and Manufacturing Engineering:* Selected, peer reviewed paper from 2011 International Conference on Mechanical, Industrial, and Manufacturing Engineering (MIME 2011)(Eds: M. Ma, Pub: Information Engineering Research Institute, USA, ISBN: 978-0-9831693-1-4, ISSN: 2070-1918), Rydges Hotel, Melbourne, Australia, 15-16 January 2011, 134-137.

Hussam, W.K., Thompson, M.C. & Sheard, G.J. 2010 Quasi-2D simulation of liquid metal flow past a cylinder in a duct exposed to a magnetic field. *In Proceedings of the* 17^{th} *Australasian Fluid Mechanics Conference* (Eds: G.D. Mallinson and J.E. Cater, Pub: The University of Auckland, ISBN: 978-0-86869-129-9), The University of Auckland, Auckland, New Zealand, 5-9 December 2010, Paper 350.

Hussam, W.K., Thompson, M.C. & Sheard, G.J. 2009 A quasi-two-dimensional investigation of unsteady transition in shallow flow past a circular cylinder in a channel. *In Proceedings of the Seventh International Conference on Computational Fluid Dynamics in the Minerals and Process Industries* (Eds: P.J. Witt and M.P. Schwarz, Pub: CSIRO Australia, ISBN: 978-0-643-09825-1), Rydges Hotel, Melbourne, Australia, 9-11 December 2009, 153ALS:1-6.

Nomenclature

A list of nomenclature used throughout the thesis is included here. Mathematical symbols are presented, followed by Greek alphabet nomenclature and English alphabet nomenclature.

Symbol	**Description**
§	Thesis section
$\int$	Integral
$\oint$	Line integral
$\log_{10}$	Logarithm to the base-10
$\log_{\mathrm{e}}$	Natural logarithm
∇	Vector gradient operator (grad)
$\nabla_\perp$	Vector gradient operator projected onto (x,y) plane (grad)
∇^2	Del squared (or div grad) operator
$\nabla^2_\perp$	Del squared (or div grad) operator projected onto (x,y) plane
$\sum_{i=a}^{b}$	Sum of arguments with i incrementing from a to b
α_d	Thermal diffusivity of the fluid
α_q	Third-order backwards-multistep coefficients
β	Blockage ratio
β_q	Third-order backwards-multistep coefficients
ψ_0	Scalar gradient of the z-averaged current
Δ	Minimum distance between the surface of the cylinder and the heated wall
Δt	Time step
δ_H	Hartmann boundary layer thickness
δ_S	Shercliff boundary layer thickness
η	Duct aspect ratio

Continued on the next page.

Continued from previous page.

Symbol	**Description**
η_{eff}	Efficiency index
ϕ	Electrical potential
γ	Offset ratio from the duct cenreline
γ_q	Third-order backwards-multistep coefficients
λ_j	Eigenvalue of operator $\mathscr{A}(\tau)\mathscr{A}^*(\tau)$
λ_n	Constant
θ	Temperature field
$\dot{\theta}_{\text{cyl}}$	Surface velocity of the cylinder
θ_f	Bulk fluid temperature
μ	Complex eigenvalue
μ_m	Magnetic permeability
ν	Kinematic viscosity
ρ	Mass density
σ	Growth rate of linear instability mode over n^{th} period in linear stability analysis
σ_e	Electrical conductivity
σ_n	Linear growth rate in the Landau equation
σ_w	Electrical conductivity of the channel walls perpendicular to the magnetic field
Ω	Computational domain
ω	Angular velocity
$\boldsymbol{\omega}$	Vorticity field
$\boldsymbol{\omega}_{\text{peak}}$	Peak vorticity
τ_w	Wall shear stress
A	Non-dimensional angular velocity amplitude
A_n	Complex amplitude in Landau equation
a	Characteristic length scale, duct height
$\mathscr{A}(\tau)$	Linear evolution operator over a time τ

Continued on the next page.

Continued from previous page.

Symbol	**Description**
$\mathscr{A}^*(\tau)$	Adjoint of linear evolution operator over a time τ
B	Magnetic field strength
$\mathbf{B}$	Magnetic field vector
B_i	Induced Magnetic field
b_n	Fourier mode of induced magnetic field
c	Wall conductance ratio
C	Constant
c_n	Landau constant
C_D	Cylinder drag coefficient
$C_{D,p}$	Pressure component of drag coefficient
$C_{D,\mathrm{visc}}$	Viscous component of drag coefficient
C_L	Cylinder lift coefficient
$C_{L,\mathrm{max}}$	Maximum lift coefficient
C_M	Cylinder moment coefficient
$C_{M,\mathrm{max}}$	Maximum Moment coefficient
C_p	Specific heat at constant pressure
d	Cylinder diameter
$\mathrm{DN}\mathbf{u}'$	Linearized advection term of perturbation field
$\mathrm{DN}^*\mathbf{u}^*$	Adjoint advection operator
$\mathbf{E}$	Electrical field vector
F_d'	Lift force per unit span of the cylinder
F_l'	Drag force per unit span of the cylinder
$\mathbf{F}_p$	Pressure force per unit span of the cylinder
$\mathbf{F}_w$	Viscous force per unit span of the cylinder
$\mathbf{F}_T$	Total force per unit span of the cylinder
f_e	Forcing frequency (dimensional)
f_s	Wake oscillation frequency
$f(z)$	Time-dependent function (employed in quasi-two–dimensional model)

Continued on the next page.

Continued from previous page.

Symbol	**Description**
G	Energy growth
G_{max}	Global maximum of energy growth
i	Imaginary number ($\mathrm{i} = \sqrt{-1}$)
h	Duct height
h_c	Convective heat transfer coefficient
Ha	Hartmann number
$Ha^\star$	Modified Hartmann number
HI	Percentage heat transfer increment when the cylinder placed symmetrically in the duct
HI_{asym}	Percentage heat transfer increment when the cylinder placed asymmetrically in the duct
HP	Pressure penalty ratio
HR	Heat transfer enhancement ratio
$\mathscr{H}$	Forward equations of field $\mathbf{q}$ operator
$\mathscr{H}^*$	Adjoint equations of field $\mathbf{q}^*$ operator
$\mathbf{J}$	Current density vector
$\bar{\mathbf{J}}$	z-averaged current density vector
$\mathbf{J_w}$	Current density vector injected at the wall
$\bar{\mathbf{J}}_\perp$	z-averaged current density vector projected onto (x,y) plane
k	Thermal conductivity
k_n	Constant
K_p	Pressure gradient
L	Length along heated bottom wall
L_R	Recirculation bubble length
$\mathbf{M}$	Moment exerted by the fluid on the cylinder
$\mathbf{M}_{\mathrm{max}}$	Peak moment exerted by the fluid on the cylinder
M'	Moment exerted by the fluid per unit span of the cylinder
N	Stuart number (Interaction parameter)

Continued on the next page.

Continued from previous page.

Symbol	**Description**
N_{el}	Number of elements employed in computations
N_p	Element polynomial degree employed in computations
n_H	Number of Hartmann walls
$\mathbf{n}$	Surface normal unit vector
Nu	Time-averaged Nusselt number
Nu_{asym}	Time-averaged Nusselt number for the cylinder placed asymmetrically in the duct
Nu_{sym}	Time-averaged Nusselt number for the cylinder placed symmetrically in the duct
$Nu_{\max}$	Peak time-averaged Nusselt number
Nu_s	Time-averaged Nusselt number for zero-oscillation
Nu_w	Local Nusselt number
Δp_{cyl}	Pressure drop due to the inclusion of a circular cylinder
Δp	Overall pressure across the channel for a circular cylinder placed asymmetrically from the channel centerline
Δp_0	Overall pressure across the channel without the cylinder
P	Scalar pressure
P_{avg}	Time-averaged power
$P_{\max}$	Maximum power
$P_{\Delta p}$	Pumping power
p	Kinematic pressure field
$\hat{p}$	Complex perturbation pressure field amplitude for linear stability analysis
$\tilde{p}$	Dimensional pressure kinematic field
P_m	Legendre polynomial of order m
p_n	Constant
Pe	Péclet number
Q_v	Flow rate
Pr	Prandtl number

Continued on the next page.

Continued from previous page.

Symbol	**Description**
$\mathbf{r}$	Moment arm vector
Re	Reynolds number
Re_c	Critical Reynolds number for the onset of vortex shedding
Re_{c1}	Critical Reynolds number for positive energy growth of optimal disturbances
Re_m	Magnetic Reynolds number
St	Strouhal number
St_c	Strouhal number at Re_c
St_e	Forcing Strouhal frequency
$St_{e,\max}$	Maximum forcing Strouhal frequency
t	time
t_H	Hartmann braking time
t_w	Thickness of the channel walls perpendicular to the magnetic field
ΔT	Temperature difference between channel side walls
T	Period of an oscillating flow
T_e	Period of an oscillating flow at f_e
τ	Time interval
$\tau_{\max}$	Maximum time for the maximum energy growth
T_0	Temperature of fluid entering channel
T_w	Temperature of hot channel side-wall
$\mathbf{U}$	Steady two–dimensional base flow velocity
u	x-direction velocity component
$\hat{u}$	Amplitude of the streawise velocity component of the perturbation field
$\tilde{u}$	x-direction dimensional velocity component
u_c	Core velocity
$\mathbf{u}$	Velocity vector
$\hat{\mathbf{u}}$	Complex perturbation velocity field amplitude for linear stability analysis

Continued on the next page.

Continued from previous page.

Symbol	**Description**
$\acute{\mathbf{u}}$	Perturbation field velocity vector for linear stability and transient growth analysis
$\mathbf{u}_f$	Driving force arising from current injection at boundaries
$\bar{\mathbf{u}}$	z-averaged velocity
$\mathbf{u}_\perp$	Velocity projected onto (x,y) plane
$\bar{\mathbf{u}}_\perp$	z-averaged velocity projected onto (x,y) plane
$\acute{\mathbf{u}}_\perp$	Velocity deviation from the averaged velocity
$\mathbf{u}^*$	Velocity field at first substep
$\mathbf{u}^{**}$	Velocity field at second substep
u_0	Peak inlet velocity
u_n	Fourier mode of velocity
v	y-direction velocity component
$\mathbf{v}_j$	Normalized eigenfunctio of operator $\mathscr{A}(\tau)\mathscr{A}^*(\tau)$
$\tilde{v}$	y-direction dimensional velocity component
$\hat{v}$	Amplitude of the transverse velocity component of the perturbation field
ω	z-direction velocity component
x	Streamwise coordinate
$\tilde{x}$	Dimensional streamwise coordinate
$\hat{\mathbf{x}}$	Unit vector in x direction
x_u	Length of upstream flow region
x_d	Length of downstream flow region
x_j	j^{th} Gauss-Legendre-Lobatto quadrature points
w_j	j^{th} Gauss-Legendre-Lobatto weighting coefficient
y	Transverse coordinate
$\tilde{y}$	Dimensional transverse coordinate
$\hat{\mathbf{y}}$	Unit vector y direction
z	Spanwise coordinate

Continued on the next page.

Continued from previous page.

Symbol	**Description**
$\hat{\mathbf{z}}$	Unit vector z direction

Contents

Chapter 1

Introduction

A numerical study of the flow and heat transfer of an electrically conducting fluid (e.g. a liquid metal) past a circular cylinder confined in a duct under an axial magnetic field is studied. In this introduction, initially, some fundamental concepts and parameters pertaining to magnetohydrodynamics are introduced. This is followed by an overview and a description of the problem. The aims of the study are stated, and finally the structure of thesis is outlined.

1.1 Fundamental Magnetohdyrodynamics Concepts

Magnetohydrodynamics (MHD) is the branch of continuum fluid mechanics which deals with the motion of electrically conducting fluids such as liquid metals, electrolytes and plasma in the presence of a magnetic field. Magnetohydrodynamics studies were initiated by the pioneering works of Hartmann (1937) and Hartmann & Lazarus (1937), who conducted a theoretical and experimental analysis of the laminar flow of mercury placed in a magnetic field.

MHD includes phenomena in electrically conducting fluids, where the velocity field and the magnetic field mutually interact. The movement of a conducting fluid in a magnetic field generates electric currents, which in turn induce a magnetic field. The resulting magnetic field interacts with the induced current density to produce a Lorentz force.

1.2 Governing Parameters in MHD

There are four non-dimensional groups which are regularly used to characterize MHD flows. The first is the Reynolds number,

$$Re = ua/\nu, \tag{1.1}$$

where a is a characteristic length scale of the motion, u is a typical flow velocity, and ν is the kinematic viscosity of the fluid. As in conventional fluid mechanics, the Reynolds number represents the ratio of inertia to viscous forces. The second and the third dimensionless groups are the Hartmann number and the interaction parameter. These characterize the square root of the ratio of electromagnetic to viscous forces, and the ratio of electromagnetic to inertia forces, respectively. They are defined as

$$Ha = a\,B\sqrt{\frac{\sigma_e}{\rho\nu}},$$

and

$$N = \frac{\sigma_e B^2 a}{\rho u},$$

where B, ρ, and σ_e are the magnetic field strength, mass density, and the electrical conductivity, respectively. The interaction parameter can also be expressed in terms of Ha and Re as $N = Ha^2/Re$. The final dimensionless group is the magnetic Reynolds number, which represents the ratio of the induced and applied magnetic fields. It is defined as

$$Re_m = \mu_m \sigma_e u a,$$

where μ_m represents the magnetic permeability. When this number is very small, u has only a small influence on B, and thus the induced magnetic field is negligible when compared with the imposed field.

1.3 MHD Flow in Ducts

The study of magnetohydrodynamic flow in ducts in the presence of a transverse magnetic field is important because of its practical applications in magnetohydrodynamic generators, pumps, and metallurgical processing (e.g. Davidson (2001);

Branover (1978)). The primary application motivating this fundamental study is magnetic confinement fusion reactors, where liquid metal (such as lithium or eutectic lithium–lead alloys $PbLi$) may be used as a coolant and as a breeder material (Münevver 1987). In most fusion reactor blankets, the liquid metal circulates within an electrically insulated duct and is exposed to a strong magnetic field. The blankets are designed to absorb the energy released from the fusion reaction and utilize the heat generated by the reaction to produce steam and drive a turbine to generate electricity as shown in Fig. 1.1. The Lorentz force arising from the interaction of the fluid with the strong magnetic field has a significant effect on the velocity distribution and the turbulence characteristics, and exerts a retarding force on the flow.

Under a strong magnetic field the flow is characterized by a laminar structure as velocity fluctuations in the direction of the magnetic field are strongly damped. Therefore, the heat transfer in the ducts of the blanket, where a large amount of heat must be removed, is dramatically decreased (Kirillov *et al.* 1995). The heat transfer problem under these conditions is schematically illustrated in Fig. 1.2. However, two–dimensional unsteady flow that consists of vortices with axes parallel to the magnetic field are not significantly damped (Lielausis 1975). An hypothesis motivating this study is that unsteady flow could be used to enhance the heat and mass transfer in these flows, if turbulence promoters such as a circular cylinder placed inside the duct of a blanket were used.

For the liquid metals used in the fusion blanket, the Hartmann number, Ha, and the interaction parameter, N, are very high (i.e. $Ha \gg 1, N \gg 1$). This implies that the electromagnetic forces dominate over the viscous forces, and following Molokov *et al.* (2007), the flow in a rectangular duct can be split into one or more quasi-inviscid core flows, separated by thin boundary or shear layers of two types, as shown in Fig. 1.3. The core occupies almost the entire duct cross section. In the core, there is a balance between pressure gradient and Lorentz force. Viscous effects are confined to the Hartmann layers where the viscosity and Lorentz force come into balance to satisfy the no-slip boundary condition at the walls (Shercliff 1975). The velocity in the core varies only slightly along

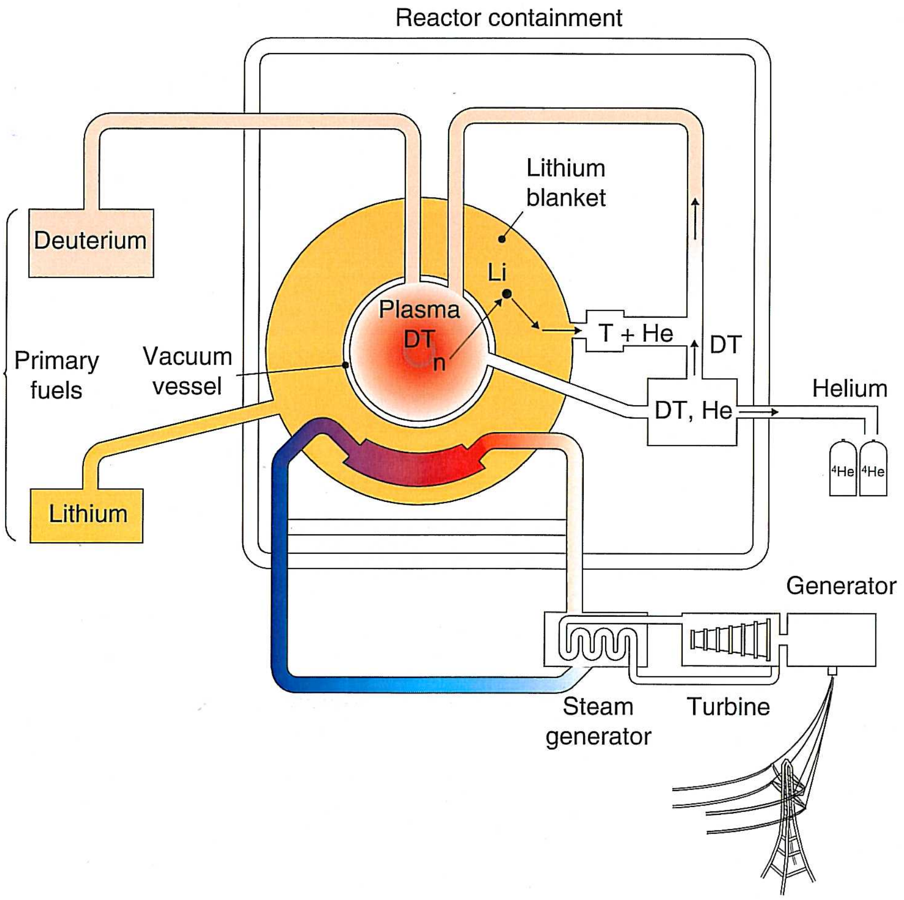

Figure 1.1: Schematic diagram of a fusion reactor for electrical power generation. The deuterium and tritium fuel burns at very high temperature in the reaction chamber where the fuels are ionized and form plasma confined by a strong magnetic field. The energy is released as neutrons and radiation is absorbed in the lithium blanket surrounding the reaction chamber. This image is reproduced from McCracken & Stott (2005).

the magnetic field lines, while in the vicinity of the walls perpendicular to the magnetic field it exhibits an exponential variation. The boundary layer on the walls perpendicular to the magnetic field is known as the *Hartmann layer* with a thickness that scales as $\delta_H \sim Ha^{-1}$, while the boundary layer along the walls parallel to the magnetic field is known as the *Shercliff layer* (or side layer), with a thickness that scales as $\delta_S \sim Ha^{-1/2}$.

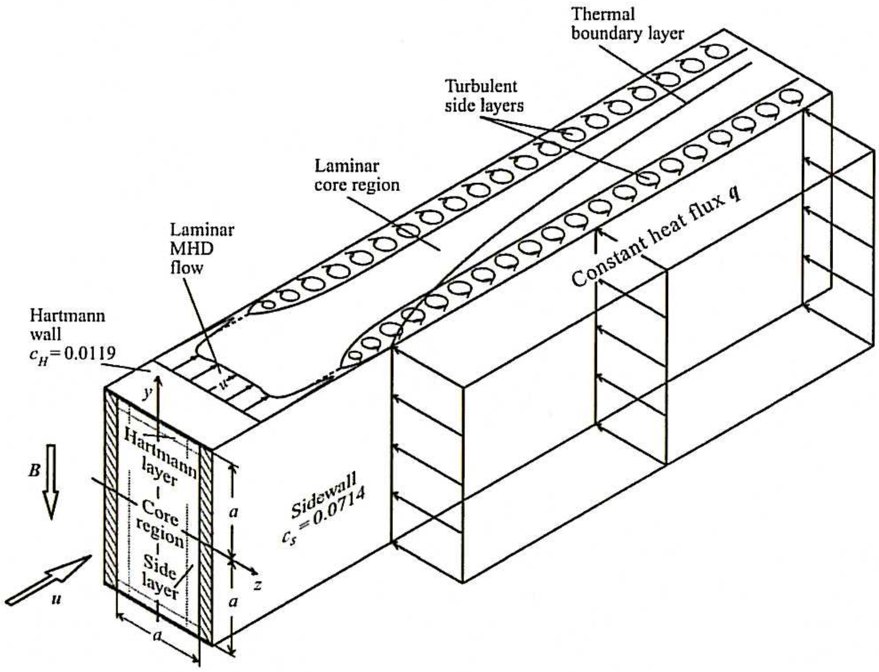

FIGURE 1.2: The heat transfer in a channel in the presence of a strong magnetic field, from Burr *et al.* (2000).

1.3.1 Vorticity

Vorticity is a fundamental concept relating the structural and dynamical properties of a flow field and is applied in this thesis to understand and characterise several features of the computed flow. Throughout this thesis, vorticity fields are used to visualize the fluid structures in the wake of the obstacles placed within the channel. It is mathematically defined as the curl of the velocity vector (Massey 2005),

$$\boldsymbol{\omega} = \text{curl}\ \mathbf{u} = \nabla \times \mathbf{u}, \tag{1.2}$$

and in magnitude is equal to twice the local angular velocity. Expanding equation (1.2) into its components in Cartesian coordinates gives

$$\omega_x = \frac{\partial \omega}{\partial y} - \frac{\partial v}{\partial z}, \tag{1.3}$$

$$\omega_y = \frac{\partial u}{\partial z} - \frac{\partial w}{\partial x}, \tag{1.4}$$

$$\omega_z = \frac{\partial v}{\partial x} - \frac{\partial u}{\partial y}, \tag{1.5}$$

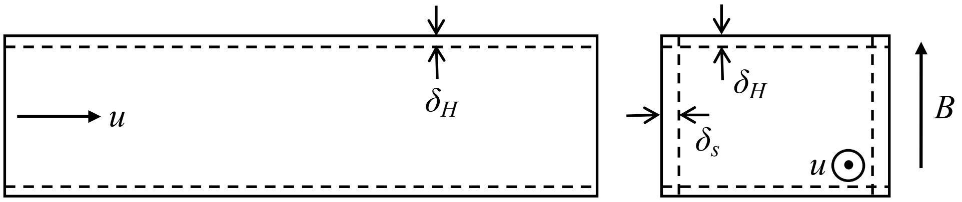

FIGURE 1.3: Subregions of the flow in a rectangular duct for Hartmann number $Ha \gg 1$. Left: A section of duct is viewed from side; Right: The duct is viewed in cross-section. The direction of the flow and magnetic field are indicated by arrows, and the Shercliff and Hartmann layers are also shown.

where in the context of this study (see Fig. 1.4), ω_x, ω_y and ω_z are refereed as streamwise, transverse and spanwise vorticity, respectively. In the case where the flow field is two–dimensional, only ω_z is non-zero, and therefore the rotational state of the flow is completely described by the z-vorticity component.

1.3.2 Prandtl Number, Péclet Number and Nusselt Number

Prandtl number provides a measure of the relative effectiveness of transport by diffusion of momentum and energy in the velocity and thermal boundary layers, respectively. It is the ratio of the momentum diffusivity to thermal diffusivity, and is defined as (Incropera *et al.* 2011)

$$Pr = \frac{\nu}{\alpha_d},$$

where α_d thermal diffusivity of the fluid. The value of Pr significantly influences the relative growth of the velocity and thermal boundary layers. Liquid metals are characterized by a small Prandtl number of the order 10^{-3} to 10^{-2}, which means that the energy diffusion rate greatly exceeds the momentum diffusion rate.

The contribution of heat transfer due to advection and diffusion is described by the Péclet number, which is defined as (Incropera *et al.* 2011)

$$Pe = \frac{ua}{\alpha_d} = \frac{1}{Re\ Pr}.$$

If the Péclet number is small, then the heat transfer is diffusion dominated, and it is advection dominated for large Péclet number. For fusion applications, Pe varies between 1 and 10^3 (Barleon *et al.* 2001).

The heat transfer at the surface boundary within a fluid is determined by the Nusselt number, which represent the ratio of convective to conductive heat transfer across the boundary (Incropera *et al.* 2011)

$$Nu = \frac{h_c a}{k},$$

where h_c is the convective heat transfer coefficient and k is the thermal conductivity. A Nusselt number close to unity means that convection and conduction are comparable, which is a characteristic of laminar flow. Small Nusselt numbers correspond to heat transfer dominated by conduction, whereas large Nusselt numbers correspond to heat transfer dominated by convection.

1.4 Overview of the Study

The present study considers the fluid flow and heat transfer of an electrically conducting, viscous and incompressible fluid (e.g. the eutectic alloy $GaInSn$) past a circular cylinder confined in a duct. The physical properties of $GaInSn$ are density $\rho = 6360$ kg m^{-3}, kinematic viscosity $\nu = 3.4 \times 10^{-7}$ m^2 s^{-1}, electrical conductivity $\sigma_e = 3.46 \times 10^6$ Ω^{-1} m^{-1}, thermal conductivity $k = 39$ W m^{-1} K^{-1} and specific heat $C_p = 320$ J kg^{-1} K^{-1}. The general configuration of the system investigated in this thesis is shown schematically in Fig. 1.4. It consists of a rectangular duct of constant aspect ratio with a cross section $(a \times h)$ with a circular cylinder of diameter (d) placed at variable distances from the centreline of the duct, aligned parallel to the magnetic field and perpendicular to the flow direction. The duct walls and the cylinder are assumed to be electrically insulated. A strong homogenous magnetic field is imposed along the cylinder axis. One of the walls located parallel to the magnetic field is heated to a constant wall temperature T_w whereas the other surfaces are kept at constant temperature T_0. A special case is also considered where a rotational oscillation is imposed on the cylinder to study the effect that has on the heat transfer into the fluid.

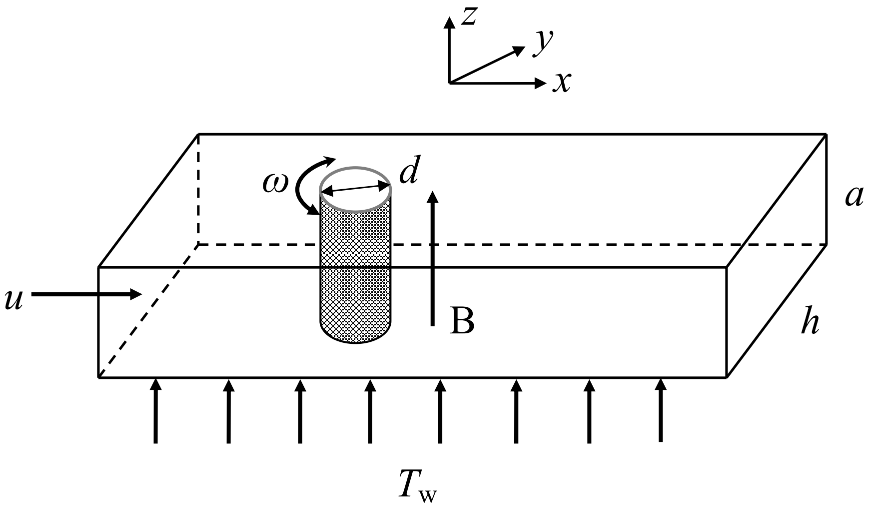

FIGURE 1.4: Schematic diagram and coordinates for the system under investigation in this study.

The control parameters in this study are the Hartmann number (Ha), Reynolds number (Re), blockage ratio (β), offset ratio from the duct centreline for the cylinder (γ), as well as the frequency of oscillation of the cylinder (f_e) and the angular amplitude (A) for the oscillating motion of the cylinder. The blockage ratio is defined as the ratio between the cylinder diameter and the duct height (i.e. $\beta = d/h$). The offset ratio specifies the separation between the body and the heated wall (i.e. $\gamma = \Delta/(h/2 - d/2)$), where Δ is the minimum distance from the surface of the cylinder to the nearest wall. The other dimensionless parameter used in this study is the Strouhal number ($St = f_s d/u$), where f_s is the shedding or wake frequency. The effect of varying these parameters on the flow characteristics and heat transfer enhancement is the major focus of this study.

1.5 Aims of the Study

The study aims to investigate the dynamics and heat transfer characteristics of a quasi–two–dimensional magnetohydrodynamic flow past a confined circular cylinder in a rectangular duct under a strong magnetic field. A parametric study is performed by changing the flow control parameters with a view to understanding and characterizing the flows and the downstream cross-stream mixing induced by the cylinder wake. Furthermore, the study aims to determine the values of the critical Reynolds number for the transition from steady to unsteady flow, Strouhal number, drag and lift coefficients, and heat transfer from the heated wall as a function of the control parameters.

A linear stability analysis and a transient growth analysis are to be applied to flows in the subcritical regime before the onset of vortex shedding, to determine the roles of global modes and optimal disturbances in the development of wake instabilities. The effects of Reynolds number, Hartmann number, and blockage ratio on the transient energy growth of disturbances in these flows will be considered. From this, it is hoped that a better understanding may be gained as to the fundamental mechanisms that govern transition to unsteady flow in this system.

In fusion blanket applications, Hartmann numbers are of the order of 10^4, which is beyond the range considered in this thesis. The work contained in this thesis is a fundamental study motivated by this application; the results should not be taken as being directly relevant to that specific application. The potential outcomes or benefits that may arise from this work include, for example, informing efforts to improve heat transfer and therefore efficiency in MHD cooling devices, and enhancing our understanding of flow transition in these systems.

1.6 Structure of the Thesis

The thesis is divided into eight chapters. Following the present introduction, chapter 2 provides a review of previous work from the literature relevant to the work undertaken in this thesis. This is followed in chapter 3 by a description of the numerical methodologies and their validation. Results are presented in chapters 4 to 7. Chapter 4 covers a numerical investigation of the flow and heat transfer past a circular cylinder in a rectangular duct. Chapter 5 details the investigation of fluid flow and heat transfer past a circular cylinder positioned offset from the duct centreline. Chapter 6 considers the optimal transient disturbances leading to vortex shedding. The details of heat transfer enhancement induced by rotationally oscillating the cylinder are presented in chapter 7. Conclusions are drawn in chapter 8, along with some suggested areas of future research relating to this thesis.

Chapter 2

A Review of the Literature

In this chapter, a review of the literature pertaining the work in this study is presented. Firstly, previous studies of the flow past a circular cylinder for the case without magnetic field are considered. This is followed by the magnetohydrodynamic flow past a circular cylinder exposed to a uniform magnetic field. Following these, studies into heat transfer enhancement in a channel for both hydrodynamic and magnetohydrodynamic cases are reviewed. Finally, studies of the transient growth analysis relating to these flows are discussed.

2.1 Flow past a Circular Cylinder

The flow past a circular cylinder in the absence of a magnetic field depends on the Reynolds number and whether the flow is bounded or unbounded by a plane channel. In a two–dimensional sense the flow can be classified into three configurations: unbounded flow past a cylinder, flow past cylinder near a wall, and the flow past a cylinder between two parallel walls. In the unbounded domain, the flow can be completely described by Reynolds number Re. However, when the circular cylinder is confined in a plane channel, the characteristics and the stability of the resulting flow changes significantly due to the blockage effect caused by the stationary walls of the plane channel. Therefore, the flow depends on Reynolds number and blockage ratio $\beta = d/h$ as the control parameters, where d is the cylinder diameter and h is the duct height.

2.1.1 Unbounded Circular Cylinder

As the Reynolds number is increased, the flow exhibits a sequence of three distinict two–dimensional regimes until the flow becomes three–dimensional beyond $Re \approx 180$. These regimes include creeping flow, separated flow, unsteady flow, and finally three–dimensional flow. Comprehensive reviews of experimental and numerical work pertaining to this flow are given in Williamson (1996) and Zdravkovich (1997, 2003).

2.1.1.1 Steady Flow

At very low Reynolds numbers the flow around a circular cylinder is dominated by viscous forces. The flow is steady and completely attached to the cylinder. The creeping flow persists without boundary layer separation up to $Re \simeq 5$ (Taneda 1956).

The characteristics of this flow were investigated experimentally by Taneda (1956), who used a glass water tank with aluminium dust suspended in the water to visualize the flow. The results demonstrated that the flow streaklines appear symmetrical upstream and downstream of the cylinder, and the flow has the property of being reversible as $Re \to 0$. An example of such a flow is shown in Fig. 2.1.

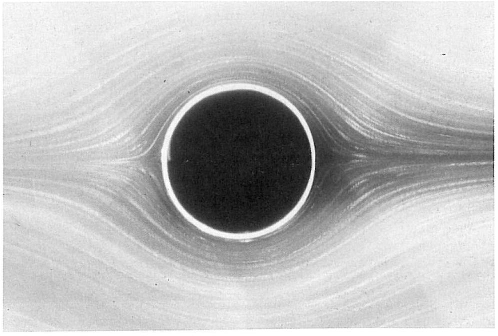

FIGURE 2.1: Creeping flow past a circular cylinder visualized by streaklines at $Re = 0.16$; from Van Dyke (1982). Flow is left to right, but nearly perfect reversibility makes this difficult to determine from photograph.

With increasing Re, the magnitude of viscous forces decreases until a topological change in the flow occurs with the separation of the flow at the downstream end of the cylinder, which results in the formation of a wake comprising of a pair of recirculating bubble zones. An example of this separated flow is shown in Fig. 2.2. The precise *Re* at which the flow separates is difficult to determine, due to the small size of the near-wake region and the low velocities in the vicinity of separation. In general, the onset of separated flow was predicted to occur somewhere within $5 < Re < 7$ (Taneda 1956; Takami & Keller 1969; Dennis & Chang 1970; Collins & Dennis 1973; Noack & Eckelmann 1994).

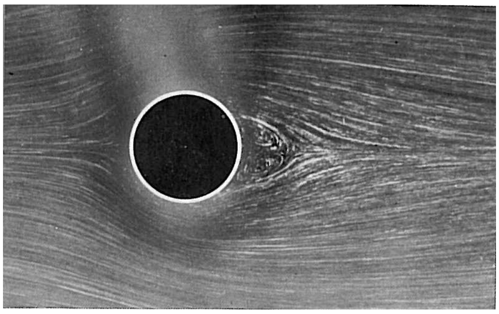

FIGURE 2.2: Separated flow past a circular cylinder at $Re = 13.1$; from Van Dyke (1982).

As Reynolds number is further increased, the steady symmetrical recirculation bubble observed in the wake, which comprises of a counter-rotating vortex pair, was found to grow approximately linearly with *Re* (Taneda 1956; Coutanceau & Bouard 1977a; Gerrard 1978). The recirculation bubble remains two–dimensional, steady and symmetrical about the cylinder centreline until $Re \approx 40$ where a transition to asymmetrical flow is observed. As the steady recirculation zones elongates, small oscillations were observed in the downstream region of the wake at $Re \approx 45$ (Taneda 1956). These oscillations precede the onset of unsteady flow, where vortices are shed alternately from the shear layer on the either side of the cylinder.

2.1.1.2 Unsteady Flow

The evolution of unsteady flow transients in the wake of a circular cylinder induced by an impulsive initiation of motion was investigated experimentally by Coutanceau & Bouard (1977b). They noticed a more rapid decay of transients at smaller Reynolds numbers. The vortex positions and separation angle were monitored and it was demonstrated that the transverse flow features evolved more rapidly than longitudinal flow features.

The stability of a two–dimensional steady flow past a flat plate and circular cylinder was considered experimentally and theoretically by Taneda (1963). The experiments were conducted in a water tank for a range of Reynolds numbers: $10 < Re < 600$ for a flat plate and $0.8 < Re < 60$ for a circular cylinder. From the measurements of wake oscillations, the critical Reynolds number below which all disturbances are damped out was $Re \approx 1$ for the flow past a circular cylinder. A theoretical analysis performed assuming parallel flow proposed a critical Reynolds number $Re \approx 3.2$ for all shapes of bluff body. However, oscillations were observed in the far-wake at $Re \approx 30$.

The detection of oscillations below the critical Reynolds number for unsteady flow can be explained by the nature of instability responsible for the evolution of the unsteady flow past a circular cylinder. The concepts of absolute and convective instability have been introduced by Provansal *et al.* (1987); Monkewitz (1988). In an absolutely unstable flow, a localized impulsive disturbance spreads in all directions and destabilizes the entire flow, whereas in a convectively unstable flow disturbances are convected away from their original position. While the disturbance grows as it convects downstream, it decays at its original position. The term local and global are also used depending on whether the instabilities develops on a local velocity profile or the whole flow field.

The stability of wake profiles for a circular cylinder at low Reynolds number was investigated by Monkewitz (1988). Stability calculations using these profiles predicted that at a Reynolds number of $Re \approx 2$ there was a transition from stability to the onset of convective instability, and at a critical Reynolds number of $Re \approx 25$ transition from convective to absolute local instability. These predictions agree with the measurements of unsteady transients downstream of the cylinder at $Re \approx 1$, and those of oscillations in the near-wake behind a circular cylinder at $Re \approx 25$ by Taneda (1963, 1956), respectively.

The critical Reynolds number for the transition from steady to unsteady flow past a circular cylinder have been found numerically to lie between $46.2 < Re < 54$. The critical Reynolds number was predicted using a low dimensional Galerkin method to be $Re \approx 54$ by Noack & Eckelmann (1994), $Re \approx 46.2$ from finite-element computations using Richardson extrapolation (Jackson 1987), and $Re \approx 47.1$ through application of the Landau model by Dušek *et al.* (1994). Recently, Morzyński *et al.* (1999) performed a highly accurate linear stability analysis computation that employed an eigensolution method for the flow past a circular cylinder, and a critical $Re = 47$ was predicted. Experimentally, the critical Reynolds number for the transition to unsteady flow past a circular cylinder has been found to vary between 47 and 49 (Williamson 1988; Norberg 1994; Williamson 1996).

Thus, at a Reynolds number of $Re \approx 47$, the flow becomes unsteady (Taneda 1956; Provansal *et al.* 1987; Jackson 1987; Henderson 1997; Dušek *et al.* 1994; Williamson 1996). The oscillation at the end of the near-wake starts to initiate a sinuous wave which propagates along the boundary of the wake recirculation in the downstream direction. The transition from steady two–dimensional flow to time dependent flow is often refereed as the *primary instability* due to an absolute instability which develops in the near-wake region (Henderson 1997). In mathematical terms, the flow is found to undergo a supercritical Hopf bifurcation that takes place without hysteresis (Provansal *et al.* 1987; Noack & Eckelmann 1994), and the wake in this regime takes the form of two–dimensional period oscillatory flow.

As the Reynolds number is increased beyond the Hopf bifurcation, the wake shear layers roll up and vortices are shed downstream from the rear of the cylinder to form the classical Bénard-von Kármán vortex street. An example of the Kármán vortex street is shown in Fig. 2.3. The vortex street is comprised of a double row of vortices that shed alternatively and regularly from both sides of the cylinder. For the range of Reynolds number $49 \lesssim Re \lesssim 150$, the wake flow field is purely two–dimensional in nature and the vortex shedding is refereed as laminar shedding.

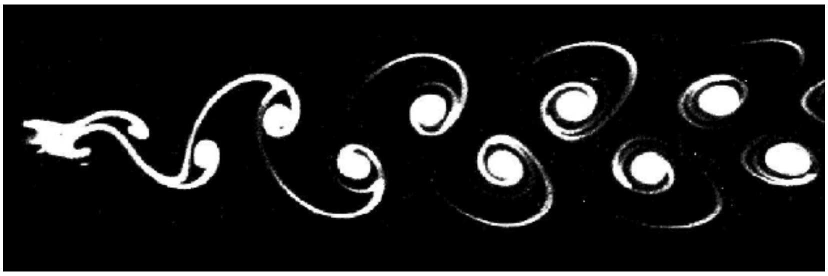

FIGURE 2.3: Kármán vortex street behind a circular cylinder at $Re = 105$; from Van Dyke (1982).

2.1.1.3 Instabilities of the Vortex Street

For the laminar shedding regime in the wake behind a circular cylinder, there have been a number of efforts to obtain the relationship between Strouhal number and Reynolds number. Roshko (1954) measured the vortex shedding frequencies past circular cylinders of different diameters in a wind-tunnel. He obtained a continuous curve describing the variation of Strouhal versus Reynolds number over the range $50 \leq Re \leq 150$ in the form

$$St = 0.212 - \frac{4.5}{Re}$$

However, later measurements by Tritton (1959) found a discontinuity in the Strouhal–Reynolds number curve resulting in a drop in the Strouhal number of around 5% for Reynolds number above the discontinuity, suggesting that a transition in the vortex street occurred at $Re \approx 90$. He proposed that this transition was due to a shift between the vortex street axis and that of the cylinder. From the flow visualization images provided in that study, it was proposed that the there was a low-speed mode that developed from an instability of the wake, and a high speed-mode that developed as a result of the interaction between the flow and the cylinder surface. Tritton (1971) repeated his experiment in a wind tunnel to verify the existence of the transition at $Re \approx 90$. A transition was found at $Re = 110$, and it was proposed that this discrepancy in the transition Reynolds number was caused by the different experimental conditions.

The experimental results performed by Gaster (1971) on the flow past a tapered cylinder found a discontinuity in the Strouhal–Reynolds number profile at $Re \approx 100$. It was suggested that the non-uniform flow along the cylinder span can produce a vortex street consisting of a number of cells with different frequencies in each cell, and the cell positions moved along the span with changes of velocity. The results suggested that the Strouhal–Reynolds number discontinuities reported by Tritton (1959, 1971) were due to the formation and movement of cells in non-uniform flow.

Later, the discontinuity in the Strouhal–Reynolds number profile was found to be caused by the development of oblique shedding in the wake (Williamson 1988, 1989; Hammache & Gharib 1991). The oblique vortices formed a periodic chevron pattern at an angle to the spanwise direction observed in this regime. It was found that the boundary conditions at the spanwise ends of the cylinder affect the angle of shedding even for a long cylinder. Williamson (1988, 1996) showed that the inclination of the vortex shedding to the axis of the cylinder caused a reduction in the Strouhal number of shedding, and if the Strouhal number was corrected according to the angle of oblique shedding, a continuous Strouhal–Reynolds number curve was obtained.

Further, it was demonstrated that the transition from parallel to oblique vortex shedding street in the wake of the circular cylinder is sensitive to the end conditions of the cylinder such as end plates or base suction (Triantafyllou 1992; Albarède & Monkewitz 1992; Williamson & Miller 1994; Leweke & Provansal 1995), which was proposed to decrease the local stability of the near-wake at the ends of the cylinders (Monkewitz 1996). As will be described in the next chapter, the flows are modelled as quasi–two–dimensional by averaging the equations of motion along the magnetic field direction for MHD flows modelled in this thesis, and hence features such as oblique shedding and vortex dislocations (Williamson & Miller 1994) will not be considered in this thesis.

2.1.2 Three–Dimensional Flow

The transition from the laminar vortex shedding to three–dimensional shedding can be observed through measurements of Strouhal number as a function of Reynolds number as shown Fig. 2.4, where the Strouhal number can be seen to drop rapidly at $Re \approx 180$. This rapid transition is referred as the *secondary instability* of the steady flow past a circular cylinder. Roshko (1993) and Williamson (1996) observed that the upper limit of Reynolds number for this transition was found to vary considerably over the range $Re = 140 - 190$. It was proposed that factors such as cylinder roughness, free-stream turbulence amplitude, blockage and end effects shift the transition of the laminar two–dimensional wake to a lower Reynolds number (Williamson 1996).

Williamson (1988) observed that the transition to three-dimensionality begins with the formation of a regular three–dimensional flow structure known as mode A. This is characterized by a wavy deformation of the primary vortex cores during the process of shedding. Three–dimensional disturbances are suppressed in the system considered in this thesis, so they will not be discussed further here. The interested reader is directed to the excellent review by Williamson (1996) for more information.

2.1.3 Higher Reynolds Number Flow: Shear Layer Instabilities

For a high Reynolds number, the distortion of the wake increases due to the presence a shear flow instabilities. The shear flow instabilities develop by the action of the Kelvin–Helmholtz mechanism that causes the shear layer to be wavy. It was demonstrated that the turbulent flow emerges increasingly in the wake to form small scale vortical structures for $Re \gtrsim 300$ (Bloor 1964; Unal & Rockwell 1988; Williamson 1996; Henderson 1997; Prasad & Williamson 1997). The development of turbulence in the wake of a circular cylinder was well described by Bloor (1964), who found that the transition point from laminar to turbulent flow in the shear layer moved upstream towards the cylinder with increasing Reynolds number.

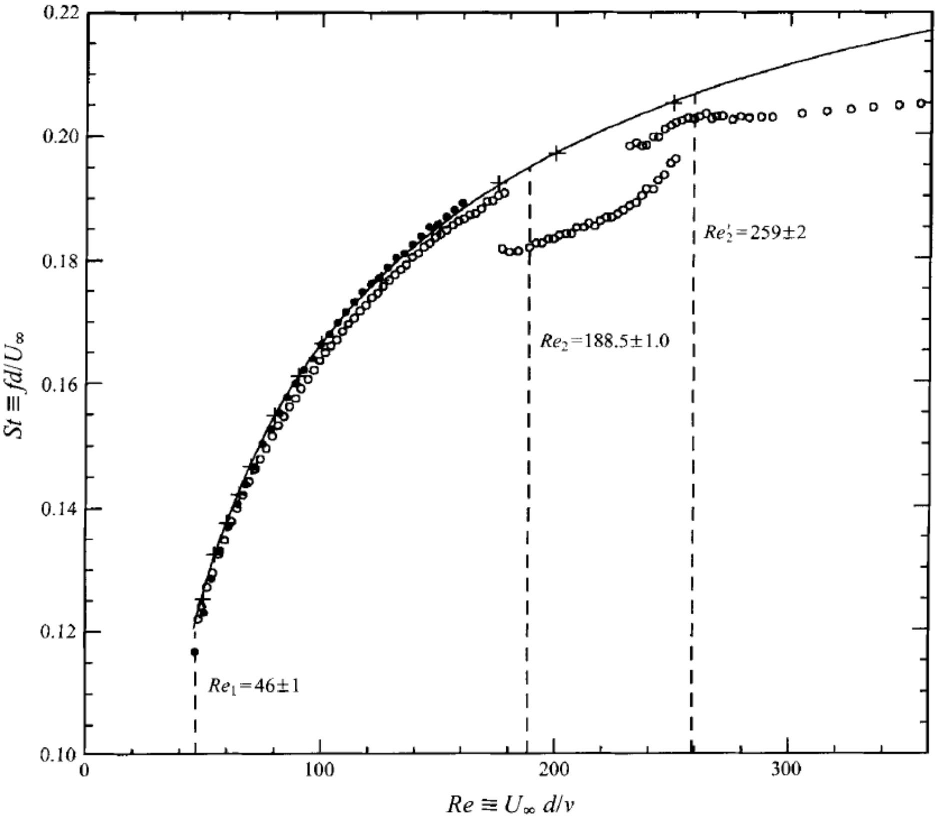

FIGURE 2.4: Strouhal–Reynolds number profile over laminar and three–dimensional transition regimes, reproduced from Barkley & Henderson (1996). Two distinct discontinuities in the Strouhal frequency are clearly shown as Reynolds number is increased. Shown are experimental results: ○, Williamson (1989); ● Hammache & Gharib (1991) and numerical results: +, Barkley & Henderson (1996).

At $Re \geq 2 \times 10^5$, a dramatic drop in both the base pressure and drag coefficients are observed as the critical transition in the wake occurs. This is due to formation of a separation-reattachment bubble in the shear layer. The flow past a circular cylinder at the critical transition was described by Roshko (1993) to experience a separation followed by reattachment, which finally allowed a separation at approximately 140° from the front of the cylinder. This resulted in a narrow wake, which in turn reduced significantly the drag and base pressure coefficients. The sharp drop in the base pressure is illustrated in Fig. 2.5. The flow below this critical transition is referred as subcritical flow where neither separation nor reattachment occurs, while the flow beyond this transition is referred as supercritical flow, where the separation-reattachment bubble is formed. However, periodic fluctuations in the wake were still detected.

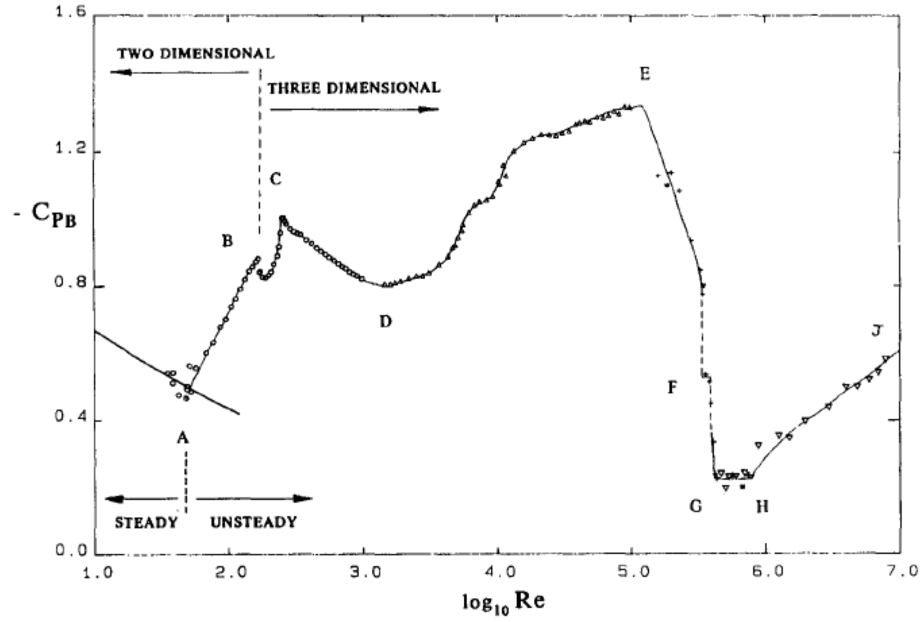

FIGURE 2.5: The base suction pressure coefficients as a function of Reynolds number; from Williamson (1996).

2.1.4 Circular Cylinder near a Wall

When a cylinder is placed adjacent to a plane wall, though the wall induces an irrotational effect on the flow, the resemblance with the unbounded case remains pertinent. The flow characteristics in the wake of a circular cylinder placed near the plane wall at different gap ratio γ has been investigated by Bearman & Zdravkovich (1978); Taniguchi & Miyakoshi (1990); Lei *et al.* (1999); Price *et al.* (2002); Wang & Tan (2008). The results showed when a cylinder approached near the wall, the forces on the cylinder and the shedding frequency were changed. The vortex shedding was suppressed for small gap ratio $\gamma \leq 0.3$. For a large gap ratio, the flow parameter such as Strouhal number remained remarkably constant and independent of the gap ratio. For intermediate gap ratios $0.3 \leq \gamma \leq 0.6$, the effect of the wall was found to be substantial, resulting in the flow developing a distinguishable asymmetry around the cylinder centerline. A review of further experimental and numerical works are given by Lei *et al.* (2000).

2.1.5 Confined Circular Cylinder

In contrast to the previous cases, the flow past a circular cylinder confined in a plane channel has received much less attention. In the case of a cylinder confined between parallel walls, two additional parameters control the dynamics of the wake, the blockage ratio ($\beta = d/h$) and the gap ratio ($\gamma = \Delta/(h/2 - d/2)$), where h and Δ are the distance separating the two walls and the minimum distance between the cylinder and the nearest wall, respectively. It has been demonstrated that the presence of the walls significantly affect hydrodynamic forces, Strouhal number, wake structure, and the first and second instabilities of vortex shedding (Taneda 1965; Coutanceau & Bouard 1977a,b; Sahin & Owens 2004; Rehimi *et al.* 2008; Camarri & Giannetti 2010; Rehimi & Aloui 2011).

2.1.5.1 Steady Flow

For a steady flow past a confined circular cylinder, the critical Reynolds number at which twin vortices appear in the wake has been found to occur at higher Reynolds numbers than that of unbounded cylinder (Coutanceau & Bouard 1977a; Anagnostopoulos *et al.* 1996). The flow downstream of the cylinder is comprised of two fixed counter-rotating vortices located behind the cylinder with opposite-sign vorticity at the adjacent walls.

The development of the wake bubble with Reynolds number at different blockage ratios has been investigated experimentally by Grove *et al.* (1964); Acrivos *et al.* (1968); Coutanceau & Bouard (1977a). The results by Grove *et al.* (1964), which were carried out in a tunnels of rectangular cross section over a range of blockage ratio $0.025 \leq \beta \leq 0.2$, indicated that the wake bubble length varied approximately linearly with Reynolds number with a slope depending on the blockage ratio. It was proposed that the slopes of the wake bubble length versus Reynolds number increased as blockage ratio was increased. In contrast, the results by Coutanceau & Bouard (1977a), which were performed in a tunnel of circular cross section over a range of blockage ratios $0.024 \leq \beta \leq 0.12$ proposed that there was a constant slope with different blockage ratios.

The length of the wake-bubble and the separation angle were found to decrease considerately as blockage ratio was increased, while the drag force was increased with increasing the blockage ratio (Grove *et al.* 1964; Chakraborty *et al.* 2004; Chen *et al.* 1995; Anagnostopoulos *et al.* 1996). Furthermore, for the case of a cylinder offset from the centreline, the growth rate of the recirculation zone was found to depend on the blockage and the gap ratios, it grew more slowly as the cylinder approaches one wall (Zovatto & Pedrizzetti 2001; Hsieh & Chen 2006).

2.1.5.2 Unsteady Flow

The effects of wall confinement on the vortex street behind a circular cylinder was investigated experimentally for a range of blockage ratios $0.33 \leq \beta \leq 0.66$ by Taneda (1965), who used a water tank with aluminium dust suspended in the water to visualize the flow. The results showed that the presence of walls acts to increase the instability of the wake and to squeeze the vortex street. The critical Reynolds number Re_c at which vortex shedding appears (i.e. the primary instability) was found to increase with increasing the blockage ratio. However, it was stated that the critical Reynolds number for this transition was difficult to determine precisely.

Behr *et al.* (1995) investigated numerically the influence of the location of the walls on the vortex shedding for the flow past a circular cylinder. The case of $Re = 100$ was chosen as a benchmark. The computations were performed with a space-time velocity-pressure formulation and a velocity-pressure-stress formulation. It was found that the distance between the cylinder and the lateral boundaries have a significant effect on Strouhal number and the hydrodynamic force coefficients C_D and C_L. They proposed that the minimum distance at which this influence vanished was 8 cylinder diameters.

Chen *et al.* (1995) studied numerically the bifurcation for the flow past a circular cylinder between parallel plates. The study focused on the mechanism by which the steady flow past a cylinder at small Reynolds loses stability as the Reynolds number was increased over a range of blockage $0.1 \leq \beta \leq 0.7$. The resulting time-dependent motions were examined to determine the critical Reynolds number in which perturbation was amplified leading to unsteady flow. The numerical results revealed that steady flow past a confined cylinder loses stability with increasing Reynolds number through a symmetry-breaking Hopf bifurcation with the value of critical Reynolds number at bifurcation depending on the blockage ratio. The critical Reynolds number characterizing the primary instability was found to increase with increasing blockage ratio until $\beta = 0.5$, thereafter decreasing.

The effect of the blockage ratio on the vortex street structure and flow parameters behind a circular cylinder placed between a plane channel was investigated numerically by Anagnostopoulos *et al.* (1996) for $Re = 160$ and blockage ratios $0.05 \leq \beta \leq 0.25$. The results demonstrated that the spacing of the vortices decreased in both the longitudinal and lateral directions as the blockage ratio was increased. In addition, they found that for a fixed Reynolds number, hydrodynamic forces and Strouhal number increased as blockage ratio increased. The effects were more pronounced at higher blockage ratio: an increment of 90% in the amplitude of lift force was reported as β was changed from 0.05 to 0.25.

The inversion of the Kármán vortex street was firstly reported by Zovatto & Pedrizzetti (2001), who used a finite-element method based on the vorticity–streamfunction formulation to analyse the flow past a circular cylinder placed inside a channel at different distance from the walls. The blockage ratio was kept constant at $\beta = 0.2$, and the range of Reynolds number was below the appearance of three–dimensional instabilities. The results showed that the transition from steady to unsteady flow was significantly delayed, and the critical Reynolds number for this transition was found to occur at higher Reynolds number as the cylinder approached one wall. This was due to the interaction of the Kármán vortices with the wall boundary layer, which presents an obstacle impeding their motion. Suppression of vortices was observed for a sufficiently small gap ratio. It was proposed that for a distances smaller than the cylinder diameter, the Kármán street changed to a single row of same sign vortices. This was due to the fact that the negative and positive vortices separated from the cylinder and from the wall formed a pair vortex sheet, which was dissipated during the induced stretching.

Sahin & Owens (2004) performed a stability analysis of a confined cylinder placed symmetrically between two parallel walls over a wide range of blockage ratios $0.1 < \beta \leq 0.9$ and Reynolds number $Re \leq 280$. The effects of the lateral wall proximity on stability, Strouhal number, hydrodynamic forces, and the wake structure were investigated. The curves of neutral stability $\beta - Re$ computed using a Krylov subspace method reproduced in Fig. 2.6. For $\beta \lesssim 0.85$, a critical Reynolds number was predicted at which a supercritical Hopf-bifurcation of a symmetric state was occurred. At Reynolds number beyond the first critical Reynolds number and $\beta \gtrsim 0.69$, a second curve of pitchfork bifurcation was observed. For $\beta \gtrsim 0.82$, the steady asymmetric flow lost its stability through Hopf-bifurcation. A transition from symmetric vortex shedding to asymmetric vortex shedding was reported to occur as blockage ratio was increased. Very strong vortices shed from the cylinder were observed, and the Strouhal frequency of the shedding was found to increase with increasing Reynolds number and blockage ratio.

The momentum and heat transfer from an asymmetrically confined circular cylinder in a plane channel was investigated numerically using FLUENT by Mettu *et al.* (2006) for a range of Reynolds number $10 \leq Re \leq 500$, blockage ratio $0.1 \leq \beta \leq 0.4$, and gap ratio $0.125 \leq \gamma \leq 1$. The critical Reynolds number for the transition from steady to unsteady flow was predicted as a function of blockage and gap ratio. For all the blockages tested, it was found that the critical Reynolds number increased as the cylinder approached one wall. However, the drag coefficient and Strouhal number were found to increase with decreasing the separating distance between the cylinder and the wall. The amplitude of oscillation of the lift coefficient was found to increase in the negative direction as this distance was increased, while it was completely suppressed when the cylinder approached one wall. The effect of separation distance between the cylinder and the wall on the Nusselt number around the cylinder was found to be negligible for all blockage ratios.

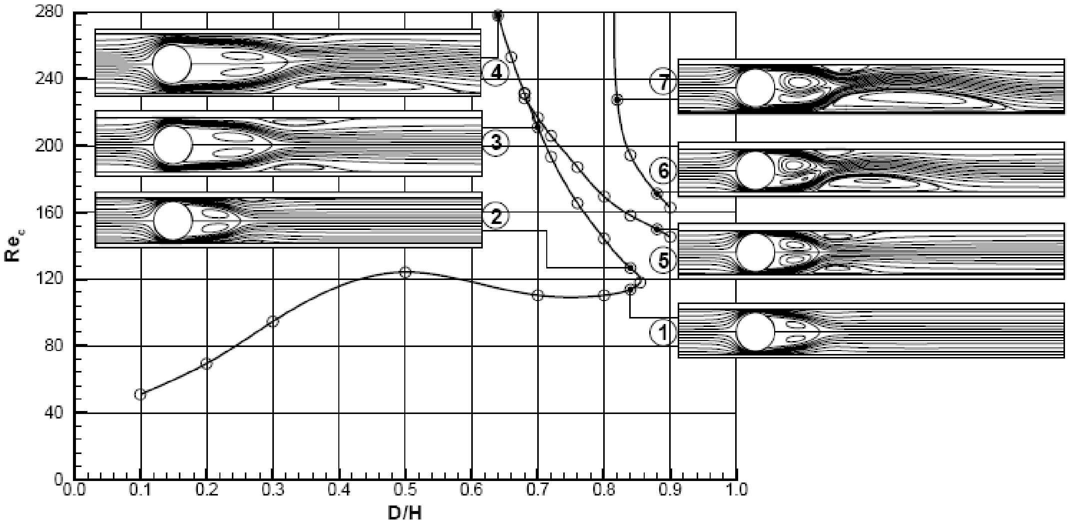

Figure 2.6: Neutral stability curve $\beta - Re$ along with the change of the base flow with Reynolds number and blockage ratio; from Sahin & Owens (2004).

2.1.5.3 Three–Dimensional Flow

Studies investigating three–dimensional effects in the flow behind a confined circular cylinder are relatively scarce. Only a few studies quite recently focused on the development of three–dimensional effects for the flow past a circular cylinder placed symmetrically in a plane channel at blockage ratio $\beta \leq 0.5$. Similar instabilities are found to what is seen behind an unbounded cylinder, and the wake inversion has no significant effect on the stability since the core of the instability modes were located in the near-wake region (Camarri & Giannetti 2010; Griffith *et al.* 2011; Rehimi *et al.* 2008; Rehimi & Aloui 2011). The differences between the confined and unconfined case is shown together with the spanwise vorticity of the base flow in Fig. 2.7.

2.2 MHD Flow past a Circular Cylinder

The characteristics of magnetohydrodynamic flow past a circular cylinder exposed to a uniform external magnetic field where the magnetic Reynolds number is much

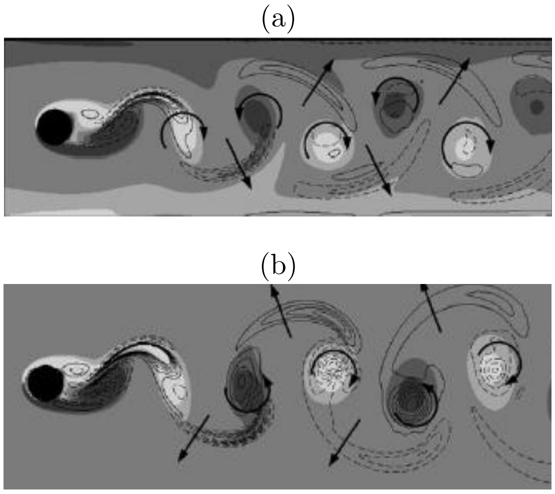

Figure 2.7: The spanwise vorticity of the base flow along with the streamwise vorticity of mode A in confined (a) and unconfined (b); from Camarri & Giannetti (2010).

smaller than unity ($Re_m \ll 1$) is reviewed. Depending on the direction of the applied field, different kinds of flow configurations and transition mechanisms exist. The orientation of the magnetic field in MHD cylinder wakes can be streamwise, transverse or spanwise. In all configurations, the magnetic field tends to enhance the flow stability, shifts the critical Reynolds numbers for flow separation and the transition to unsteadiness to higher values, and to invoke the vortices along the magnetic field direction. Furthermore, the location of the Hartmann and Shercliff layers depends on the orientation of the magnetic field.

2.2.1 Streamwise Magnetic Field

The case where the direction of the magnetic field is parallel to the streamwise direction has been investigated numerically by Shatrov *et al.* (1997); Mutschke *et al.* (1997, 1998, 2001); Yoon *et al.* (2004); Sekhar *et al.* (2005, 2007); Grigoriadis *et al.* (2010) and experimentally by Lahjomri *et al.* (1993); Josserand *et al.* (1993).

The evolution of the pressure coefficient C_{pb} around a circular cylinder in an MHD flow aligned with a magnetic field was investigated experimentally by Josserand *et al.* (1993) for a range of interaction parameter $0 \leq N \lesssim 8$ and Reynolds number up to 34000. A non-monotonic behaviour of C_{pb} against N was observed. For $N \lesssim 1$, the base pressure was found to increase compared to the non-MHD case, while it decreased due to the dominance of Joule dissipation for higher values of N. They found that this decreasing was scaled with $\sqrt{N}$.

The effect of a magnetic field on unsteady and two–dimensional MHD flow past a circular cylinder was investigated by Shatrov *et al.* (1997), who used a finite difference method based on a stream function vorticity formulation to analyse the flow over a range of $Re < 2000$ and magnetic interaction parameter $N < 10$. Two cases of a magnetic field aligned both with and transverse to the flow were considered. Their results demonstrated that the vortex street was damped, the recirculation bubble length and the separation angle were decreased as the magnetic field strength was increased. The influence of the transverse field was found to be more pronounced than with the streamwise alignment. The recirculation length was completely suppressed and the flow approached a potential flow for a high transverse magnetic field, while the recirculation did not disappear for the parallel magnetic field case. A stability curve for the streamwise and transverse fields in $Re - N$ space for the transition from steady to unsteady flow was proposed. A similar remark is to be found in Lahjomri *et al.* (1993), who investigated experimentally the wake of a circular cylinder subjected to an external streamwise magnetic field.

Mutschke *et al.* (1997, 1998) numerically investigated the effect of a magnetic field on the two–dimensional and three–dimensional instabilities in the wake of a circular cylinder. The cylinder was placed in an electrically conducting fluid and exposed to a uniform magnetic field. The range of Reynolds number and interaction parameter were $100 < Re < 250$ and $N \leq 10$, respectively. Both streamwise and transverse magnetic field directions were considered. A strong magnetic field was found to stabilize the two–dimensional flow and to suppress the vortex shedding of the wake. Furthermore, a linear stability analysis were performed for both the steady and periodic base flow to investigate the influence of the magnetic field on the three–dimensional instabilities of the MHD cylinder wake. A reversal of the order of instabilities was reported in which three–dimensional instability was predicted to occur at lower Reynolds number than that of two–dimensional instabilities.

Later, Mutschke *et al.* (2001) extended their previous results of the linear stability analysis (Mutschke *et al.* 1997, 1998). Their study focused on the mechanism of three–dimensional transition in the magnetohydrodynamic cylinder wake when the oncoming flow and the magnetic field were parallel. A non-monotonic behaviour of three–dimensional disturbance versus the interaction parameter was observed. It was found that for small values of the interaction parameter the instability was either damped or amplified, and was dependant on the Reynolds number. For a strong magnetic field, three–dimensional instability was amplified and the cylinder wake was found to exhibit three–dimensional steady flow. The critical Reynolds number for this transition was predicted to occur at $Re \approx 150$, which was lower than the critical Reynolds number for the onset of mode A instability in the hydrodynamic cylinder flow.

The characteristics of two–dimensional MHD flow and heat transfer past a circular cylinder in an aligned magnetic field were investigated numerically by Yoon *et al.* (2004) using a spectral element method for Reynolds numbers of 100 and 200 and Prandtl numbers of 0.7 and 7 in the range of interaction parameter $0 \leq N \leq 10$. The details of flow and thermal parameters on the cylinder surface was reported. The influence of magnetic field was found to damp the oscillation of the vortex shedding behind the cylinder and to decrease the amplitude of oscillation of lift and drag coefficients. The temperature field and thus Nusselt number that characterise the heat transfer from the cylinder surface were found to vary significantly with the intensity of the magnetic field.

Using a finite difference method, Sekhar *et al.* (2005, 2007) studied numerically the flow of a steady and unsteady two–dimensional conducting fluid around a circular cylinder with a magnetic field oriented parallel to the flow direction for Reynolds numbers $40 \leq Re \leq 500$ and interaction parameters $0 \leq N \leq 15$. It was found that the separation bubble length and separation angle was decreased as the magnetic field strength was increased. The pressure drag coefficient, total drag coefficients, and the pressure at the rear stagnation point were found to vary with $\sqrt{N}$ for $Re \leq 40$. For small values of the interaction parameter $N \lesssim 0.1$, the upstream and downstream pressures on the surface of the cylinder was observed to increase. For $100 \leq Re \leq 500$, the upstream pressure increased slightly with increasing of N whereas downstream it decreased.

Grigoriadis *et al.* (2010) performed a three–dimensional numerical simulation using an immersed boundary method (IB) for the flow of a conducting fluid past a circular cylinder under a streamwise and transverse magnetic field. The range of Reynolds number was up to $Re \leq 200$ with a magnetic interaction parameter $0 \leq N \leq 5$. The study was focused on the performance of the IB method for the computation of MHD flows in complex geometries. A non-monotonic variation of the drag coefficient and recirculation bubble length was reported, and the drag coefficient was found to be smaller than the corresponding hydrodynamic value. Their results for the critical interaction parameter, Strouhal frequency, the drag and lift coefficients and the recirculation length were in a good agreement with the results by Mutschke *et al.* (1997). The reversal of stability order detected by Mutschke *et al.* (2001) was also verified in this study. In the case with a transverse magnetic field, the damping effect on the vortex street was found to be stronger than that of streamwise case.

2.2.1.1 Transverse Magnetic Field

The number of studies dedicated to investigate the effect of a perpendicular magnetic field on the flow around circular cylinder are small. It has been investigated experimentally by Kolesnikov & Tsinober (1971, 1976) and numerically by Mutschke *et al.* (1998, 2001); Grigoriadis *et al.* (2010). These results indicate that the effect of magnetic forces on the flow parameters in this configuration were much stronger than that of the streamwise case. Therefore, the vortex shedding is damped faster and the recirculation length is completely suppressed.

2.2.2 Spanwise Magnetic Field

The focus of present study is the case where the magnetic field is aligned parallel to the cylinder axis. This case has received little attention to date. This case has been investigated experimentally by Kit *et al.* (1969, 1970); Kolesnikov &

Tsinober (1972b); Andreev & Kolesnikov (1997b,a); Frank *et al.* (2001) and numerically by Muck *et al.* (2000); Ueno *et al.* (2001); Dousset & Pothérat (2008); Hussam *et al.* (2011).

The measurements of velocity fluctuations with a conduction anemometer conducted by Kit *et al.* (1969, 1970) for the wake behind a cylinder placed in a channel in the presence of a magnetic field parallel to the cylinder axis reported that the magnetic field significantly affected the instability behind the cylinder in different ways. The experiments were carried out with mercury in a channel with height of 0.04 m and the cylinder diameter was 10 mm. The Reynolds number was up to $Re \approx 17500$ with a magnetic interaction parameter $0.009 \leq N \leq 1.33$. It was found that the magnetic field considerably amplified the intensity of the disturbances whose axis was parallel to the field, while the intensity of the disturbances whose axis was perpendicular to the field was predicted to be less than the noise of the flow. The intensification of disturbances was reported to occur at $Ha \simeq 0.97Re^{1/2}$.

The characteristics of a turbulent flow in the wake behind a circular cylinder with the axis parallel to a strong magnetic field was studied experimentally by Kolesnikov & Tsinober (1972a). Their experiments were carried out in a horizontal mercury channel similar to that described in Kit *et al.* (1969, 1970). A conduction anemometer and a thermoanemometer were used for the velocity measurements. It was demonstrated that under a strong magnetic field the flow acquired the characteristics of two–dimensional turbulent flow with an energy transfer from small to large scale structures.

Andreev & Kolesnikov (1997a,b) investigated experimentally the flow of an eutectic alloy *GaInSn* around a conducting cylinder placed in a rectangular non-conducting channel in the presence a homogeneous magnetic field parallel to the cylinder axis. The velocity and spectrum measurements were used to determine the instability around the cylinder. The cylinder diameter was 10 mm and the cross section of the duct was 40 × 40 mm, which yielded a blockage ratio of $\beta = 0.25$. The range of Reynolds number and Hartmann number were $0 \leq Re \leq 6000$ and $0 \leq Ha \leq 2160$, respectively. Their measurements indicated that the critical Reynolds number for the onset of vortex shedding in a strong magnetic field was found to increase fortyfold compared to the case without magnetic field, and the drag coefficient around the cylinder decreased threefold as the intensity of the magnetic field was increased. The results also demonstrated that the presence of a Hartmann friction on the walls perpendicular to the field influenced significantly the characteristics of the flow around the cylinder. The separation of the attached vortices around the cylinder was observed to be delayed. However, the instability developed in the shear layer parallel to the field which envelops the cylinder and thus was not affected considerably.

Using an array of potential probes in the Hartmann walls to visualize the flow, Frank *et al.* (2001) investigated experimentally a wake behind circular cylinder of quasi two-dimensional eutectic alloy *GaInSn* in rectangular duct for the condition of high Reynolds and Hartmann numbers. The blockage ratio was kept constant at $\beta = 0.1$ for a range of Reynolds number100 $\leq Re \leq$ 10000 and Hartmann number $500 \leq Ha \leq 1200$, which gave an interaction parameter between $10 \leq N \leq 576$. The test section was comprised of an insulated circular cylinder of diameter $d = 6$ mm which was inserted between an electrically insulated Hartmann walls as shown in Fig. 2.8.

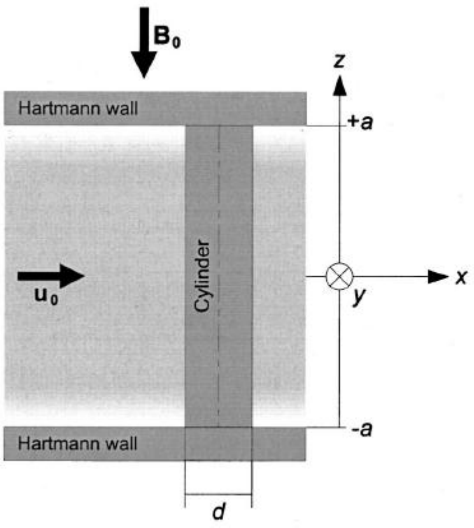

FIGURE 2.8: The geometry of the quasi-two–dimensional cylinder wake; from Frank *et al.* (2001).

They proposed a linear dependence of critical Reynolds number on Hartmann number, $Re_c/Ha \approx 0.94$, for the onset of time-dependent vortex shedding. From the visualization of the vortex street behind the cylinder, a breakup of the two-dimensional vortex street was observed to occur at $Re = 5000$, and the value of critical Reynolds number was increased as Ha was increased. The authors conclude that the dissipation of vortex energy was not achieved by a cascade towards smaller structures, but instead by the typically quasi–two–dimensional (Q2D) linear damping term, which led to a continuous decrease in vortex intensity. For a fixed Reynolds number, a minimal decrease (-0.02) of the Strouhal number was measured when the Hartmann number was doubled. A stability diagram for the onset of vortex shedding was also determined in this study as shown in Fig. 2.9

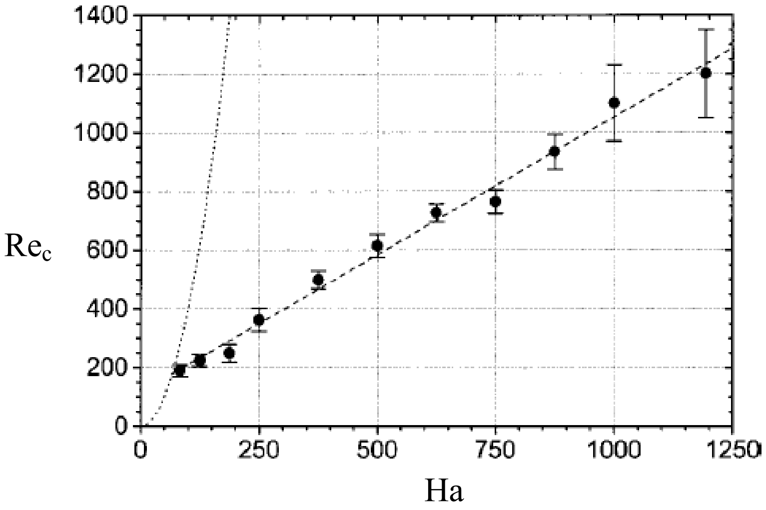

FIGURE 2.9: The stability curve $Re_c - Ha$ of the quasi–two–dimensional cylinder wake for $\beta = 0.1$. The dotted line is for $N = 10$ curve. This image is reproduced from Frank *et al.* (2001).

For the same configuration, Muck *et al.* (2000) performed a three dimensional DNS for a liquid metal flow around a square cylinder placed in a rectangular channel. Current sheets with infinitesimal thickness were used to represent the Hartmann layers. The interaction parameter and Hartmann number were varied in the range $0 \leq N \leq 36$ and $0 \leq Ha \leq 85$, respectively. The numerical simulations were carried out for two fixed values of Reynolds number $Re = 200$ and 250 with a constant blockage ratio $\beta = 0.1$. A transition from a time dependent three–dimensional flow to a time dependent quasi–two–dimensional flow was found to occur for $N \gtrsim 1$, which confirms the experimental finding of Kolesnikov & Tsinober (1972a). A complete damping of vortex shedding was observed at a high value of the interaction parameter as shown in Fig. 2.10 , which was in a good agreement with the experimental finding by Frank *et al.* (2001). The features of quasi–two–dimensional predicted by Sommeria & Moreau (1982) in which the vortices have their ends perpendicular to the Hartmann walls was also confirmed by three–dimensional visualization in this study.

A similar problem was studied by Ueno *et al.* (2001), who performed a three dimensional direct numerical simulation of magnetohydrodynamic flow past a rectangular column placed in a channel to investigate the spatial development of vortex shedding between insulated Hartmann walls for Reynolds number $Re = 250$ and 500 for a range of Hartmann number $10 \leq Ha \leq 30$. Their results reported that three–dimensional vortices was reduced to quasi–two–dimensional vortices downstream by magnetohydrodynamic diffusion under a strong magnetic field.

More recently, Dousset & Pothérat (2008) studied numerically the wake behind a circular cylinder of quasi two-dimensional liquid metal flow placed in a square duct under a strong magnetic field parallel to the cylinder axis. The duct walls and the cylinder were insulated. The blockage ratio was kept constant at $\beta = 0.25$. The simulations were carried out over a range of Reynolds number $0 \leq Re \leq 6000$ and Hartmann number in the range $0 \leq Ha \leq 2160$. The resulting flow was found to exhibit a sequence of four regimes and the transitions between these regimes were controlled by friction parameter Re/Ha. The first three regimes were found to be similar to those of two dimensional cylinder wakes without magnetic field. The last regime was characterized by an irregular Kármán vortex street where the vortices generated with the Shercliff layers separated from the side walls and interacted with the flow regime of the regular Kármán vortex

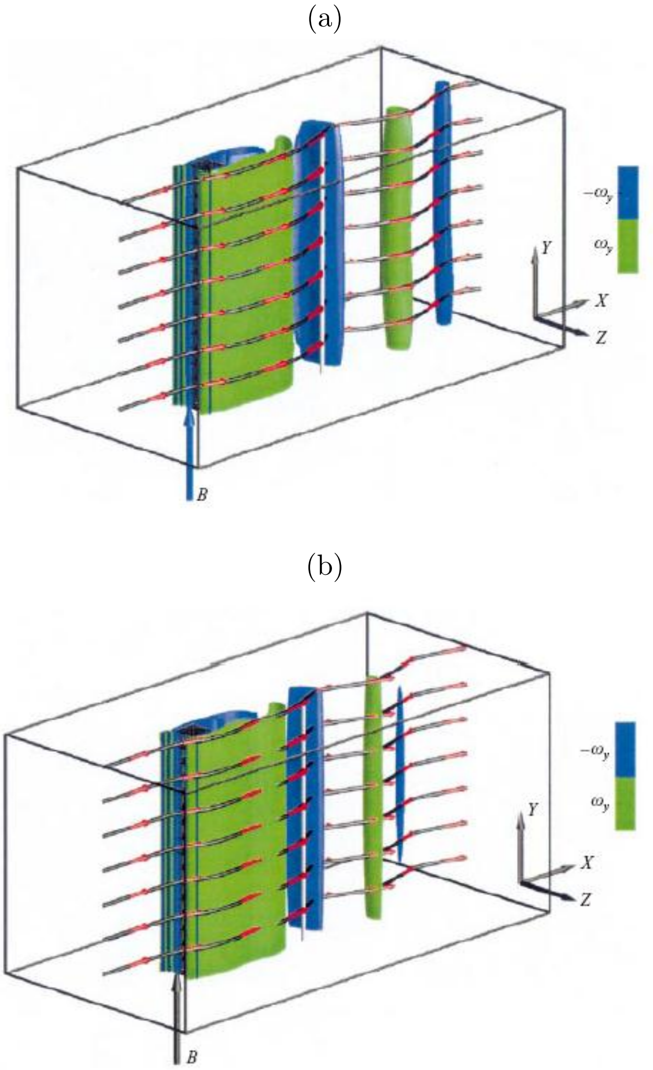

FIGURE 2.10: Iso-surface visualization of vorticity of cylinder wake for $\beta = 0.1$ (a) $Re = 200$ and $Ha = 100$, and (b) $Re = 200$ and $Ha \approx 265$; from Muck *et al.* (2000). The alignment of the shed vortices in the magnetic field direction can be clearly noticed and the diameter vortices decreases rapidly as they convected downstream.

street. In addition, a breakup of the two-dimensional vortex street was predicted to occur at Re around 5000. For the first three regions of the flow, the results reported that the drag coefficient and the length of circulation were controlled by the parameter $Re/Ha^{0.8}$, and for $Re = 30000$ and $Ha = 1120$, Kelvin–Helmholtz instability was observed.

2.3 Heat Transfer Enhancement in a Channel

Many techniques have been proposed to enhance the heat transfer rate in a channel for engineering applications such as the cooling of electronic components, cooling of turbine blades, and heat exchangers. One of these methods is to use a bluff body placed in the channel as a vortex generator. The disturbances resulting from these promoters increase the fluid mixing and disrupt the development of the thermal boundary layer resulting in a remarkable enhancement in heat transfer (Valencia 1995; B.Celik & Beskok 2009).

2.3.1 Heat Transfer Enhancement in a Channel Using a Fixed Bluff Body

Oyakawa & Mabuchi (1981) studied experimentally the heat transfer enhancement in a duct with a fixed circular cylinder placed perpendicular to the flow direction over a range of blockage ratios $\beta = 0.4 \sim 0.8$ and Reynolds number $Re \leq 2.2 \times 10^5$. Their results demonstrated that the side wall vortices which were generated by inducing the Kármán vortex street effectively increased the heat transfer rate along the heated wall in the duct. Heat transfer correlations were proposed to calculate the local heat transfer variations with respect to the maximum heat transfer position for different values of blockage ratios.

The heat transfer and pressure drop generated in a channel with a built-in rectangular cylinder placed at the channel centre plane was investigated numerically by Valencia (1995). The computations were performed for Reynolds number $Re = 200 - 400$ at blockage ratios $\beta = 0.25$ and 0.5. The results showed that the oscillatory flow structure and the crisscross motion of the vortices resulted in a significant heat transfer enhancement but also in a significant pressure drop increase. The maximum augmentation in the heat transfer was about 45% in the computing range.

Yao *et al.* (1995) investigated experimentally a turbulent channel flow obstructed with a square rod placed at different distances from the lower wall in a range of Reynolds number $Re \geq 6000$ and constant blockage ratio $\beta = 0.2$. Dye injection and hydrogen bubble methods were used to track the motion of the Kármán vortex and to visualize the near-wall flow. The study focused on the effect of the resulting flow downstream of the inserted body on the heat transfer enhancement. A noticeable heat transfer enhancement was achieved on the wall located closer to the rod. This was due to the formation of discrete vortices near the channel wall which induced a rotational fluid motion around it. Therefore, the cooler fluid was entrained toward the hot region of the channel and the hot fluid near the wall was circulated to mix with the cold fluid.

The effect of an oblique plate on the heat transfer enhancement of mixed convection in a horizontal block heated channel was investigated numerically using a finite element method by Wu & Perng (1999). The oblique angle of the plate was varied between 30° and 90° in the range of Reynolds number $Re = 260 - 530$ and constant Prandtl number $\mathrm{Pr} = 0.7$. Their results demonstrated that the vortex shedding induced by the oblique plate could effectively enhance the heat transfer performance of mixed convection in the horizontal channel. The heat transfer was enhanced up to approximately 40%.

The oscillatory behaviour of the flow and heat transfer was investigated by Valencia (1998), who performed numerical computations for a horizontal channel flow obstructed with two rectangular cylinders placed perpendicular to the flow direction in the channel centreline for Reynolds numbers $100 \leq Re \leq 400$ and cylinder separation distances $1 \leq S/H \leq 4$. The predicted heat transfer improvement on the channel walls was about 78% for $S/H = 2, 3$ and 4 at Reynolds number $Re = 400$. For $S/H = 1$, only an 8% heat transfer augmentation was reported. However, for $Re = 100$, the cylinder separation distance was found not to affect the heat transfer, only changing the flow losses.

Tsui *et al.* (2000) developed a three–dimensional computational method to investigate the flow and heat transfer from multilobe vortex generators inserted in a circular tube for Reynolds numbers $Re =$ 1000–2000. The irregular shape of the lobe was treated using curvilinear non-staggered grids. Their results indicated that the multilobe invoked secondary vortices that resulted in a significant enhancement in the heat transfer and the wall friction. The maximum heat transfer enhancement was approximately 60%.

Using transient liquid crystal thermography, Liou *et al.* (2000) reported the details of the flow and heat transfer in a square duct with different shaped vortex generators for a constant Reynolds number $Re = 1.2 \times 10^4$. The results found that the fluid dynamics factors such as the direction and the strength of the secondary flow tend to affect the heat transfer enhancement along the channel wall. This is followed by the convective velocity and the turbulent kinetic energy.

The effects of blockage and offset ratios on the heat transfer enhancement and flow behaviour in a horizontal duct obstructed with a blunt body studied experimentally by Oyakawa *et al.* (2005). These were carried out over the range of offset ratio $0.5 \leq \gamma \leq 0.275$, blockage ratio $(0.3 \leq \beta \leq 0.5)$ and Reynolds number $6300 \leq Re \leq 21800$. A dye visualization method was used to visualize the changed in flow patterns and a T-type thermocouple was used to measure the wall temperature of the heated surface. The characteristics of heat transfer were found to depend on the effect of the reattachment shear layer separated from the body at offset ratio $(0.05 \leq \gamma \leq 0.1)$ and the effects of both the reattachment flow and the separation vortex at offset ratio $(0.15 \leq \beta \leq 0.2)$. Furthermore, it was depended on the effect of sidewall vortices induced by Kármán vortices at offset ratio $(0.25 - 0.275)$. It was also found that at low Reynolds number the heat transfer enhancement was due to the reattachment flow, while it was due the sweeping of the heating surface by the side vortex induced by Kármán vortex at large Reynolds number. A power law relationship between the Nusselt number and Reynolds number at different blockage and offset ratios was suggested.

More recently, Farhadi *et al.* (2010) studied numerically the effect of wall proximity of a triangular bluff body on the fluid flow and heat transfer enhancement in a plane channel. The computations were performed for a constant blockage ratio $\beta = 0.25$ at Reynolds number $100 \leq Re \leq 450$ and gap width range of $(0.5 - 1)$. Their results demonstrated that the vortex formation downstream the bluff body were significantly increased the heat transfer rate along the heated surface in the duct. It was found that increasing the distance between the body and the wall resulted in suppression of the vortex shedding and consequently the heat transfer rate was decreased at low Reynolds number. The maximum heat transfer enhancement was about 100% in the computing range.

2.3.2 Heat Transfer Enhancement in a Channel Using an Oscillating Bluff Body

There has been a limited number of studies dedicated to investigate the vortex dynamics of an oscillating cylinder in a straight channel (Beskok & Warburton 2001; Celik *et al.* 2008; B.Celik & Beskok 2009), and the studies relevant to heat transfer enhancement in a straight channel using an oscillating obstacle are very rare.

Employing a Galerkin finite element formulation with moving meshes to solve the governing flow equation, Yang (2003) investigated heat transfer enhancement in a channel under the effect of a transversely oscillating square cylinder. An arbitrary Lagrangian–Eulerian kinematic method was used to depict the flow and thermal fields. The computations were carried out for a constant blockage ratio $\beta = 0.25$ and constant Prandtl number $\mathrm{Pr} = 0.71$ in the range of Reynolds number varying from 100 to 800. The oscillation frequency, oscillation amplitude, and maximum speed of the bar were examined to analyse the flow structures and the heat transfer enhancement. A remarkable heat transfer enhancement with increasing oscillation amplitude was reported. This was due to the formation of transverse vortices downstream of the bar, which transported the low temperature and high speed flow in the center of the duct toward the heated region of the channel. Consequently, the high temperature fluid was convected away from the heated regions of the channel to mix with the low temperature core flow. The heat transfer was enhanced approximately 205% in some cases.

Using a moving boundary formulation and the arbitrary Lagrangian method modified by Yang (2003), Fu & Tong (2004) performed a numerical simulation to study the effect of the flow passing an transversely oscillating circular cylinder on the heat transfer enhancement in a horizontal blocked heated channel. The blockage ratio was kept constant at $\beta = 0.25$ and the Reynolds number was varied between 100 and 500. The influences of the oscillating amplitude and oscillating frequency on the resulted flow and heat transfer characteristics were investigated.

Their results indicated that the heat transfer rate was improved substantially in the lock-in regime. It was also found that the influence of the oscillating amplitude of the cylinder on the heat transfer rate was remarkable when it was larger than 0.1. The maximum heat transfer enhancement was about 116% in the computational range.

More recently, the heat transfer enhancement in a heated slot channel due to vortices shed from a transversely oscillating circular cylinder was investigated by Celik *et al.* (2010), who performed numerical simulations using a spectral element discretization of the governing flow equations in a moving domain based on an arbitrary Lagrangian-Eulerian formulation. The computations were performed for a constant blockage ratio $\beta = 0.3$ at Reynolds number $Re = 100$ in the range of Prandtl number $0.1 \leq \mathrm{Pr} \leq 10$. The cylinder oscillation amplitude were kept constant, while the frequency of the oscillation was varied from 0.75 to 1.25 of the Strouhal frequency of a fixed circular cylinder. Their results demonstrated that the transverse oscillations of a cylinder significantly enhanced heat transfer, and the maximum augmentation was observed to occur at the frequency $f_e = 0.75$. This was due to the presence of high intensity vortices near the channel walls, which has significant effect on the heat transfer enhancement from the walls.

2.3.3 MHD Heat Transfer Enhancement in a Channel

The motion of electrically conducting fluid in a strong magnetic field induces electric currents, which interact with the applied magnetic field and produce electromagnetic forces that affect the velocity distribution, turbulence characteristics, and exerts a retarding force on the flow. Therefore, magnetohydrodynamic duct flows is characterized by laminar flow structures because velocity fluctuations are significantly damped Joule dissipation. This laminarization results in a considerable decrease in heat transfer from the heated wall in such flow, and hence an intense enhancement of a convective heat is required in order to keep the wall temperature below the acceptable limit. However, the strong anisotropic feature of the electromagnetic forces leads to the formation of extended vortex tubes located parallel to the magnetic field (Sommeria & Moreau 1982; Moreau & Sommeria

1988). These vortices are suppressed only weakly and can form quasi–two–dimensional structures in the plane perpendicular to the magnetic field, which can be invoked to enhance the heat transfer.

Although the number of studies dedicated to investigate the vortex dynamics in a straight channel under a strong magnetic field are limited, the studies pertaining to heat transfer enhancement in a straight channel under these conditions are very scarce. Two approaches are proposed to enhance the heat transfer for this flow: the first includes conducting strips mounted on the channel walls perpendicular to the magnetic field (i.e. non-uniform electrical wall conductivity), and the second includes turbulence promoters such a circular or rectangular cylinder placed between these walls. For the both approaches, the Nusselt number is several times larger than that in the empty channel (Barleon *et al.* 2001). The concept of using the conducting insertions and turbulent promoters in the channel walls are shown in Fig. 2.11.

2.3.4 Heat Transfer Enhancement by Electromagnetic and Mechanical Promoters

Using a number of conducting spots arranged in the main flow direction near the heated wall, Andreev & Kolesnikov (1993) reported an intense transverse convective exchange of fluid in their experiments which were conducted in a circular closed channel under the influence of uniform axial magnetic field. The averaged and fluctuating velocities as well as the temperature distributions were measured with conduction and thermocouple probes. Their results indicated the time-dependent vortices increased the heat transfer by a factor of between 5 and 7 and the wall temperature was decreased by 45% compared with the insulating wall duct.

The possibility of generating a vortex type flow for heat transfer improvement without significant increase in magnetohydrodynamic pressure drop by the inclusion of conducting strips in the Hartmann walls was investigated by Bühler (1996), who performed a numerical simulation of magnetohydrodynamic flows between parallel walls for $Ha \gg 1$ and $N \gg 1$. Due to the unstable mean velocity

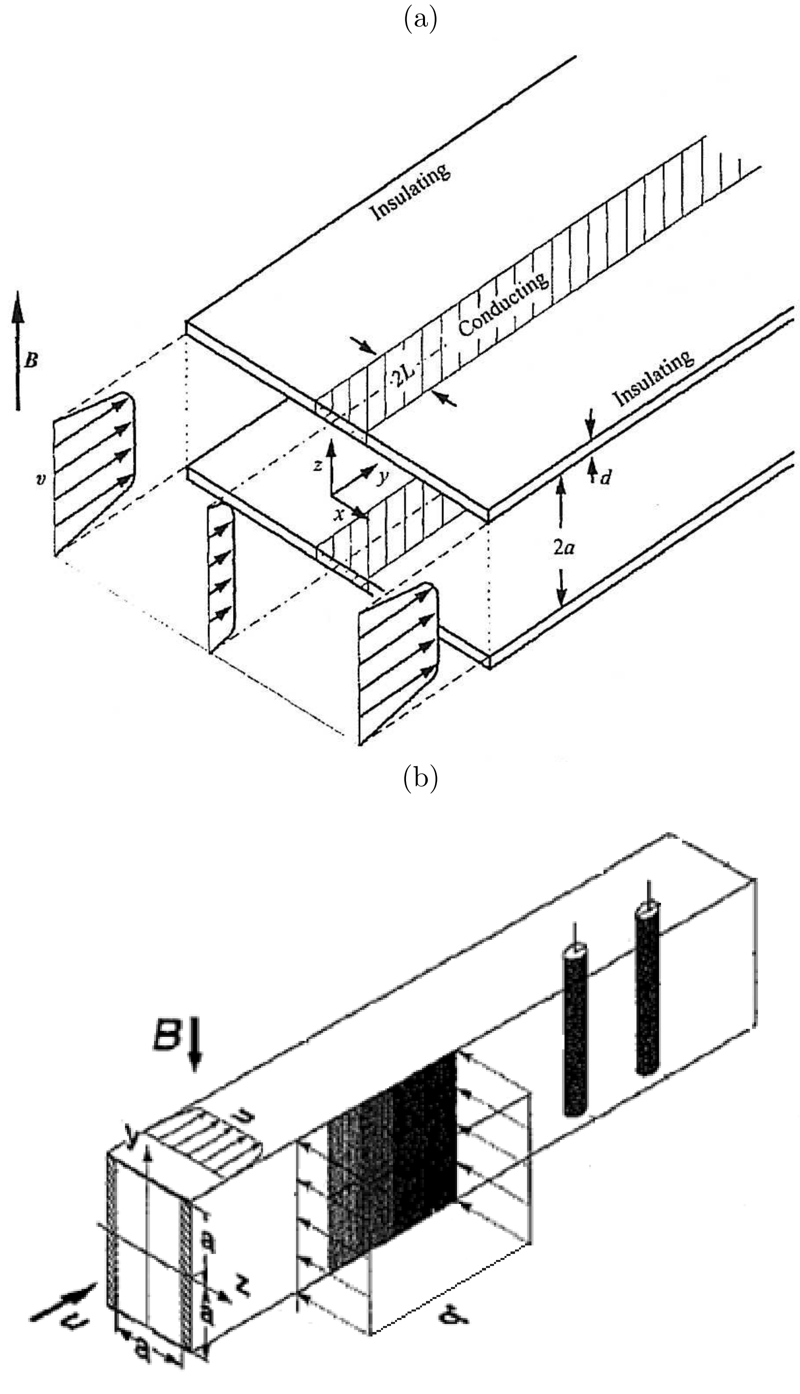

FIGURE 2.11: Vortex generation for the heat transfer enhancement in a channel in the presence of a strong magnetic field using different methods. (a) non-uniform conductivity of the channel walls, and (b) mechanical turbulent promoters. Images (a) and (b) are reproduced from Bühler (1996) and Barleon *et al.* (2001), respectively.

profile, regular vortices similar to those in the Kármán vortex street behind bluff bodies were observed. The use of longitudinal conducting strips as a heat transfer promoter were also considered by Smolentsev & Dazhi (1996), who carried out numerical calculations of heat transfer in a fully developed laminar MHD flow in a rectangular duct with a conducting inclusion in one of the Hartmann walls. Their results suggested that depending on the strip location and their width, the heat transfer could be increased by more than a factor of two compared to the case without strips, though the MHD pressure drop was not increased considerably. This idea is not new and has been previously applied by Moreau & Sommeria (1988) to study the MHD decay of vortex patterns in insulated ducts.

The heat transfer intensification using electrically conductive obstacles in an annular insulated channel of a rectangular cross section in the presence of a strong axial magnetic field was studied experimentally by Kolesnikov & Andreev (1997). They used eutectic alloys *InGaSn* as a working fluid. In this experiment, an intensive flow of vorticity was generated on the boundaries of conducting cylinders which were placed downstream on the heated wall parallel to the magnetic field. The cylinders were mounted with different steps on the azimuthal direction on the inner heated wall to ensure more effective heat transfer. Their results demonstrated that the heat transfer between the hot and cold walls was increased six times compared with an empty channel and the hot wall temperature was decreased by more than three times. This was due to the effect of electromagnetic vortices generated in the flow by the conducting cylinders, resulting in formation of stagnant zones above and below the cylinders that was stretched along the magnetic field.

Experiments on magnetohydrodynamic heat transfer improvement under fusion relevant conditions in thin-walled and electrically insulated ducts were conducted by Barleon *et al.* (1995, 2000, 2001). The experiments were focused on the enhancement of heat transfer using a bluff body as a turbulence promoter in the range of Hartmann number $0 \leq Ha \leq 5 \times 10^3$, Reynolds number $0 \leq Re \leq 1.3 \times 10^5$ and Péclet Number $0 \leq Pe \leq 2.9 \times 10^3$. The working fluid was sodium potassium eutectic alloy *NaK*. Their results indicated that the heat transfer under these conditions was improved by turbulent transport by a factor of about 2 compared to slug flow, and the corresponding pressure drop was kept almost constant although the flow was changed from laminar to turbulent. The turbulence was generated due to the effect of shear flow of the side wall jets which are a characteristic of the MHD duct flow. Using electromagnetic promoters which were installed close to the heated wall, no measurable enhancement of heat transfer was observed within the range of $Re = 10^3 - 10^5$. An increment of the pressure drops up to 20% was reported for this case. The results of this case is reproduced in Fig. 2.12.

A circular cylinder which was placed near the heated wall of the insulated duct improved the heat transfer up to 7 times compared to slug flow, but the corresponding pressure drop increases within the measured range of Reynolds number up to 300%. The results of this case is presented in Fig. 2.13.

2.4 Transient Growth Analysis

Although global stability analysis has been highly successful in predicting the onset of the Hopf bifurcation and three–dimensional transitions for many different types of flow problems, there are a number of other flows in which the stability predictions do not describe the experimental behaviour. Examples are two–dimensional Poiseuille and Couette flow which undergo turbulent transition despite the fact that flow is linearly stable. Therefore, an extension of stability analysis has received renewed interest recently, which is known as a non-modal stability analysis or transient growth analysis (Schmid & Henningson 2001; Blackburn *et al.* 2008a). In a transient growth, the linear growth of infinitesimal perturbations over a time span are tested without assuming eigenmodal growth of the linearized operator. Non-modal interaction between leading eigenmodes of the linearized evolution operator of the governing equations can create very large short-term amplifications of a perturbation.

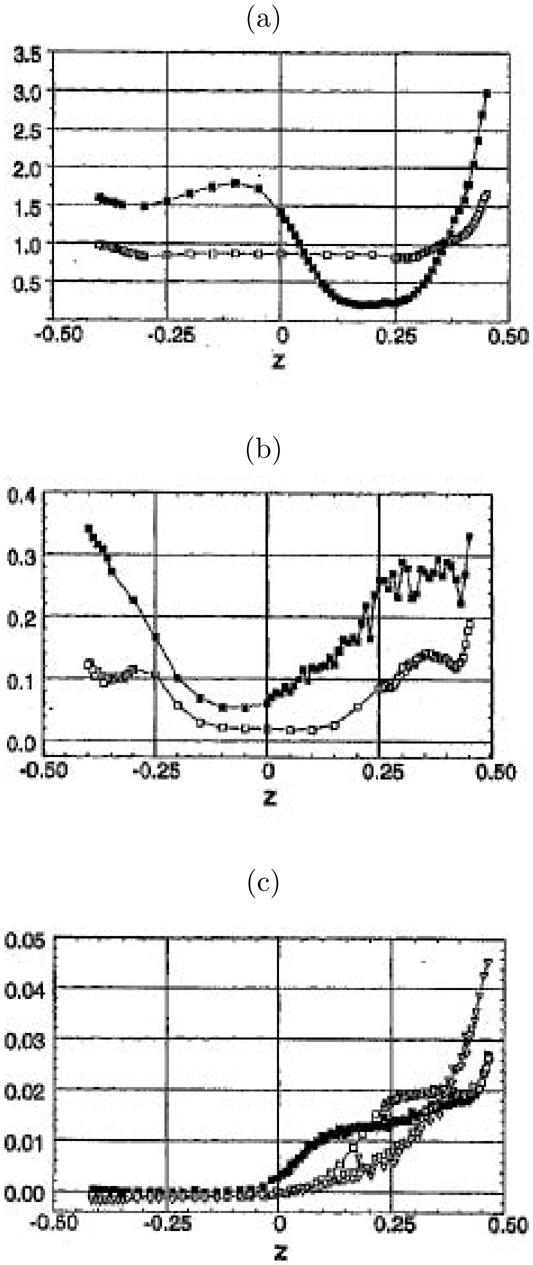

FIGURE 2.12: Measured (a) velocity, (b) turbulence intensity and (c) temperature in the electrically conducting duct for $Ha = 4.8 \times 10^3$, $Re = 5.8 \times 10^4$ in the mid plane $y = 0$ (□, no promotor; ■, with promoter) plotted against z, where z is perpendicular to the magnetic field direction (see Fig. 2.11b). The symbols ▽ and ▼ represent without and with promoter, respectively for the case of $Ha = 0$. Reproduced from Barleon *et al.* (2001).

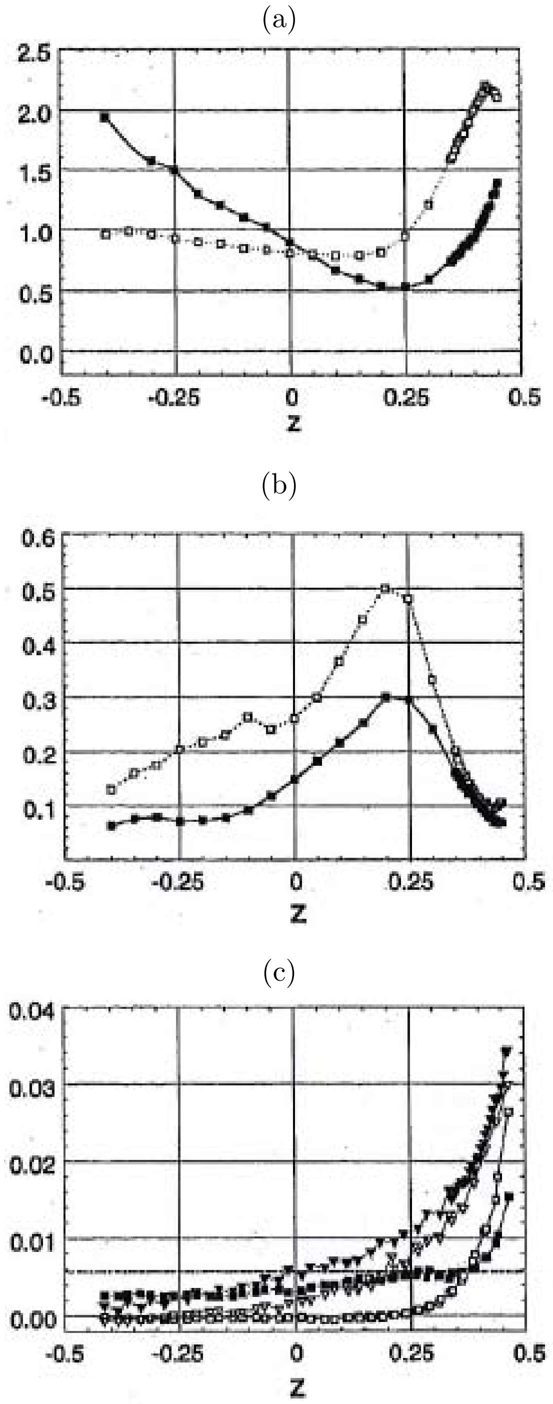

FIGURE 2.13: Measured (a) velocity, (b) turbulence intensity and (c) temperature in the insulated duct for $Ha = 5 \times 10^3$, $Re = 7.2 \times 10^4$ in the mid plane $y = 0$ (□, no promotor; ■, with promoter) plotted against z, where z is perpendicular to the magnetic field direction (see Fig. 2.11b). The symbols ▽ and ▼ represent without and with promoter, respectively for the case of $Ha = 0$. Reproduced from Barleon *et al.* (2001).

2.4.1 Optimal Growth in non-MHD Flow

Stable flow may be sensitive to transient growth of disturbances for some time before decaying to zero (Schmid & Henningson 2001). In purely hydrodynamic parallel shear flows, transient growth has been reported for the plane channel (Reddy *et al.* 1998), pipe (Zikanov 1996), rectangular duct (Biau *et al.* 2008), and abrupt geometrical expansion flows (Blackburn *et al.* 2008a,b; Cantwell & Barkley 2010). This growth can be attributed to the non-normality of the eigenmodes associated with many shear flows (Schmid & Henningson 2001; Chomaz 2005).

For free stream cylinder wakes without magnetic field, the adjoint and direct eigenmodes in the region of primary instability have been investigated numerically by Chomaz (2005); Giannetti & Luchini (2007) to understand the sensitivity of the flow to external disturbances. Recently, the transient response of the subcritical and supercritical flow of the circular cylinder wake in an open flow has been investigated by Marquet *et al.* (2008); Cantwell & Barkley (2010). Abdessemed *et al.* (2009a) also studied the transient growth in supercritical and subcritical flow of the circular cylinder wake in an open flow. Their analysis showed that the optimal growth modes were concentrated in the near wake of the cylinder, and that the energy of these modes were amplified up to three orders of magnitude over a time span horizon of $\tau = 30$.

More recently, Marais *et al.* (2011) investigated experimentally the impulse response of a freestream cylinder wake below the critical Reynolds number of the vortex shedding instability using two–dimensional particle image velocimetry PIV. The measured values of transient growth were considerably less than those reported by Abdessemed *et al.* (2009a); Cantwell & Barkley (2010).

2.4.2 Optimal Growth in MHD Flow

The effect of an applied magnetic field on the transient growth for the case of steady Hartmann flow (channel flow of an electrically conducting fluid in the presence of a uniform magnetic field) has been analysed by Gerard-Varet (2002); Airiau & Castets (2004); Krasnov *et al.* (2004). The optimal modes were found to have the form of streamwise rolls confined to the Hartmann layers. In addition it was found that the energy gain of the optimal perturbations is proportional to $(Re/Ha)^2$, and the critical Reynolds number was much higher than for Poiseuille flow.

More recently, Boeck *et al.* (2009); Krasnov *et al.* (2010) analysed the optimal linear growth of perturbations in a rectangular duct with different aspect ratio subjected to a uniform transverse magnetic field. The disturbances of optimal growth are confined to the Shercliff layers. The optimal perturbations are significantly damped by the magnetic field irrespective of the duct aspect ratio. They conclude that the Hartmann boundary layers perpendicular to the magnetic field do not contribute to the transient growth.

2.5 Review Summary

The previous studies into the hydrodynamic and magnetohydrodynamic flow past a circular cylinder, heat transfer enhancement in a channel using a bluff body and transient growth analysis have been extensively reviewed. The preceding review of the literature reveals that much emphasis has been placed on the flow past a circular cylinder where no magnetic field is presented, and the case of a confined cylinder has received less attention. For the magnetohydrodynamic flow past a confined circular cylinder, there is a clear deficiency in our understanding of the case where the magnetic field direction is parallel to the cylinder axis. The studies of heat transfer enhancement in a straight channel using a bluff body under these conditions are very scarce, as are investigations into the augmentation of heat transfer in this type of flow.

Furthermore, it is unknown how the addition of a cylinder into an magnetohydrodynamic duct flow will affect the transient response of the flow, and whether this may be exploited to further improve heat transfer. Therefore, further studies are required to better understand the flow characteristics and heat transfer enhancement of this flow. These quantities will be addressed in this thesis.

In the next chapter, methodologies for numerical and analytical aspects of the study are discussed, and the validation tests of the numerical system are performed.

Chapter 3

Theoretical Framework, Numerical Methodology and Validations

This chapter presents the numerical techniques applied for the simulations conducted for this thesis. A spectral-element method is employed to compute the magnetohydrodynamic flow and temperature fields under investigation.

The equations governing three-dimensional magnetohydrodynamic, boundary conditions, magnetohydrodynamic flow are presented in § 3.1, § 3.1.1 and § 3.2, respectively. The quasi-two-dimensional (Q2D) magnetohydrodynmic flow model formulation is described in § 3.2.3. The equations governing the flow and heat transfer in the present project are given in § 3.3. Spatial and temporal discretisation methods are presented in § 3.4.1 and § 3.4.2, respectively. A linear stability analysis and transient growth technique applied for the Q2D model are described in § 3.5 and § 3.6, respectively. The reliability and accuracy of the numerical approach is presented in § 3.7.

3.1 Equations of Magnetohydrodynmic Flows

The complete set of three-dimensional magnetohydrodynamic (MHD) equations for incompressible, Newtonian, homogeneous fluids includes the Navier–Stokes equations of motion, equation of mass continuity, Ohm's law and Maxwell's equations (Davidson 2001; Moreau 1990; Roberts 1967)

$$\frac{\partial \mathbf{u}}{\partial t} + (\mathbf{u} \cdot \nabla)\mathbf{u} = -\frac{1}{\rho}\nabla p + \nu \nabla^2 \mathbf{u} + \frac{\mathbf{J} \times \mathbf{B}}{\rho} \tag{3.1}$$

$$\nabla \cdot \mathbf{u} = 0 \tag{3.2}$$

$$\mathbf{J} = \sigma_e(\mathbf{E} + \mathbf{u} \times \mathbf{B}) \tag{3.3}$$

$$\nabla \times \mathbf{E} = -\frac{\partial \mathbf{B}}{\partial t} \tag{3.4}$$

$$\nabla \times \mathbf{B} = \mu_m \mathbf{J} \tag{3.5}$$

$$\nabla \cdot \mathbf{J} = 0 \tag{3.6}$$

$$\nabla \cdot \mathbf{B} = 0. \tag{3.7}$$

Here $\mathbf{u}, \mathbf{J}, \mathbf{E}, \mathbf{B}$ and p are, respectively, the velocity vector, current density, electrical field, magnetic field and pressure. The symbols ρ, ν, σ_e, and μ_m, are the mass density, kinematic viscosity, the electrical conductivity and the magnetic permeability of the liquid metal. The magnetic induction equation is obtained by taking the curl of both sides of equation (3.3). Substituting equations (3.4) and (3.5) gives

$$\nabla \times \frac{\mathbf{J}}{\sigma_e} = \nabla \times \mathbf{E} + \nabla \times (\mathbf{u} \times \mathbf{B}) \tag{3.8}$$

$$\therefore \frac{\nabla \times (\nabla \times \mathbf{B})}{\mu_m \sigma_e} = -\frac{\partial \mathbf{B}}{\partial t} + \nabla \times (\mathbf{u} \times \mathbf{B}). \tag{3.9}$$

Using the vector identity

$$\nabla \times (\nabla \times \mathbf{B}) = \nabla(\nabla \cdot \mathbf{B}) - \nabla^2 \mathbf{B},$$

along with equation 3.7 leads to

$$\frac{\partial \mathbf{B}}{\partial t} = \nabla \times (\mathbf{u} \times \mathbf{B}) + \frac{1}{\mu_m \sigma_e} \nabla^2 \mathbf{B}. \tag{3.10}$$

Equation (3.10) indicates that the motion of a conducting fluid in an applied magnetic field induces a magnetic field in the fluid. The total field is the sum of the applied and the subsequently induced field. The strength of the induced field is characterized by the magnetic Reynolds number, Re_m, which represents the ratio between the induced and the applied magnetic field. When the magnetic Reynolds number $Re_m \ll 1$, the magnetic field induced by the flow is negligible compared to the externally applied field, i.e. the effect of velocity on the magnetic field is negligible (Branover 1978; Moreau 1990). Thus the total magnetic field is effectively equal to the applied magnetic field only. Using u_0, $\rho {u_0}^2$, $\sigma u_o B$, $u_0 BL$ as respective velocity, pressure, current density and electric potential scaling, the inductionless magnetohydrodynamic equations (in non-dimensional form) reduces to (Müller & Bühler 2001)

$$\nabla \cdot \mathbf{u} = 0, \tag{3.11}$$

$$\frac{\partial \mathbf{u}}{\partial t} + (\mathbf{u} \cdot \nabla)\mathbf{u} = -\nabla p + \frac{1}{Re}\nabla^2 \mathbf{u} + \frac{Ha^2}{Re}(\mathbf{J} \times \mathbf{B}), \tag{3.12}$$

$$\nabla \cdot \mathbf{J} = 0, \tag{3.13}$$

$$\mathbf{E} = -\nabla \phi, \tag{3.14}$$

$$\mathbf{J} = -\nabla \phi + \mathbf{u} \times \mathbf{B}, \tag{3.15}$$

where ϕ is the electrical potential, $Ha = LB\sqrt{\sigma/(\rho\nu)}$ is the Hartmann number, which is described shortly, and $Re = u_0 L/\nu$ is the Reynolds number.

3.1.1 Boundary Conditions

From the governing equations presented in previous section, physical solutions can be obtained if reasonable initial conditions are defined. The initial conditions are required to define all the flow variables at this initial instant over the whole domain and the boundary conditions required at all boundaries of the flow domain. For many engineering applications the fluid is confined in a finite domain bounded by an interface, Γ, comprising of rigid walls.

Kinematic constraints must be applied at the interface between the fluid and the rigid walls. For the case of a rigid non-moving boundary, due to viscosity, the velocity is zero at the interface, Γ, between the fluid and the boundary. The boundary condition is expressed as a no-slip condition e.g. , Müller & Bühler (2001)

$$\mathbf{u} = 0 \text{ at } \Gamma. \tag{3.16}$$

The kinematic boundary condition requires some modification in the cases of moving walls or a free surface.

The electromagnetic boundary conditions are controlled by the electrical conductivity (σ_w) of the channel wall. For the case of insulating walls ($\sigma_w = 0$), no current can enter into the wall from the fluid side, as a result, the component of the current density normal to the interface vanishes at the wall

$$\mathbf{J} \cdot \mathbf{n_n} = 0 \text{ at } \Gamma. \tag{3.17}$$

For the case of perfectly conducting walls ($\sigma_w \to 0$), the component of the current density tangential to the interface vanishes at the wall

$$\mathbf{J} \cdot \mathbf{n_t} = 0 \text{ at } \Gamma, \tag{3.18}$$

where $\mathbf{n_n}$ and $\mathbf{n_t}$ represent a vector normal and tangential to the interface Γ.

For engineering and industrial applications such as piping systems, channel walls often consists of metallic material with finite electrical conductivity (σ_w). The boundary condition for the current density can be derived using equations (3.3) and (3.4)

$$\mathbf{J} \cdot \mathbf{n_n} = \frac{\sigma}{\sigma_w} \mathbf{J_w} \cdot \mathbf{n_n} \text{ at } \Gamma, \tag{3.19}$$

but throughout this thesis the duct walls are assumed to be electrically insulated so that the boundary condition relevant to the case of perfectly conducting walls will not be described hereafter.

In the quasi-two-dimensional model for MHD duct flow considered in this thesis, the electrical boundary conditions on the duct walls influence the velocity field. Details of the relationship between the electrical boundary conditions and the velocity-pressure formulation of the quasi-two-dimensional model are given in § 3.2.3.

3.2 Magnetohydrodynamic Flow in Channels and Ducts

In this thesis, the magnetohydrodynamic flow and heat transfer past a circular cylinder in a duct are considered. So, it is imperative to introduce the fundamentals of magnetohydrodynamic flow between two parallel infinite walls and in a rectangular duct.

3.2.1 Flow between Parallel Planes (Hartmann Flow)

The flow of an electrically conducting fluid between two parallel and insulated plates is known as Hartmann flow. It is the purely hydromagnetic analogue of Poiseuille flow in hydrodynamic ($\mathbf{B} = 0$) flow. This problem was first solved by Hartmann (1937) and Hartmann & Lazarus (1937). Consider the flow of an electrically conducting fluid in a rectangular channel exposed to an externally uniform magnetic field, which is transverse to the channel axis (i.e. $\mathbf{B} = B\hat{\mathbf{z}}$). The flow is driven by a constant pressure gradient.

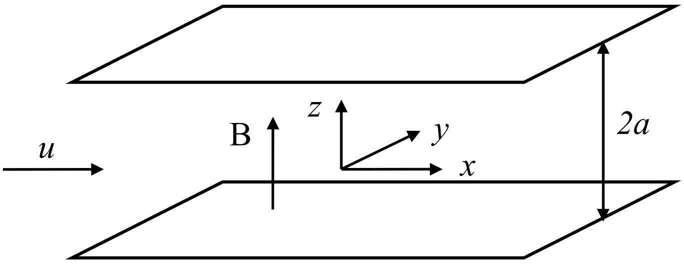

FIGURE 3.1: Schematic diagram of magnetohydrodynamic flow between parallel infinite walls in the presence of a transverse magnetic field.

The configuration of this channel arrangement is depicted in Fig. 3.1. The transverse direction here is defined as being perpendicular to the direction of the channel flow, and the walls are located at $z = \pm a$. The channel is assumed to extended infinitely in the y-direction. Therefore, the flow variables depend only the z–coordinate. The velocity has only one component parallel to the streamwise direction. From the induction equation (3.10), since the flow is unidirectional and perpendicular to the applied magnetic field, it follows that the induced magnetic field is of the form $\mathbf{B}_i = B_i(z)\hat{\mathbf{z}}$.

The induced field is related to the current density by Ampere's law (equation (3.5)), so that the Lorentz force $\mathbf{J}\times\mathbf{B}$ in equation (3.12) can be expressed in terms of B_i. For fully developed flows, the left-hand side of the both equations (3.5) and (3.12) are neglected. Introducing a and $\frac{a^2(-\partial P/\partial x)}{\rho\nu}$ as respective characteristic length and velocity scales, then the magnitude of pressure gradient can be evaluated to unity. The non-dimensional equations representing the Hartmann flow are the x–momentum equation (3.20), the x–induction equation (3.21) together with the boundary conditions (3.22) (Müller & Bühler 2001), i.e.

$$Ha\frac{\partial B_i}{\partial z} + \frac{\partial^2 u}{\partial z^2} = -1, \tag{3.20}$$

$$Ha\frac{\partial B_i}{\partial z} + \frac{\partial^2 B}{\partial z^2} = 0 \ \ \text{for} -1 < z < 1, \tag{3.21}$$

$$u = 0, \ \pm\frac{\partial B_i}{\partial z} + \frac{1}{c}B_i = 0 \text{ at } z = \pm 1. \tag{3.22}$$

Here c and Ha are respectively, the wall conductance ratio and Hartmann number. The Hartmann number and wall conductance ratio are given respectively as

$$Ha = a \ B \sqrt{\frac{\sigma_e}{\rho\nu}}, \tag{3.23}$$

$$c = \frac{t_w \ \sigma_w}{a \ \sigma_e}, \tag{3.24}$$

where B_i, a, σ_w and t_w represent the induced magnetic field, characteristic length, electrical conductivity of the channel walls perpendicular to the field, and the thickness of the walls perpendicular to the field, respectively. For electrically insulating walls and perfectly conducting walls, $c \to 0$ and $c \to \infty$, respectively.

The details of the solution of the above equations are given in Moreau (1990) and Müller & Bühler (2001), with the final solution given as

$$u = u_c \left[1 - \frac{\cosh\,(Ha\ z)}{\cosh\,(Ha)}\right], \tag{3.25}$$

$$B_i = -\frac{z}{Ha} + u_c\frac{\sinh\,(Ha\ z)}{\cosh\,(Ha)}, \tag{3.26}$$

with

$$u_c = \frac{c+1}{Ha\,(cHa + \tanh\,(Ha))}. \tag{3.27}$$

Fig. 3.2 plots the velocity profile obtained from equation (3.25) over the width of the channel as a function of the Hartmann number. At $Ha = 0$ the familiar quadratic profile for Poiseuille flow is obtained, and as Ha is increased, the profile becomes fuller, flattening towards a “top-hat” profile as $Ha \to \infty$. For large Hartmann number (i.e. $Ha \gg 1$), the hyperbolic functions asymptotically approach

$$\sinh\,(Ha) \to \frac{1}{2}\,e^{Ha}, \cosh\,(Ha) \to \frac{1}{2}\,e^{Ha}, \tanh\,(Ha) \to 1.$$

Substituting these expressions into equations (3.25) and (3.26), shows that for $Ha \gg 1$ these equations simplifies to

$$u = u_c \left\{1 - e^{Ha(|z|-1)}\right\}, \tag{3.28}$$

$$B_i = -\frac{z}{Ha} \pm u_c\,e^{Ha(|z|-1)}, \tag{3.29}$$

with

$$u_c \to \frac{1+c}{Ha\,(cHa+1)}. \tag{3.30}$$

Equations (3.28) and (3.29) demonstrate that for $Ha \gg 1$, the velocity and the induced magnetic field decrease exponentially in the vicinity of the Hartmann layer whose thickness scales with Ha^{-1}. The velocity profile for Hartmann flow is dependent on Ha, but is independent of the conductivity of the wall. Also, it can be seen from Fig. 3.2 that with increasing Hartmann number, a constant core region in the interior of the channel is formed with Hartmann boundary layers near the channel walls. For insulating and perfectly conducting channel walls the core velocity (u_c) at $Ha \gg 1$ simplifies to

$$u_c = Ha^{-1} \quad \text{for } c = 0, \tag{3.31}$$

$$u_c = Ha^{-2} \quad \text{for } c \to \infty. \tag{3.32}$$

Integration of the velocity distribution across the channel cross section yields the non-dimensional flow rate

$$Q_v = \int_{-1}^{1} u\ \mathrm{d}z = 2u_c \left[1 - \frac{1}{Ha}\tanh\,(Ha)\right]. \tag{3.33}$$

This equation can be used to predict the non-dimensional pressure gradient (K_p) as a function of the flow rate (Müller & Bühler 2001)

$$K_p = \frac{2}{Q_v} = \frac{1}{u_c\left[1 - \frac{1}{Ha}\tanh\,(Ha)\right]}. \tag{3.34}$$

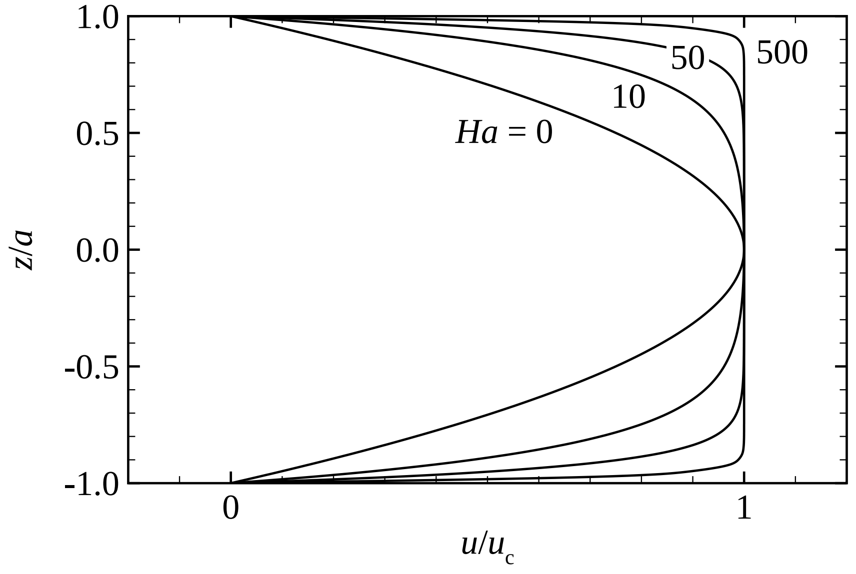

FIGURE 3.2: The velocity profile in Hartmann flow for different values of Hartmann numbers as indicated.

3.2.2 Duct Flow

The flow of an electrically conducting fluid in a rectangular duct where all walls are insulated in a presence of a transverse magnetic field is known as Shercliff flow. This configuration was first solved by Shercliff (1953). Consider a fully developed flow of an electrically conducting fluid in a rectangular duct exposed to an externally homogeneous magnetic field, which is perpendicular to the duct axis (i.e. $\mathbf{B} = B\hat{\mathbf{z}}$). The duct walls are assumed to be insulated and the flow is driven by a constant pressure gradient. The configuration is shown in Fig. 3.3.

The walls perpendicular and parallel to the magnetic field are separated by $2a$ and $2b$, respectively. The walls on which the magnetic field has a normal component are called *Hartmann walls*, whereas the walls tangential to the field are called *Shercliff walls*. In the centre of the duct (the *core*), the Lorentz force tends to retard the flow as it acts in the direction opposite to the flow direction. In this region, the Lorentz force balances the driving pressure gradient. In the boundary layer region near the Hartmann walls, the velocity drops significantly and the direction of the induced current in this region is opposite to that in the

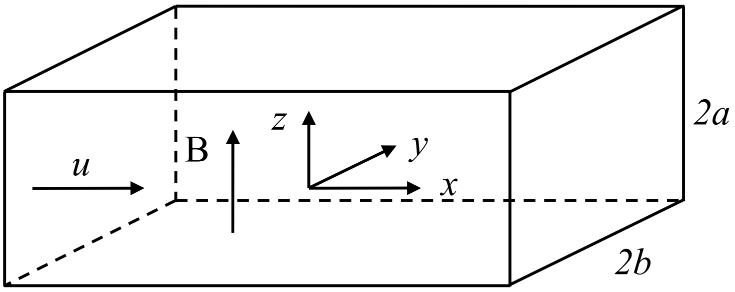

Figure 3.3: The configuration of the magnetohydrodynamic flow in rectangular duct placed in a uniform magnetic field. The walls perpendicular and parallel to the magnetic field are Hartmann and Shercliff walls, respectively.

core. Here there is a balance between the Lorentz and the viscous forces. For an electrically insulated duct (i.e. $\sigma_w = 0$), no current can enter the walls. Therefore, the currents induced in the core flow are closed in through the Hartmann layers, where the current magnitude is small and the electric resistance is high. In the configuration considered here, the current density is perpendicular and parallel to the magnetic field in the Hartmann and Shercliff layers, respectively. The thickness of the Hartman layers is smaller than that of the Shercliff layers ($\delta_H \sim Ha^{-1}$ and $\delta_S \sim Ha^{-1/2}$).

For a fully developed flow, the velocity and the induced magnetic field are independent on the flow direction and have only one component such that $\mathbf{u} = u(y,z)\hat{\mathbf{x}}$ and $\mathbf{B_i} = B_i(y,z)\hat{\mathbf{x}}$.

The non-dimensional momentum and induction equations representing this problem for $-\eta \leq y \leq \eta$ and $-1 \leq z \leq 1$ (Müller & Bühler 2001) are

$$\nabla^2 B_i + Ha\frac{\partial u}{\partial y} = 0, \tag{3.35}$$

$$\nabla^2 u + Ha\frac{\partial B_i}{\partial y} = -1, \tag{3.36}$$

where $\eta = b/a$. Here y and z are non-dimensionlized by a. A no-slip boundary condition is imposed at the walls for the velocity (i.e. $u = 0$ at $z = \pm 1$ and $y =$

$\pm\eta$). The boundary condition for the induced magnetic field at $z = \pm 1$ and $y = \pm\eta$ is derived from equation (3.5) as

$$J = \frac{1}{Ha}\nabla \times B_i\hat{\mathbf{x}} = \frac{1}{Ha}\left(\frac{\partial B_i}{\partial z}\hat{\mathbf{y}} + \frac{\partial B_i}{\partial y}\hat{\mathbf{z}}\right). \tag{3.37}$$

Inspection of this equation reveals that $(\mathbf{B_i}/Ha)$ represents the stream function for current density in the plane of the duct cross-section (i.e. lines of constant B_i are the current streamlines). If the wall is insulating, then the duct perimeter represents one of these streamlines. The value of this constant can arbitrarily be set to zero, and the boundary condition for the induced magnetic field at $z = \pm 1$ and $y = \pm\eta$ as $B_i = 0$.

The governing flow equations can be separated using Elsasser variables $A_1 = u + B_i$ and $A_2 = u - B_i$, so that the solution of A_1 is sufficient to determine A_2, u and B_i. Expanding the velocity and the induction field in the equations (3.35) and (3.36) as a Fourier series on $-1 \leq z \leq 1$ and $-\eta \leq y \leq \eta$ (Müller & Bühler 2001) gives

$$u(y, z) = \sum_{n=1,3,5,\ldots}^{\infty} u_n(z)\cos(\lambda_n y) \tag{3.38}$$

$$B_i(y, z) = \sum_{n=1,3,5,\ldots}^{\infty} b_n(z)\cos(\lambda_n y) \tag{3.39}$$

with

$$u_n(z) = \frac{k_n}{{\lambda_n}^2}\left[1 - \frac{\sinh(p_{n2})\cosh(p_{n1}z) - \sinh(p_{n1})\cosh(p_{n2}z)}{\sinh(p_{n2} - p_{n1})}\right]$$

$$b_n(z) = \frac{k_n}{{\lambda_n}^2}\left[\frac{\sinh(p_{n1})\sinh(p_{n2}z) - \sinh(p_{n2})\sinh(p_{n1}z)}{\sinh(p_{n2} - p_{n1})}\right]$$

$$p_{n1,2} = \frac{1}{2}\left(Ha \pm \sqrt{Ha^2 + 4{\lambda_n}^2}\right)$$

$$k_n = 2\frac{\sin(\lambda_n\eta)}{\lambda_n\eta}$$

$$\lambda_n = \frac{n\pi}{2\eta}$$

For the case of large Hartmann number $Ha \gg 1$, equations (3.38) and (3.39) can be further simplified (Müller & Bühler 2001; Moreau 1990).

The integration of the velocity profile (i.e. equation (3.38)) over the duct cross section yields the flow rate

$$Q_v = 2\eta \sum_{n=1,3,5,\ldots}^{\infty} k_n \int_0^1 u_n(z)\, \mathrm{d}z, \tag{3.40}$$

and the non-dimensional pressure drop

$$K_p = \frac{4\eta}{Q_v} = \frac{2}{\sum_{n=1,3,5}^{\infty} k_n \int_0^1 u_n(z) dz}. \tag{3.41}$$

For large Hartmann number $Ha \gg 1$, the non-dimensional pressure drop can be determined asymptotically (Shercliff 1953; Müller & Bühler 2001) as

$$K_p = \frac{Ha}{1 - \alpha_w/\eta Ha^{-1/2} - Ha^{-1}}. \tag{3.42}$$

Here α_w represent a coefficient depending on the conductivity of the side walls. For insulating side walls, it was evaluated by Shercliff (1953) to $\alpha_w \approx 0.825$ and for perfectly conducting side walls to $\alpha_w \approx 0.95598$ (Hunt & Stewartson 1965). Equation (3.42) distinguishes the three contributions to the pressure drop in the denominator. The first term is caused by the core flow where there is a balance between pressure gradient and the Lorentz force. The second and third terms are due the Shercliff and Hartmann layers, respectively.

The distribution of the current and the velocity profile depends mainly on the electric conductivity of the Hartmann wall. The core velocity scales with Ha^{-1} and Ha^{-2} if the walls are insulated and perfectly conducting, respectively (see equations (3.31) and (3.32)), while the velocity in the Shercliff layers scales with Ha^{-1} whether the walls are conducting or non-conducting (Hunt & Stewartson 1965). Therefore, for a perfectly conducting Hartmann wall and insulated Shercliff walls, an M-shape velocity profile is obtained with a uniform velocity of order Ha^{-2} in the core region and velocity of order Ha^{-1} in the Shercliff layers.

3.2.3 A Quasi–Two–Dimensional Magnetohydrodynamic Model for $Ha \gg 1$ and $N \gg 1$ Flow in a Duct

For a high Hartmann number $Ha \gg 1$, the velocity profile becomes flat in the core region while it decreases exponentially in the vicinity of the Hartmann layer.

Furthermore, the thickness of the Hartmann layer is very thin and the core flow occupies a very large part of the cross-section. Resolving these boundary layers in a full three–dimensional computation become very expensive, which motivates the use of an approximation known as the quasi–two–dimensional (Q2D) approach. With the quasi–two–dimensional approach, the problem is formulated in terms of core variables, and the effect of the boundary layers is included through an additional term in the momentum equation accounting for the wall friction. It reduces the computational effort of solving a three–dimensional problem to a two–dimensional flow formulation for the core flow variables.

For a strong magnetic field such that the Hartmann number $Ha \gg 1$ and the interaction parameter $N \gg 1$, velocity components parallel to the field will be suppressed significantly (Branover 1978). The energy of vortices perpendicular to the magnetic field are removed by Joule dissipation and the vortices are strongly damped. However, vortices aligned with the field are not affected by it and the eddies are elongated as shown schematically in Fig. 3.4.

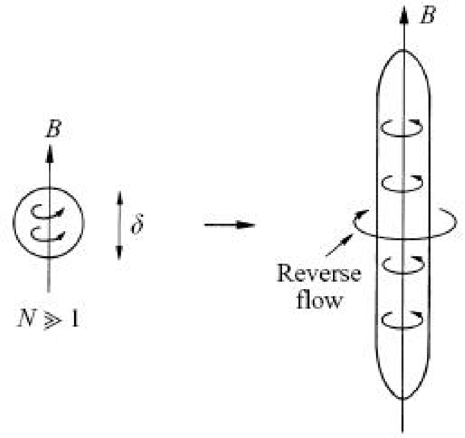

FIGURE 3.4: Magnetic damping of a parallel vortex at high Ha and N. The schematic diagram shows the structure of the flow at large times, from Davidson (2001).

Therefore, a quasi–two–dimensional structure of convective rolls parallel to the direction of the magnetic field will develop along the walls perpendicular to the field direction (Burr *et al.* 2000; Davidson 1995). The quasi–two–dimensional eddies extending between the plane walls have their ends embedded in the

Hartmann layers, i.e. the currents induced by the motion of these structures can close in the Hartmann layers. As a result, the flow experiences some breaking as shown in Fig. 3.5. This process is called Hartmann braking (Sommeria & Moreau 1982).

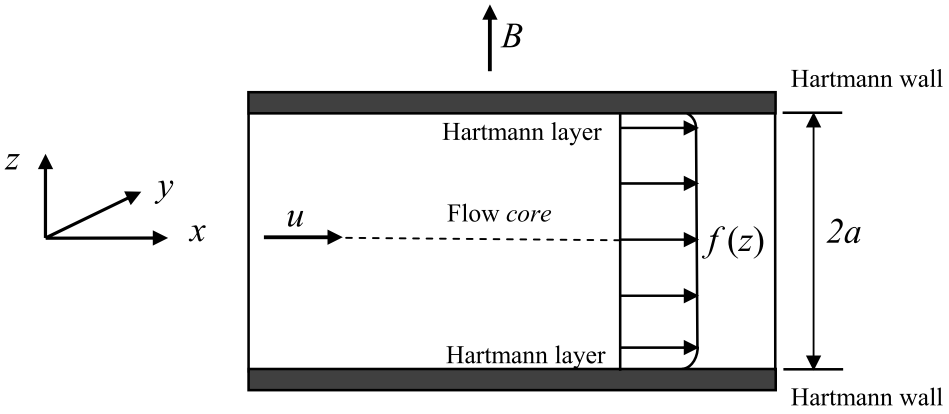

FIGURE 3.5: Quasi-two-dimensional MHD geometry. The core velocity decay to zero to satisfy the no-slip boundary condition on the walls

Consider the flow of incompressible, viscous, and electroconducting fluid between two parallel electrically insulating walls, which are perpendicular to the applied magnetic field and spaced a distance $2a$ apart. The configuration is similar to that shown in Fig. 3.1. Following Sommeria & Moreau (1982), the interaction parameter and Hartmann number are assumed to be much greater than unity ($N \gg 1$ and $Ha \gg 1$), and magnetic Reynolds number is assumed as to be much less than unity ($Re_m \ll 1$).

The electromagnetic force in the momentum equation can be expressed as a unidirectional diffusion term. By eliminating current density and including the irrotational part of the $(\mathbf{J} \times \mathbf{B})$ force in the pressure, the momentum equation becomes (Sommeria & Moreau 1982)

$$\frac{\partial \mathbf{u}}{\partial t} + (\mathbf{u}\cdot \nabla)\mathbf{u} = -\nabla p^* + \nu {\nabla_\perp}^2 \mathbf{u} - \frac{\sigma B^2}{\rho} {\nabla_\perp}^{-2} \left(\frac{\partial^2 \mathbf{u}}{\partial z^2} \right), \tag{3.43}$$

where p^* is the augmented pressure and ∇^{-2} is the inverse of the Laplacian operator. The subscript $\perp$ refers to vector quantities projected in the direction of the magnetic field, i.e. the (x, y) plane. By taking the curl of this equation, the parallel component of vorticity w_z can be written as

$$\frac{\partial w_z}{\partial t} = \nu {\nabla_\perp}^2 w_z - \frac{\sigma B^2}{\rho} {\nabla_\perp}^{-2} \left(\frac{\partial^2 w_z}{\partial z^2} \right), \tag{3.44}$$

The application of operator ∇^{-2} is equivalent to multiplication by the square of the length scale perpendicular to the magnetic field (${l_\perp}^2$) in Fourier space. Therefore, the electromagnetic force tends to damp the velocity components normal to the magnetic field and stimulates a diffusion of vorticity along the direction of the magnetic field. The length scale parallel to the magnetic field ($l_\parallel$) evolves at a rate

$$l_\parallel = \frac{l_\perp}{(t/t_J)^{1/2}}. \tag{3.45}$$

From the above equation, an anisotropic state is reached during the typical turnover time where ($l_\parallel / l_\perp \sim N^{1/2}$) if $l_\perp N^{1/2}$ is smaller than the spacing of the walls perpendicular to the magnetic field. This anisotropic features leads to the formation of extended vortex tubes located parallel to the magnetic field provided that the applied field is strong, i.e. the Joule dissipation time t_J is small compared with the vorticity turnover time scale ($t_{tu} = l/u$)

$$t_J = \frac{\rho}{\sigma B^2} \ll \frac{l}{u}, \tag{3.46}$$

where l and u are the characteristic length and characteristic velocity scales, respectively, so that the interaction parameter is large compared to unity, i.e. $N = t_{tu}/t_J \gg 1$. In contrast, if $t_J \gg t_{tu}$, i.e. $N \ll 1$, inertial forces dominates the Lorentz force , which is expected to have a negligible effect on the flow turbulence (Moffatt 1967).

The three–dimensional flow velocity $\mathbf{u}$ can be expressed in the form (Bühler 1996)

$$\mathbf{u}(x, y, z, t) = \left\{ \begin{array}{c} \mathbf{u}(x, y, t) \\ \mathbf{v}(x, y, t) \\ 0 \end{array} \right\} \cdot f(z), \tag{3.47}$$

with

$$f(z) = 1 - e^{Ha(|z|-1)}. \tag{3.48}$$

For $Ha \gg 1$, the function $f(z)$ is equal to unity in the core region and must satisfy non-lip conditions at the walls, i.e. $f(\mp 1) = 0$. Consequently, the flow can be split into a core region separated by thin boundary layers. In the core, there is a balance between the pressure gradient and Lorentz force. The viscous effects are confined to the Hartmann layers where the viscosity and Lorentz force balance each other (Shercliff 1975). The velocity in the core presents only a very slight variation along the magnetic field lines. However, in the vicinity of the walls perpendicular to the magnetic field it exhibits an exponential profile (see equation (3.28)).

This behavior led Sommeria & Moreau (1982) to derive a two–dimensional core model for the flow bounded between insulating walls, based on the exponential velocity profile by integrating the Navier–Stokes equations from one Hartmann wall to the other (i.e. $-1 \leq z \leq 1$), and expressing an equation for the velocity field projected in the perpendicular direction $u_\perp$.

Rewrite the equations of motion (3.11, 3.12, 3.13 and 3.15) in terms of velocities and currents parallel and perpendicular to the magnetic field, i.e. $(\mathbf{u}_\perp, w)$ and $(\mathbf{J}_\perp, J_z)$, then the non-dimensional equations of motion become (Pothérat *et al.* 2000)

$$\nabla_\perp \cdot \mathbf{u}_\perp + \frac{\partial w}{\partial z} = 0, \tag{3.49}$$

$$\frac{1}{N}\left(\frac{\partial \mathbf{u}_\perp}{\partial t} + \mathbf{u}_\perp \, . \, \nabla_\perp \mathbf{u}_\perp + w\frac{\partial \mathbf{u}_\perp}{\partial z}\nabla_\perp p\right) - \frac{1}{Ha^2}\nabla_\perp^2 \mathbf{u}_\perp - \frac{1}{Ha^2}\frac{\partial^2 \mathbf{u}_\perp}{\partial z^2} = \mathbf{J}_\perp \ \times \ \hat{\mathbf{z}}, \tag{3.50}$$

$$\frac{1}{N}\left(\frac{\partial w}{\partial t} + \mathbf{u}_\perp \, . \, \nabla_\perp w + w\frac{\partial w}{\partial z} + \frac{\partial p}{\partial z}\right) - \frac{1}{Ha^2}\nabla_\perp^2 w - \frac{1}{Ha^2}\frac{\partial^2 w}{\partial z^2} = 0, \tag{3.51}$$

$$\nabla \perp \cdot \mathbf{J}_\perp + \frac{\partial J_z}{\partial z} = 0, \tag{3.52}$$

$$\mathbf{J} = -\nabla \phi + \mathbf{u} \times \hat{\mathbf{z}}. \tag{3.53}$$

The $z-$ averaged of momentum equation can be expressed as

$$\frac{1}{N}\left[\frac{\partial \bar{\mathbf{u}}_\perp}{\partial t} + (\bar{\mathbf{u}}_\perp \ \cdot \ \nabla_\perp)\bar{\mathbf{u}}_\perp + \overline{(\acute{\mathbf{u}}_\perp \ \cdot \ \nabla_\perp)\acute{\mathbf{u}}_\perp} + \nabla_\perp \bar{p}\right] = \frac{1}{Ha^2}\nabla_\perp^2 \bar{\mathbf{u}}_\perp + \frac{1}{Ha^2}\tau_w + \bar{\mathbf{J}}_\perp \times \hat{\mathbf{z}}, \tag{3.54}$$

where a, u_0, a/u_0, ρu_0^2, $(\rho\sigma u_0/a)Ha$ and $(\sigma B u_0/Ha)$ were used as respective length, velocity, pressure, shear stress and electric current density. The overbar represents z–averaging across the fluid depth and $\acute{\mathbf{u}}_\perp$ represents the deviation from the averaged velocity $\bar{\mathbf{u}}$ (i.e. $\acute{\mathbf{u}}_\perp = \mathbf{u}_\perp - \bar{\mathbf{u}}_\perp$). The subscript $\perp$ refers to vector quantities projected in the direction of the magnetic field, i.e. (x, y) plane. Similarly, to turbulent flow, z–average of $(\mathbf{u}_\perp \cdot \nabla_\perp)\mathbf{u}_\perp$ does not reduce to $(\bar{\mathbf{u}}_\perp \cdot \nabla_\perp)\bar{\mathbf{u}}_\perp$. Instead, a Reynolds stress $\overline{(\acute{\mathbf{u}}_\perp \cdot \nabla_\perp)\acute{\mathbf{u}}_\perp}$ appears, which involves the deviation of $\acute{\mathbf{u}}_\perp$ from the z-averaged velocity. τ_w denotes the sum of the viscous stress at both walls

$$\tau_w = -\left[\left(\frac{\partial \mathbf{u}_\perp}{\partial z}\right)_{z=-1} - \left(\frac{\partial \mathbf{u}_\perp}{\partial z}\right)_{z=1}\right].$$

Neglecting the higher order terms of order $O(Ha^{-1},\ N^{-1})$, equation (3.54) gives the *SM82* model in which the inertial effects occurring inside the Hartmann layer are neglected. When this model is applied to the Shercliff flow, the boundary layers along the wall parallel to the magnetic field (Shercliff layers) are three-dimensional in nature. Since this model assumes that diffusion along the magnetic field lines occurs faster than lateral diffusion of the angular momentum, the error using this model with the three–dimensional solution (e.g. Moreau (1990)) has been shown to be in order of 10% (Pothérat *et al.* 2005). The *SM82* model requires electrically insulated walls perpendicular to the magnetic field, the assumption of a quasi–two–dimensional flow fails if strong velocity jets at the Hartmann layers are introduced. In addition, this model fails to describe the flow of inertially driven recirculation (Ekmann pumping) in the Hartmann layers such as occurs in rotating flows for instance. This defect can be corrected by including inertial effects within Hartmann layers (i.e. , the term of order Ha^{-1}) in equation (3.54), which has been implemented by Pothérat *et al.* (2005).

Following Pothérat *et al.* (2000), τ_w can be calculated from the velocity profile inside the Hartmann layer as $\tau_w = -n_H Ha \bar{\mathbf{u}}_\perp$, where n_H denotes the number of Hartmann walls: $n_H = 2$ for a flow confined between two rigid walls, and $n_H = 1$ for a free surface flow. The electromagnetic term $\bar{\mathbf{J}}_\perp \times \hat{\mathbf{z}}$ can be determined using the current density injected into the fluid through the walls. The z– averaged of equation (3.52) gives

$$\nabla_\perp \cdot \bar{\mathbf{J}}_\perp = J_w, \tag{3.55}$$

and the z– averaged of equation (3.53) (using $\nabla \perp \cdot \bar{\mathbf{u}}_\perp = 0$) gives

$$\nabla_\perp \times \bar{\mathbf{J}}_\perp = 0, \tag{3.56}$$

where J_w represents the current injected at the walls. Therefore, the z–averaged current can be expressed as the gradient of the scalar ψ_0, which is defined as

$$\bar{\mathbf{J}}_\perp = \frac{1}{Ha}\nabla\psi_o, \tag{3.57}$$

$$\frac{1}{Ha}\nabla_\perp^2\psi_o = -J_w \tag{3.58}$$

Following Pothérat *et al.* (2005), the scalar potential ψ_0 is determined from the current source J_w through the solution of the Poisson equation (3.58), which is unique for a given current flux $\bar{\mathbf{J}}_\perp \cdot \mathbf{n}$ at the lateral boundaries. Defining the velocity field associated with the stream function ψ_0 as $\mathbf{u}_f$, the electromagnetic force in equation (3.54) is found to depend on the electric current boundary condition through $\bar{\mathbf{J}}_\perp \times \hat{\mathbf{z}} = \mathbf{u}_f$. The velocity $\mathbf{u}_f$ thus represents a driving force that arises from current injection at boundaries.

In order to model the case of an insulated duct, the vector field $\mathbf{u}_f = 0$. However, in order to model current injection, a non-zero $\mathbf{u}_f$ is required. For example, Pothérat *et al.* (2005) describe (for the case of an electrode used to inject current into a duct) the use of a Dirac-delta function with an integral equal to the total injected current to approximate J_w, which in turn can be used to determine $\mathbf{u}_f$.

Finally, the Reynolds stress term of order $O(Ha^{-1}\,N^{-1})$ from equation (3.54) is neglected, yielding (Pothérat *et al.* 2005)

$$\frac{\partial \mathbf{u}_\perp}{\partial t} + (\mathbf{u}_\perp \cdot \nabla_\perp)\mathbf{u}_\perp + \nabla_\perp p = \frac{1}{Re}\nabla_\perp^2\mathbf{u}_\perp + \frac{1}{t_H}(\mathbf{u}_f - n_H\mathbf{u}_\perp). \tag{3.59}$$

Here $t_H = a^2/\nu Ha$, is the Hartman braking time. The linear damping term $-\mathbf{u}_\perp/t_H$ represents the effect of the Hartmann layers on the core flow with a characteristic time t_H. From equation (3.59), it can be seen that the effect of the Lorentz force is contained within the last term.

This model has been modified by (Bühler 1996) to be more general by taking into account walls with varying conductivity,

$$t_H = \frac{a^2}{\nu\ Ha}\left[\frac{1 + c\ Ha}{1 +\ Ha}\right], \tag{3.60}$$

where c is the electrical conductivity of the walls given in equation (3.24). The key feature of this model is that it provides a set of modified two–dimensional Navier–Stokes equations with forcing and linear braking terms that represent the electromagnetic force effects and the friction in the Hartmann layers.

In conclusion, the *SM82* model is formally valid provided $Ha \gg 1$ and $N \gg 1$. The computational implementation of this model is effective and gives flow dynamics predictions of reasonable accuracy. It reduces the substantial computational efforts of solving a three-dimensional problem by reducing it to a two–dimensional flow form. Therefore, the required CPU cost is much lower compared with that of three-dimensional DNS. The theoretical accuracy of this model is $(Ha^{-1},\ N^{-1})$ for the velocity and pressure. The quasi two-dimensional model has been successfully used for different magnetohydrodynamic flows confined between parallel planes such parallel layers, for example (Moreau & Sommeria 1988; Bühler 1996; Pothérat *et al.* 2000; Cuevas *et al.* 2006; Dousset & Pothérat 2008; Smolentsev *et al.* 2012; Hussam *et al.* 2012). It gives good results when inertia forces are small. The quasi–two–dimensional approach of integrating out a dimension of a flow is not new and has been used before to model the Hele-Shaw flow of a viscous fluid between two parallel closely spaced plates. Quasi–two–dimensional flows occur in a number of other special cases. For example, the flow of a soap film (Couder 1986), stratified flows (Voropayev *et al.* 1991), and the flows of a rotating fluid (Zavala Sansón *et al.* 2001).

3.3 The Governing Flow Equations

The numerical scheme used in this project solves the viscous, incompressible quasi-two–dimensional magnetohydrodynamic Navier–Stokes and energy equations. For a high Hartmann number the magnetic Reynolds number Re_m is assumed to be very small. Thus, the induced magnetic field is negligible and the resulting magnetic field is imposed in the z–direction only. Under these conditions the flow is quasi two–dimensional and consists of a core region, where the velocity is invariant along the direction of the magnetic field, and a thin Hartmann layer at the wall perpendicular to the magnetic field.

In this case, for the configuration shown in Fig. 1.4 where the duct was electrically insulated, the non-dimensional magnetohydrodynamic equations of continuity, momentum, and energy reduce to

$$\nabla\cdot \mathbf{u} = 0, \tag{3.61}$$

$$\frac{\partial \mathbf{u}}{\partial t} + (\mathbf{u}\cdot \nabla)\mathbf{u} + \nabla p = \frac{1}{Re}\nabla^2 \mathbf{u} - 2\left(\frac{d}{a}\right)^2 \frac{Ha}{Re}\mathbf{u}, \tag{3.62}$$

$$\frac{\partial \theta}{\partial t} + (\mathbf{u}\cdot \nabla)\theta = \frac{1}{Pe}\nabla^2 \theta, \tag{3.63}$$

where $\mathbf{u}$, p and θ are the velocity, pressure, and temperature fields, respectively, projected onto the x-y plane. Lengths are scaled by the cylinder diameter d, pressure by ρu_0^2, where ρ is the density and u_0 is the peak inlet velocity, time by d/u_0, and temperature by the imposed temperature difference between the bottom and top walls, $\Delta T = T_w - T_0$ (Burr *et al.* 2000; Sheard & King 2011). The non-dimensional variables are defined as follows

$$u = \frac{\tilde{u}}{u_0}, \quad v = \frac{\tilde{v}}{u_0}, \quad x = \frac{\tilde{x}}{d}, \quad y = \frac{\tilde{y}}{d}, \quad t = \frac{\tilde{t}u_0}{d}, \quad p = \frac{\tilde{p}}{\rho u_0^2},$$

$$\theta = \frac{T - T_0}{T_w - T_0}, \quad Re = \frac{u_0\, d}{\nu}, \quad Ha = a\, B\sqrt{\frac{\sigma_e}{\rho\nu}}, \quad Pe = Re\, Pr,$$

where ν, σ_e and B are the kinematic viscosity, electrical conductivity, applied magnetic field, respectively. Here a represents the distance between the Hartmann walls as, per Sommeria & Moreau (1982), rather than the channel half-height used earlier in the work of Frank *et al.* (2001). A Prandtal number of $Pr = 0.022$ is used throughout, representative of the eutectic alloy GaInSn.

It also makes sense to define the *modified Hartmann number*

$$Ha^\star = \left(\frac{d}{a}\right)^2 Ha, \tag{3.64}$$

since this non-dimensional parameter defines the relative influence of the magnetic damping term to the viscous diffusion term for quasi–two–dimensional flow. This variable is important because throughout this thesis the effect of varying blockage ratio $\beta = d/h$ is examined, i.e. the cylinder diameter d is varied while keeping the duct width h and depth a constant.

It is noted that the energy equation is sometimes written to include terms describing the effects of viscous dissipation and Joule heating (e.g., see (Hossain 1992)). However, here these terms are omitted (following (Burr *et al.* 2000; Yoon *et al.* 2004) and others), after an order of magnitude calculation confirmed their contributions were between 500 times and 10^7 times smaller than those of the included terms for applications motivating this study, such as eutectic alloy flows.

The local Nusselt number along the lower heated wall of the channel is defined as

$$Nu_w(x,t) = \frac{1}{(\theta_f - \theta_w)} \left. \frac{\partial \theta}{\partial y} \right|_{wall} . \tag{3.65}$$

θ_f is the bulk fluid temperature, which is calculated using the velocity and temperature distribution as

$$\theta_f(x,t) = \frac{\int_0^h u\theta \, \mathrm{d}y}{\int_0^h u \mathrm{d}y}, \tag{3.66}$$

where h is the non-dimensional width of the duct and u is the streamwise component of velocity.

A time-averaged Nusselt number for heat transfer through the heated wall of the channel is calculated by first taking the time average of the local Nusselt number ($\overline{Nu_w}$) at each x-station, and then integrating over the non-dimensional length of the heated bottom wall, L, using

$$Nu = \frac{1}{L} \int_0^L \overline{Nu_w}(x) \, \mathrm{d}x. \tag{3.67}$$

To characterize the effect on the heat transfer due to the addition of a cylinder to the channel, the overall increment of heat transfer is defined as

$$HI = \frac{Nu - Nu_0}{Nu_0} \times 100, \tag{3.68}$$

where Nu_0 is the time-averaged Nusselt number of the heated region of the duct without the cylinder.

The lift, drag and moment coefficients (per unit span) are defined according to

$$C_L = \frac{F_l'}{\frac{1}{2} \rho u_0^2 d}, \tag{3.69}$$

$$C_D = \frac{F_d'}{\frac{1}{2} \rho u_0^2 d}, \tag{3.70}$$

$$C_M = \frac{M'}{\frac{1}{4}\,\rho u_0^2 d^2}, \tag{3.71}$$

where F_l', F_d' and M' are the lift, drag and moment exerted by the fluid per unit length of the cylinder. The total force acting on the cylinder surface is due to pressure and viscous components, which can be computed by direct integration over the surface of the cylinder. The pressure and viscous forces per unit span are respectively given as

$$\mathbf{F}_p = \oint p\mathbf{n}\ \mathrm{d}s, \tag{3.72}$$

$$\mathbf{F}_w = \oint \tau_w\ \mathrm{d}s, \tag{3.73}$$

$$\mathbf{F}_T = \mathbf{F}_p + \mathbf{F}_w, \tag{3.74}$$

where $\mathbf{n}$ is the unit outward vector normal of the fluid domain. This leads to the following moment contribution

$$\mathbf{M} = \oint \mathbf{r} \times (p\mathbf{n} + \tau_w)\mathrm{d}s, \tag{3.75}$$

where $\mathbf{r}$ is a moment arm vector.

The wake oscillation frequency f is parameterized by the Strouhal number

$$St = \frac{fd}{u_0}. \tag{3.76}$$

3.4 Numerical Scheme

A nodal spectral-element method is used to discretise the governing flow and energy equations (3.61-3.63) in space, and a third-order scheme based on backwards differentiation is employed for time integration (Karniadakis *et al.* 1991). The spectral element method is similar to the finite element method, in that the fluid domain is divided into a mesh of individual elements. However, instead of employing a low-order (e.g. linear) basis over each element, a high-order polynomial basis is instead used, permitting very rapid convergence with increasing polynomial degree (Karniadakis *et al.* 1991). The spectral element technique uses the tensor product of higher-order Lagrangian polynomials to interpolate the solution variables in each direction within each element.

Lagrange polynomials are defined as (Karniadakis & Sherwin 2005)

$$L_i(\xi) = \prod_{g=1, g\neq i}^{p+1} \frac{(\xi - \xi_g)}{(\xi_i - \xi_g)}, \tag{3.77}$$

where ξ is the spatial coordinate, i and g are the indices of data points, and $p+1$ is the number of data points.

The code is an in-house formulation, which has been validated against experimental data (Sheard *et al.* 2007, 2009) and a separate implementation of a similar algorithm (Blackburn & Sheard 2010), and has previously been employed to study channel flows (Neild *et al.* 2010). The chosen scheme employs a Galerkin finite element method in two dimensions, with high-order Lagrangian interpolants used within each element. The nodes points within each element correspond to the Gauss-Legendre-Lobatto quadrature integration points, producing diagonal mass matrices. As the functions at the internal nodes only depend on the boundary nodes, matrix manipulation allows the internal nodes to be eliminated from the matrix subproblem of the pressure and diffusion substeps through static condensation. This greatly improves the efficiency of the scheme.

3.4.1 Spatial Discretisation

The computational domain in the $x - y$ plane is broken up into quadrilateral elements. Within each element, Gauss-Lobatto-Legendre quadrature is employed for integration, which leads to pleasing exponential spatial convergence for the scheme. The Gauss-Lobatto-Legendre quadrature points are the roots of the equation (Karniadakis & Sherwin 2005)

$$(1 - \xi)P_m'(\xi) = 0 \quad \text{with} \quad -1 \leq \xi \leq 1. \tag{3.78}$$

Using Rodriguez's formula, the Legendre polynomial (P_m) can be written

$$P_m = \frac{1}{2^m m!}\frac{d^m}{d\xi^m}(\xi^2 - 1)^m \quad \text{where} \quad m = 0, 1, 2, ... \tag{3.79}$$

The Galerkin weighted residual methods is used to form equations for the solution variables at the nodal points. The flow equations are multiplied by the nodal weight function and integrated over space. The resulting integrals only depend on the local and neighbouring elements as the weighting functions are non-zero only within the element. The weighting coefficients of Gauss-Legendre-Lobatto quadrature are given by

$$w_j = \frac{2}{m(m+1\,)}\frac{1}{\,)}[P_m(x_j)] \quad \text{with} \quad j = 0, 1, 2, ..., m. \tag{3.80}$$

Then, an integral to be evaluated can be approximated in a standard domain (which extends from -1 to 1)

$$\int_{-1}^{1} f(\xi) d\xi = \sum_{j=0}^{Q-1} w_j f(\xi_j) + R(u), \tag{3.81}$$

where ξ_j are the Q discrete quadrature points (or zeroes) at which the function $f(\xi)$ is evaluated and $R(u)$ denotes the approximation error, which is equal to zero if $f(\xi)$ is a polynomial of degree $2Q-1$ or less. The weighting coefficients and knowledge of the function at the quadrature points allows the solution to the integral in the standard domain to be determined. A simple transformation is then used to apply the solution to the physical domain. The weighting coefficients and quadrature points allow the integral equation resulting from the application of the weighted residual method to be determined using Gauss-Legendre-Lobatto quadrature in two dimensions.

3.4.2 Temporal Discretisation

A three-step splitting scheme is used for temporal discretisation of Navier–Stokes as described by Karniadakis *et al.* (1991). This method is known as an operator-splitting or a fractional step method. It consists of separating the Navier–Stokes equations into convection, pressure and diffusion terms, and integrating them in three separate substeps.

In the first substep, an intermediate velocity field $\mathbf{u}^*$ is calculated from the non-linear convection term and Hartmann friction term of equation 3.62 as

$$\frac{\mathbf{u}^* - \sum_{q=0}^{J-1} \alpha_q \mathbf{u}^{n-q}}{\Delta t} = -\sum_{q=0}^{J-1} \beta_q \left\{ (\mathbf{u}^{n-q} \cdot \nabla)\mathbf{u}^{n-q} + 2\left(\frac{d}{a}\right)^2 \frac{Ha}{Re} \mathbf{u}^{n-q} \right\}, \tag{3.82}$$

which is solved explicitly by a third-order backwards–multistep technique, which are based on backwards differentiation (i.e. the solution is evaluated at time $n+1$,

Coefficient	**Value**
γ_0	11/6
α_0	3
α_1	-3/2
α_2	-1/3
β_0	3
β_1	-3
β_2	1

TABLE 3.1: Third-order backwards-multistep scheme coefficients.

and the appropriate order backwards difference scheme dictates the combination of $\mathbf{u}$ values at previous times required to approximate the right-hand-side terms at the $n+1$ time).

In the second substep, a second intermediate velocity field $\mathbf{u}^{**}$ is computed from the pressure using

$$\frac{\mathbf{u}^{**}-\mathbf{u}^{*}}{\Delta t} = -\nabla p^{n+1}. \tag{3.83}$$

The divergence of equation (3.83) is taken and continuity is enforced for $\mathbf{u}^{**}$ using equation (3.61) resulting in a Poisson equation for the pressure,

$$\nabla^2 p^{n+1} - \frac{1}{\Delta t}\nabla\cdot\mathbf{u}^{*} = 0. \tag{3.84}$$

In the third substep, the velocity field $\mathbf{u}^{n+1}$ is calculated from

$$\frac{\gamma_0\mathbf{u}^{n+1}-\mathbf{u}^{**}}{\Delta t} = \frac{1}{Re}\nabla^2\mathbf{u}^{n+1}. \tag{3.85}$$

This step is solved as an implicit Helmholtz problem. The values of explicit and implicit coefficients γ_0, α_q, and β_q for the third-order scheme (i.e. $J = 3$) are given in Table 3.1.

Overall, the splitting scheme achieves third-order time accuracy by enforcing a Neumann condition on the pressure field on boundaries (Karniadakis *et al.* 1991).

For the energy equation, the same third-order backwards differentiation scheme is used as for the velocity field

$$\frac{\theta^{*}-\sum_{q=0}^{J-1}\alpha_q\theta^{n-q}}{\Delta t} = -\sum_{q=0}^{J-1}\beta_q\left\{(\mathbf{u}^{n-q}\cdot\nabla)\theta^{n-q}\right\}, \tag{3.86}$$

$$\frac{\gamma_0\theta^{n+1}-\theta^*}{\Delta t}=\frac{1}{Pe}\nabla^2\theta^{n+1}. \tag{3.87}$$

3.5 Linear Stability Analysis

The methods applied for examining linear stability of disturbances are based on time integration of the linearized Navier–Stokes equations. It has been successfully applied in the wake of various bluff bodies to predict the flow transitions including cylinders (Barkley & Henderson 1996; Blackburn *et al.* 2005; Sheard *et al.* 2009), toroids (Sheard *et al.* 2003) and elliptical leading edge plates (Ryan *et al.* 2005). These equations are derived by substituting velocity and pressure fields decomposed into a two–dimensional base flow and infinitesimal fluctuating components, such that the new velocity and pressure fields become

$$\mathbf{u}(x,y,t)=\mathbf{U}(x,y,t)+\mathbf{u}'(x,y,t), \tag{3.88}$$

$$p(x,y,t)=P(x,y,t)+p'(x,y,t), \tag{3.89}$$

Here perturbations are restricted to be two–dimensional owing to the quasi–2D treatment of the underlying flow (see § 3.2.3). Substituting the above equations (3.88-3.89) into the Navier–Stokes equations, subtracting the base flow equations, and neglecting the products of perturbation velocities yields the linearized quasi–2D Navier–Stokes equations

$$\frac{\partial\mathbf{u}'}{\partial t}=-\mathrm{DN}\mathbf{u}'-\nabla p'+\frac{1}{Re}\nabla^2\mathbf{u}'-2\left(\frac{d}{a}\right)^2\frac{Ha}{Re}\mathbf{u}', \tag{3.90}$$

$$\nabla\cdot\mathbf{u}'=0, \tag{3.91}$$

which govern the perturbation field, the growth of which can be then monitored over time. Therefore, the stability of a perturbation field $\mathbf{u}'$ can be determined as a function of Re and Ha. The linearized advection term is defined as

$$\mathrm{DN}\mathbf{u}'=(\mathbf{U}\cdot\nabla)\mathbf{u}'+(\mathbf{u}'\cdot\nabla)\mathbf{U}.$$

Let $\mathscr{A}(\tau)$ denote the linear evolution operator over a time τ defined by equations (3.91) and (3.90),

$$\mathbf{u}'(t+\tau)=\mathscr{A}(\tau)\mathbf{u}'(\tau). \tag{3.92}$$

For flows with a time period T an eigenvalue problem in terms of operator $\mathscr{A}(T)$ is obtained

$$\mathscr{A}(\tau)\hat{\mathbf{u}} = \mu\hat{\mathbf{u}}, \tag{3.93}$$

$$\mu \equiv \mathrm{e}^{(\sigma+i\omega)\ T}, \tag{3.94}$$

where σ and ω are the growth rate and angular frequency of a linear instability mode over the n^{th} period and angular frequency, respectively. Note that μ is the complex eigenvalue and $\hat{\mathbf{u}}$ the eigenvector field. Eigenvector solutions can be written as

$$\hat{u}(x,y,t+T) = \hat{u}(x,y,t)e^{(\sigma+i\omega)\ T}, \tag{3.95}$$

$$\hat{v}(x,y,t+T) = \hat{v}(x,y,t)e^{(\sigma+i\omega)\ T}, \tag{3.96}$$

$$\hat{p}(x,y,t+T) = \hat{p}(x,y,t)e^{(\sigma+i\omega)\ T}. \tag{3.97}$$

The stability analysis may be performed on either a steady or unsteady base flow. For unsteady periodic flow, T corresponds a single flow period of the unsteady base flow, while for steady base flows, T represents an arbitrary time interval over which the growth of the mode is recorded. The stability of the base flow is then determined from dominant eigenvalues μ with the largest modulus. If $|\mu| > 1$, then the flow is unstable, and if $|\mu| < 1$, the flow is stable. Neutral stability occurs when $|\mu| = 1$, which represents a system in which the perturbation will neither grow nor decay. The Reynolds number for the flow giving $|\mu| = 1$ is the critical Reynolds number for the onset of the instability.

To perform this technique numerically, the following steps are taken. An initial perturbation field consisting of random noise is constructed. The perturbation equations are integrated forward in time simultaneously with the base flow equations. To obtain the Floquet multiplier μ, eigenmode solution approaches including the power method or Krylov subspace methods described by Blackburn & Lopez (2003) may be used. The present formulation of the stability analysis technique adopts the implicitly restarted Arnoldi method (Sheard *et al.* 2003) to determine the leading eigenvalues and corresponding eigenvectors.

3.6 Transient Growth Analysis

In this section, a method for considering the transient growth of disturbances is described. In this case, the base flow may be linearly stable, but the perturbation fields may exhibit significant transient response due to the interaction between non-normal eigenmodes (Schmid & Henningson 2001). The approach applied for examining transient growth of disturbances are based on time integration of the linearized Navier–Stokes equations (3.90-3.91) along with backwards time integration of adjoint equations presented shortly.

Typically, transient growth is defined with respect to the energy norm of the perturbation field, derived from the L_2 inner product

$$2E_k(\mathbf{u}') = (\mathbf{u}', \mathbf{u}') \equiv \int \mathbf{u}' \cdot \mathbf{u}' \ \mathrm{d}\mathbf{V}, \tag{3.98}$$

where E_k is the kinetic energy per unit mass of the perturbation, integrated over the full domain. Since the governing equations are linear it is sufficient to consider the initial perturbation field $\mathbf{u}'(0)$ to have unit norm. The transient energy growth over interval τ is (Blackburn *et al.* 2008b)

$$\frac{E_k(\tau)}{E_k(0)} = (\mathbf{u}'(\tau), \mathbf{u}'(\tau)). \tag{3.99}$$

In terms of the operator $\mathscr{A}(\tau)$ and its adjoint $\mathscr{A}^*(\tau)$ in the L_2 inner product

$$\frac{E_k(\tau)}{E_k(0)} = (\mathscr{A}(\tau)\mathbf{u}'(0), \mathscr{A}(\tau)\mathbf{u}'(0)) = (\mathbf{u}'(0), \mathscr{A}^*(\tau)\mathscr{A}(\tau)\mathbf{u}'(0)), \tag{3.100}$$

where $\mathscr{A}^*(\tau)$ is obtained by integrating the adjoint linearized Navier–Stokes equations backwards over interval τ. The adjoint quasi two–dimensional Navier–Stokes equations differ slightly from the form derived in Barkley *et al.* (2008a) due to the addition of the Hartmann friction term. Adapting the nomenclature used in their work to compactly present the adjoint problem, the perturbation and adjoint fields are expressed as

$$\mathbf{q} = \begin{pmatrix} \mathbf{u}' \\ p' \end{pmatrix}, \quad \mathbf{q}^* = \begin{pmatrix} \mathbf{u}^* \\ p^* \end{pmatrix}, \tag{3.101}$$

where Ω is the spatial domain, and τ is an arbitrary positive final time.

The action of the forward and adjoint equations on fields $\mathbf{q}$ and $\mathbf{q}^*$ are given by the operators

$$\mathscr{H} = \left[\begin{array}{c|c} -\partial_t - \mathrm{DN} + \nu\nabla^2 - 2\left(\frac{d}{a}\right)^2 \frac{Ha}{Re} & -\nabla \\ \nabla\cdot & 0 \end{array} \right] \tag{3.102}$$

and

$$\mathscr{H}^* = \left[\begin{array}{c|c} \partial_t - \mathrm{DN}^* + \nu\nabla^2 + \alpha_H & -\nabla \\ \nabla\cdot & 0 \end{array} \right], \tag{3.103}$$

respectively, where α_H is the form of the Hartmann friction term in the adjoint equation which is to be determined. The adjoint advection operator is defined such that $\mathrm{DN}^*\mathbf{u}^* = -\left(\mathbf{U}\cdot\nabla\right)\mathbf{u}^* + \left(\nabla\mathbf{U}\right)^{\mathrm{T}}\cdot\mathbf{u}^*$.

For $\mathscr{H}^*$ to be the adjoint of $\mathscr{H}$, the bilinear concomitant equation must be satisfied for any fields $\mathbf{q}$ and $\mathbf{q}^*$ with compact support (values and derivatives zero on all boundaries), i.e.

$$\langle \mathscr{H}\mathbf{q}, \mathbf{q}^* \rangle - \langle \mathbf{q}, \mathscr{H}^*\mathbf{q}^* \rangle = 0. \tag{3.104}$$

The contribution of all terms in the standard linearized and adjoint Navier–Stokes equations have already been determined by Barkley *et al.* (2008b) so all that remains is to solve for the contribution made by the additional Hartmann friction term,

$$\int_0^\tau \int_\Omega \mathscr{H}\mathbf{q}\cdot\mathbf{q}^* \mathrm{d}v\,\mathrm{d}t - \int_0^\tau \int_\Omega \mathbf{q}\cdot\mathscr{H}^*\mathbf{q}^* \mathrm{d}v\,\mathrm{d}t = 0$$

$$\therefore \int_0^\tau \int_\Omega -2\frac{d^2}{a^2}\frac{Ha}{Re}\mathbf{u}'\cdot\mathbf{u}^* \mathrm{d}v\,\mathrm{d}t = \int_0^\tau \int_\Omega \mathbf{u}'\cdot\alpha\mathbf{u}^* \mathrm{d}v\,\mathrm{d}t,$$

which holds if $\alpha = -2\left(\frac{d}{a}\right)^2 \frac{Ha}{Re}$. Therefore, the adjoint equations can be expressed as

$$\frac{\partial\mathbf{u}^*}{\partial t} = -\mathrm{DN}^*\mathbf{u}^* - \nabla p^* + \frac{1}{Re}\nabla^2\mathbf{u}^* - 2\left(\frac{d}{a}\right)^2 \frac{Ha}{Re}\mathbf{u}^*,$$

$$\nabla\cdot\mathbf{u}^* = 0.$$

The transient growth of the system is determined by solving an eigenvalue problem. Let λ_j and $\mathbf{v}_j$ denote eigenvalues and normalized eigenfunctions of the operator $\mathscr{A}^*(\tau)\mathscr{A}(\tau)$, then

$$\mathscr{A}^*(\tau)\mathscr{A}(\tau)\mathbf{v}_j = \lambda_j \mathbf{v}_j.$$

The maximum possible energy growth, denoted $G(\tau)$, over a specified time τ, is then given by the dominant eigenvalue of $\mathscr{A}^*(\tau)\mathscr{A}(\tau)$, i.e.

$$G(\tau) = \max(\lambda_j).$$

The global maximum for any time interval is denoted by

$$G_{max} = \max(G(\tau)).$$

Aside from the additional Hartmann friction term in the forward and adjoint equations, the direct transient growth technique applied here is identical to that described in Blackburn *et al.* (2008a), and the linearized eigenmode solver employed here has been validated in Sheard *et al.* (2009) and Blackburn & Sheard (2010).

3.7 Validation of the Numerical Approach

Validation was performed against published results to ensure the accuracy of the present formulation and model. The literature review related to the work of this thesis demonstrated that few works have been dedicated for the magnetohydrodynamic flow and heat transfer past a circular cylinder in the presence of a strong magnetic field. Therefore, the numerical system was first tested for the case of non-magnetohydrodynamic (non-MHD) flow and heat transfer, for which a large number of studies are available. Then, a magnetohydrodynamic (MHD) case was validated.

3.7.1 Non-MHD Validation Tests

The first test concerns the critical Reynolds number Re_c and associated Strouhal number St_c at the transition from steady to unsteady flow in a zero-Ha flow (i.e. no magnetic field) for different blockage ratios. Results are compared with the published numerical results from linear stability analysis of Chen *et al.* (1995),

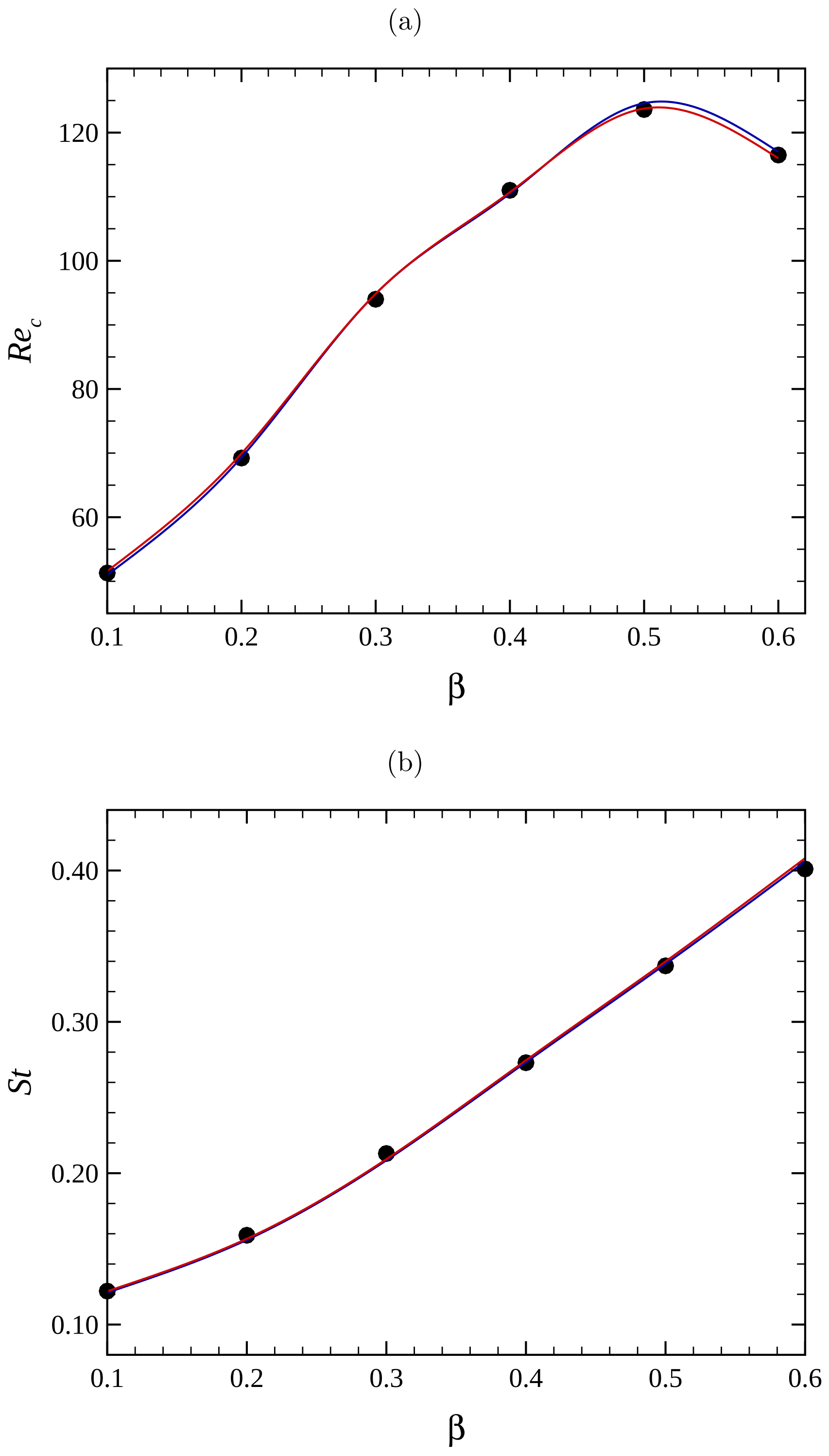

FIGURE 3.6: (a) Re_c and (b) St_c plotted against β. Symbols show the present data, while blue and red lines show data published in (Sahin & Owens 2004) and (Chen *et al.* 1995), respectively.

and direct numerical simulation of Sahin & Owens (2004) in Fig. 3.6, and an exceptionally close agreement can be observed. Critical Reynolds numbers were determined using the linear stability analysis below transition, and direct numerical simulation above transition, to extrapolate growth rates and mode amplitudes, respectively, to zero. This gives two independent estimates of the critical Reynolds number, which were found to be very close. The mean of the absolute values of the percentage difference between the present and the published results for Re and St were 0.25% and 0.15%, respectively.

Fig. 3.7 presents a comparison between the results of the present solver and those predicted by Griffith *et al.* (2011) for $Re = 188$ at blockage ratios $\beta = 0.3$ and 0.5. The vortices forming on the walls of the channel are drawn inwards and interact with the vortex street. Also, it can be noted in these cases the inversion of the vortex street in which the vortices forming on one side of the cylinder end up further downstream nearer the opposite wall of the channel. The results reproduced from Griffith *et al.* (2011) and those computed using present implementation are visually indistinguishable.

Next, the heat transfer capabilities of the solver were tested. Computed Nusselt numbers for heat transfer with $Pr = 0.7441$ at blockage ratios of 0.1 and 0.2 are compared against both a theoretical curve (Khan *et al.* 2004) and numerical results (Mettu *et al.* 2006) in Fig. 3.8. Again, a very good agreement with published data is found, with the mean of the absolute values of the percentage difference between the results found to be 0.75% and 1.0% for $\beta = 0.1$ and 0.2, respectively.

The respective temperature contours for $\beta = 0.1$ and 0.2 at different Reynolds numbers are shown in Fig. 3.9, which demonstrate the ability of the solver to resolve the thermal boundary layer around the cylinder. It can be noted that the isotherm contours are very close to the cylinder surface and far apart away from it. This indicates that large temperature gradients exit near the cylinder surface and small gradients far away.

Simulations for a rotating oscillating cylinder were also performed for comparison. Since the cylinder is rotated sinusoidally in time at forcing frequency

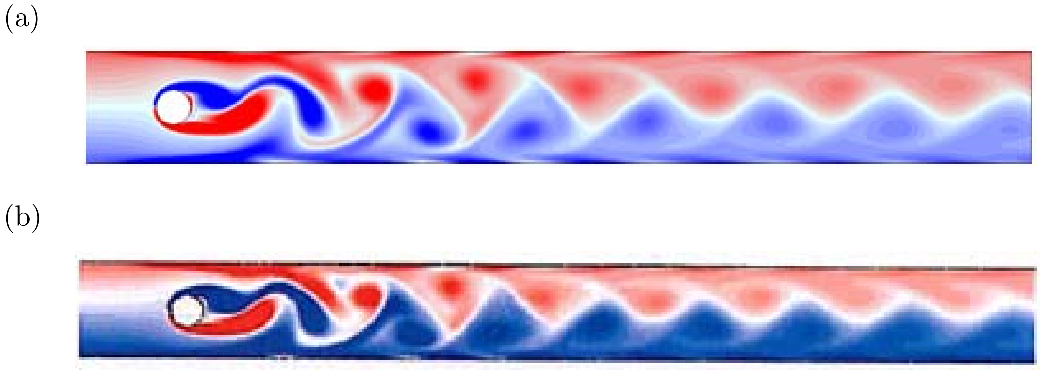

$\beta = 0.1$

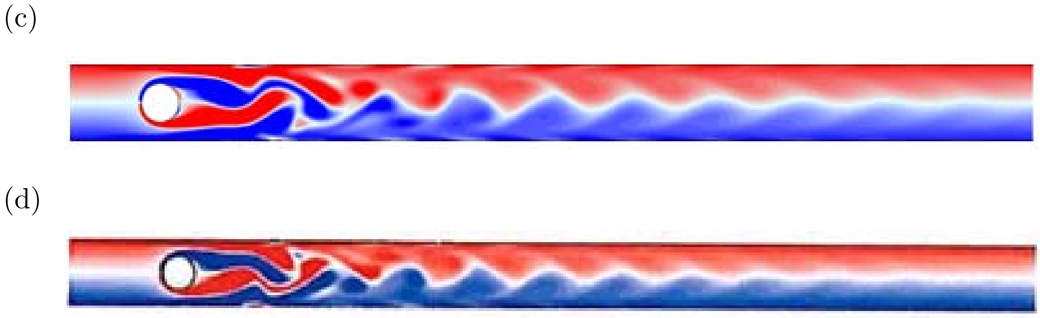

$\beta = 0.2$

FIGURE 3.7: Contours of vorticity plotted at $Re = 188$ and different blockage ratios as indicated. (a) and (c) represent the contours predicted by the present simulation. (b) and (d) represent the corresponding results reproduced from Griffith *et al.* (2011). Red and blue contours representing positive and negative vorticity, respectively.

(a) $\beta = 0.1$

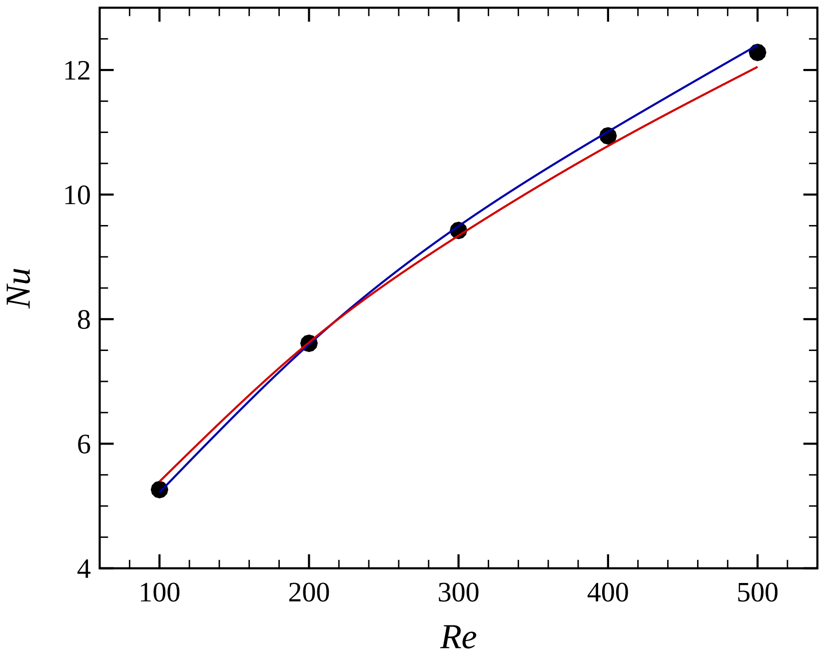

(b) $\beta = 0.2$

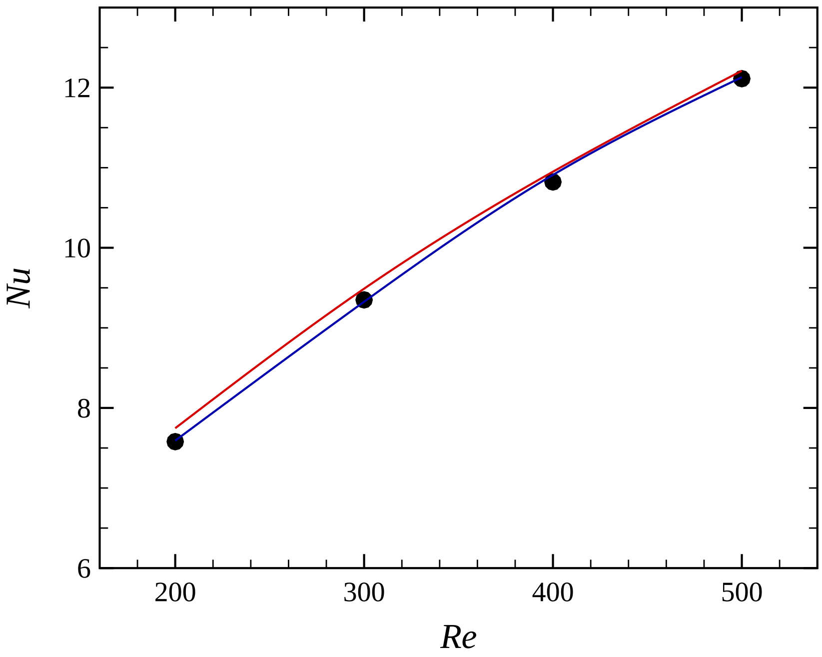

FIGURE 3.8: Comparison of average Nusselt number over the surface of the cylinder with the results from other studies at different Reynolds numbers for the case without a magnetic field for blockage ratios as indicated. Symbols show the present results, while blue and red lines show data from Mettu *et al.* (2006) and Khan *et al.* (2004), respectively.

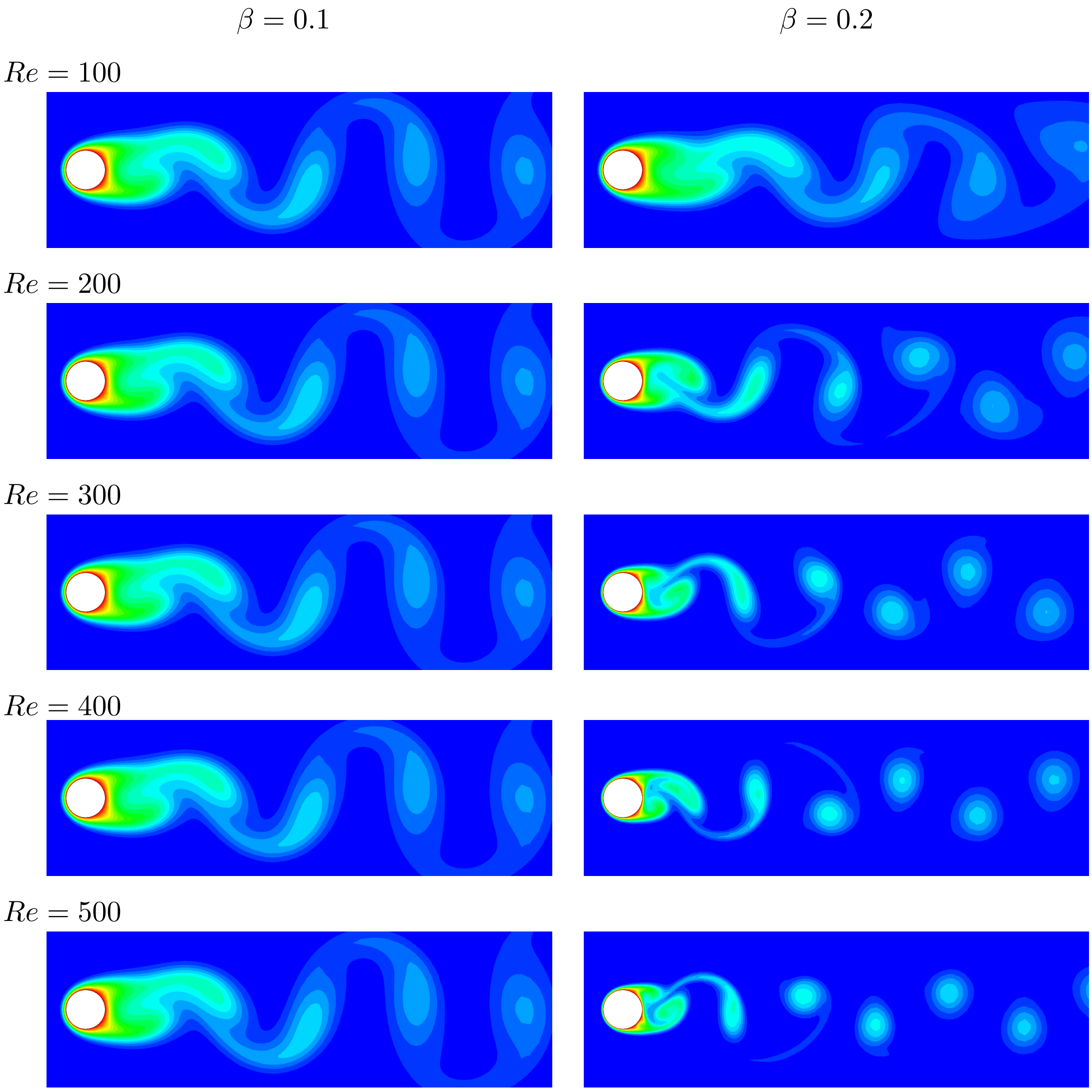

FIGURE 3.9: Instantaneous dimensionless temperature contours for $\beta = 0.1$ and 0.2 for different Reynolds numbers as indicated, obtained from the present algorithm. Red and blue shading shows hot and cold fluid, respectively.

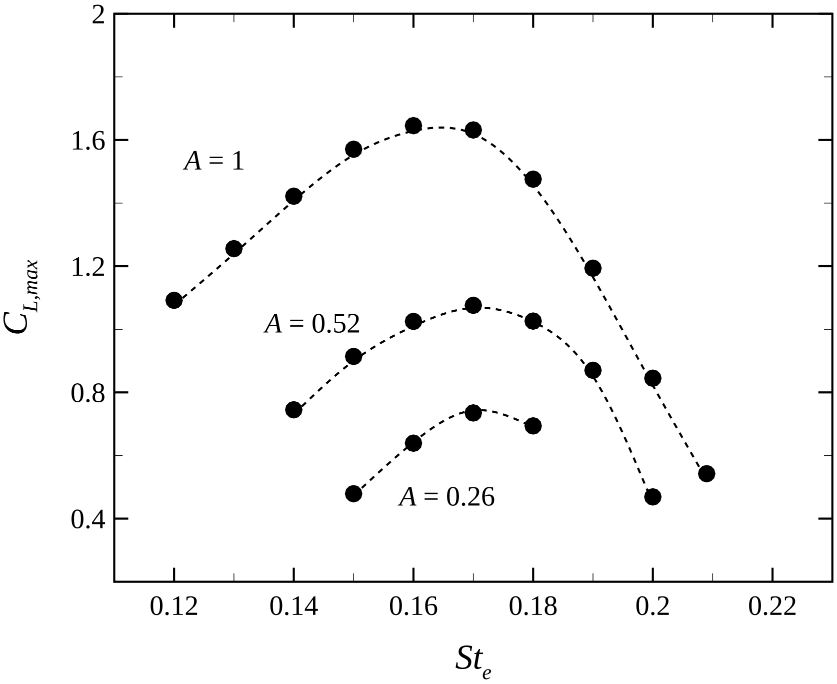

FIGURE 3.10: Comparison of $C_{L,\max}$ distribution in the lock-on range with the results obtained from Baek & Sung (1998) and those predicted by present simulations at different oscillating frequency for $Re = 110$ and three different values of the maximum angular velocity as indicated. Symbols show the present results, while dashed lines show data from Baek & Sung (1998).

St_e, the non-dimensional surface velocity of the cylinder can be expressed by

$$\dot{\boldsymbol{\theta}}_{\text{cyl}} = A \sin(2\pi St_e t), \tag{3.105}$$

where A is non-dimensionalized by u_0/d and the forcing Strouhal frequency is $St_e = f_e d/u_0$. The present results for the maximum distribution of the lift coefficient $C_{L,\max}$ as a function of St_e at different A was compared with results from Baek & Sung (1998), where the flow is within the lock-on range. As indicated in Fig. 3.10, an excellent agreement was found, which strongly supports the accuracy of the present rotary simulations to be described in chapter 7. The mean percentage differences between the present and the published results for the range of A and St_e tested were less than 1%. Furthermore, the mean moment coefficient C_M as a function of rotational velocity α at $Re = 1000$ is also compared with the numerical results of Chew *et al.* (1995) in Fig. 3.11. Again a very good

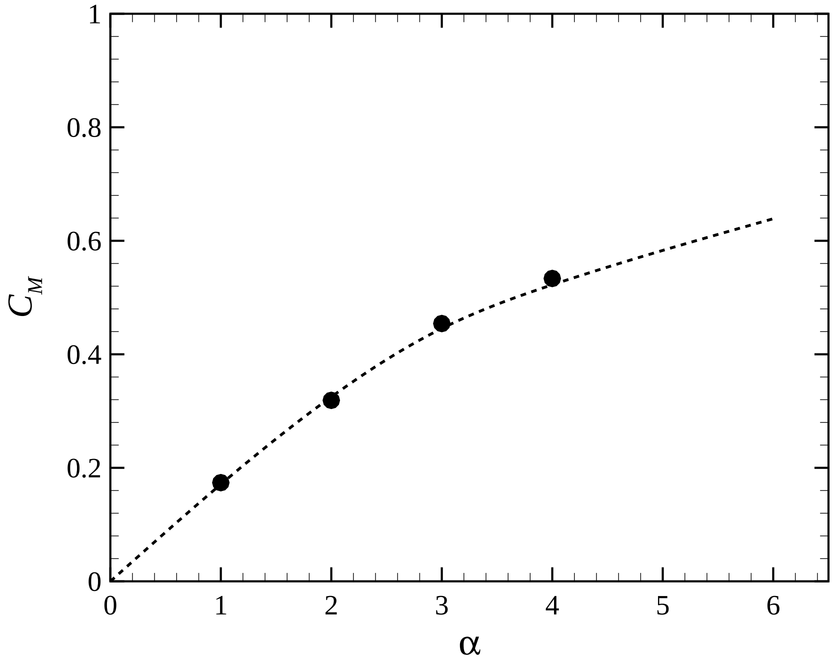

FIGURE 3.11: The variation of C_M with α for $Re = 1000$. Symbols show the results predicted by present simulations, while dashed lines show the results obtained from Chew *et al.* (1995).

agreement was found. The mean percentage differences between the present and the published results for the range of α tested were less than 2%.

In addition, the heat transfer from a rotating oscillating cylinder was tested. Computed average Nusselt numbers Nu for heat transfer with $Pr = 0.7$ for $A = 0.78$ and 1.57 at $Re = 100$ and 200 were compared against the numerical results of Mahfouz & Badr (2000). The results of this comparison are plotted in Fig. 3.12, which compare well with the published data. The mean percentage of differences between the Nu predicted by the present simulations and those of the previous study was less than 1%. The highest heat transfer was found to occur when the oscillation frequency was synchronized with the vortex shedding frequency. This may be attributed to the strong fluid motion in the vicinity of the cylinder which results in an increase in the rate of heat transfer.

The temperature contours patterns for the lock-on regime for $A = 0.78$ and 1.57 at $Re = 100$ and 200 for the forcing frequency St_e where the maximum Nus-

(a) $A = 0.78$

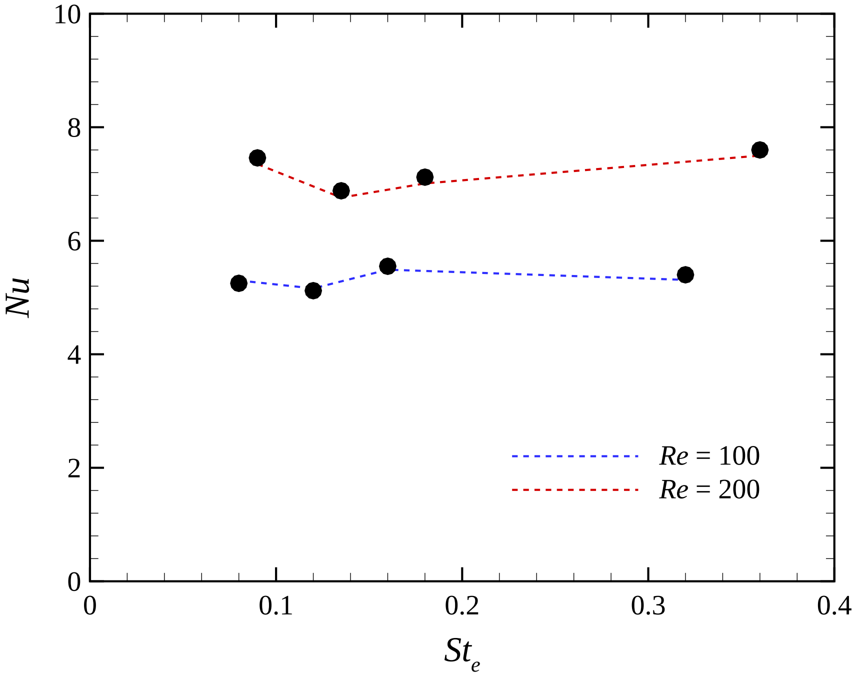

(b) $A = 1.57$

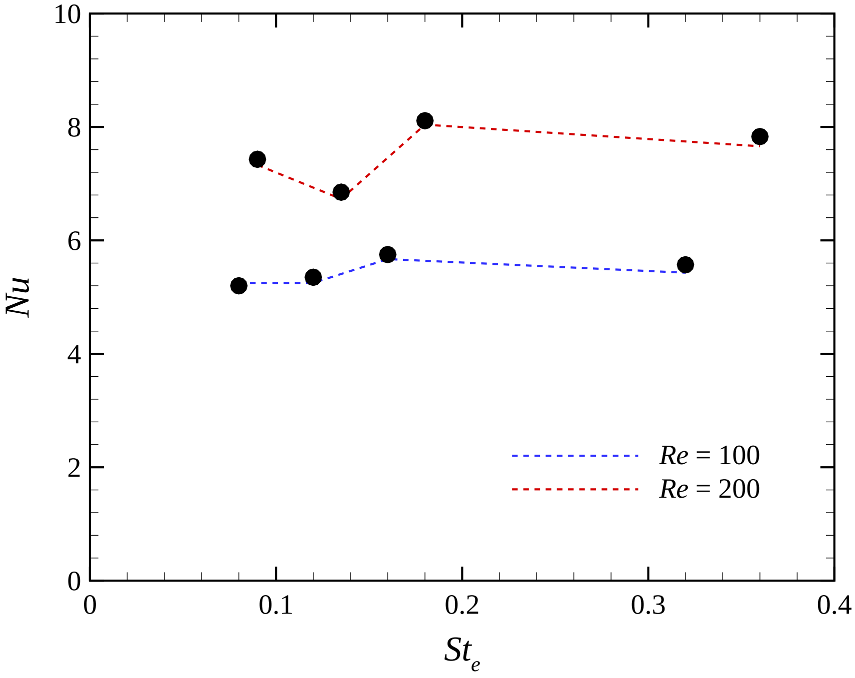

FIGURE 3.12: Comparison of average Nusselt number over the surface of the cylinder with the results from other studies at different oscillating frequency and Reynolds number as indicated (a) $A = 0.78$ and (b) $A = 1.57$. Symbols show the present results, while lines show data from Mahfouz & Badr (2000).

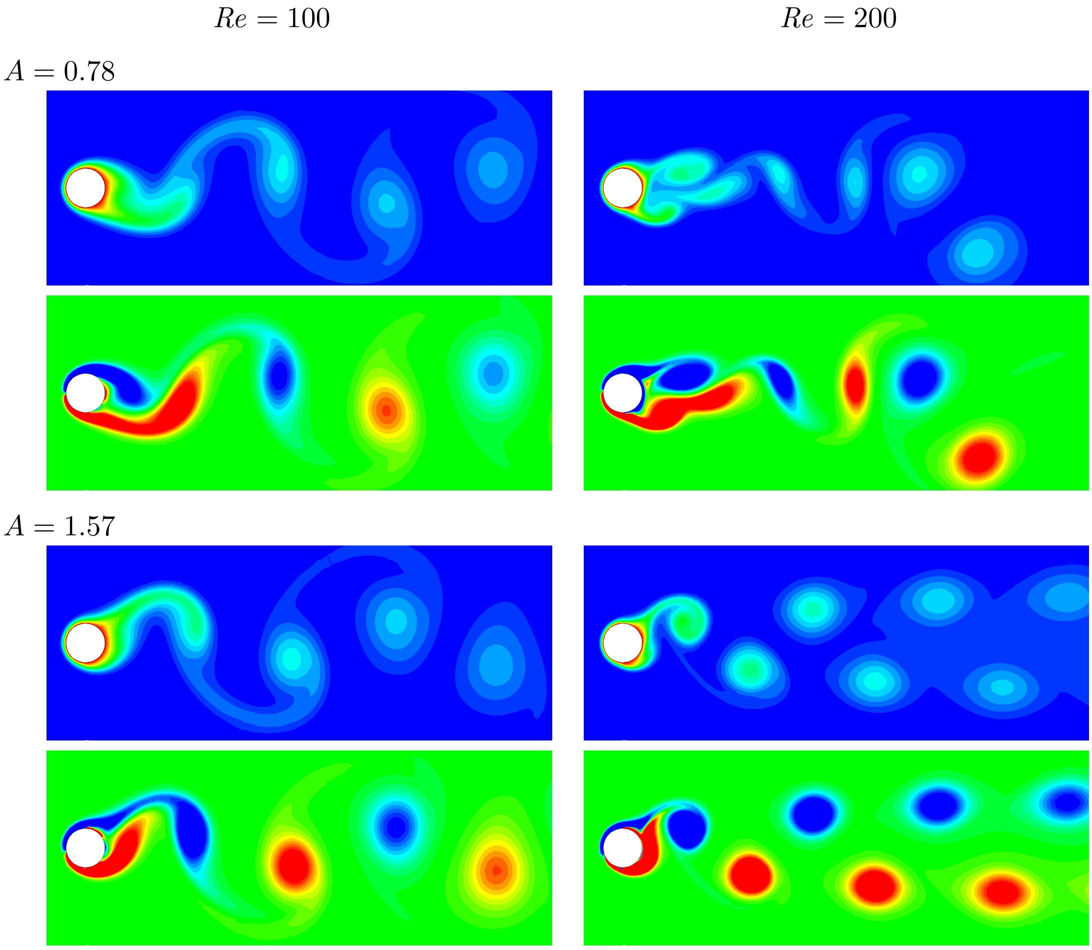

FIGURE 3.13: Isotherm (above) and vorticity contours (below) for $Re = 100$ and 200 at different $\omega_{\max}$ and St_e of the lock-on regimes. For isotherm contours, red and blue ergions shows hot and cold fluid, respectively. For vorticity, red and blue contours represent positive and negative vorticity, respectively.

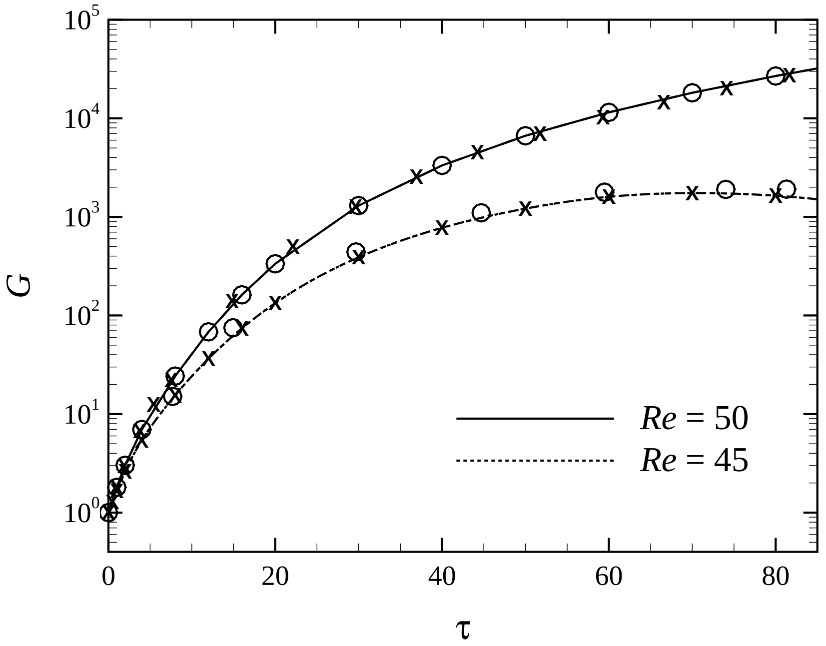

FIGURE 3.14: The Prediction of energy growth (G) plotted against τ, for the flow past a circular cylinder in an open flow at $Re = 45$ and $Re = 50$ without a magnetic field. Results using the present solver (◯) and data from Ref (Abdessemed *et al.* 2009a) (×) are shown. The solid and dashed curve show a spline fit to the present data for guidance.

selt number occurs are shown in Fig. 3.13. The location of the thermal structures the thermal wake are precisely the same as in the vorticity contour plots.

Next, the reliability of the transient growth solver was tested. To this end, the present transient growth analysis implementation is validated firstly for a non-magnetohydrodynamic flow. The flow past a circular cylinder in an open flow at sub and supercritical Reynolds numbers $Re = 45$ and 50 are considered as a test case, which was investigated recently by Abdessemed *et al.* (2009a). A comparison between the results of the present solver and the previous study is shown in Fig. 3.14, where a pleasing agreement is seen.

The respective structure and the evolution of the optimal disturbance field at $Re = 50$ is shown in Fig. 3.15(b-e). In Fig. 3.15(b), the vorticity of the base flow around the circular cylinder at this Reynolds number is shown. Fig. 3.15(c) shows the initial perturbation associated with a time interval $\tau = 32$. It is observed that the optimal disturbance structures are concentrated around the region of the boundary layer separation in the near wake. In Fig. 3.15(d), the evolution from this optimal initial disturbance to time $t = 32$ is shown. The optimal disturbance is shown to evolve to a flow structure comprising a series of counter-rotating spanwise rollers. The disturbance structures reproduced from Abdessemed *et al.* (2009a) are virtually indistinguishable from those computed using our implementation. This, in addition to the excellent agreement found for predicted energy growths G in Fig. 3.14 (within less than 1.0% mean difference), verifies that our implementation is performing correctly.

The experimental investigations of transient growth in the subcritical flow of circular cylinder wake in an open flow have demonstrated that these results are very sensitive to domain size (Marais *et al.* 2011), but that domain size is expected to be less important in high Ha quasi–two–dimensional flows due to the rapid damping of disturbances brought by the effect of Hartmann damping on the flow.

3.7.2 MHD Validation Tests

At this stage, the present numerical model correctly computes the flow and heat transfer patterns of non-MHD cases. The respective Re_c, St_c, Nu, $C_{L\max}$ and G are accurately predicted and compare well with published data. Now, it is important to verify that the present numerical formulation is also reliable for MHD cases. To this end, the experimental setup of Frank *et al.* (2001) for $\beta = 0.1$ is considered. In their configuration both Ha and N are much greater than unity, and therefore, the Q2D model is well suited to capture the flow dynamics. The flow equations (3.61) and (3.62) are simulated using the present spectral element code to determine the critical Reynolds number Re_c under the influence of a magnetic field. The present results are compared with experimental results from Frank *et al.* (2001) in Fig. 3.16(a), which again exhibits a close agreement. The close fit of the present data to that of Frank *et al.* (2001) confirms that the trend is not in fact linear. The mean difference between the results was 3%.

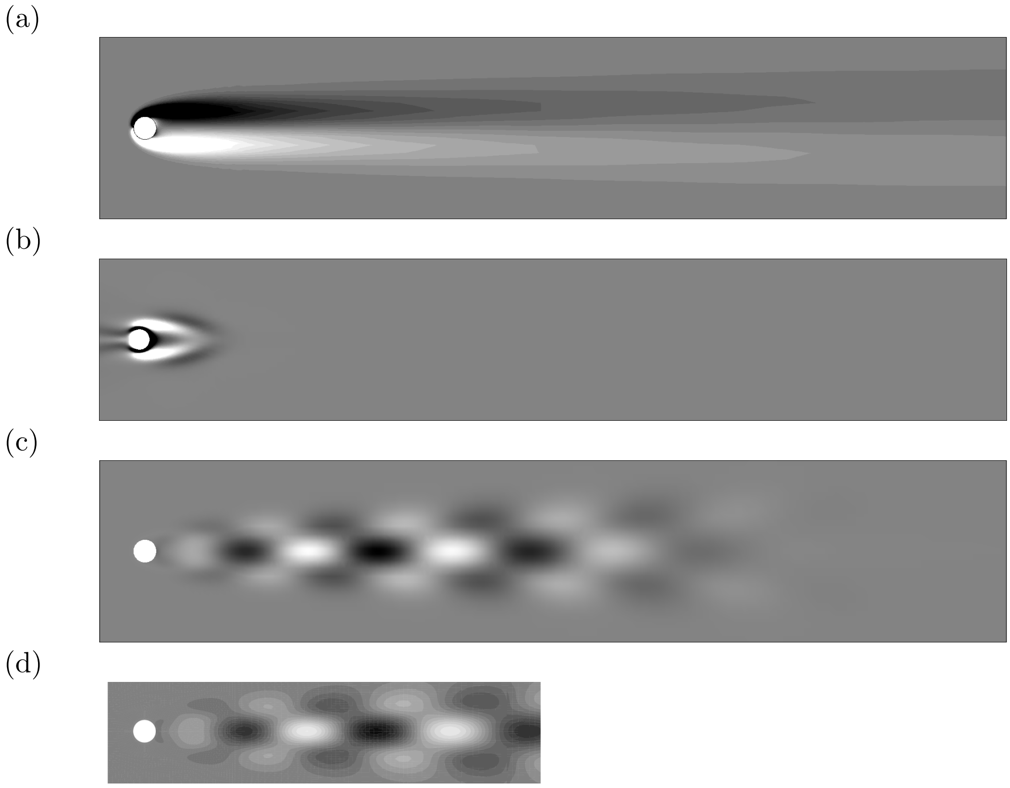

FIGURE 3.15: (a-d) Contours of vorticity plotted at $Re = 50$ for the case without magnetic field. (b) The two–dimensional base flow. (b) The predicted optimal initial condition. (c) The evolution of the optimal disturbance to time $t = \tau = 32$. (d) The corresponding result at $\tau = 32$ and $Re = 50$ reprinted from (Abdessemed *et al.* 2009a). Contour levels over $|\omega| \leq 1$ and $|\omega| \leq 0.01$ are plotted in (a) and (b), respectively.

Also, Frank *et al.* (2001) reported that no evidence of hysteresis was observed for the transition from steady to unsteady flow. The theory of non-linear mode evolution pertaining to the Landau model provides a means for studying the non-linear behaviour near the transition Reynolds number. The Landau model has been widely used in describing and classifying bluff body wake transitions previously, including the Hopf bifurcation of a circular cylinder wake (Provansal *et al.* 1987; Dušek *et al.* 1994; Zielinska & Wesfreid 1995), the three dimensional Mode A and B instabilities in the wake of a circular cylinder (Henderson 1997), and the transition of quasi–two–dimensional magnetohydrodynamic flow past a cylinder in a duct (Hussam *et al.* 2011). Landau & Lifshitz (1976) proposed the

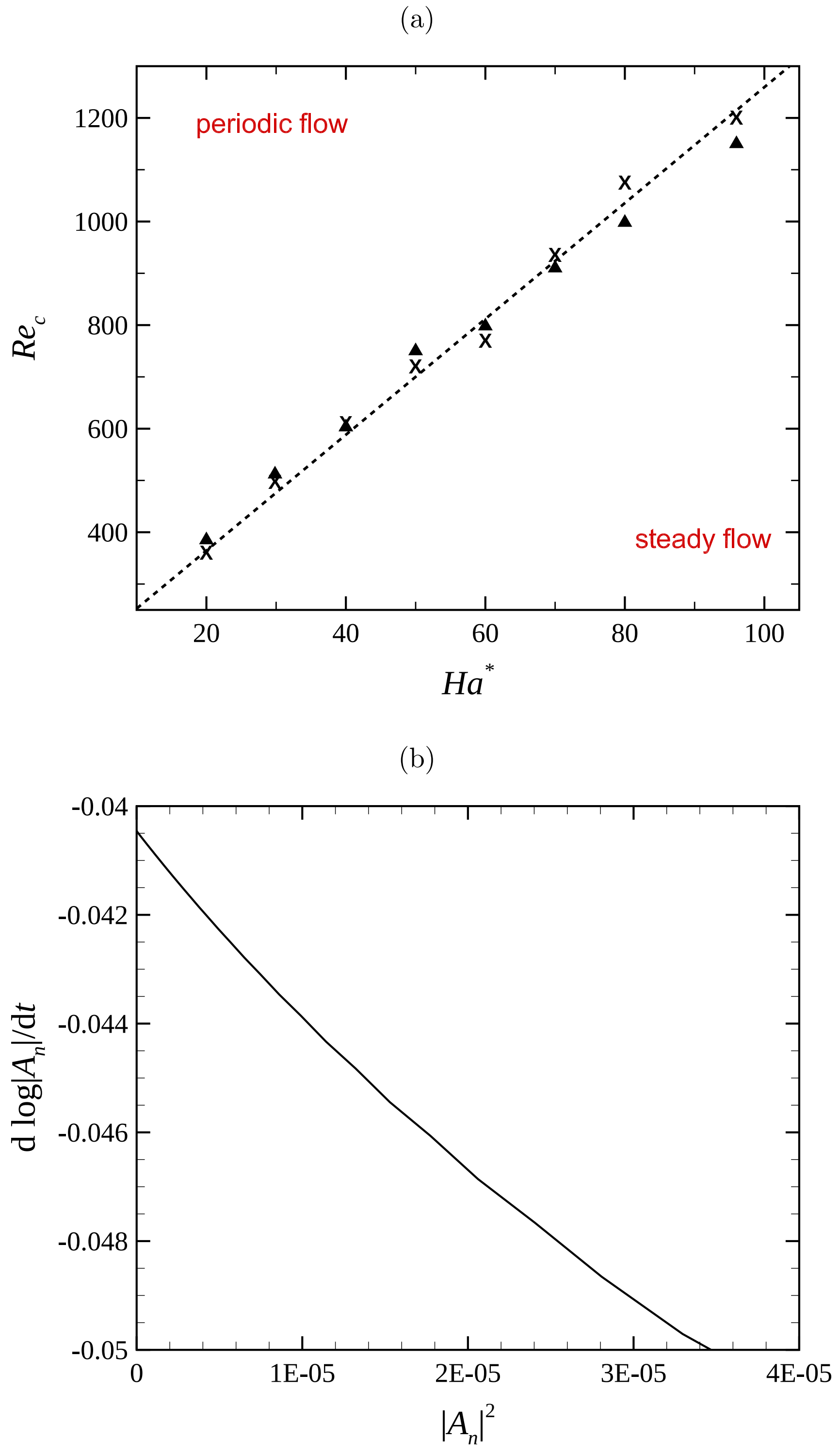

FIGURE 3.16: (a) A plot of Re_c against $Ha^\star$ at $\beta = 0.1$, where ▲ and × show the present data and experimental data from Frank *et al.* (2001), respectively, and the dotted line is a linear fit proposed by Frank *et al.* (2001). (b) The time derivative of mode amplitude logarithm plotted against the square of the amplitudes for $Ha^\star = 40$ and $\beta = 0.1$, demonstrating supercritical behaviour.

Landau model to describe the growth and saturation of a perturbation as

$$\frac{\mathrm{d}A_n}{\mathrm{d}t} = (\sigma_n + i\omega)A_n - l(1 + ic_n)|A_n^2|A_n + ..., \tag{3.106}$$

where A_n is a measure of the amplitude of the evolving instability as a function of time, and the righthand side of the equation represents the first two terms of a series expansion. According to Landau model theory, on a plot of $\mathrm{d}\log|A_n|/\mathrm{d}t$ against $|A_n|^2$ (Fig. 3.16b), the value at $|A_n|^2 = 0$ corresponds to the linear growth rate of the instability, and the sign of the gradient at this point determines the non-linear evolution characteristics of the instability. A positive gradient indicates a subcritical bifurcation, which permits hysteresis (bi-stability) in the vicinity of the transition; a negative gradient indicates a supercritical bifurcation, which does not exhibit hysteresis. Fig. 3.16(b) demonstrates that this transition is supercritical. Frank *et al.* (2001) reported that no evidence of hysteresis was observed, which is confirmed by the Landau modeling of the transition carried out here. It is therefore concluded that the present numerical model is able to recover the MHD flow past a circular cylinder for both high Hartmann and Reynolds numbers.

Finally, a check of the transient growth analysis implementation incorporating the Hartmann friction term is performed. For $\beta = 0.1$, $Ha^\star = 50$, and $Re = 580$, the predicted optimal initial disturbances were evolved using the linearized quasi-two–dimensional Navier–Stokes solver, and energy time histories normalized by the initial energy were recorded. Correct performance of the transient growth solver is confirmed by the normalized energy time histories agreeing with the corresponding predicted energy growth factors (G). Of course, since the transient growth solver depends on the linearized two–dimensional Navier–Stokes solver, this test only validates the former implementation relative to the latter. The results of this test are shown in Fig. 3.17, which demonstrates the accurate performance of the current implementation of transient growth analysis technique for quasi–two–dimensional magnetohydrodynamic flows.

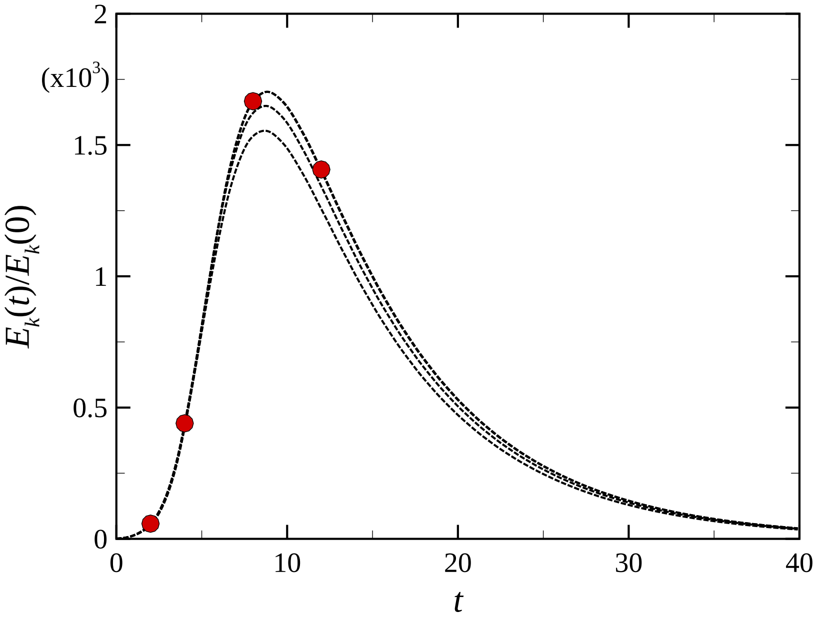

FIGURE 3.17: Comparison between predicted energy amplifications (G, symbols) computed at several time intervals (τ), and time histories of the normalized energy in perturbations initiated from the corresponding optimal initial disturbances computed for $\beta = 0.1$ and $Re = 580$ at $Ha^\star = 50$ initialized with small perturbation of the initial optimal growth mode for different time intervals (solid curves). The correctness of the adjoint quasi two–dimensional equation is verified by the alignment between the computed energy time histories and the predicted energy growths at times $t = \tau$.

3.8 Chapter Summary

In this chapter, the numerical methods applied in this thesis have been presented and detailed. The spectral-element method for computing quasi–two–dimensional flow and heat transfer past a confined circular cylinder under a strong magnetic field has been introduced, as well as the frameworks for the linear stability and transient growth analysis.

The quasi-two-dimensional model is derived (Sommeria & Moreau 1982) by averaging the flow quantities along the magnetic field direction. The formulation of this flow and the corresponding conditions have been described. The key feature of this model is that it provides modified two–dimensional Navier–Stokes equations with forcing and linear braking terms which represent the electromagnetic force effects and the friction in the Hartmann layers. It has been shown that the results of the present simulations compare favorably with those of a number of previous studies, and the numerical system accurately captures the flow physics of the flow past a circular cylinder.

The specific model setup and grid independence studies will be included for each individual case presented in each of the results chapters to follow.

Chapter 4

Flow and Heat Transfer Past a Circular Cylinder on the Centreline of a Rectangular Duct

This chapter presents results for fluid flow and heat transfer of a liquid metal past a circular cylinder positioned on the centreline of a rectangular duct under a strong transverse magnetic field. First, a description of the geometry and boundary conditions is given in § 4.1. This is followed by a grid-resolution study from which the computational domain size and spatial resolution are determined § 4.2. In the following section, the dynamics of the flow are presented in § 4.3. The structure of the wake is considered for steady and unsteady flow at a ranges of Hartmann number, Reynolds number, and blockage ratio. The transition of the flow from steady to unsteady flow regimes is determined as a function of Hartmann number $Ha^\star$ and blockage ratio β. The effects of $Ha^\star$ and β on the critical Reynolds number from steady to unsteady flow, Strouhal number, wake bubble length, drag, and lift forces are determined. Finally, heat transfer from the heated wall and the mixing induced by the vortex shedding is presented in § 4.4. The effect of $Ha^\star$ and β on the time-averaged Nusselt number, local Nusselt number and pressure drop are determined.

Some of the results in this chapter have previously been published in Hussam *et al.* (2011).

4.1 Geometry and Boundary Conditions

The system of interest is a rectangular duct confining a circular cylinder placed at the centre of the duct parallel to the magnetic field and perpendicular to the flow direction. A schematic representation of the system considered in this chapter is shown in Fig. 4.1. The duct walls and the cylinder are assumed to be electrically insulated. A homogeneous vertical magnetic field with a strength B is imposed along the cylinder axis. One of the walls oriented parallel to the magnetic field is heated and maintained at a constant wall temperature T_w whereas the other surfaces are kept at constant temperature T_0. As described in chapter 3, for a high Hartmann number, the magnetic Reynolds number Re_m, which represents the ratio between the induced and the applied magnetic field is very small. Thus, the induced magnetic field is negligible and the resulting magnetic field is maintained in the z-direction only. Under these conditions the flow is quasi two–dimensional and consists of a core region, where the velocity is invariant along the direction of the magnetic field, and a thin Hartmann layer at the wall perpendicular to the magnetic field, as previously outlined in § 3.2.3.

The inlet boundary condition imposed at the channel inlet is specified as the analytical parallel flow solution of equations (3.61) and (3.62) in an unobstructed plane channel. The non-MHD and MHD cases are respectively given by

$$u(-L_u/d, y) = 1 - \left(\frac{yd}{h/2}\right)^2$$

$$u(-L_u/d, y) = \frac{\cosh(yd\sqrt{2Ha}/a - \cosh(h\sqrt{2Ha}/2a))}{1 - \cosh(\sqrt{2Ha}/2a)}$$

A constant reference pressure is imposed at the outlet, and a high-order Neumann pressure boundary condition is imposed on the Dirichlet velocity boundaries to preserve the third-order time accuracy of the scheme. No-slip boundary conditions (equation 3.16) for velocity are imposed on the side walls and the cylinder. The temperature of the incoming stream and top wall is taken as T_o, and at the bottom wall as T_w. The cylinder is thermally insulated (a zero normal temperature gradient is imposed at its surface).

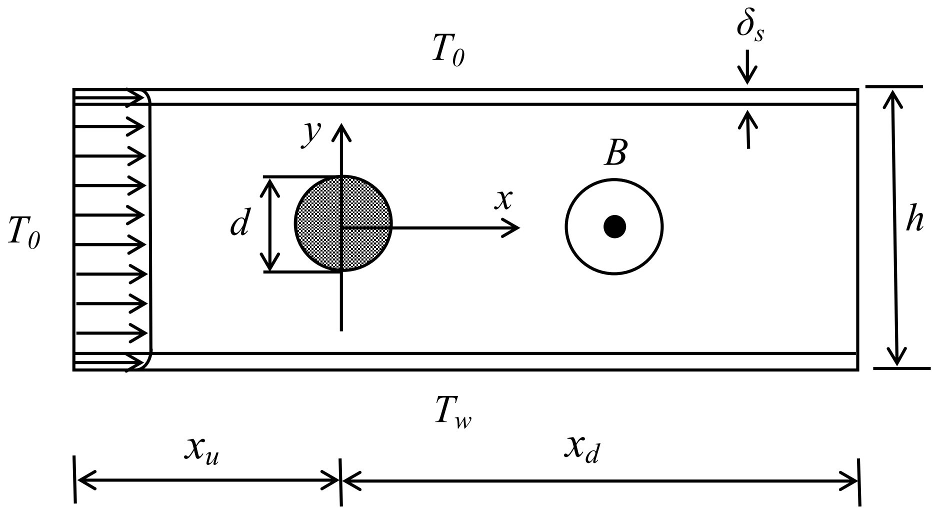

FIGURE 4.1: Schematic representation of the system under investigation. The magnetic field B acts in the out-of-plane direction, parallel to the cylinder axis. δ_S is the thickness of the Shercliff layer, and h and d are the duct width and cylinder diameter, respectively. The blockage ratio $\beta = d/h$.

4.2 Grid Resolution Study

A thorough grid resolution study was performed to ensure adequate domain sizes, and spatial and temporal resolutions to accurately resolve all features of the flow field for the Reynolds numbers, the Hartmann numbers and the blockage ratios under consideration in this study. The spectral element method employed in this thesis offers the flexible property that resolution may be controlled either by varying the number of elements (h-type refinement) or the polynomial order of shape functions within each element (p-type refinement). Karniadakis & Sherwin (2005) describe that smooth solutions (such as would be expected in the problems considered in this thesis) typically exhibit exponential convergence via p-type refinement (i.e. increasing the order of elemental polynomial shape functions while keeping the number of elements and their distribution fixed), whereas only an algebraic convergence is obtained via h-refinement (increasing the number of elements in the mesh). The exponential convergence properties of

p-type refinement are typical of polynomial spectral methods (Gottlieb & Orszag 1977). The superior convergence of p-type over h-type refinement means that near-optimal spectral element simulations in terms of run-time efficiency for a given error threshold tend to be achieved by designing a relatively coarse h-type mesh with consideration being given to increasing the local element density in regions of expected flow gradients (such as boundary layers, separated flow regions, wakes, etc.), and employing p-type refinement to meet the target error threshold. A well-designed h-type mesh will typically provide results with high accuracy for relatively modest polynomial orders (e.g. between 5 and 15). Accurate solutions can still be obtained for poor meshes (such as a mesh with too few elements, and/or poorly distributed elements), but these may require a very high polynomial order for the desired accuracy, which can be costly from both storage and compute-time perspectives. For illuminating discussion and analysis of the complexities of optimizing spectral/hp element simulations, see Vos (2011) and references therein.

With this in mind, the process used to develop grid-independent solutions for the simulations described in this thesis firstly required the careful creation of a family of h-type meshes which employed a distribution of elements with higher density at duct walls, around the surface of the cylinder, and in the expected wake region immediately downstream of the cylinder. Preliminary test cases were simulated to facilitate an iterative optimization of the distribution and number of elements within the meshes to eliminate any localized regions of significantly poorer resolution than the rest of the mesh. Following this phase, a domain size study was conducted by adding or subtracting elements from the upstream and downstream ends of the mesh to investigate the effect of truncation of the domain on the solutions. Finally, the minimum polynomial order required for grid independence of the computed solutions was determined through a p-type refinement study.

The determination of the inlet length x_u and the outlet length x_d is described in § 4.2.1. In § 4.2.2, spatial resolutions are selected for the domains such that the requirement of the computational accuracy is fulfilled.

	$\beta = \mathbf{0.1}$			$\beta = \mathbf{0.4}$		
	$\mathbf{M_1}$	$\mathbf{M_2}$	$\mathbf{M_3}$	$\mathbf{M_1}$	$\mathbf{M_2}$	$\mathbf{M_3}$
$\mathbf{N_{el}}$	1172	1340	1484	1052	1196	1308
$\mathbf{x_u/d}$	5	8	12	5	8	12
$\mathbf{x_d/d}$	15	25	40	15	25	40

TABLE 4.1: Domain lengths defining the meshes. N_{el} is the number of elements, and x_u and x_d describe the inlet and outlet domain sizes, respectively.

4.2.1 Domain Size Study

For each blockage ratio, three families of meshes were tested. The pressure and viscous component of the time-averaged drag coefficient ($C_{D,p}$, $C_{D,\text{visc}}$) and the Strouhal frequency of vortex shedding (St) were monitored, as they are known to be sensitive to the domain size and resolution. The upstream and downstream domain lengths chosen for this study for blockage ratios $\beta = 0.1$ and $\beta = 0.4$ are shown in Table 4.1. Elements with polynomial degree 7 were used, and parameters $Re = 3000$ and $Ha^\star = 120$ were chosen to produce periodic flows on the test meshes at each blockage ratio, which represent the upper end of the parameters range of this study, and therefore represent a strenuous test of the domain size and mesh resolution. A difference of less than 1% was found when comparing values of St and C_D between the M_2 and M_3 meshes. Based on this, the M_2 mesh sizing was used hereafter for all blockage ratios. For a summary of the domain lengths chosen for the domain length study, see Table 4.1. For all meshes, the density and distribution of elements around the cylinder was kept constant and the mesh becomes sparser both upstream and downstream. Therefore, the number of elements increases much less than linearly with the length of the domain.

4.2.2 Spatial Resolution Study

The meshes applied in the grid-resolution study for $\beta = 0.1$ and $\beta = 0.4$ are shown in Fig. 4.2. The spatial resolution study varied the polynomial order of each macro-element of the chosen mesh based on the domain length parameters from the mesh domain size study of § 4.2.1.

	$\beta = \mathbf{0.1}$			$\beta = \mathbf{0.4}$		
	$\mathbf{M_1}$	$\mathbf{M_2}$	$\mathbf{M_3}$	$\mathbf{M_1}$	$\mathbf{M_2}$	$\mathbf{M_3}$
St	0.24414	0.23804	0.23727	0.31509	0.31281	0.31052
$C_{D,p}$	1.69943	1.65044	1.64385	2.55108	2.55000	2.54760
$C_{D,\text{visc}}$	0.07762	0.07597	0.07576	0.10536	0.10518	0.10500
C_D	1.77705	1.72640	1.71961	2.65644	2.65518	2.65260

TABLE 4.2: Convergence of the flow field parameters for the meshes applied at $Ha^\star = 120$ and $Re = 3000$ to determine suitable domain sizes for the meshes employed throughout this study.

	$\beta = \mathbf{0.1}$				$\beta = \mathbf{0.4}$			
N_p	St	C_D	$C_{D,p}$	$C_{D,\text{visc}}$	St	C_D	$C_{D,p}$	$C_{D,\text{visc}}$
4	0.24872	1.82950	1.75278	0.07671	0.24071	2.30801	2.19119	0.11682
5	0.24071	1.71071	1.64593	0.07546	0.31166	2.62995	2.72005	0.10990
6	0.23880	1.72188	1.64746	0.07589	0.32875	2.65702	2.59305	0.10397
7	0.23866	1.72335	1.64746	0.07589	0.31281	2.65518	2.55000	0.10518
8	0.23801	1.72404	1.64826	0.07618	0.31246	2.65760	2.55386	0.10574
9	0.23804	1.72419	1.64802	0.07617	0.31243	2.65759	2.55361	0.10595

TABLE 4.3: Convergence of the flow field parameters for the mesh M_2 at $Ha^\star = 120$ and $Re = 3000$ for blockage ratios as indicated.

Computations have been performed with variation of the element polynomial degree from 4 to 9, while keeping the macro-element distribution unchanged. Two sets of computations are performed: one with $\beta = 0.1, Re = 3000$, and $Ha^\star = 120$, and the other at $\beta = 0.4, Re = 3000$, and $Ha^\star = 120$. Again, the parameters St, $C_{D,p}$, $C_{D,\text{visc}}$ and C_D were monitored. To ensure that uncertainty due to spatial resolution was smaller than that due to domain size, a target of 0.3% uncertainty was chosen, and this was found to be achieved with polynomial degree 7, which is used hereafter. Table 4.3 show the convergence characteristics with an increase in polynomial order for the flow field quantities.

Efforts was taken when building meshes for other blockage ratios to ensure that the meshes densities employed for these test meshes were preserved across all meshes.

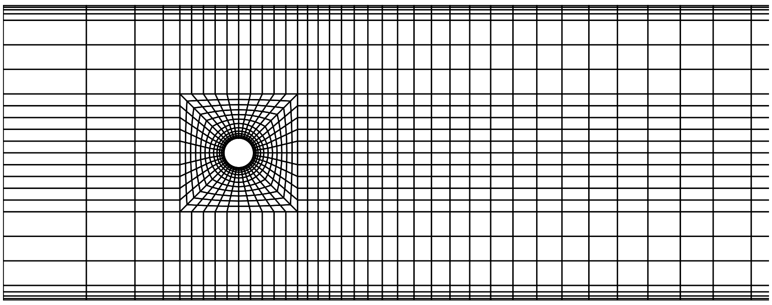

(a) $\beta = 0.1$

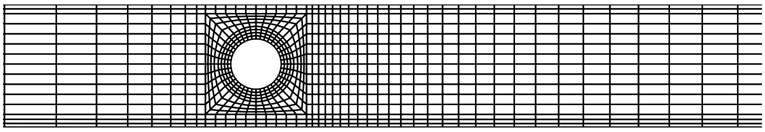

(b) $\beta = 0.4$

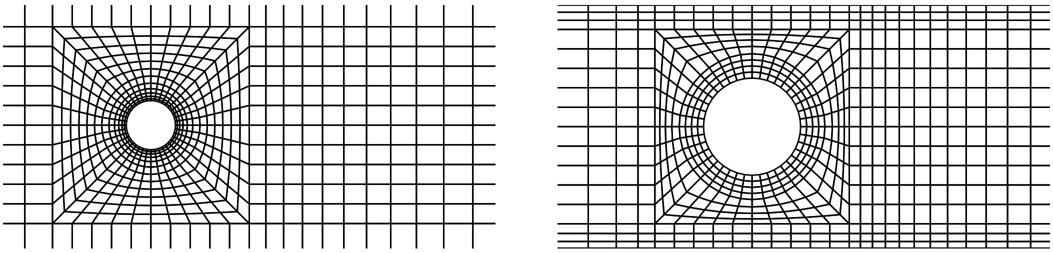

(c) details of M_2 for $\beta = 0.1$

(d) details of M_2 for $\beta = 0.4$

FIGURE 4.2: Meshes used to test the effect of the domain lengths of the confined cylinder meshes. (a) mesh M_2 used for $\beta = 0.1$ and (b) mesh M_2 used for $\beta = 0.4$, extending $25d$ downstream and $8d$ upstream. (c) and (d) represent the details of the meshes around the cylinder for $\beta = 0.1$ and $\beta = 0.4$, respectively.

4.3 Dynamics of the Flow

4.3.1 Variation of Critical Re with β and Ha

Limited data relating Re_c to β and $Ha^\star$ exists in the literature. A comprehensive coverage of the parameter space has therefore been undertaken. The results of critical Reynolds and associated Strouhal number are plotted in Fig. 4.3.

For a given β, Re_c is found to increase with increasing $Ha^\star$. The increase in

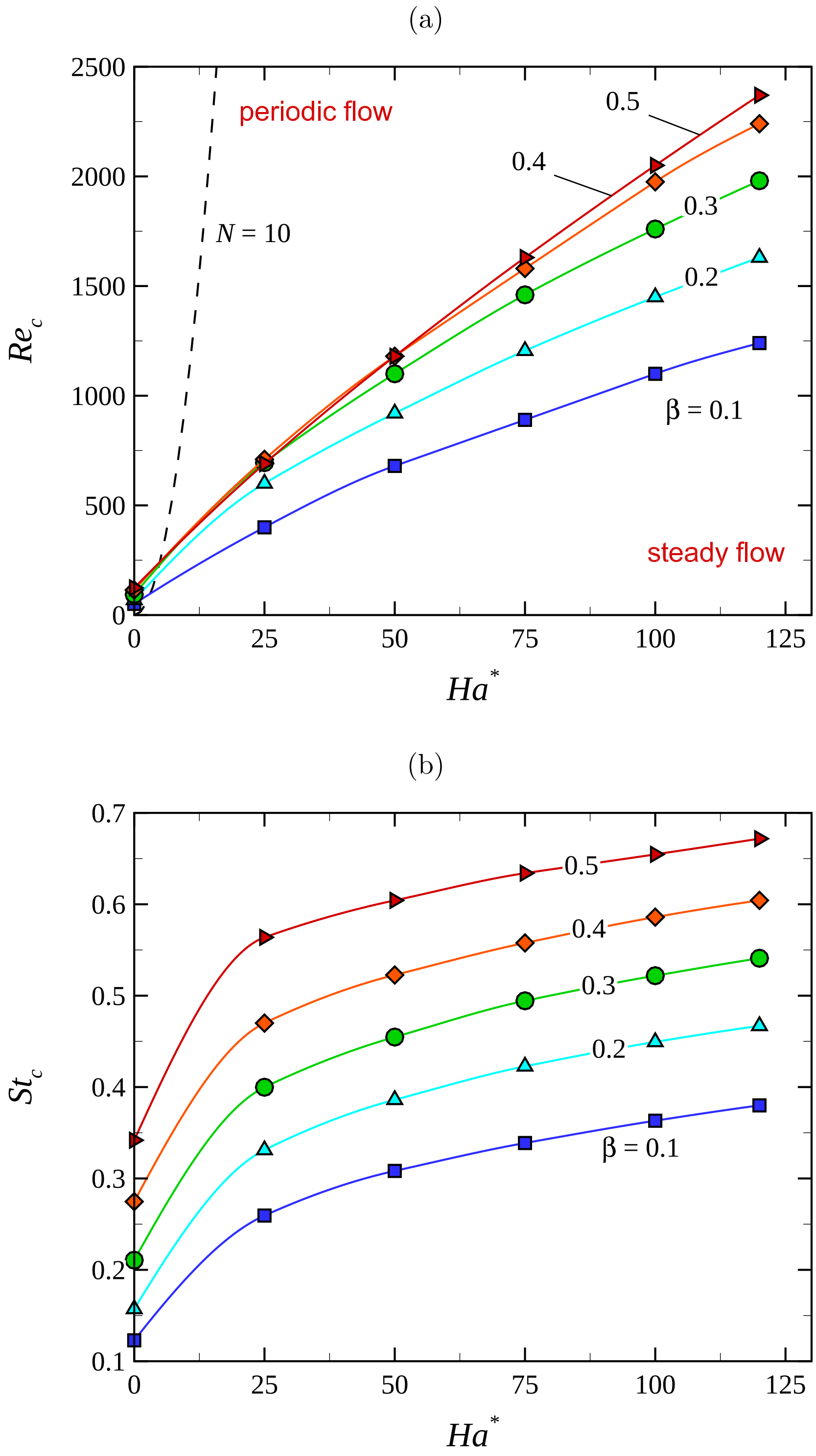

FIGURE 4.3: (a) Re_c and (b) St_c plotted against $Ha^\star$ at blockage ratios as indicated. The dotted line shows the $N = 10$ parabola: the data predominantly lies to the right of that curve, demonstrating the suitability of the quasi-two–dimensional assumption (as $N \gg 1$).

Re_c is more pronounced at high Ha and β. This is attributed to the effect of $Ha^\star$ and β which delay the transition from steady to periodic flow regimes, resulting in the enhanced stability of the flow. Higher Hartmann number (i.e. a stronger magnetic field) acts to dampen transverse fluctuations in the channel, which delays transition, resulting in a higher Re being required to invoke transition. In addition, as the cylinder moves closer to the confined walls (higher blockage ratios), the interaction between the wall boundary layer and that of the cylinder suppresses the wake instability from the cylinder (Sahin & Owens 2004; Mettu *et al.* 2006).

For a constant Hartmann number, Re_c varies strongly with β at small blockage ratios ($\beta \lesssim 0.3$). Beyond $\beta \gtrsim 0.4$, though, Re_c varies only slightly with β. This may be attributed to the fact that as the lateral walls approach the cylinder, the local acceleration of the flow near the cylinder causes it to experience an effectively higher Re flow, making it more unstable, offsetting the damping effect caused by the vicinity of the approaching side walls.

4.3.2 Steady Flow: Wake Structure and Scaling

The steady flow is characterized by a pair of symmetric counter-rotating vortices on either side of the wake centerline, immediately behind the cylinder. Fig. 4.4 shows isocontours of the stream function (streamlines) at $Re = 580$ and different blockage ratios and Hartmann numbers. It can be seen that an increase in the Hartmann number acts on the wake by decreasing the length of the recirculation bubble. This is due to the domination of the Lorentz forces which results in a damping in a direction opposite to the flow, resulting in a decrease in the wake length. Similarly, increasing the blockage ratio was also found to decrease the wake length. For $\beta = 0.1$, the recirculation bubble is visible up to $Ha^\star = 120$, but for $\beta = 0.4$, additional computations (not shown) determined that it was suppressed completely beyond $Ha^\star \gtrsim 300$.

Increasing the Reynolds number broadly acts to increase the wake length, while increasing the blockage ratio and Hartmann number both act to decrease the wake length. To quantify these observations, the wake length (L_R/d, taken as

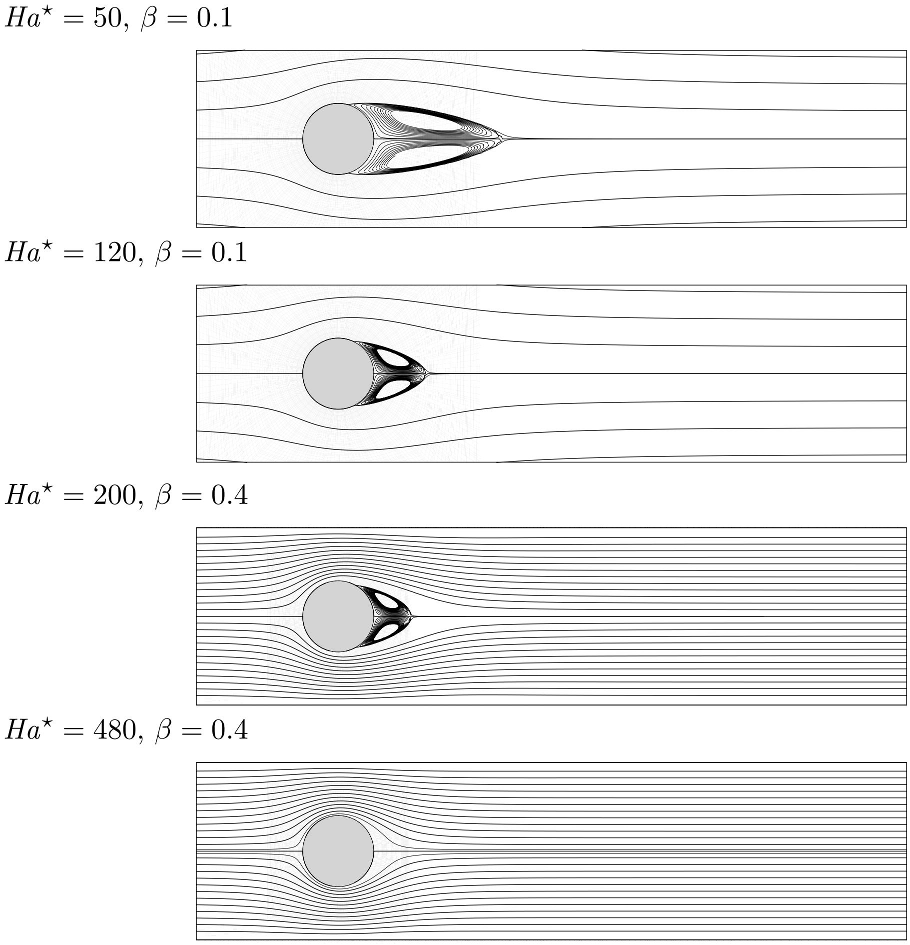

FIGURE 4.4: Streamlines of the steady base flows at $Re = 580$, blockage ratios $\beta = 0.1$ (top) and 0.4 (bottom), and Hartmann numbers as indicated. Flow is left to right in each frame.

the distance from the aft surface of the cylinder to the stagnation point defining the end of the recirculation bubble) was recorded at a large number of points in the Re–$Ha^\star$–β parameter space. For a single β, L_R/d increases almost linearly with increasing Re for a constant $Ha^\star$, and decreases with $Ha^\star$ for a constant Re. Dousset & Pothérat (2008) proposed for $\beta = 0.25$ that L_R/d data collapsed onto a universal curve when plotted against $Re/Ha^{\star 0.8}$, but in this study a more general universal relationship is sought that also incorporates the blockage ratio. A non-linear optimization was conducted to find exponents A, B and C accurate to three significant figures that serve to maximize the square of the correlation coefficient (r^2) of a linear least-squares fit to the L_R/d data when plotted against

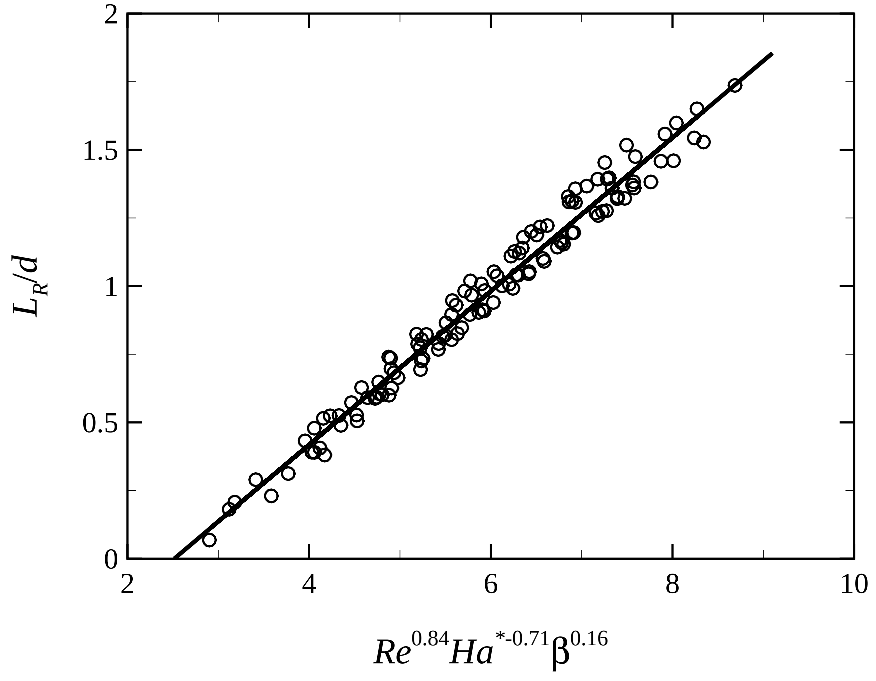

FIGURE 4.5: Collapse of recirculation zone lengths over ranges of Hartmann number $50 \leq Ha^\star \leq 50$, Reynolds number $50 \leq Re \leq 2050$ and blockage ratios $0.1 \leq \beta \leq 0.4$ when plotted against $(Re^{0.844}Ha^{\star-0.711}\beta^{0.166})$.

$Re^A Ha^{\star B}\beta^C$. The optimal exponents were determined to be $A = 0.84$, $B = -0.71$ and $C = 0.16$. The universal relationship between recirculation length, Reynolds number, Hartmann number and blockage ratio is thus approximated by

$$L_R/d = 0.28\left(Re^{0.84}Ha^{\star-0.71}\beta^{0.16}\right) - 0.71, \tag{4.1}$$

and the pleasing collapse of the data obtained as a result of this analysis is shown in Fig. 4.5.

Equation (4.1) can be used to estimate at which values of the parameters the separation bubble will first appear (i.e. by solving for $L_R/d = 0$). This gives

$$Re = 2.98\ Ha^{\star 0.84}\beta^{-0.2}.$$

For the bookend blockage ratios considered in this study ($\beta = 0.1$ and 0.4), the separation bubble threshold is defined by

$$Re = 4.69\ Ha^{0.84} \tag{4.2}$$

and

$$Re = 3.57\ Ha^{0.84}, \tag{4.3}$$

respectively. To illustrate the application of these relationships, Fig. 4.4 plots flow streamlines at several combinations of $Ha^\star$ and β, and constant Reynolds number $Re = 580$. For $\beta = 0.1$, equation (4.2) estimates critical Reynolds number of $Re = 127$ at $Ha^\star = 50$ and $Re = 256$ for $Ha^\star = 120$. The plotted Reynolds number exceeds both of these critical Reynolds numbers, and therefore for both of these cases a wake recirculation bubble would be expected. The plots in the first two frames of Fig. 4.4 confirm this. For $\beta = 0.4$, equation (4.3) estimates critical Reynolds number of $Re = 310$ (less than $Re = 580$) at $Ha^\star = 200$ and $Re = 648$ (greater than $Re = 580$) at $Ha^\star = 480$. Hence a wake recirculation bubbles is expected to be observed in the former case but not the latter, which is consistent with the observation of the results in Fig. 4.4 that produce wake recirculation bubbles, the wake lengths estimated by equation (4.1) are $L_R/d = 1.85$, 0.66 and 0.49, respectively, which compare well with the wakes seen in the figure.

4.3.3 Unsteady Flow: The Dependence on Ha and β of Vortex Shedding Evolution

Here the effect of the Ha and β on the structure of the wakes behind the cylinder are considered. Figs. 4.6 and 4.7 illustrate instantaneous vorticity fields at $Re = 2000$, Hartmann numbers $Ha^\star = 50$ and 120, and different blockage ratios. For $\beta = 0.1$, the structure of the Kármán vortex street consists of regular positive and negative vortices shed alternately from the shear layers either side of the cylinder. This is similar to what is produced behind a circular cylinder in open non-MHD flows (Williamson 1988). At high Hartmann number, $Ha^\star = 120$, the vortices diffuse rapidly as they convect downstream. This diffusion occurs as a result of increased Hartmann damping at higher Ha, which is discussed in more details shortly. A similar behaviour was also found at $\beta = 0.2$.

For $\beta = 0.3$, and modified Hartmann number of 50, boundary layer entrainment from the walls (the Shercliff layers) occurs downstream of the cylinder. The vortex street comprises regular vortices shed from the cylinder, observable by the

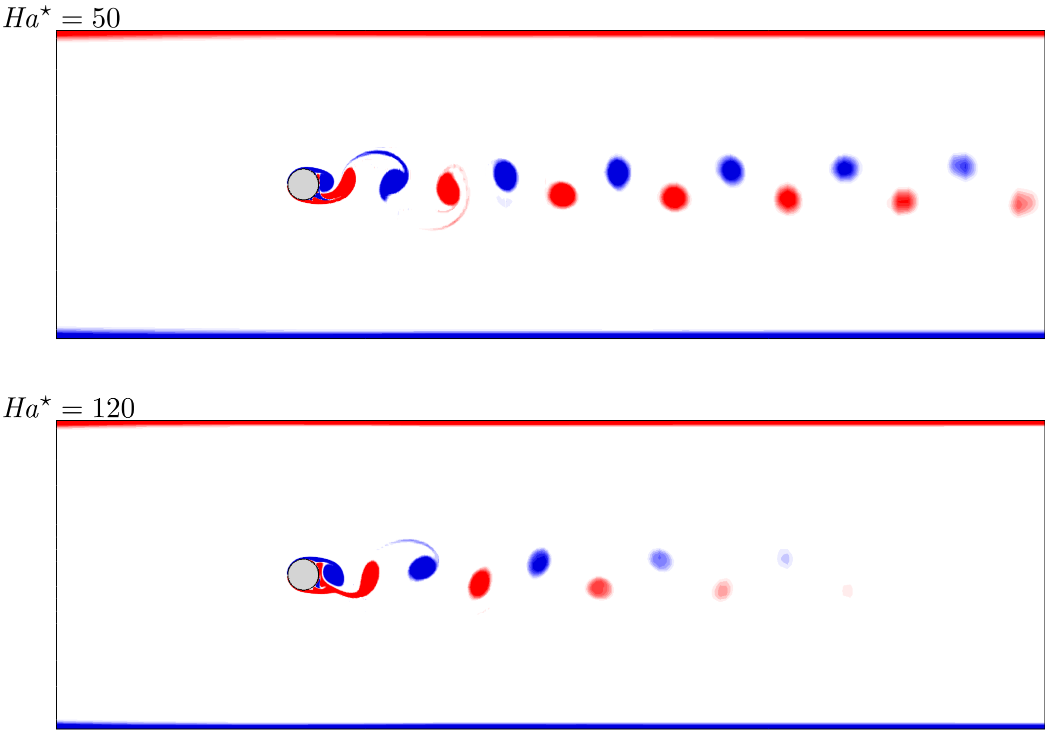

$\beta = 0.1$

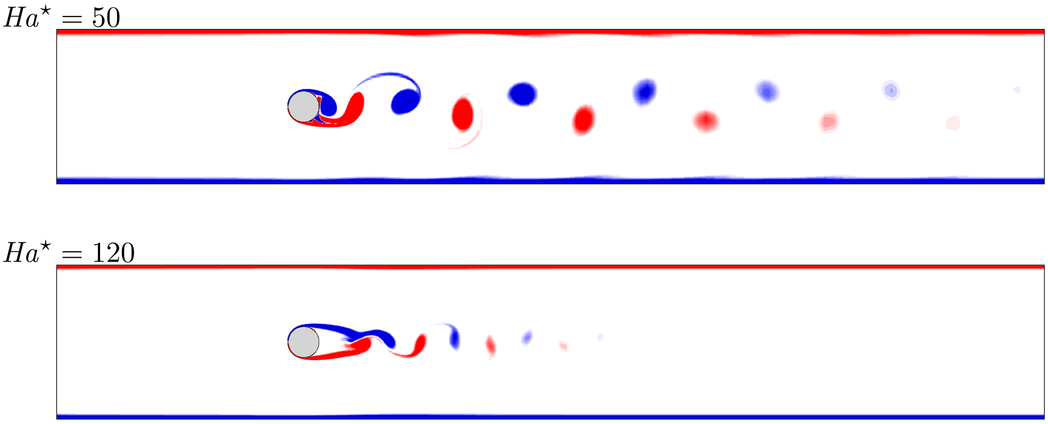

$\beta = 0.2$

FIGURE 4.6: Vorticity contour plots for $Re = 2000$, β of 0.1 and 0.2 at low and high Hartmann number. 20 contour level are displayed between $-2 \leq \omega \leq 2$, with red and blue contours representing negative and positive vorticity, respectively.

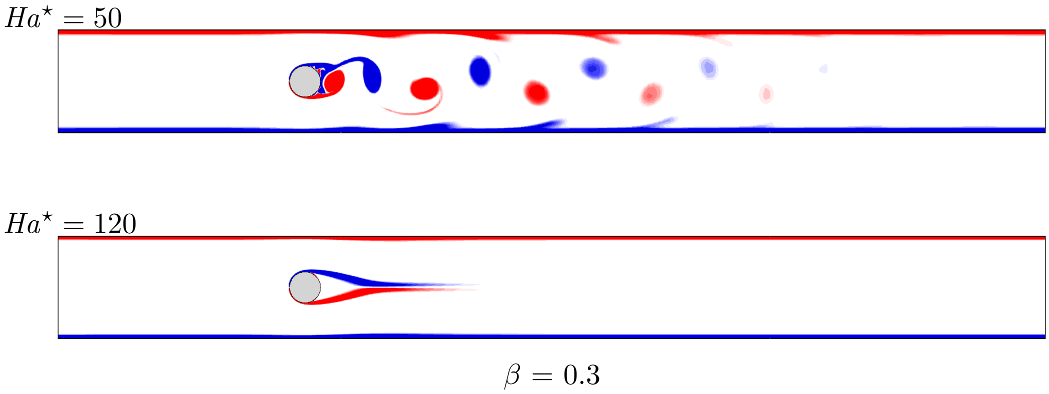

FIGURE 4.7: Vorticity contour plots for $Re = 2000$, β of 0.3 at low and high Hartmann number. 20 contour level are displayed between $-2 \leq \omega \leq 2$, with red and blue contours representing negative and positive vorticity, respectively.

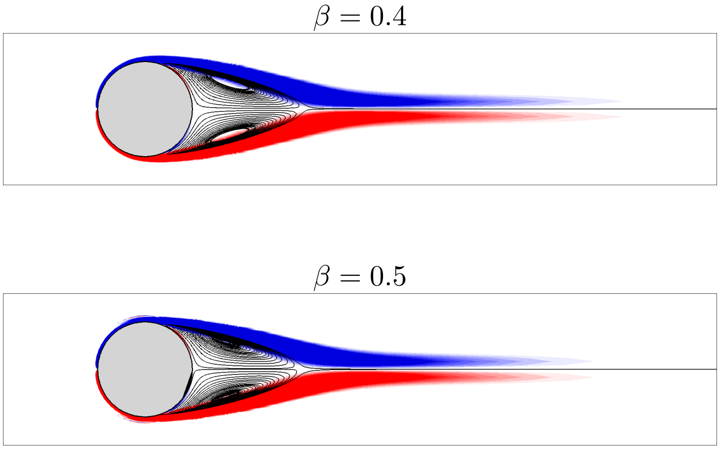

FIGURE 4.8: Plots showing streamlines in the near wake overlaid on contours of vorticity for $Re = 2000$, $\beta = 0.4$ and 0.5 at a Hartmann number of 120. 20 contour levels are displayed between $-2 \leq \omega \leq 2$, with red and blue contours representing negative and positive vorticity, respectively.

entrainment of vorticity from the walls towards the wake. The boundary-layer detachment from the walls was observed to increase gradually as the blockage ratio increases through 0.4 and 0.5 at $Ha^\star = 50$ (not shown). Vorticity is drawn into the channel and interacts with the Kármán vortex street, which creates an obstacle that impedes its motion.

For $\beta \geq 0.3$ at $Ha^\star = 120$, vortex shedding is completely suppressed (Fig. 4.8). At $\beta = 0.4$ and 0.5, the recirculation region has almost constant length and separation angle, and the shape of the circulation zone changes little.

The momentum equation of the quasi-two–dimensional Navier–Stokes equations provides insight into the rate of vorticity decay in the wake. Taking the curl of equation (3.62), and recognizing that the velocity field $\mathbf{u}$ is two–dimensional, gives

$$\frac{\mathrm{D}\omega}{\mathrm{D}t} = \nu\nabla^2\omega - 2\left(\frac{d}{a}\right)^2 \frac{Ha}{Re}\omega, \tag{4.4}$$

where ω is vorticity. The first term is the material derivative, the second term is the viscous diffusion term, and the third term is the Hartmann friction term. As a first approximation, in the high-Reynolds number limit

$$\frac{\mathrm{D}\omega}{\mathrm{D}t} \approx -2\left(\frac{d}{a}\right)^2 \frac{Ha}{Re}\omega, \tag{4.5}$$

which implies for a convecting packet of vorticity that

$$\frac{\mathrm{d}(\log_e \omega)}{\mathrm{d}t} \approx -2\left(\frac{d}{a}\right)^2 \frac{Ha}{Re}. \tag{4.6}$$

$$\frac{\mathrm{d}(\log_e \omega)}{\mathrm{d}t} \approx -2\frac{Ha^\star}{Re}. \tag{4.7}$$

To test this prediction, the peak vorticity magnitude (ω_{peak}) in an individual wake vortex was recorded as it convected downstream in each of the $\beta = 0.1$ flows shown in Fig. 4.6. Time histories of vorticity decay are plotted in Fig. 4.6. This data demonstrates that vortex decay, even at moderate Reynolds numbers, is dominated by Hartmann damping. Viscous diffusion appears to play a negligible role over the timeframe plotted in the figure. This behaviour has often been assumed to be the case in quasi–two–dimensional turbulence (Sommeria & Moreau 1982; Davidson 1997; Pothérat *et al.* 2005). At $\beta = 0.1$ and $Re = 2000$, the

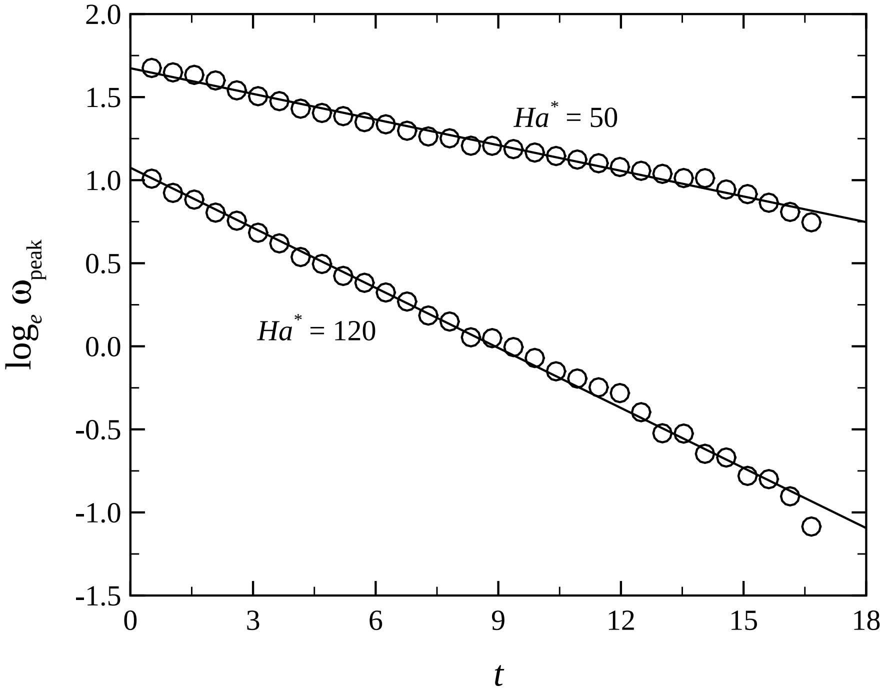

FIGURE 4.9: Time history of the natural logarithm of peak vorticity in a vortex convecting down the wake. Symbols show data points calculated at $\beta = 0.1$, $Re = 2000$, and Hartmann numbers $Ha^\star = 50$ and 120. Lines of best fit have gradients of -0.055 and -0.128.

gradients predicted by equation (4.7) for $Ha^\star = 50$ and 120 are -0.05 and -0.12, respectively. These are extremely close to the gradients -0.055 and -0.128 found for the least-squares linear fits to the data in Fig. 4.9.

4.3.4 Lift and Drag Coefficients

The variation of the time history of the lift coefficient with Hartmann number at different blockage ratios and $Re = 2000$ is shown in Fig. 4.10. At $\beta = 0.1$, the lift coefficient maintains a time-dependent oscillation at $Ha^\star = 50$ and 120. However, at $Ha^\star = 120$ and $\beta = 0.4$, no oscillation is detected as vortex shedding is suppressed. As the blockage ratio increases, the amplitude of lift coefficient decreases and the frequency increases. The respective Fourier spectra of lift coefficient signals presented in Fig. 4.10(a)-(b) are shown in Fig. 4.11.

(a) $\beta = 0.1$

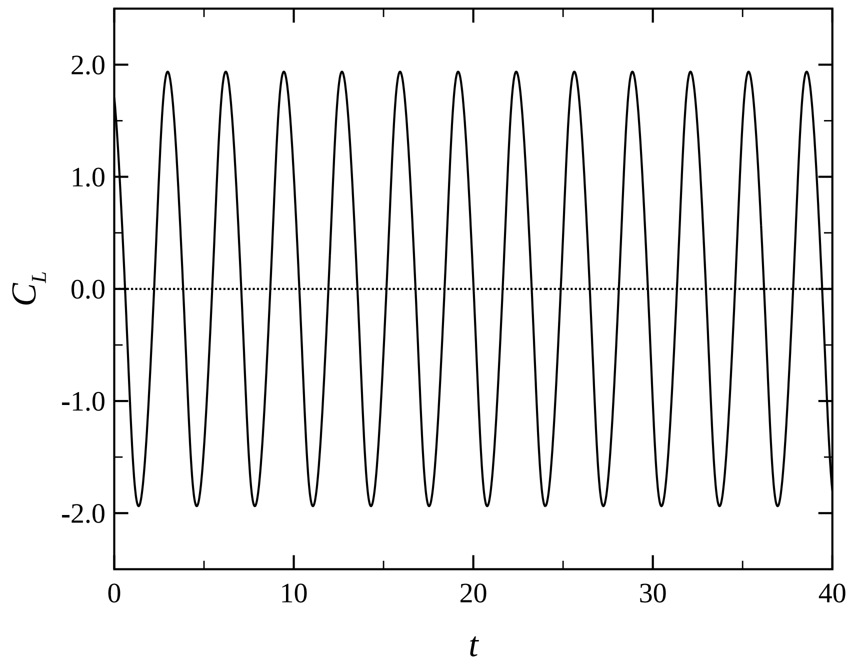

(b) $\beta = 0.4$

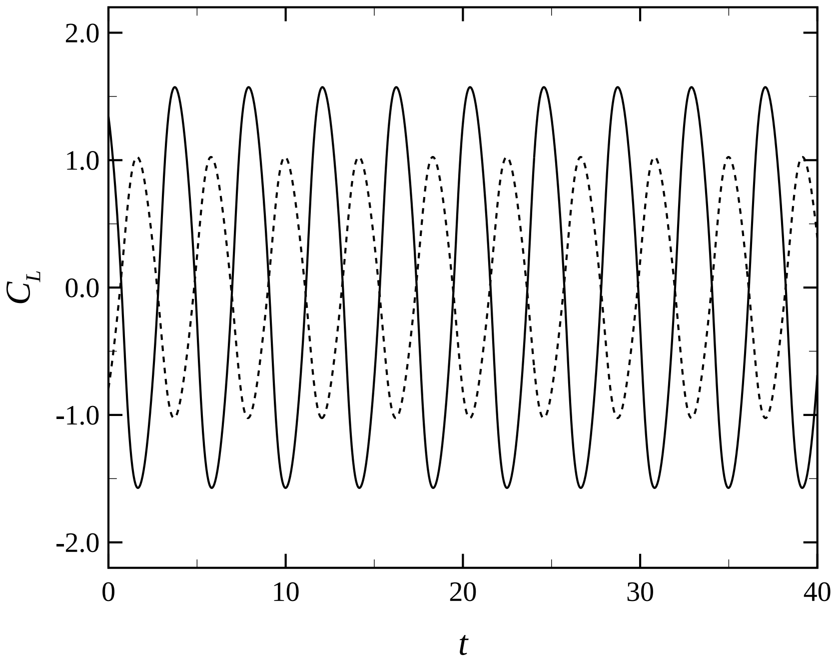

FIGURE 4.10: Time history of lift force coefficient for a blockage ratio of 0.1 (a) and 0.4 (b) at Hartmann numbers $Ha^{\star} = 50$ (solid line) and 120 (dashed line) for $Re = 2000$.

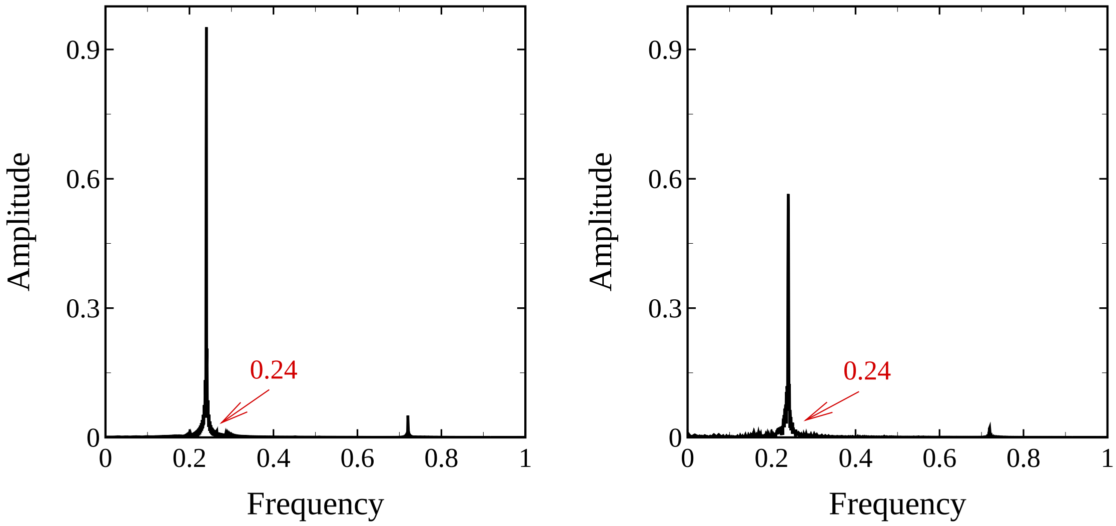
(a) $\beta = 0.1$ & $Ha^{\star} = 50$

(b) $\beta = 0.1$ & $Ha^{\star} = 120$

(c) $\beta = 0.4$ & $Ha^{\star} = 50$

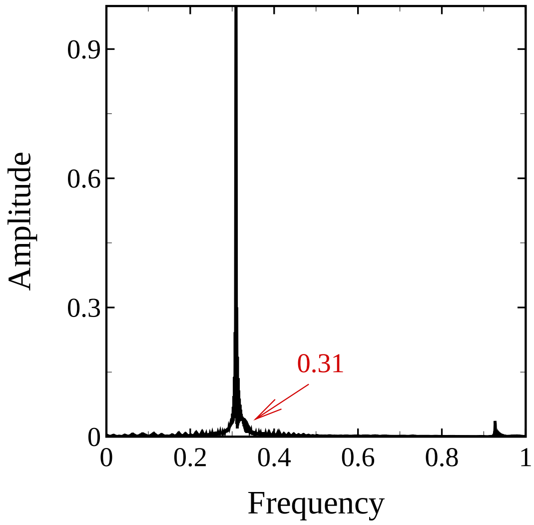

FIGURE 4.11: Fourier spectra of lift coefficient signal for $Re = 2000$ at different Hartmann numbers and blockage ratios. (a) $Ha^{\star} = 50,\ \beta = 0.1$, (b) $Ha^{\star} = 120,\ \beta = 0.1$ and (c) $Ha^{\star} = 50,\ \beta = 0.4$.

Since there is no signal at $\beta = 0.4$ and $Ha^{\star} = 120$, in the absence of the vortex shedding, no spectra are observed. In addition, it is observed that an increase in the blockage ratio shifts the location of the peak power towards higher frequency, i.e. higher Strouhal number St. The strong narrow peak in the power spectrum indicates the flow is indeed periodic.

Fig. 4.12 illustrates the phase between instantaneous lift and drag coefficients at $Re = 2000$ and $Ha^{\star} = 50$ during one period of oscillation of vortex shedding. The closed phase diagram shows that the flow is completely time-periodic, and the double rings indicates that the time period of oscillations of C_L is twice that of C_D. In this diagram, the location represents the mean lift and drag, while the amplitude of oscillation is represented by the size of the ring. For a blockage ratio of $\beta \leqslant 0.3$, the amplitude of the lift oscillation remains almost constant while that of the drag fluctuation decreases in the range. However for $\beta = 0.4$, the amplitude of the lift oscillation increases significantly and that of the drag oscillation remains constant.

Next, the effect of $Ha^{\star}$ and β on the time-averaged drag coefficient is considered. Figs. 4.13 and 4.14 presents the effect of the Hartmann number on the time-averaged drag coefficient, C_D, for different blockage ratios. For all β, it is found that C_D first decreases then subsequently increases with an increase in $Re/Ha^{\star 0.8}$. The choice of $Re/Ha^{\star 0.8}$ comes from Dousset & Pothérat (2008), who demonstrated for $\beta = 0.25$ that at low values of $Re/Ha^{\star 0.8}$, data collapses onto a universal curve. Similar collapses are observed at each blockage ratio, though to distinct curves, hence the collapse is blockage-ratio dependent. At higher $Re/Ha^{\star 0.8}$, the drag coefficient increases, and displays a dependence on Hartmann number. All data presented in Fig. 4.13 represents time-dependent flows. In the low-$Re/Ha^{\star 0.8}$ regime, the flow dynamics is dominated by Hartmann damping. Conversely, at higher $Re/Ha^{\star 0.8}$, Hartmann damping is no longer dominant, and the wake resembles vortex shedding in the absence of a magnetic field. Examples of these regimes are, respectively, the $Ha^{\star} = 120$ and $Ha^{\star} = 50$ flows at $\beta = 0.1$ plotted in Fig. 4.6.

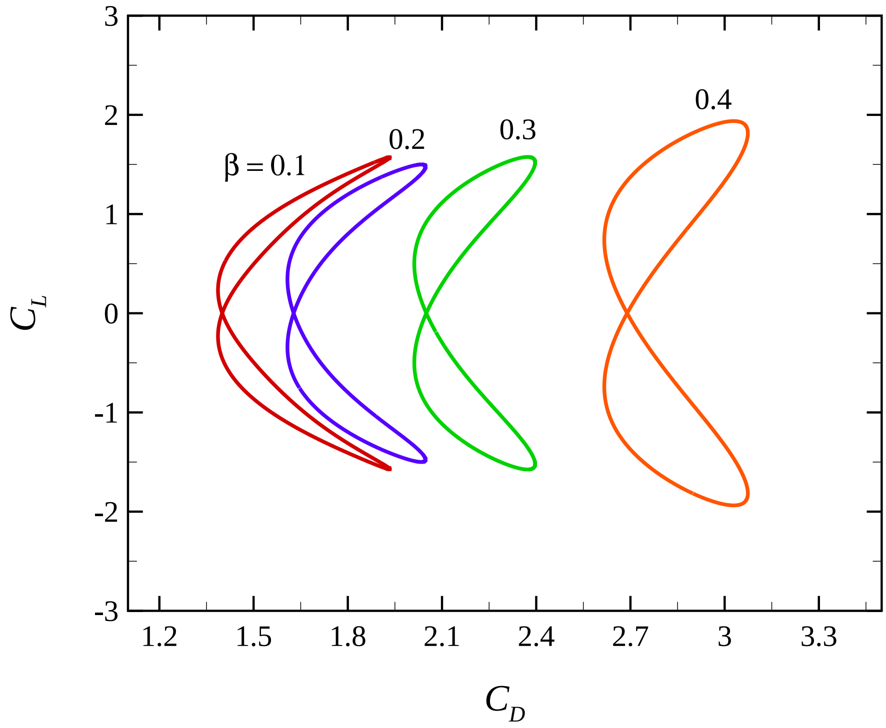

FIGURE 4.12: The trajectories of C_D and C_L at $Re = 2000$ and $Ha^\star = 50$ over one period of oscillation for different blockage ratios as indicated.

4.4 Heat Transfer

4.4.1 Mixing Induced by Vortex Shedding

Figs. 4.15 and 4.16 present the distribution of instantaneous temperature contours for blockage ratios $\beta = 0.1$, 0.2, 0.3 and 0.4, and Hartmann numbers $Ha^\star = 50$ and 120 at $Re = 2000$. For all β, when $Ha^\star = 50$ the temperature fields are time-dependent because the flow is unsteady. As the blockage ratio is further increased, the velocity of the flow near the heated wall increases. Therefore, the low-temperature fluid is transported toward the hot region of the channel and the high-temperature fluid near the heated wall is convected away to mix with the low-temperature fluid. Consequently, the heat transfer is enhanced remarkably. However, as $Ha^\star$ is increased to 120, the unsteadiness in the flow is suppressed at $\beta = 0.2$, and the flow is steady as β increases to 0.3. This increases the thickness of the thermal boundary layer, and hence the temperature gradient along the

(a) $\beta = 0.1$

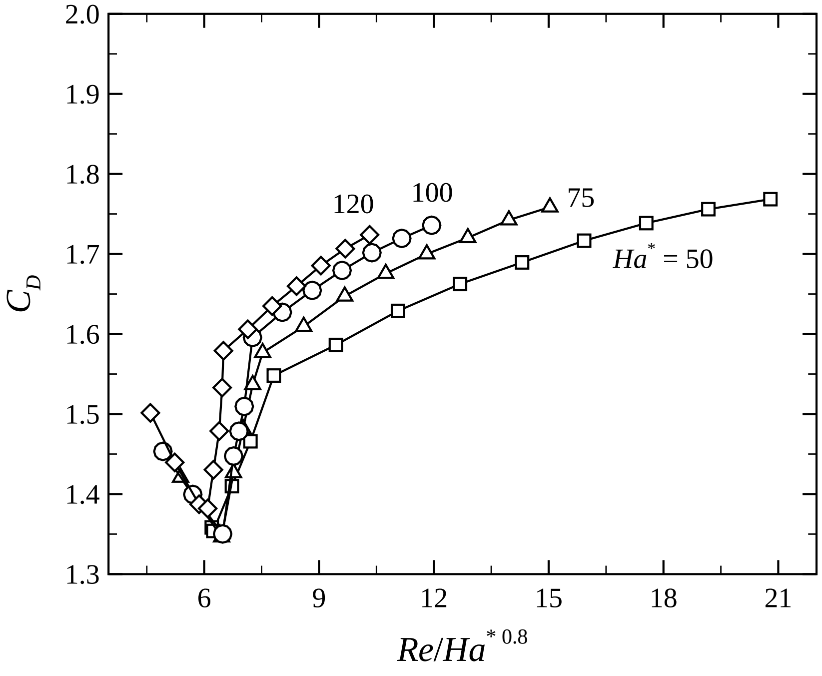

(b) $\beta = 0.2$

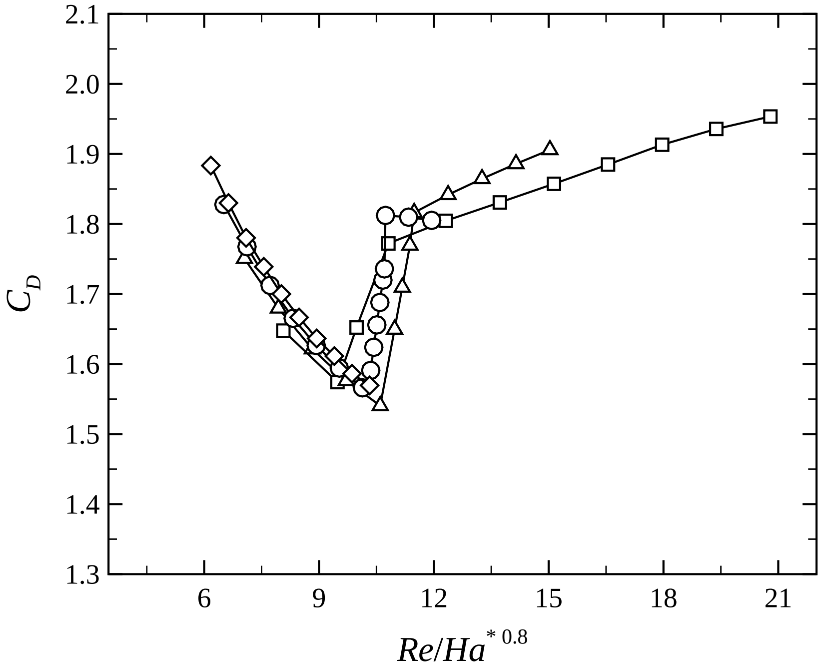

FIGURE 4.13: Time-averaged drag coefficients as a function of $Re/Ha^{0.8}$ at different Hartmann numbers and blockage ratios (a) $\beta = 0.1$ and (b) $\beta = 0.2$.

(a) $\beta = 0.3$

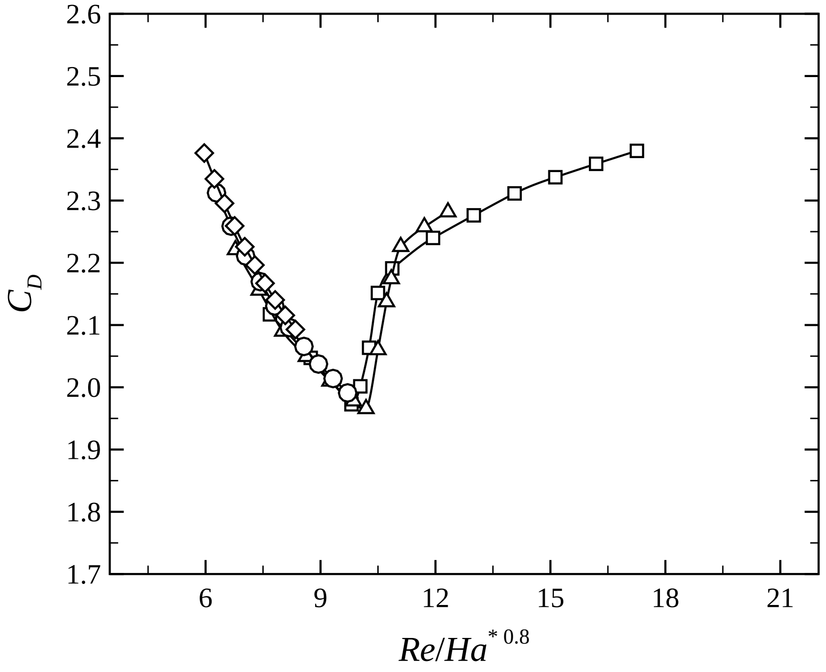

(b) $\beta = 0.4$

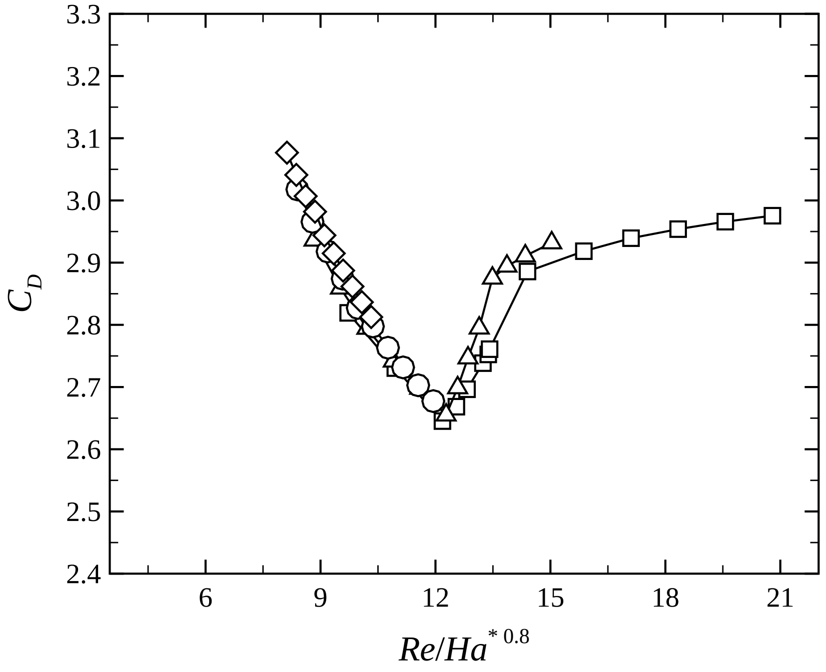

FIGURE 4.14: Time-averaged drag coefficients as a function of $Re/Ha^{0.8}$ at different Hartmann numbers and blockage ratios (a) $\beta = 0.3$ and (b) $\beta = 0.4$ (symbols as per Fig. 4.13).

heated wall decreases.

4.4.2 Time-Averaged and Local Nusselt Number

Fig. 4.17 shows the effect of the blockage ratio on the time-averaged Nusselt number of the heated wall, Nu, for Hartmann numbers $Ha^\star = 50$ and 120 at $Re = 2000$ and 3000. The heat transfer is shown to be higher at higher Reynolds numbers. At $Ha^\star = 50$, there is a remarkable increase in Nu for both Reynolds numbers as β is increased from 0.1 to 0.4. The increase is more pronounced at $\beta \geq 0.2$. However, Nu reduces as the Hartmann number is increased to $Ha^\star = 120$.

To gauge the improvement to the heat transfer generated by placing a cylinder in the duct, the percentage increment of the overall heat transfer is calculated using equation (3.68) for the flows considered in this study. For $Re = 2000$ and $Ha^\star = 50$, the percentage increment for $0.1 \leq \beta \leq 0.4$ ranges between 3% and 89%. At $Ha^\star = 120$, the increments are smaller, ranging up to 25%. For $Re = 3000$, the overall heat transfer increments range between 7% and 128% at $Ha^\star = 50$, and between 6% and 34% at $Ha^\star = 120$. Thus at $Ha^\star \approx 50$ and $Re \gtrsim 3000$, in channels with blockage ratios $\beta \approx 0.4$, heat transfer is enhanced by more than 100% by placing a cylinder within the channel.

Figs. 4.18 and 4.19 show the distribution of the local Nusselt number along the heated wall Nu_w as a function of streamwise coordinate x for different Hartmann numbers at $Re = 2000$. The effect of Hartmann number is found to be negligible for small blockage ratio ($\beta = 0.1$). Similarly, at $\beta = 0.2$, the variation of the local Nusselt number with Hartmann number is independent, except that of $Ha^\star = 50$. However, as the blockage ratio increases further from 0.2 to 0.4, the change in the distribution of Nu_w is remarkable with changing Hartmann number. The change is more pronounced at low Hartmann number. The plot also demonstrates that the curves collapse to a single curve at high Hartmann number and small blockage ratio. It can be noted that Nu seems to depend on Hartmann number at high blockage ratio. An explanation of this can be deduced from the vorticity contour plots shown in Figs. (4.6-4.8) and temperature contour plots shown in

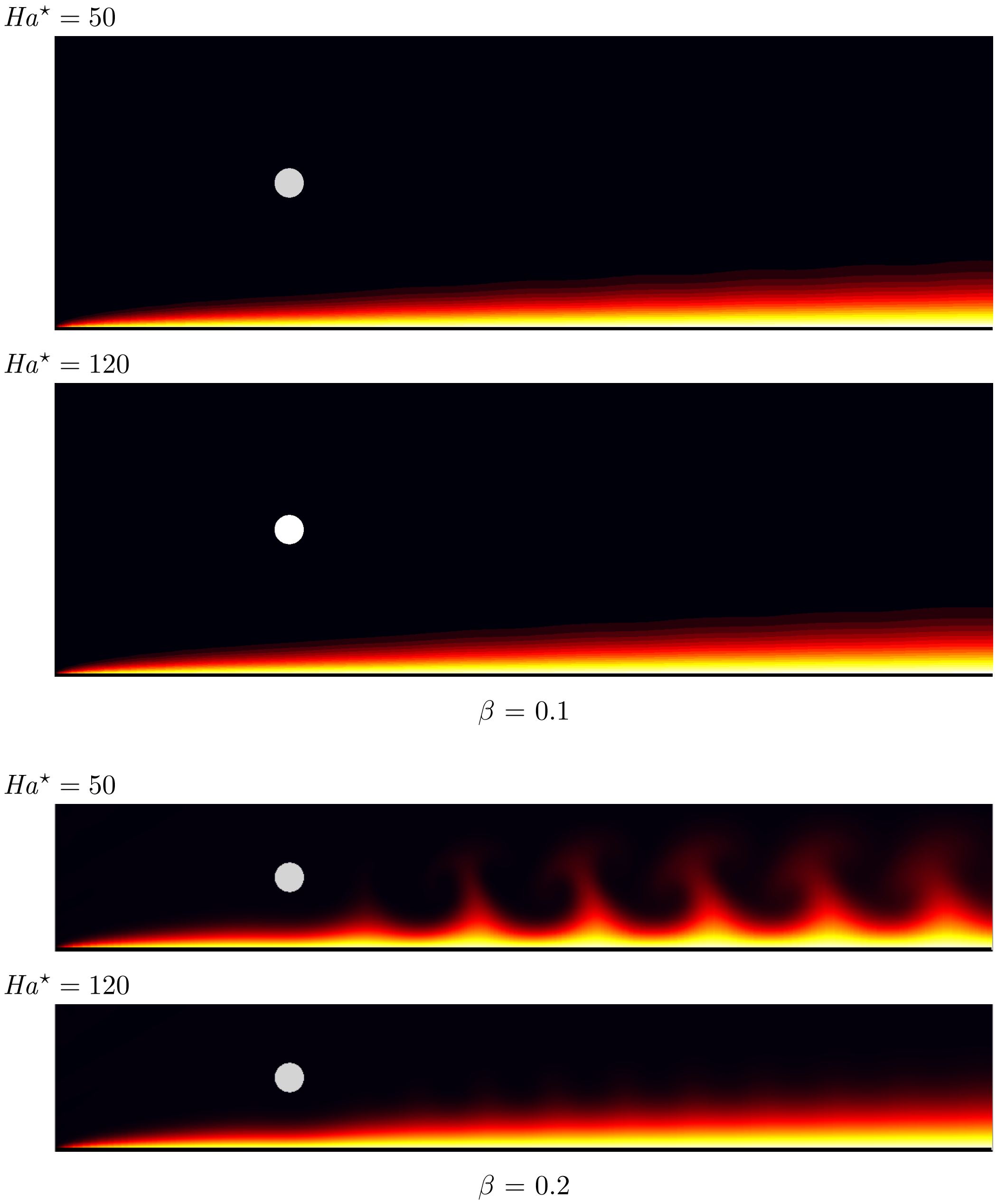

FIGURE 4.15: Instantaneous dimensionless temperature contours at $Re = 2000$ for $\beta = 0.1$ and $\beta = 0.2$ at low and high Hartmann number. Light and dark shading shows hot and cold fluid, respectively.

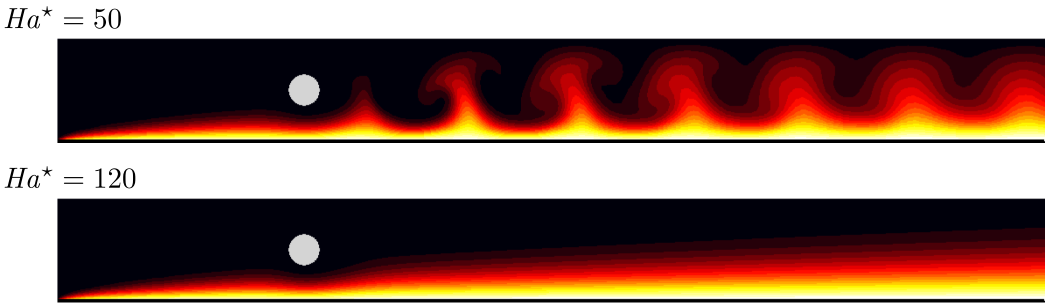

$\beta = 0.3$

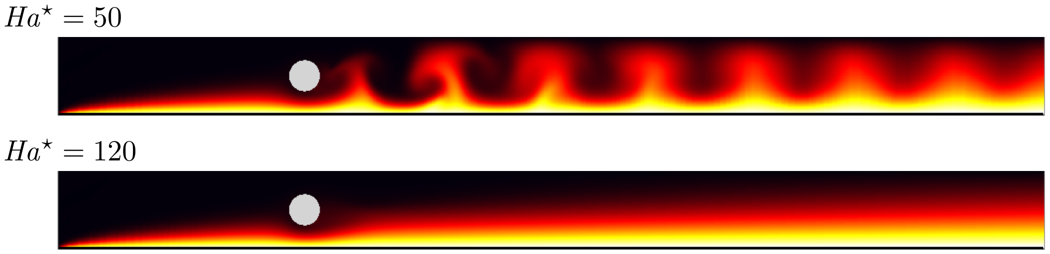

$\beta = 0.4$

FIGURE 4.16: Instantaneous dimensionless temperature contours at $Re = 2000$ for $\beta = 0.3$ and $\beta = 0.4$ at low and high Hartmann number. Light and dark shading shows hot and cold fluid, respectively.

Figs. (4.15-4.16). It can be noted that for small blockage ratios (wide channel) at $Re = 2000$, the flow is unsteady for the all the range of Hartmann number considered in this study. A regular vortex street is observed to comprise of regular positive and negative vortices shed alternately from the shear layers either side of the cylinder, with very weak boundary layer detachment from the walls. The boundary layer detachment from the walls increases as the blockage ratio increases (narrow channel); as a result the heat transfer from the heated wall increases significantly due to the sweeping of the heating surface by the wake vortices at low Hartmann number. On other hand, the unsteadies in the flow is reduced significantly at high Hartmann number (it is completely damped for $\beta = 0.3$ at $Ha^\star = 120$), which leads to an increase the thickness of the thermal boundary layer, and hence the heat transfer along the heated wall decreases markedly. Therefore, Nu_w is dependent on Hartmann number for higher blockage ratios.

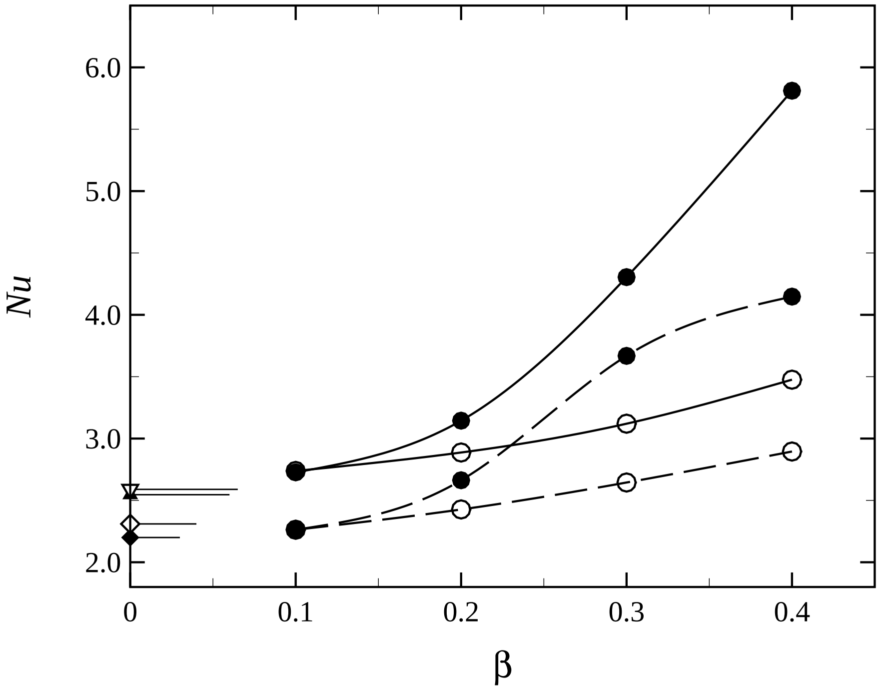

FIGURE 4.17: Effect of Hartmann number and blockage ratio on the time-averaged Nusselt number for Reynolds numbers $Re = 2000$ (dashed lines) and 3000 (solid lines). Solid symbols show $Ha^\star = 50$ and open symbols show $Ha^\star = 120$. For reference, Nusselt number values for the channel without a cylinder present are also provided: (♦, ◇) represent $Re = 2000$ at $Ha^\star = 50$ and 120, respectively. (▲, ▽) represent $Re = 3000$ at $Ha^\star = 50$ and 120, respectively.

4.4.3 Pressure Drop

In magnetohydrodynamic channel flows, the pressure drop becomes large at high Harmann number. Thus in the context of this study, it is prudent to consider the additional pressure drop penalty incurred by adding a cylinder to the channel. In Fig. 4.20, the pressure drop penalty is plotted. The data demonstrates that at low blockage, there is only a small increase in pressure drop due to the addition of the cylinder. However, as the blockage increases (particularly through $\beta = 0.3$ and 0.4), the increase in pressure drop is also more substantial. The pressure drop penalty displays an increased dependence on Hartmann number as the blockage ratio increases, with increasing Hartmann number resulting in an increased pressure drop penalty. Demonstrating the significant effect of Hartmann number on

(a) $\beta = 0.1$

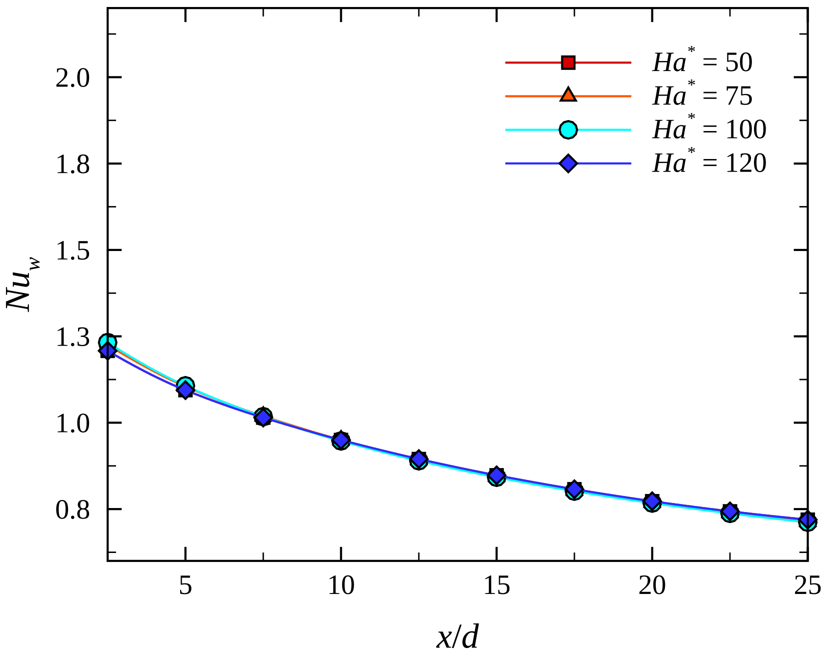

(b) $\beta = 0.2$

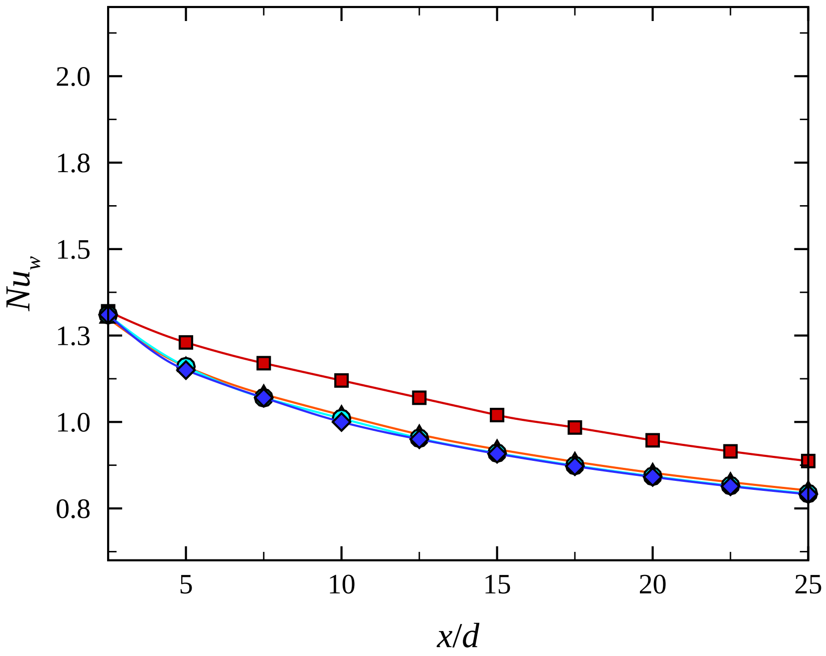

FIGURE 4.18: Local Nusselt number over the heated surface of the side wall as a function of x/d at $Re = 2000$ and different Hartmann numbers, and blockage ratios as indicated.

(a) $\beta = 0.3$

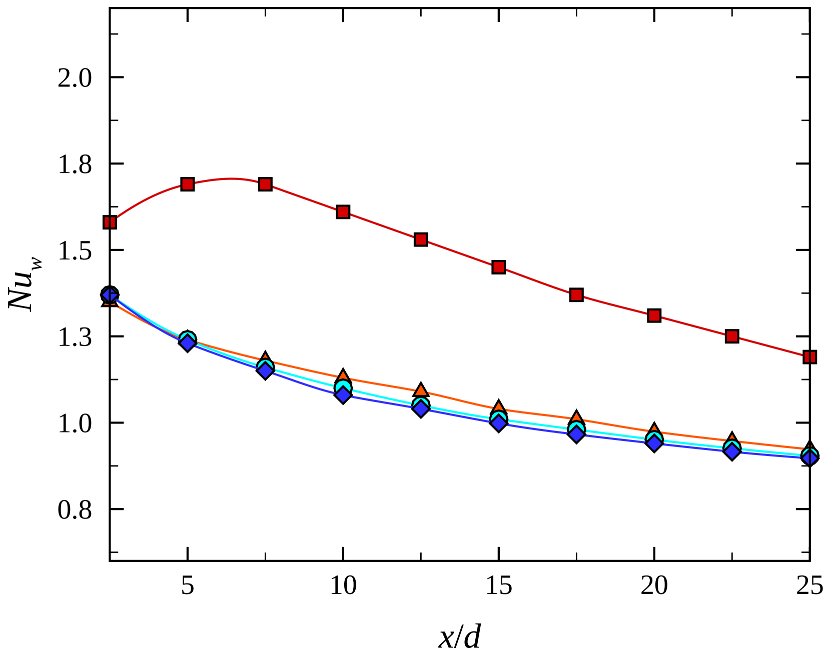

(b) $\beta = 0.4$

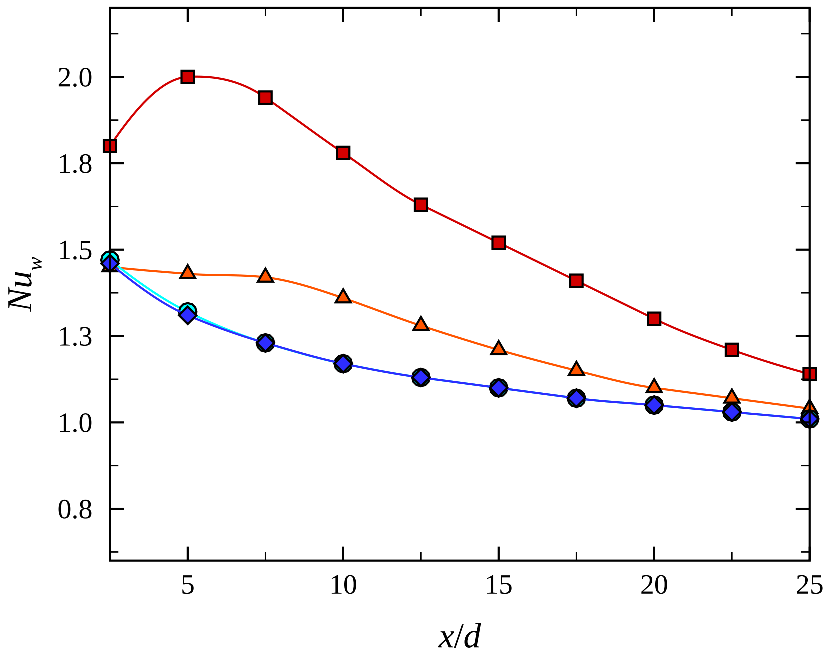

FIGURE 4.19: Local Nusselt number over the heated surface of the side wall as a function of x at $Re = 2000$ and different Hartmann numbers (symbols as per Fig. 4.18), and blockage ratios as indicated.

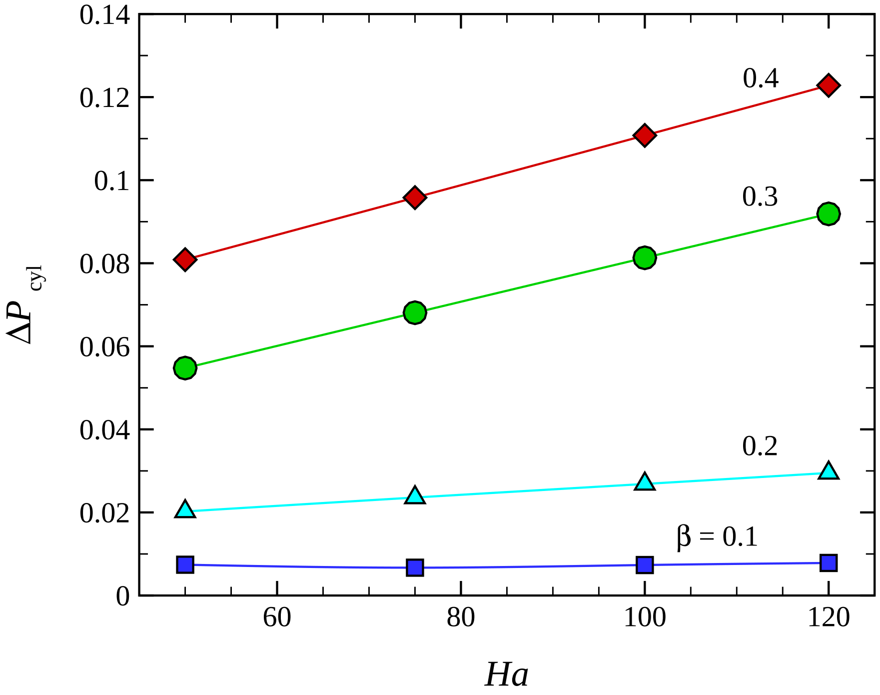

FIGURE 4.20: Pressure drop penalty at $Re = 2000$ due to inclusion of a circular cylinder within the duct, plotted against $Ha^\star$. The pressure drop penalty is the difference in pressure drop across identical channels with and without a circular cylinder. Spline fit are included for guidance.

the pressure drop penalty, at $Ha^\star = 50$ the penalty at $\beta = 0.4$ is 11 times that at $\beta = 0.1$, and at $Ha^\star = 120$ this ratio increases to 16. The blockage effect rapidly comes into effect between $\beta = 0.2$ and 0.3. Between these blockage ratios, the gradient of pressure drop penalty with Hartmann number increases by a factor of 4, whereas a much more modest increase is observed as blockage ratio increases to 0.4.

4.5 Chapter Summary

In this chapter, the fluid flow and heat transfer of liquid metal past a symmetrical circular cylinder in a rectangular duct under a strong axial magnetic field has been examined in detail. Under these conditions the flow is quasi-two-dimensional and the modified Navier–Stokes equations are solved in a two–dimensional domain.

The formulation of the geometries under investigation and the corresponding flow and boundary conditions have been described. Meshes have been developed that accurately model a range of blockage ratios at low and high Hartman numbers. The details of domain length length and grid-resolution study have been presented.

The transition Reynolds number from steady to unsteady flow past a circular cylinder confined within a plane channel is determined as a function of $Ha^{\star}$ and β. The effect of Hartmann layers on the out-of-plane channel walls are described through the Hartmann friction term added to the Navier–Stokes equations.

The critical Reynolds number at which the transitions from steady to unsteady flow occurs was found to increase with increasing $Ha^{\star}$ for all values of β. The increase in Re_c was more pronounced at high $Ha^{\star}$ and β.

In the steady flow regime, for small blockage ratio, the recirculation bubble was found to be visible up to $Ha^{\star} = 120$, though it was suppressed completely beyond $Ha^{\star} \lesssim 500$. This is due to the effect of Lorentz forces which produce a force in the direction opposite the flow resulting in the decrease of the wake length. The recirculation length, Reynolds number, Hartmann number and blockage ratio were related as $L_R/d + 0.709 \propto Re^{0.844} Ha^{\star -0.711} \beta^{0.166}$.

In the unsteady flow regime, at $Re = 2000$, $\beta \leq 0.2$ and $Ha^{\star} = 50$ and 120, the structure of the Kármán vortex street consists of regular positive and negative vortices shed respectively from the bottom and the top of the cylinder. As β is increased to 0.3, at $Ha^{\star} = 50$, the boundary layer detachment from the side wall of the duct occurs downstream of the cylinder. The detachment of the boundary layer increased gradually as β increases further to 0.4 and 0.5. For $\beta \geq 0.3$, at $Ha^{\star} = 120$, vortex shedding is completely suppressed.

For all β, it is found that the drag coefficient C_D first decreases and then increases as the Reynolds number is increased. The viscous contribution to the drag coefficient for the cylinder was much smaller than the pressure drag. Therefore, C_D is dominated by the pressure contribution. This is attributed to the effect of Hartmann friction and the confinement of the walls that delay the transitions of the flow to a higher Reynolds number. As a result, the viscous contribution is much smaller than that of the pressure. Also, for all β, it was found that at each blockage ratio the curves collapse to universal curves at lower values of $Re/Ha^{\star 0.8}$.

The heat transfer rate is strongly dependent on the Hartmann number and blockage ratio. For small Hartmann number, it increases significantly as blockage ratio is increased. However, there is a gradual increase in the Nusselt number for high Hartmann number as blockage ratio is increased. Overall, though, the enhancement of heat transfer was significantly augmented with increasing blockage ratio, in some cases by more than two-fold.

The effect of the Hartmann number on the local Nusselt number from the heated wall of the duct, Nu_w, is found to be negligible for small blockage ratios. However, for high blockages, the change in Nu_w was found to be significant with different Hartmann number.

The pressure drop penalty incurred by adding a cylinder to the channel is found to increase with both blockage ratio and Hartmann number, and the penalty is increasingly dependent on Hartmann number at higher blockage ratios.

Chapter 5

Flow and Heat Transfer for a Cylinder Offset from the Duct Centreline

This chapter builds upon the previous chapter by considering the same flow system except that the cylinder will now be offset from the channel centreline. It has been demonstrated in chapter 4 that both the heat transfer from the heated wall and the pressure drop penalty invoked by adding a cylinder to the channel increase significantly as the blockage ratio increases. By placing a small cylinder in the channel near one wall, its size will not produce a large pressure drop penalty, but the action of vortex shedding near the heated wall should improve the heat transfer.

In this chapter, the fluid flow and heat transfer of a liquid metal flowing past a circular cylinder positioned offset in a rectangular duct under a strong axial magnetic field are investigated. The effects of varying the gap between the body and the duct heated wall, blockage ratio and Reynolds number at constant Hartmann number on the heat transfer characteristics and the flow behavior are examined. Firstly, a description of the geometry, boundary conditions and grid resolution is given in § 5.1. In the next section, the dynamics of the flow is outlined. The effects of blockage and gap ratios β and γ on the flow structure in the gap region are presented in § 5.2.1. Also, the effect of these parameters on the lift and drag forces are determined in § 5.2.2 and § 5.2.3, respectively. Finally, heat transfer from the heated wall and the mixing invoked by placing

γ	$\Delta/d(\beta = 0.1)$	$\Delta/d(\beta = 0.2)$	$\Delta/d(\beta = 0.3)$	$\Delta/d(\beta = 0.4)$
1	4.5	2.0	1.15	0.75
0.5	2.25	1.0	0.58	0.38
0.25	1.13	0.5	0.29	0.19

Table 5.1: The minimum distance from the surface of the cylinder to the heated wall of the duct at different blockage ratios.

a circular cylinder positioned asymmetrically in the duct is presented in § 5.3.1. The effect of β, γ and the Reynolds number on the time averaged Nusselt number and the gain of heat transfer enhancement, local Nusselt number, are determined in § 5.3.2, § 5.3.3, and § 5.3.4, respectively.

5.1 Geometry and Boundary Conditions

The geometry of the problem under consideration is shown in Fig. 5.1. A rectangular duct contains a circular cylinder placed at a position defined by a gap ratio γ. The gap ratio is defined as $\gamma = \Delta/(h/2 - d/2)$ where Δ is the minimum distance from the surface of the cylinder to the nearest wall. The value of γ is equal to 1 when the cylinder is placed symmetrically between the plane walls and 0 when it touches one of the walls. Table 5.1 summarises the distance Δ considered in this study at different blockage and gap ratios.

The setup of the system is the same as that described in the earlier chapters. The cylinder is located at $8d$ and $25d$ from the inlet and outlet, respectively, which is sufficient to obtain domain independent results as demonstrated previously in § 4.2.1.

Elements are concentrated in the vicinity of the cylinder and the heated wall to capture the small-scale structures in the flow. The meshes comprise between 1196 and 2391 elements, depending on blockage and gap ratios. The details of the layout of these meshes are shown in Fig. 5.2. The asymmetrically positioned cylinder requires the creation of new meshes, and thus further grid-independence tests are performed to ensure that adequate spatial resolution is maintained for the simulations described in this chapter.

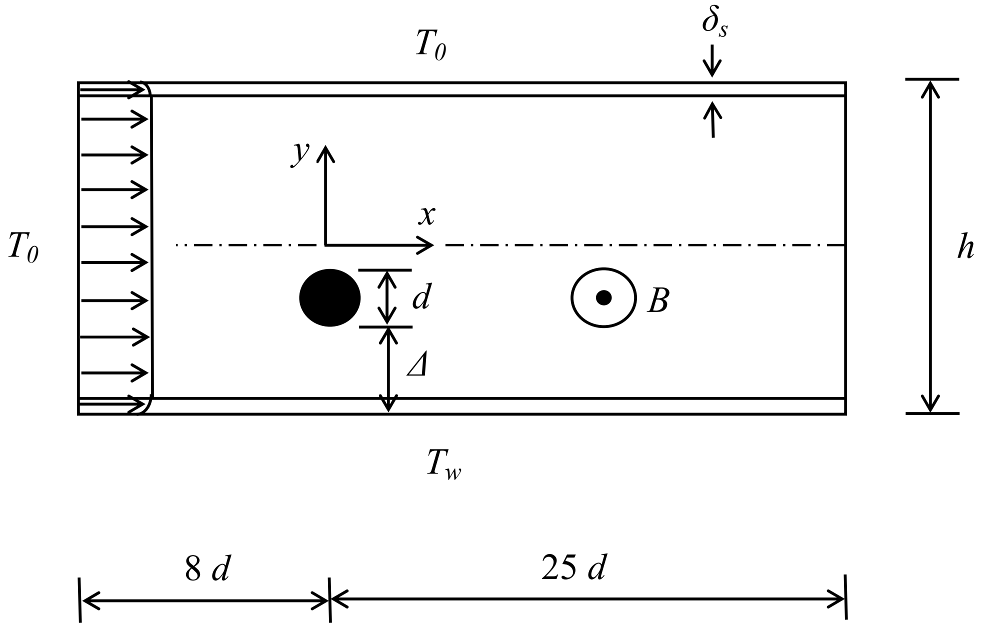

FIGURE 5.1: Schematic for the flow past an asymmetrically confined circular cylinder. The magnetic field B acts in the out-of-plane direction, parallel to the cylinder axis. δ_S is the thickness of the Shercliff layer, and h and d are the duct width and cylinder diameter, respectively. The blockage ratio $\beta = d/h$ and the gap ratio $\gamma = \Delta/(h/2 - d/2)$.

As in the previous chapters, spatial resolution tests have been performed by varying the element polynomial degree between 4 and 9, while keeping the macro-element distribution unchanged. The parameters St and C_D were monitored. Convergence tests were performed on two cases, chosen at the upper end of the parameter range of this study. The first case has $\beta = 0.1, Re = 3000$, $Ha^\star = 50$ and $\gamma = 0.25$, and the other case has $\beta = 0.4, Re = 3000$, $Ha^\star = 50$ and $\gamma = 0.25$. A target of 0.3% uncertainty was desired and this was found to be achieved with polynomial degree 7, which is used hereafter. Also, the results were tested to ensure that the solution was independent of the size of the time step Δt. Varying the time step from 0.001 to 0.0005 for the flow conditions given above, resulted in minimal variation in St and C_D. The boundary conditions imposed here are similar to those used for the symmetrical channel geometry described in § 4.1.

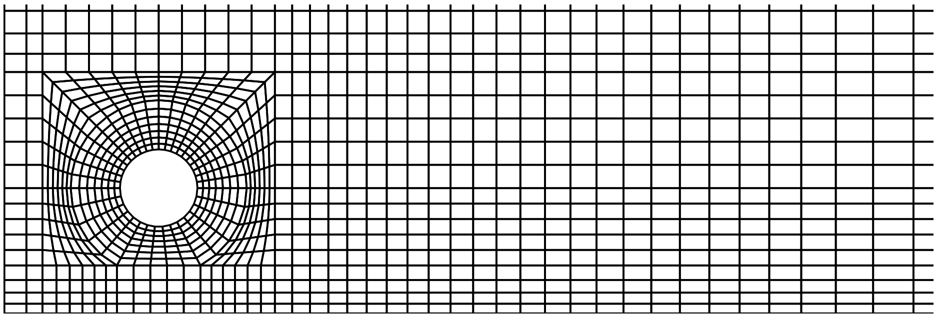

(a) $\beta = 0.1$

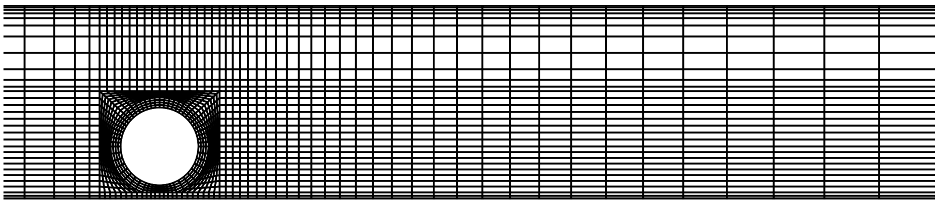

(b) $\beta = 0.4$

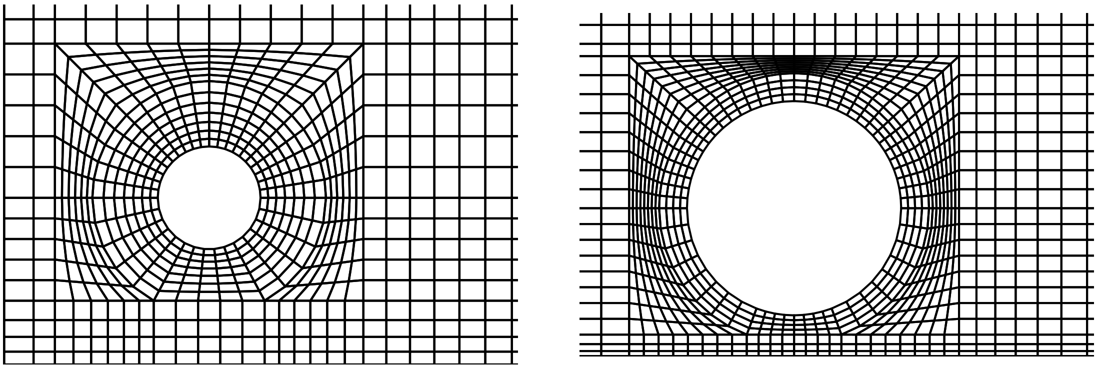

(c) details for $\beta = 0.1$

(d) details for $\beta = 0.4$

FIGURE 5.2: Meshes of the confined asymmetrical cylinder with the details of the region near the body. (a) mesh used for $\beta = 0.1$ and $\gamma = 0.25$. (b) mesh used for $\beta = 0.4$ and $\gamma = 0.25$. The meshes extend $25d$ downstream and $8d$ upstream. (c) and (d) represent the details of the meshes around the cylinder for $\beta = 0.1$ and $\beta = 0.4$, respectively.

At the channel inlet, a Hartmann velocity profile for the axial velocity is applied (Moreau 1990). No-slip boundary conditions for velocity are imposed on the side walls and the cylinder. At the outlet, a constant reference pressure is imposed and a high-order Neumann condition for pressure is imposed on the Dirichlet velocity boundaries to preserve the third-order time accuracy of the scheme (Karniadakis *et al.* 1991). The temperature of the incoming stream and top wall is taken as T_o, and at the bottom wall as T_w. The cylinder is thermally insulated (a zero normal temperature gradient is imposed at its surface).

5.2 Dynamics of the Flow

5.2.1 Flow Structures: The Dependence on γ and β of Vortex Shedding Evolution

When a cylinder is located asymmetrically in a duct, the dynamics of the flow differ due to the presence of the fixed wall closer to the cylinder surface. A Reynolds number of 2000 and Hartmann number $Ha^\star = 50$ have been chosen to demonstrate the interaction of the wall boundary layers parallel to the magnetic field and that of the cylinder. Figs. 5.3–5.6 illustrate the effect of the blockage ratio β and gap ratio γ on vortex shedding from the cylinder for these parameters. The instantaneous vorticity fields are presented to show the effect of offsetting the cylinder from the duct centerline. For $\beta = 0.1$, when the cylinder is symmetrically in the plane channel (i.e. $\gamma = 1$) a wake comprising two well-defined rows of vortices is formed with clockwise negative and counter-clockwise positive vortices shed from the top and the bottom separating shear layers from the cylinder, respectively. When $\gamma = 0.5$, the wake behind the cylinder is still characterized as a two-row vortex street convected throughout the entire downstream region. At this gap ratio, the wall shear layers (Shercliff layers) that develop along the surface of the duct parallel to the magnetic field at the cylinder location are still far from the lower shear layer on the cylinder surface. Therefore, these two shear layers interact weakly with each other in the wake region. As γ is decreased to 0.25, the wall boundary layer expands and separates from the wall downstream of the cylinder to form a negative vortex structure. This negative vortex interacts with the negative vortex shed from the upper shear layer on the cylinder. In this case the Kármán vortex street almost becomes a single row of vortices.

Although, for $\beta = 0.2$ and $\gamma = 1$, the structure of the vorticity field was found to resemble that of $\beta = 0.1$ at $\gamma = 1$, the lower wall shear layer is seen to interact weakly with the negative shear layer on the cylinder surface. Therefore, the development of the vorticity is not affected substantially and the vortex shedding from the cylinder is not suppressed by the wall shear layer at this gap ratio. However, the detachment of the wall shear layer at the cylinder location was observed to increase significantly as the gap ratio decreases from 1 to 0.5. As a consequence, the lower shear layer on the cylinder interacts strongly with the wall shear layer. On further decreasing of gap ratio, the structure of the vortex shedding changes dramatically with further decrease in gap ratio. The vortex street is observed farther away from the wall and convected downstream, maintaining its state in the outflow region.

For $\beta \geq 0.3$ at $\gamma = 1$, the wall shear layers interact significantly with the Kármán vortex street causing the wake vortices to decay much more quickly. For $\gamma \geq 0.5$, the boundary layer along the lower side of the cylinder and the shear layer along the wall effectively merge and roll up together before travelling further downstream. At the smallest gap ratio of $\gamma = 0.25$ for $\beta = 0.4$, the wake vorticity on the upper side of the cylinder is stretched out as the wake advects downstream.

It can be noted that for $\Delta/d \approx 2 - 2.25$ at small blockage ratios ($\beta = 0.1$ and 0.2), the wake behind the cylinder is characterized by two-row vortex street extending throughout the entire downstream. The wall boundary layer that develops along the surface parallel to the magnetic field at the cylinder location are far from the lower shear layer on the cylinder surface. On the other hand, for $\Delta/d \approx 0.75 - 1.15$ at $\beta = 0.1$, 0.2 and 0.3, the structure of the wake behind the cylinder is almost the same, while the wall boundary layer expands and separates from the wall downstream of the cylinder to form negative-sign vortex structures. For $\Delta/d \approx 0.5 - 0.58$ at $\beta = 0.2$ and 0.3, the vortex street is observed to interact strongly with the near-wall boundary layer, before deflecting away from the wall and into the duct interior.

For small blockage ratios, it is expected that the instability in the wake region should change character from being absolutely unstable at large gaps to convectively unstable at small gaps. This was found previously for non-magnetohydrodynamic bluff body flows (Triantafyllou & Dimas 1989; Reichl *et al.* 2005).

5.2.2 Fluctuating Lift Coefficient

Figs. 5.7 and 5.8 present the time evolution of the lift coefficient at different gap ratios for $Re = 2000$, $Ha^{\star} = 50$ and blockage ratios of 0.1 and 0.4, respectively. It can be seen that at the small blockage ratio $\beta = 0.1$ for all gap ratios tested, the shedding is perfectly periodic, so the lift coefficient oscillates regularly. There is no apparent difference in the time history of the lift coefficient at these three gap ratios. However, for $\gamma = 0.25$ and $\beta = 0.4$, the amplitude of the oscillations of the fluctuating lift coefficient decreases significantly and the signal becomes irregular.

The change in the amplitude and the degree of regularity of the oscillating lift are consistent with the change to the nature of the wake. For all gap ratios at $\beta \leq 0.3$, the lift coefficient oscillates regularly with a large amplitude consistent with the existence of time periodic vortex shedding from the cylinder (see Figs. 5.3-5.5). At the gap ratio $\gamma = 0.25$ for $\beta = 0.4$, the amplitude reduction and the irregularity of the fluctuating lift correlate with vortex formation much further from the cylinder and reduced regularity of shedding overall. The respective Fourier spectra of the lift coefficient signals presented in Figs. 5.7 and 5.8 are shown in Fig. 5.9. As expected, Fig. 5.9(a) shows a single harmonic peak at $\beta = 0.1$ for all the gap ratios considered. However, the spectrum for $\beta = 0.4$ and $\gamma = 0.25$ shows distinguishable and interesting features as indicated in Fig. 5.9(b). A broad range of flow frequencies is apparent but with three primary peaks present. The existence of the two incommensurate frequencies $(0.45, 0.59)$ correspond to a loss of periodicity of the lift signal. The figure also demonstrates that an increase in the blockage and gap ratios shifts the location of the main peak towards higher frequency. The change in frequency is more pronounced at high blockage and gap

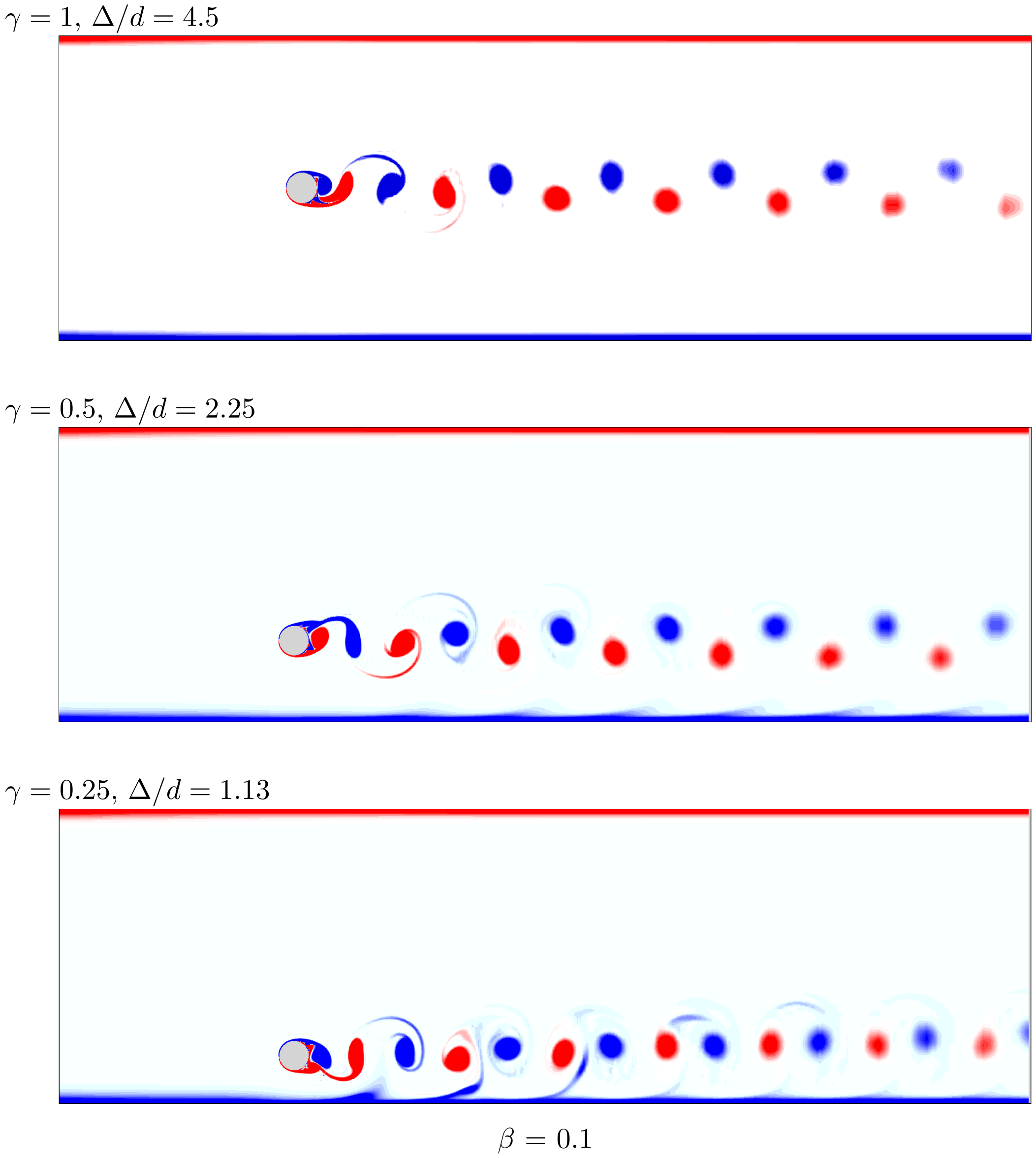

FIGURE 5.3: Instantaneous vorticity contour plots at $Ha^{\star} = 50$, $Re = 2000$ and β of 0.1 for various gap ratios γ. 20 contour level are displayed between $-2 \leq \omega \leq 2$, with red and blue contours representing negative and positive vorticity, respectively.

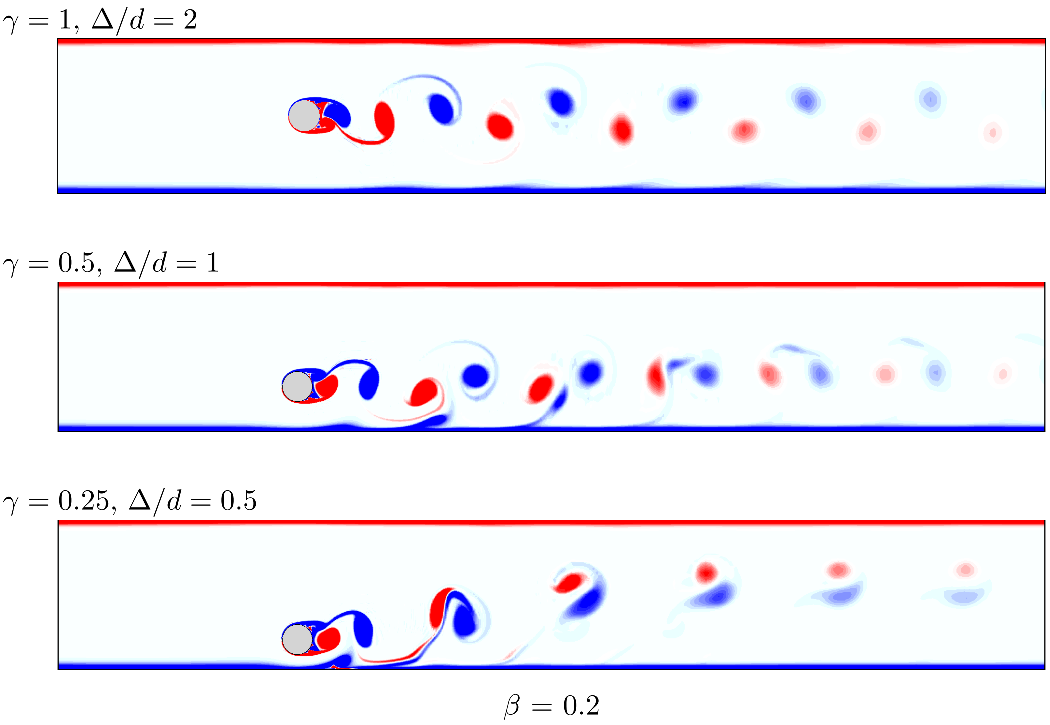

FIGURE 5.4: Instantaneous vorticity contour plots at $Ha^{\star} = 50$, $Re = 2000$ and β of 0.2 for various gap ratios γ. 20 contour level are displayed between $-2 \leq \omega \leq 2$, with red and blue contours representing negative and positive vorticity, respectively.

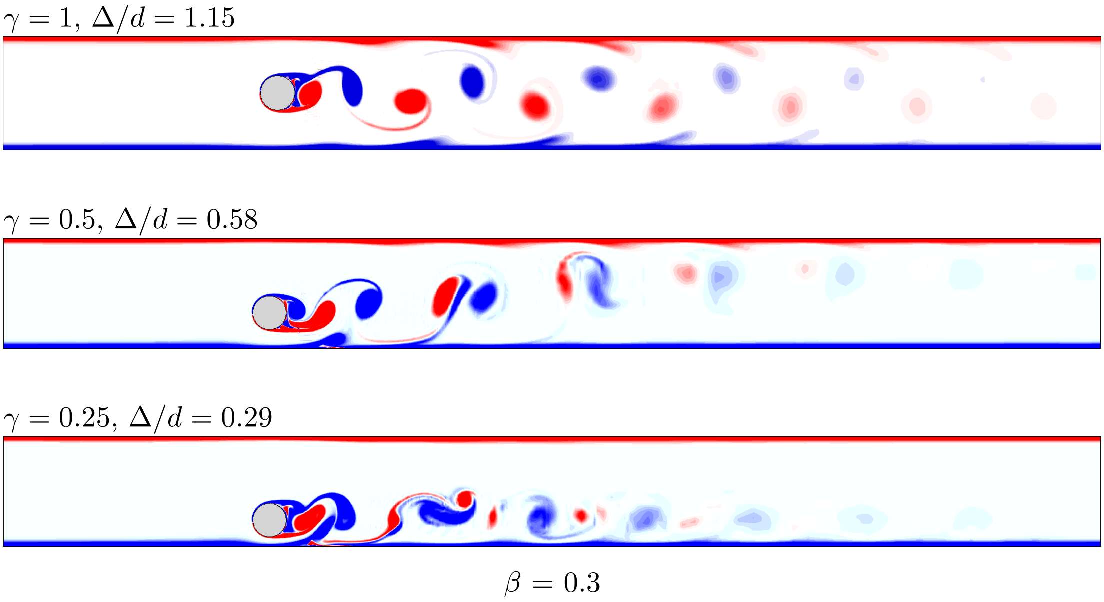

FIGURE 5.5: Instantaneous vorticity contour plots at $Ha^{\star} = 50$, $Re = 2000$ and β of 0.3 for various gap ratios γ. 20 contour level are displayed between $-2 \leq \omega \leq 2$, with red and blue contours representing negative and positive vorticity, respectively.

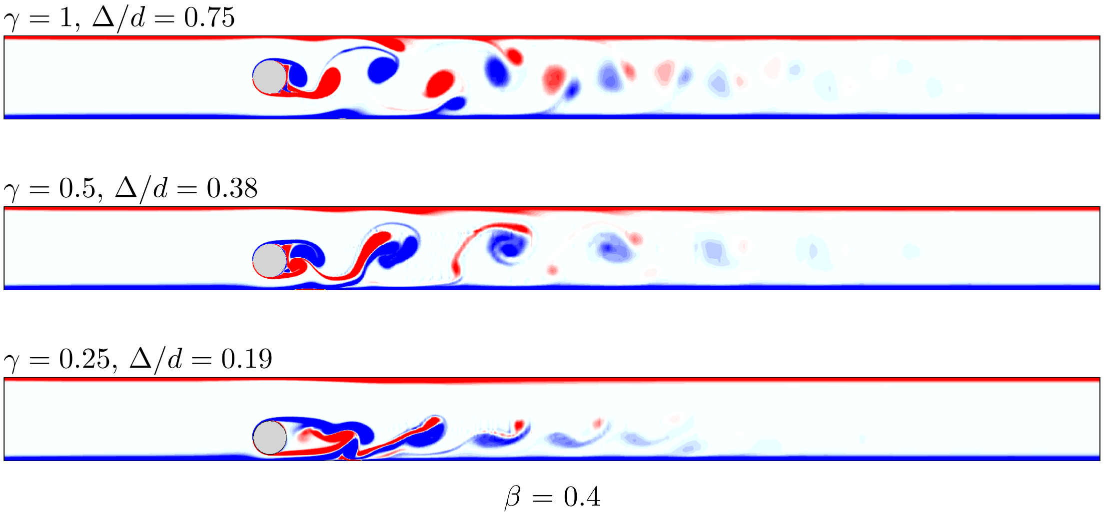

FIGURE 5.6: Instantaneous vorticity contour plots at $Ha^{\star} = 50$, $Re = 2000$ and β of 0.4 for various gap ratios γ. 20 contour level are displayed between $-2 \leq \omega \leq 2$, with red and blue contours representing negative and positive vorticity, respectively.

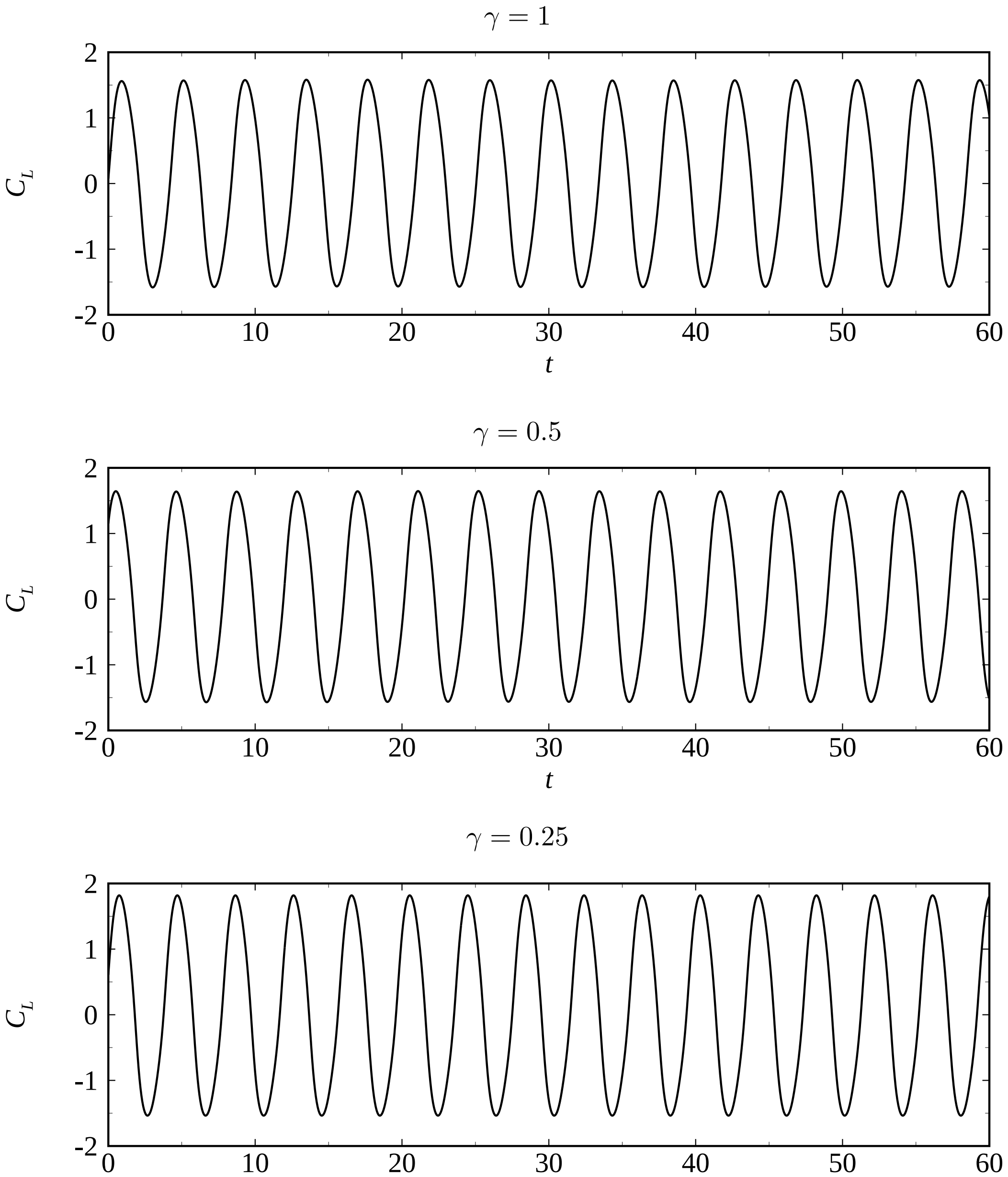

$\beta = 0.1$

FIGURE 5.7: Time history of lift force coefficient at different gap ratios for a blockage ratio of 0.1, Hartmann numbers $Ha^{\star} = 50$ and $Re = 2000$.

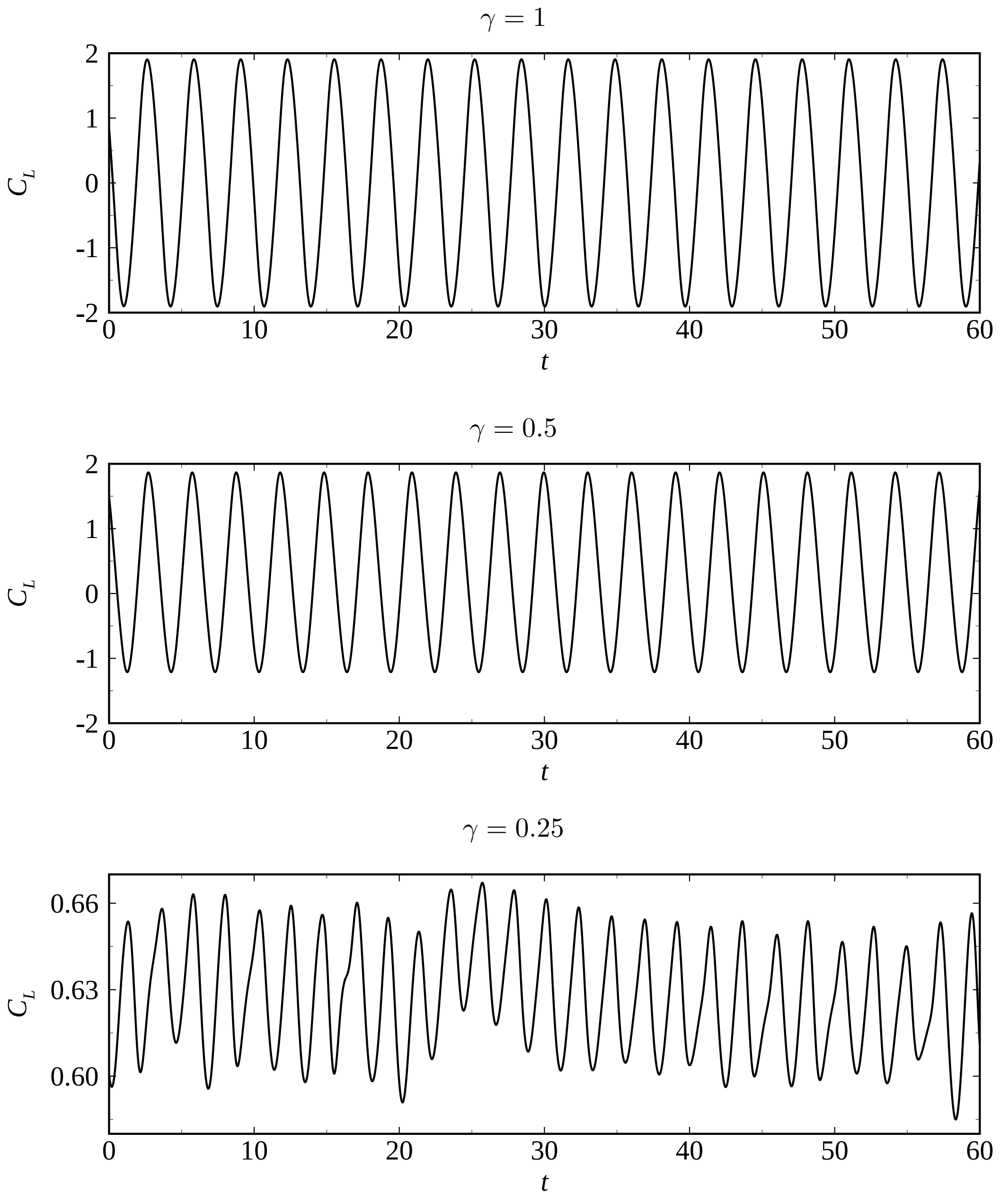

$\beta = 0.4$

FIGURE 5.8: Time history of lift force coefficient at different gap ratios for a blockage ratio of (a) 0.1 and (b) 0.4 at Hartmann number $Ha^{\star} = 50$ and $Re = 2000$.

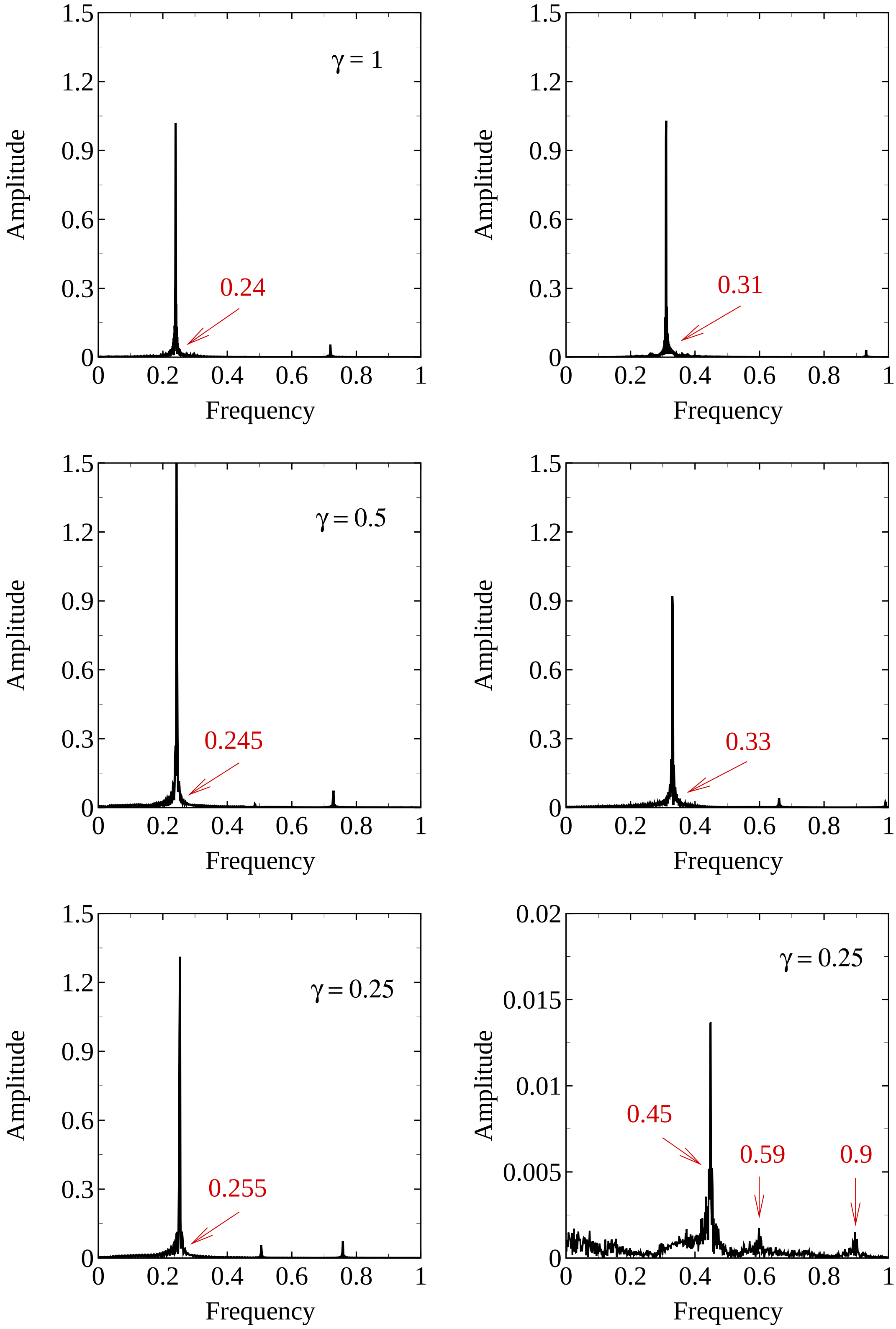

(a) $\beta = 0.1$

(b) $\beta = 0.4$

FIGURE 5.9: Fourier spectra of lift coefficient signal for $Re = 2000$ and $Ha^{\star} = 50$ at different gap blockage ratios. (a) $\beta = 0.1$ and (b) $\beta = 0.4$.

ratios. For example, at $\beta = 0.4$ and $\gamma = 0.25$ the Strouhal frequency is almost twice that at $\beta = 0.1$.

5.2.3 Drag Coefficient

Figs. 5.10 and 5.11 present the effect of gap ratio on the time-averaged drag coefficient C_D for different blockage ratios at $Ha^\star = 50$. It is clearly seen that for $\beta = 0.1$ and $Re \leq 2000$, as the cylinder approaches the lower confining wall, there is a small increase in C_D as γ decreases from 1 to 0.25. However, the change in C_D is negligible for $Re > 2000$ as γ is decreased. For $\beta = 0.2$, C_D increases gradually at low Reynolds numbers but it does not change for $Re \geq 2500$. For $\beta \geq 0.3$, the effect of decreasing γ on C_D is more pronounced at low Reynolds numbers and high blockage ratios. For example at $\beta = 0.1$ and $Re = 1000$, the increase in C_D as γ decreases from 1 to 0.25 is 6.15%, whereas at $\beta = 0.4$ the increase in C_D is 15.5%. Also, for high blockage ratios at $Re \gtrsim 2200$, C_D decreases with further increasing of the gap ratio. This is due to the fact that when the cylinder moves closer to the lower wall (i.e. small γ), the gap between the cylinder and the wall is filled by the shear/boundary layers of the cylinder and the wall where viscous forces are dominant. In this case the contribution from the viscous force exerted on the cylinder outweighs the pressure force, resulting in a decrease in the total drag coefficient.

5.3 Heat Transfer

Firstly, the effect of blockage and gap ratio for a fixed value of Re is presented, and subsequently the dependence on Re is considered.

5.3.1 Mixing Induced by Vortex Shedding in the Gap Region

Figs. 5.12–5.15 show the distribution of instantaneous temperature contours for different blockage ratios for gap ratios $\gamma = 1$, 0.5 and 0.25 at $Re = 2000$ and $Ha^\star = 50$. These correspond to the instantaneous vorticity contours as shown in Fig 5.3–Fig 5.6. For blockage ratio $\beta \geq 0.2$, as the gap ratio increases, the heat

(a) $\beta = 0.1$

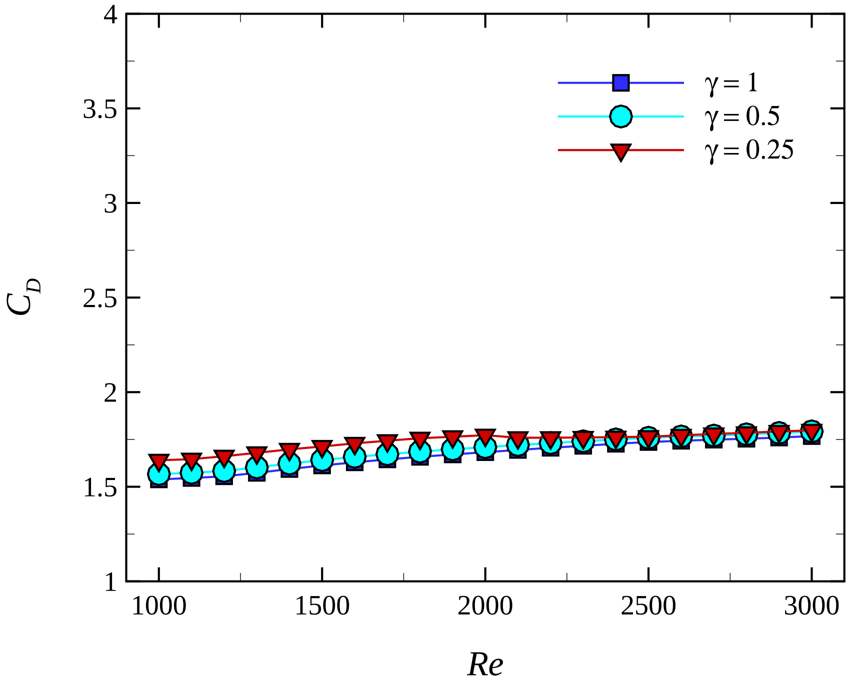

(b) $\beta = 0.2$

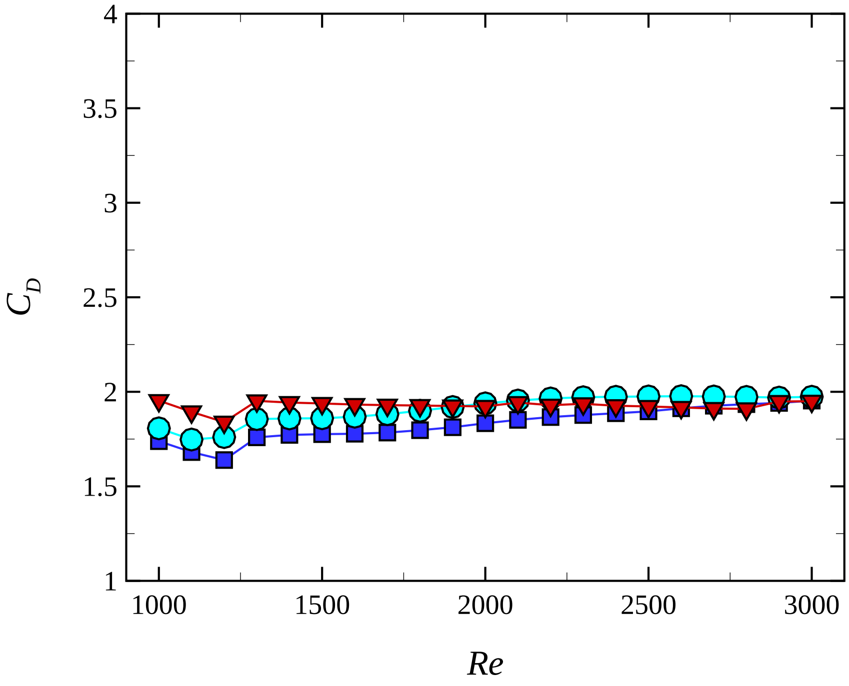

FIGURE 5.10: Time-averaged drag coefficients as a function of Reynolds number at different gap ratios, $Ha^{\star} = 50$ and blockage ratios (a) $\beta = 0.1$ and (b) $\beta = 0.2$.

(a) $\beta = 0.3$

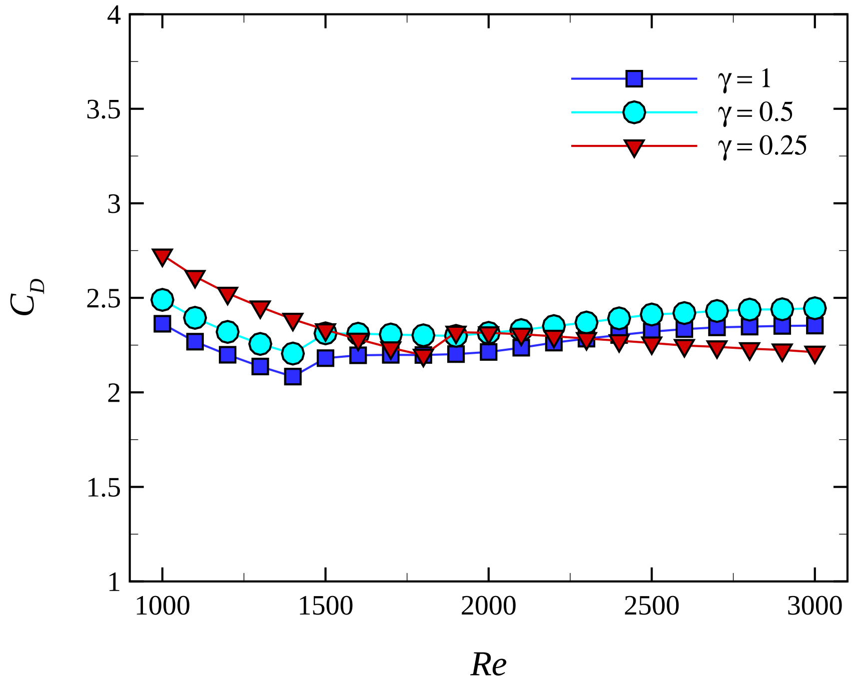

(b) $\beta = 0.4$

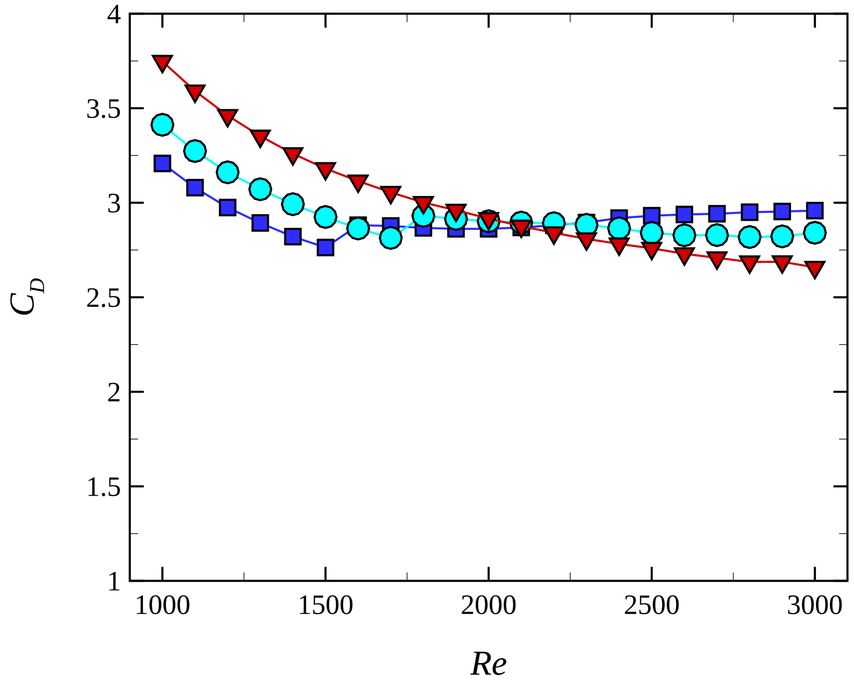

FIGURE 5.11: Time-averaged drag coefficients as a function of Reynolds number at different gap ratios, $Ha^{\star} = 50$ and blockage ratios (a) $\beta = 0.3$ and (b) $\beta = 0.4$.

$\gamma = 1,\ \Delta/d = 4.5$

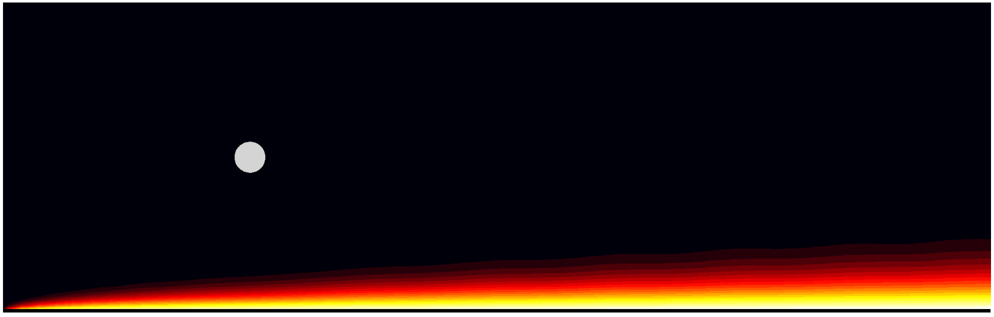

$\gamma = 0.5,\ \Delta/d = 2.25$

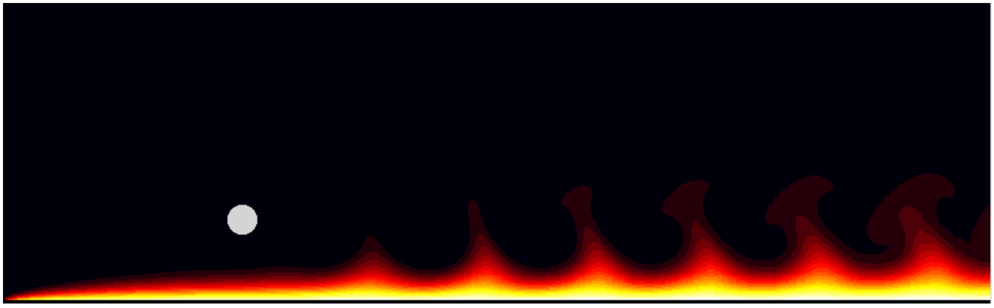

$\gamma = 0.25,\ \Delta/d = 1.13$

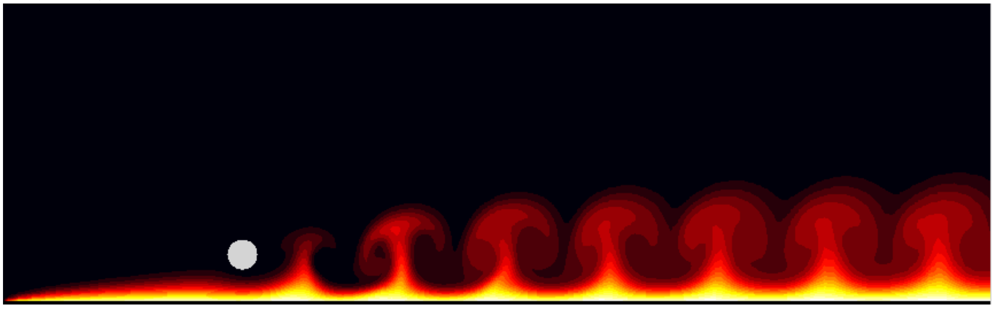

$\beta = 0.1$

FIGURE 5.12: Instantaneous dimensionless temperature contours at $Ha^{\star} = 50$, $Re = 2000$ and β of 0.1 for various gap ratios γ as marked. Light and dark shedding shows hot and cold fluid, respectively.

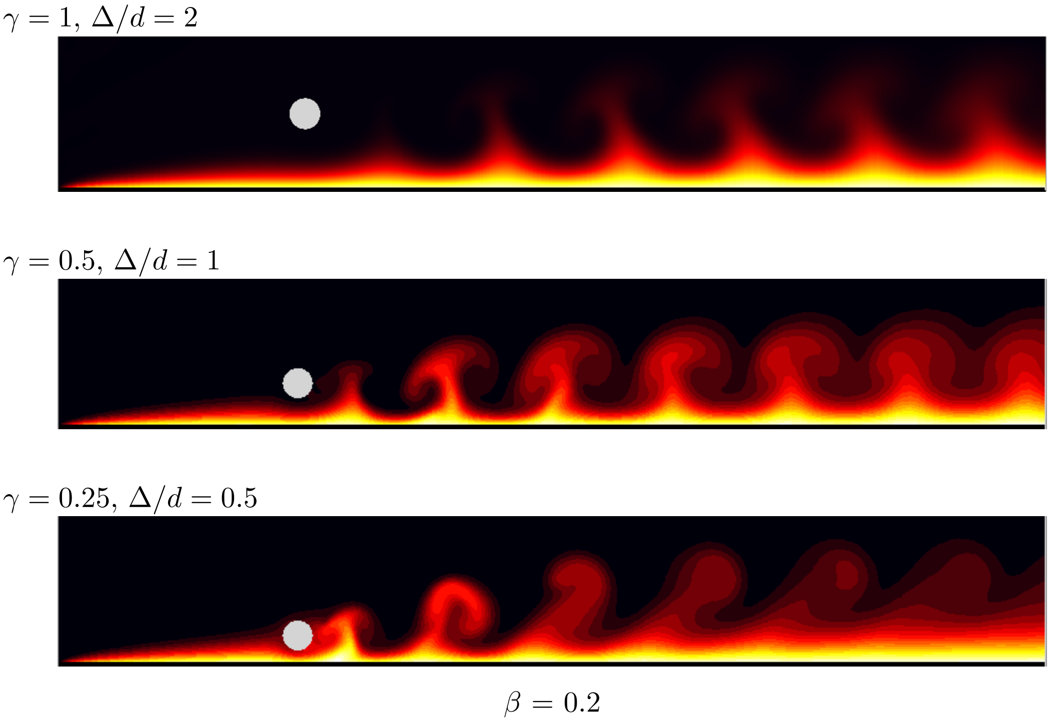

FIGURE 5.13: Instantaneous dimensionless temperature contours at $Ha^{\star} = 50$, $Re = 2000$ and β of 0.2 for various gap ratios γ as marked. Light and dark contours show hot and cold fluid, respectively.

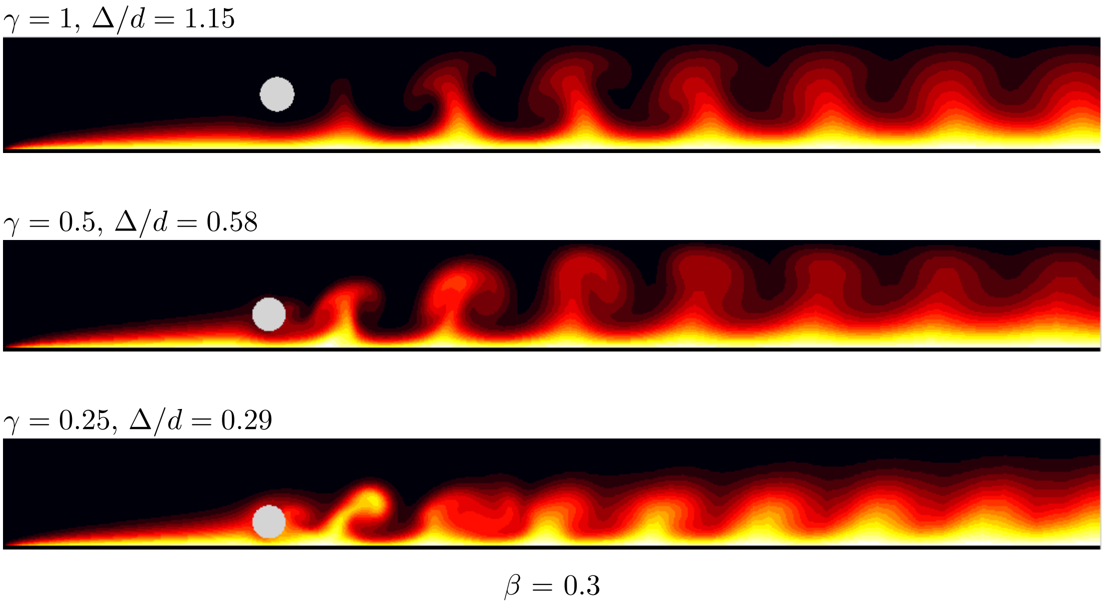

$\gamma = 1,\ \Delta/d = 1.15$

$\gamma = 0.5,\ \Delta/d = 0.58$

$\gamma = 0.25,\ \Delta/d = 0.29$

$\beta = 0.3$

FIGURE 5.14: Instantaneous dimensionless temperature contours at $Ha^{\star} = 50$, $Re = 2000$ and β of 0.3 for various gap ratios γ as marked. Light and dark contours show hot and cold fluid, respectively.

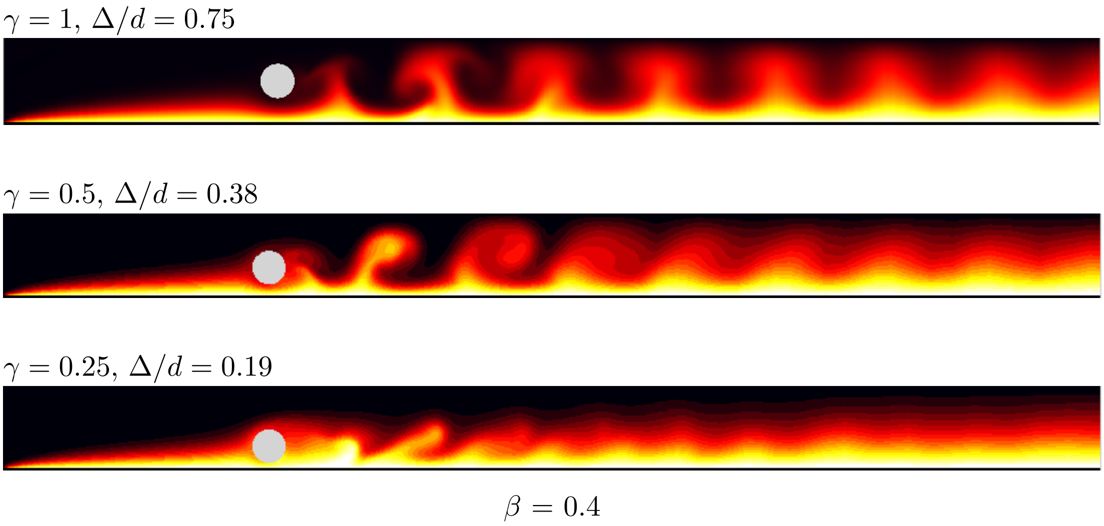

$\gamma = 1,\ \Delta/d = 0.75$

$\gamma = 0.5,\ \Delta/d = 0.38$

$\gamma = 0.25,\ \Delta/d = 0.19$

$\beta = 0.4$

FIGURE 5.15: Instantaneous dimensionless temperature contours at $Ha^{\star} = 50$, $Re = 2000$ and β of 0.4 for various gap ratios γ as marked. Light and dark contours show hot and cold fluid, respectively.

transfer increases significantly. This is due to the sweeping of the heating surfaces by the wake vortices. Therefore, the low-temperature fluid is transported towards the lower wall of the channel and the high-temperature fluid near the heated wall is convected away to mix with the low-temperature fluid. Accordingly, the heat transfer is enhanced significantly. However, as the gap ratio is decreased to $\gamma = 0.25$, the unsteadiness in the flow is reduced significantly for $\beta \geq 0.4$. This increases the thickness of the thermal boundary layer, and hence the temperature gradient along the heated wall decreases markedly.

5.3.2 Average Nusselt Number of the Heated Wall: Offset Ratio Dependence

Fig. 5.16(a) shows the effect of the offset ratio on the time-averaged Nusselt number from the heated wall at different blockage ratios β for $Ha^\star = 50$ and $Re = 2000$. It can be noted that for a given blockage ratio, there is a remarkable change in Nu as the offset ratio varies from $\gamma = 1$ to 0.25. The change is more pronounced at $\beta = 0.1$ and 0.4. For blockage ratio $\beta = 0.1$, the Nusselt number increases substantially as offset ratio is decreased from $\gamma = 1$ to 0.25. Similarly, the effect of changing the offset ratio from $\gamma = 1$ to 0.5 on Nu is found to be remarkable for $\beta = 0.2$. It increases significantly, then it decreases gradually for further decrease in the gap ratio. For $\beta = 0.3$, there is a slight increase in heat transfer as γ is decreases to 0.5, after that it gradually decreases. As expected, for blockage ratio $\beta = 0.4$, the Nusselt number drops more steeply as offset ratio is further decreased to $\gamma = 0.25$.

The variation of pressure drop with the offset ratio for different blockage ratios at $Re = 2000$ and $Ha^\star = 50$ is presented in Fig. 5.16(b). Here, the pressure drop penalty is the difference in pressure drop across identical channels with and without a cylinder placed asymmetrically in the duct. For $\beta \leq 0.2$, there is only a small increase in pressure drop as the offset ratio is changed from 1 to 0.5, then it remain steady for further increase in γ. However, for $\beta \geq 0.3$, the pressure drop increased gradually as it changes from 1 to 0.5. The pressure drop exhibits an increased dependence on offset ratio as the blockage ratio increases, with increasing offset ratio resulting in an increased pressure drop. To demonstrate the significant effect of γ on ΔP_{cyl}, the pressure drop at $\beta = 0.4$ is nearly 8.6 times that at $\beta = 0.1$ as γ changes from 1 to 0.25. For $\beta = 0.3$ and 0.2, it increases by factors 5.5 and 2, respectively.

In order to estimate the improvement of the heat transfer by placing a cylinder asymmetrically in the duct, the percentage increment of the overall heat transfer is calculated using equation (3.68) for the flow considered in this study. The percentage increment for $Re = 2000$ at $\gamma = 1$, 0.5 and 0.25 for $0.1 \leq \beta \leq 0.4$ varies between 3% – 45%, 22% – 39%, 62% – 68% and 43% – 89%, respectively. For $Re = 3000$, the increments lie in the ranges 8% – 58%, 24% – 70%, 70% – 85% and 60% – 128%, respectively.

To characterize the quality of heat transfer improvement in this study, both the heat transfer and the pressure drop on the channel are considered. The efficiency index is adopted (Tsui *et al.* 2000; Yang 2003) and defined as

$$\eta_{\text{eff}} = \frac{HR}{PR}, \tag{5.1}$$

where HR and PR are the heat transfer enhancement ratio and pressure penalty ratio, respectively. Note that HR and PR are given by

$$HR = \frac{Nu}{Nu_0}, \tag{5.2}$$

$$PR = \frac{\Delta P}{\Delta P_0}, \tag{5.3}$$

where ΔP is the overall pressure drop across the channel where a circular cylinder is shifted from the channel centerline and ΔP_0 is the overall pressure drop without a cylinder. The results of percentage heat transfer increments HI, heat transfer enhancement ratio HR, pressure penalty ratio PR and efficiency index η_{eff} for different blockage and offset ratios are listed in Table 5.2. The results in this table demonstrate that the improvements in heat transfer are much higher at small blockage ratios, but they are not as great when the cylinder approaches the heated wall (small gap ratio) as it is when the cylinder is located at the mid-plane. It is also noticed from this table that the efficiency index η_{eff} is greater

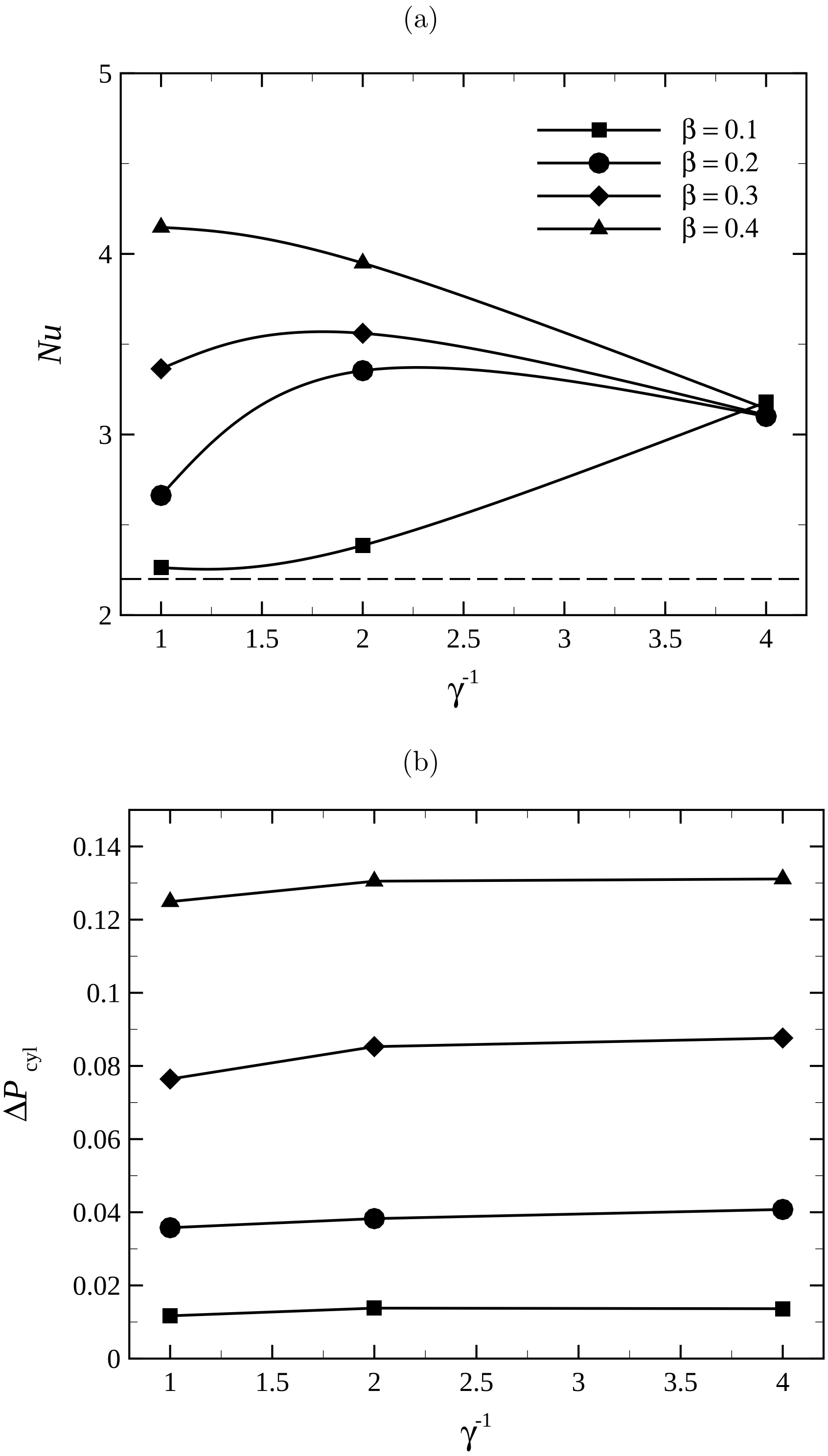

FIGURE 5.16: (a) Time-averaged Nusselt number of the heated wall and (b) pressure drop penalty plotted against γ^{-1} at blockage ratios as indicated for $Re = 2000$ and $Ha^{\star} = 50$. For reference, Nusselt number for the channel without a cylinder present are also provided and indicated as a dash line.

Re	β	γ	HI	HR	PR	η_{eff}
2000	0.1	1	3%	1.03	1.04	0.99
2000	0.1	0.5	9%	1.08	1.04	1.04
2000	0.1	0.25	45%*	1.45	1.04	1.39*
2000	0.2	1	22%	1.21	1.05	1.15
2000	0.2	0.5	53%*	1.52	1.06	1.44*
2000	0.2	0.25	39%	1.41	1.06	1.33
2000	0.3	1	67%	1.53	1.08	1.42
2000	0.3	0.5	62%	1.62	1.09	1.49*
2000	0.3	0.25	68%*	1.41	1.09	1.30
2000	0.4	1	89%*	1.89	1.09	1.72*
2000	0.4	0.5	80%	1.80	1.10	1.63
2000	0.4	0.25	43%	1.43	1.10	1.30
3000	0.1	1	8%	1.05	1.06	0.99
3000	0.1	0.5	14%	1.12	1.10	1.02
3000	0.1	0.25	58%*	1.55	1.08	1.43*
3000	0.2	1	24%	1.21	1.09	1.11
3000	0.2	0.5	70%*	1.67	1.08	1.55*
3000	0.2	0.25	52%	1.61	1.07	1.51
3000	0.3	1	70%	1.66	1.12	1.48
3000	0.3	0.5	85%*	1.82	1.15	1.58*
3000	0.3	0.25	79%	1.70	1.11	1.54
3000	0.4	1	128%*	2.24	1.16	1.94*
3000	0.4	0.5	83%	2.07	1.64	1.26
3000	0.4	0.25	60%	1.66	1.13	1.47

TABLE 5.2: Percentage increment of the overall heat transfer and efficiency index obtained by adding the cylinder at different gap ratios from the heated wall. Superscript $*$ shows the maximum values at each blockage ratio.

than 1 or nearly 1 for all the cases tested, which indicates that the heat transfer enhancement for this flow is viable.

In addition, to characterize the gain in heat transfer generated by placing the cylinder in the channel near to the wall with that at the centerline, the overall percentage increment in heat transfer is calculated as

$$HI_{\text{asym}} = \frac{Nu_{\text{asym}} - Nu_{\text{sym}}}{Nu_{\text{sym}}} \times 100, \tag{5.4}$$

where $Nu_{,\text{asym}}$ and Nu_{sym} represent the time-averaged Nusselt number of the heated surface for the cylinder placed symmetrically or asymmetrically in the duct. The effect of the gap ratio on heat transfer improvement is quite clear in Table 5.3 where the cylinder approaches the heated wall, higher heat transfer is

Re	β	γ	HI_{asym}
2000	0.1	0.5	5.45%
2000	0.1	0.25	40.5%*
2000	0.2	0.5	26%*
2000	0.2	0.25	16.5%
2000	0.3	0.5	5.85%*
2000	0.3	0.25	-7.65%
3000	0.4	0.5	-4.8%
3000	0.4	0.25	-24.5%
000	0.1	0.5	6%
3000	0.1	0.25	47%*
3000	0.2	0.5	37.5%*
3000	0.2	0.25	32.5%
3000	0.3	0.5	9.70%*
3000	0.3	0.25	2.58%
3000	0.4	0.5	-7.85%
3000	0.4	0.25	-26%

TABLE 5.3: Percentage increment of the overall heat transfer HI_{asym} obtained by adding the cylinder at different gap ratios from the heated wall. Superscript $*$ shows the maximum percentage increment at each blockage ratio.

obtained at small blockage ratio ($\beta \leq 0.2$). The reason for this increase may be attributed to the increased velocity of the flow in the vicinity of the heated surface caused by the wake vortices, which leads to an effective mixing between the hot region flow and core cold flow, leading to a significant increase in heat transfer. The maximum increment in heat transfer is 40.4%, which is obtained at $\gamma = 0.25$ for $\beta = 0.1$ and $Re = 2000$ while for $\beta = 0.2$, the maximum heat transfer improvement is occurres at $\gamma = 0.5$, and is 26%. For $Re = 3000$, the increments are 47% and 37.5%, respectively. From Table 5.3, it can be seen that the heat transfer improvement significantly decreases as the cylinder is further from the heated wall of the channel for blockage ratio $\beta \geq 0.3$.

5.3.3 Reynolds Number Dependence

Figs. 5.17 and 5.18 show the variation of time-averaged Nusselt number Nu of the heated wall with Reynolds number for different blockage and gap ratios at $Ha^{\star} = 50$. It is can be noted that for all Reynolds numbers considered in this study, the variation of the time-averaged Nusselt number shows different behaviour for different ranges of blockage and gap ratios, because the flow and the temperature field have different distributions depending on these two parameters. For $\beta = 0.1$ and $\gamma \leq 0.5$, there is a slight increase in Nu as the Reynolds number increases. However, it increases significantly at $\gamma = 0.25$. For $\beta = 0.2$, the effect of changing the gap ratio on Nu is negligible for $Re \leq 1300$. For the remaining range of Reynolds number, there is a considerable increase in Nu as γ varies between 1 and 0.5. However, as the gap ratio is further decreased to 0.25, Nu declines substantially for $Re \geq 2100$. Similarly, for $\beta \geq 0.3$, the effect of changing the gap ratio on Nu is negligible for the range $Re \lesssim 1500$. In fact, for $\beta = 0.3$, there is a gradual decrease in Nu as γ varies between 0.5 and 0.25 for $Re \geq 2000$. The decrease in Nu is more pronounced at $\beta = 0.4$ as γ is increased.

5.3.4 Streamwise Distribution of Local Nusselt Number

The local Nusselt number along the heated wall as a function of streamwise coordinate x with Reynolds number is given in Figs. 5.19–5.22 for $\gamma = 1$, 0.5 and 0.25, and $Ha^{\star} = 50$ at different blockage ratios. For small blockage ratio ($\beta = 0.1$), the effect of Reynolds number is found to be small for $\gamma = 1$ and 0.5. The distribution reaches a maximum at $x/d = 5$ and falls gradually at $\gamma = 0.25$. Similarly, at $\beta = 0.2$, the variation of local Nusselt number is small at $\gamma = 1$. The maximum occurs at $x/d = 5$ for $\gamma = 0.5$ and $\gamma = 0.25$, then the Nusselt number decreases steadily. However, as the blockage ratio increases further from 0.2 to 0.4, the change in the distribution of Nu_w is considerable with changing Reynolds number. For $\beta = 0.3$, the distribution reaches a maximum at $x/d = 5$ and falls noticeably as γ and Reynolds number increase. However, for $\beta = 0.4$, the maximum position shifts to $x/d \approx 8.5$, as Reynolds number increases for $\gamma = 1$, which is quite different from the other cases. The plots also demonstrate that the distribution of local Nusselt number maintains its shape for $\beta \leq 0.2$ at high gap ratio. For high blockage ratio, the distribution is identical, but the position of the maximum Nusselt number shifts downstream as Reynolds number increases at high gap ratio. As expected, the local Nusselt number is seen to have higher values with an increase in the Reynolds number and blockage ratio.

(a) $\beta = 0.1$

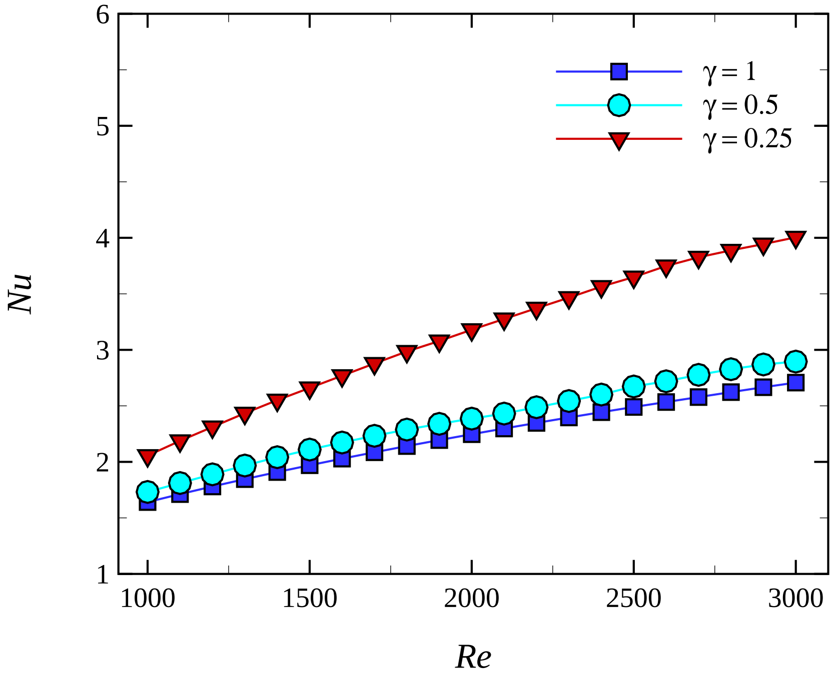

(b) $\beta = 0.2$

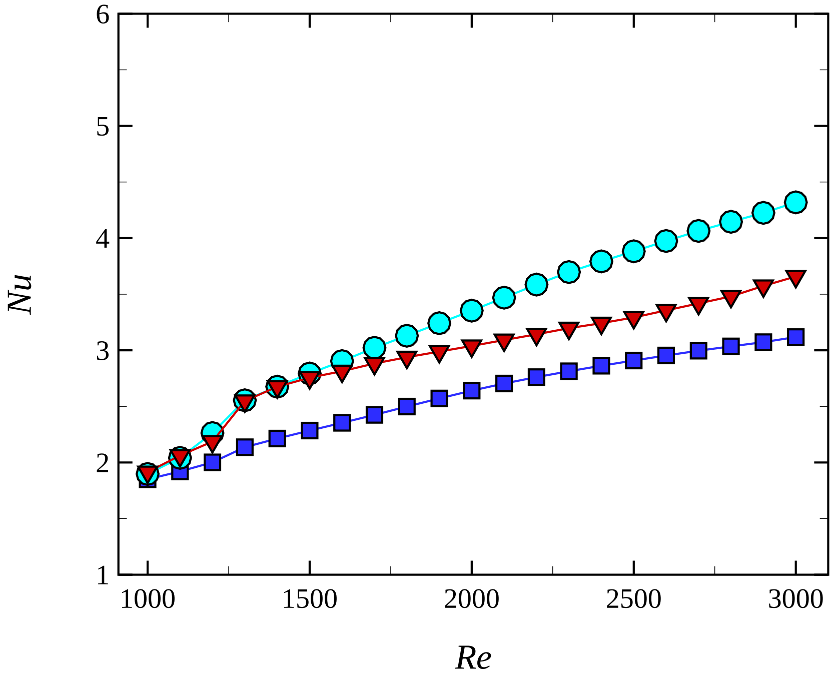

FIGURE 5.17: Variation of time-averaged Nusselt number with Rynolds number for different gap ratio at $Ha^{\star} = 50$ and blockage ratios (a) $\beta = 0.1$ and (b) $\beta = 0.2$.

(a) $\beta = 0.3$

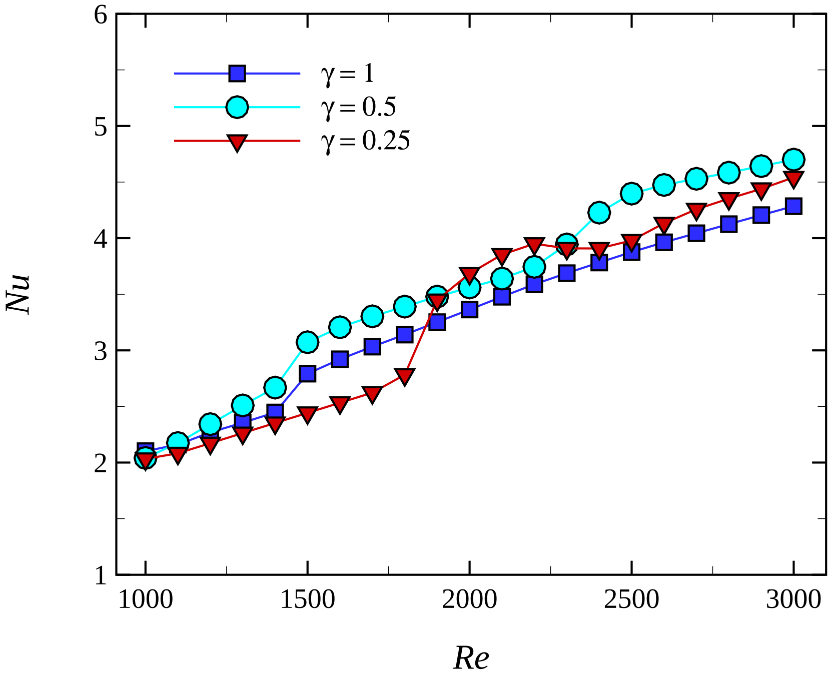

(b) $\beta = 0.4$

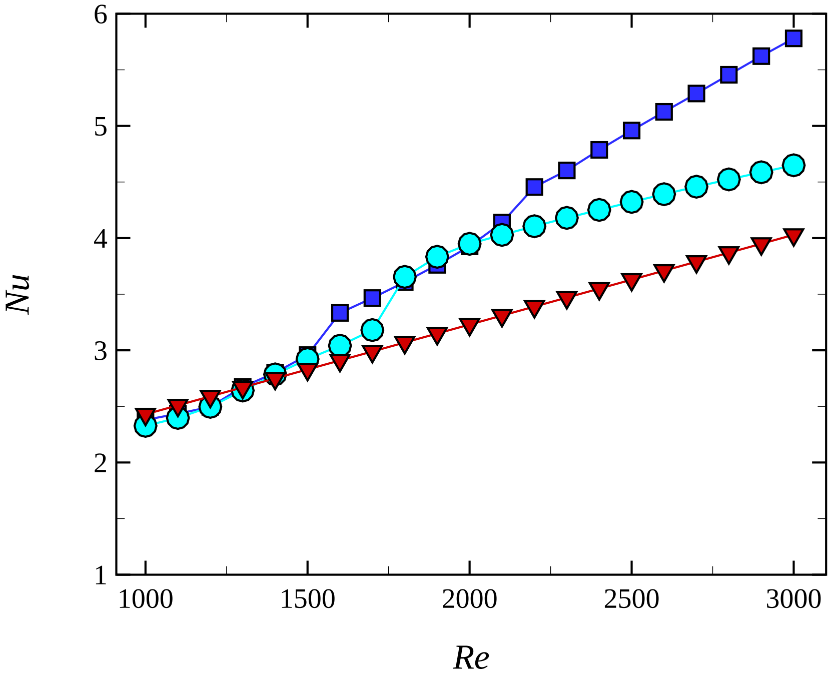

FIGURE 5.18: Variation of time-averaged Nusselt number with Rynolds number for different gap ratio at $Ha^{\star} = 50$ and blockage ratios (a) $\beta = 0.3$ and (b) $\beta = 0.4$.

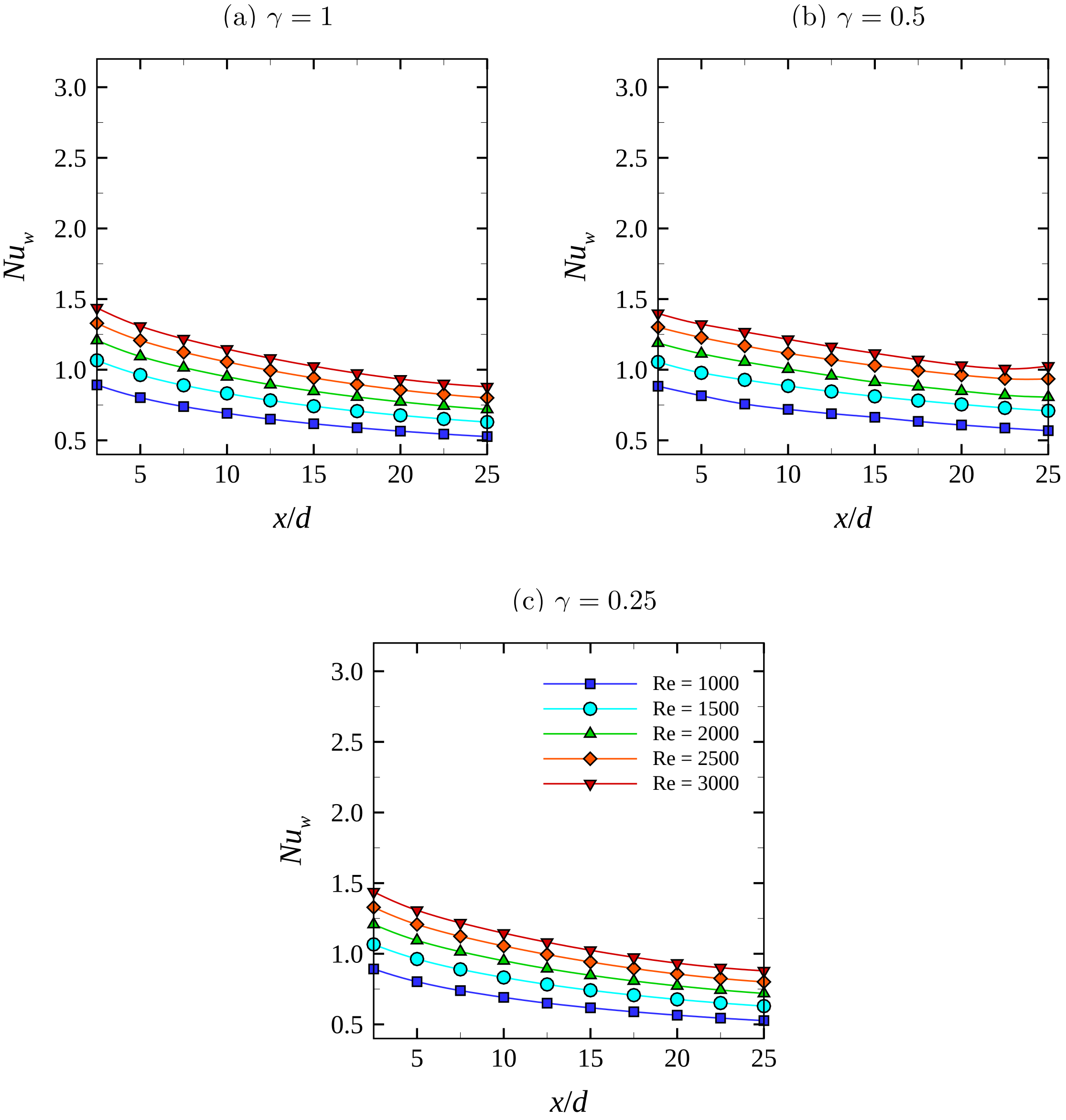

(a) $\gamma = 1$

(b) $\gamma = 0.5$

(c) $\gamma = 0.25$

FIGURE 5.19: Streamwise time-averaged local Nusselt number over the heated surface of the side wall for $Ha^{\star} = 50$, $\beta = 0.1$ at different Reynolds numbers and gap ratios as indicated.

(a) $\gamma = 1$ (b) $\gamma = 0.5$

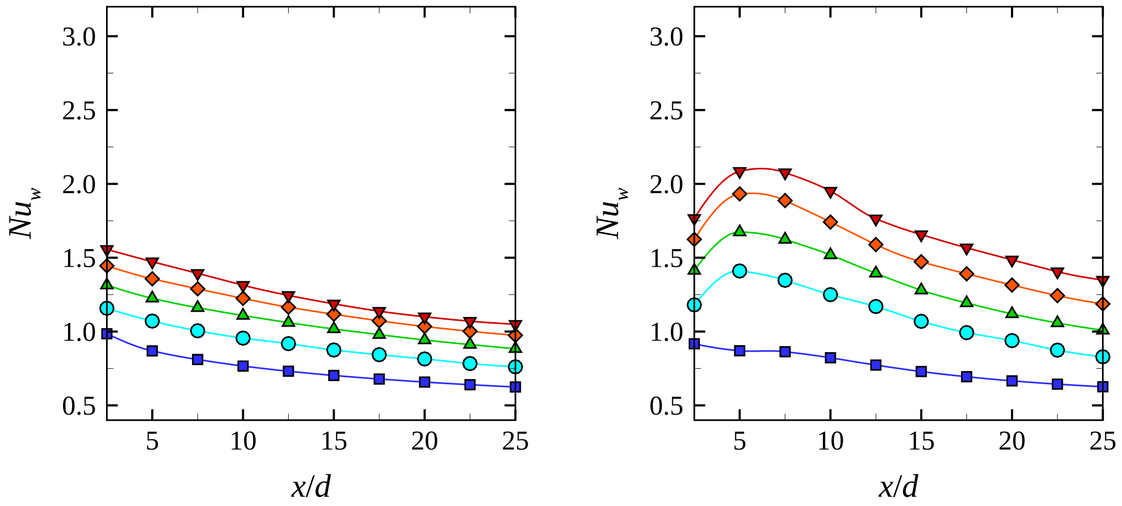

(c) $\gamma = 0.25$

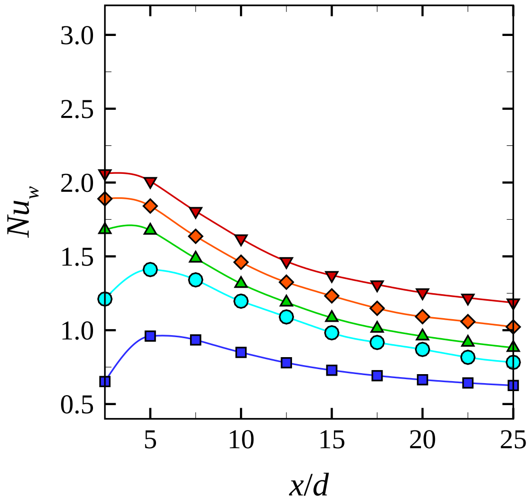

FIGURE 5.20: Streamwise time-averaged local Nusselt number over the heated surface of the side wall for $Ha^{\star} = 50$, $\beta = 0.2$ at different Reynolds numbers and gap ratios as indicated. Symbols as per Figs. 5.19.

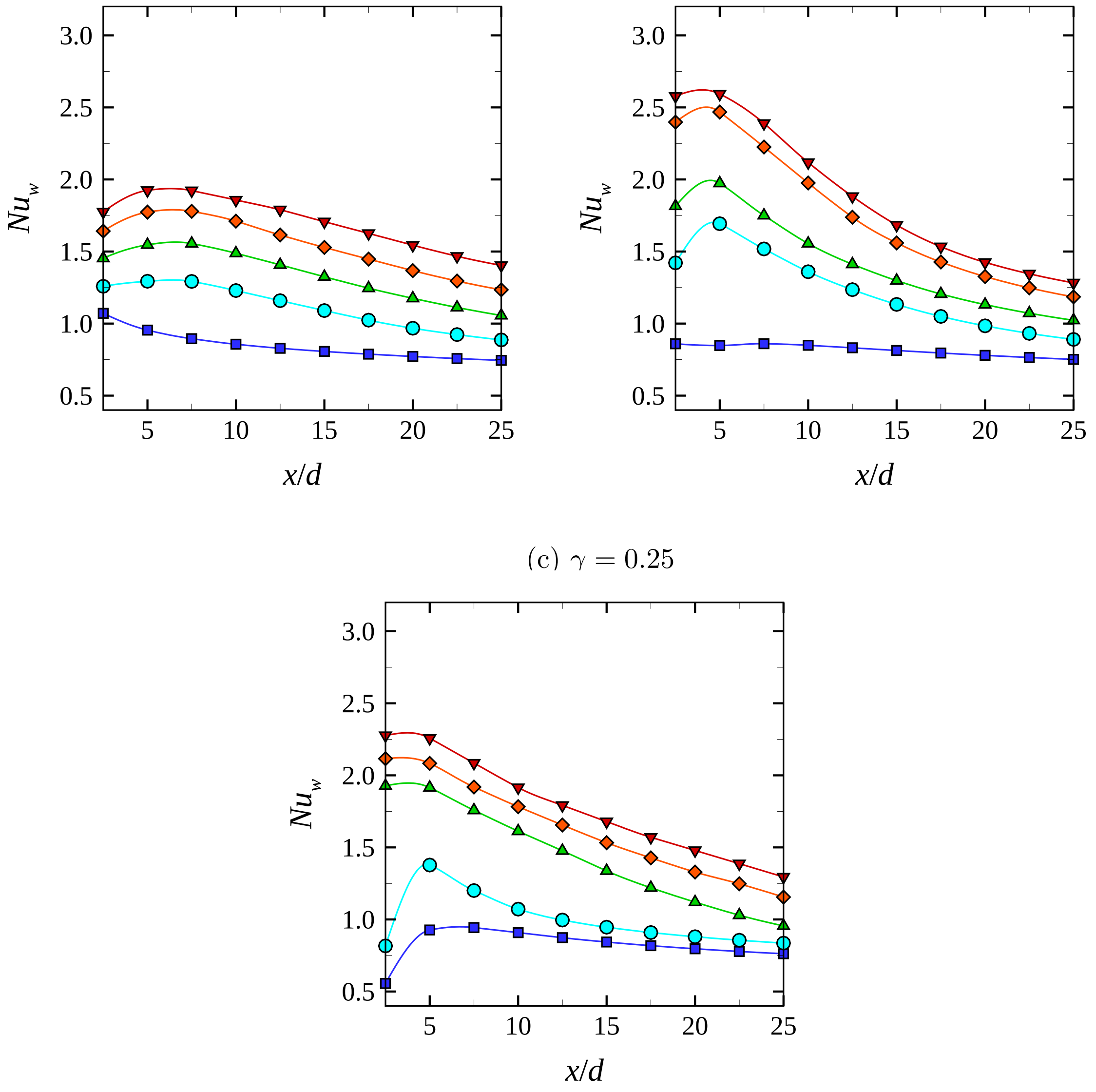

(a) $\gamma = 1$

(b) $\gamma = 0.5$

(c) $\gamma = 0.25$

FIGURE 5.21: Streamwise time-averaged local Nusselt number over the heated surface of the side wall for $Ha^\star = 50$, $\beta = 0.3$ at different Reynolds numbers and gap ratios as indicated. Symbols as per Figs. 5.19.

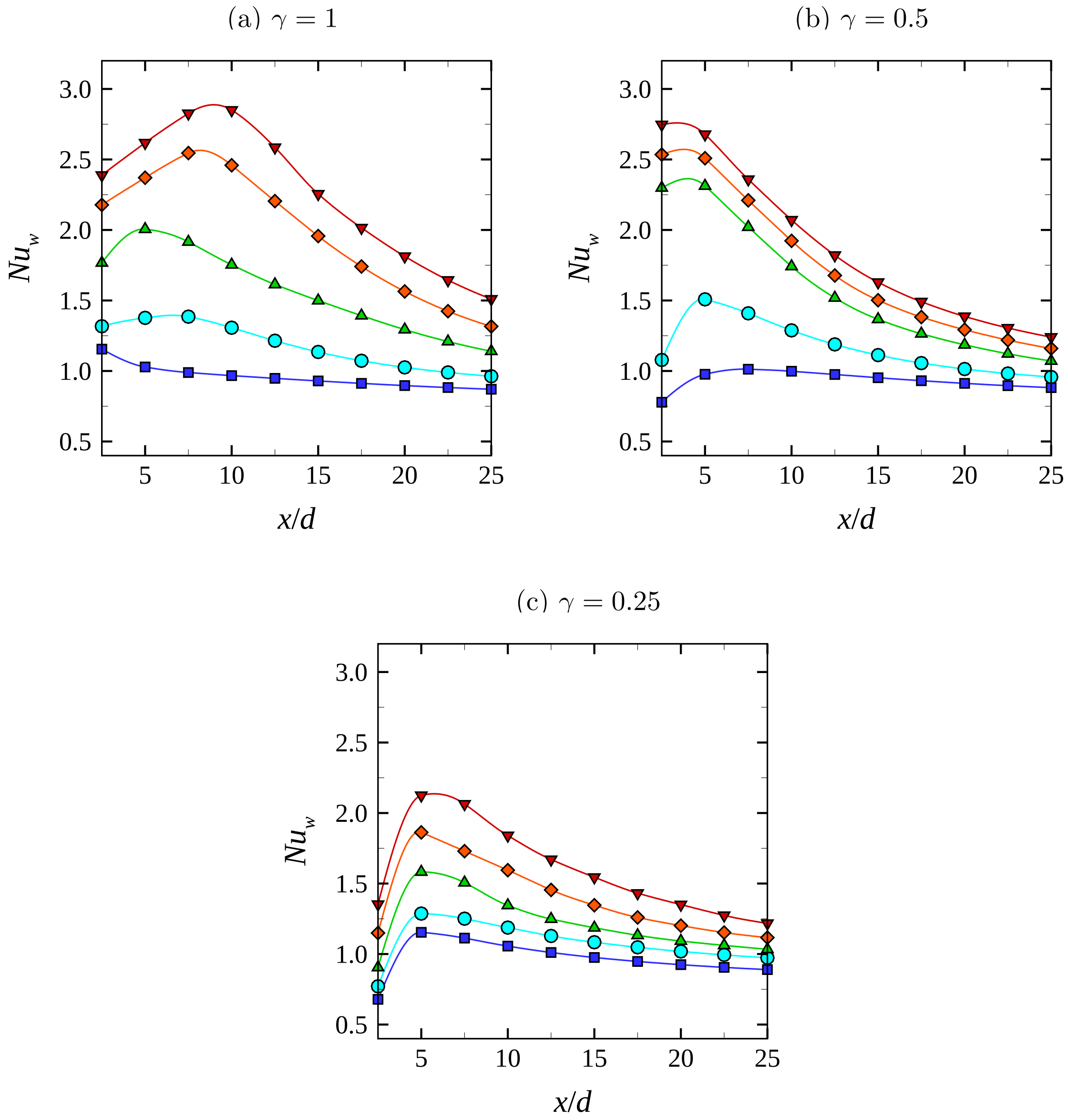
(a) $\gamma = 1$

(b) $\gamma = 0.5$

(c) $\gamma = 0.25$

FIGURE 5.22: Streamwise time-averaged local Nusselt number over the heated surface of the side wall for $Ha^\star = 50$, $\beta = 0.4$ at different Reynolds numbers and gap ratios as indicated. Symbols as per Figs. 5.19.

5.4 Chapter Summary

This chapter was dedicated to investigate the details of fluid flow and heat transfer of liquid metal past a circular cylinder positioned offset from the duct centreline under a strong axial magnetic field. As before, under these conditions the flow is quasi-two-dimensional and the modified Navier–Stokes equations are formulated in a two–dimensional domain.

New numerical meshes have been developed that model a range of blockage and gap ratios. The details of domain size and grid-resolution studies have been presented.

The proximity of the cylinder to a wall has a significant influence on the flow and heat transfer characteristics. At $Re = 2000$, $\beta = 0.1$ and $0.25 \leq \gamma \leq 1$, a two-row vortex street is formed with clockwise negative and counter-clockwise positive vortices shed from the top and the bottom shear layers of cylinder maintaining their offsets from the centreline. For $\beta \geq 0.2$, the structure of the vortex shedding changes dramatically on further decreasing of gap ratio. The vortex street drifts further away from the wall and convects downstream with long slow decay. For high blockage ratios at $\gamma \geq 0.5$, the separating shear layer from the lower side of the cylinder and the boundary layer from the wall effectively merge before combined structures travel further downstream. At the smallest gap ratio, the wake vorticity on the upper side of the cylinder elongates as it travels downstream due to the effect of the wall. It is expected that the instability in the wake region should transform from being absolutely unstable at large gaps to convectively unstable at small gaps, which is consistent with the previous findings for non-magnetohydrodynamic bluff body flows.

For all gap ratios at $\beta \leq 0.3$, it is found that lift coefficient oscillates regularly with a large amplitude, which is correlated with the existence of periodic vortex shedding from the cylinder. At the gap ratio $\gamma = 0.25$ for $\beta = 0.4$, the reduction and the irregularity of the fluctuating lift signal is consistent with vortex formation further downstream from the rear of the cylinder and development of irregularity in the wake.

For $\beta \leq 0.2$, the effect of changing γ from 1 to 0.25 on C_D was found to be small for $Re \leq 2000$ and it was negligible for $Re > 2000$. For $\beta \geq 0.3$, there was a significant change in C_D at low and high Reynolds numbers.

The characteristics of heat transfer depend strongly on the proximity of the cylinder to the heated wall. This is due to interaction of the boundary layer with the shear layers separating from the cylinder surface. For small blockage ratios, it increases significantly as the gap ratio decreases from 1 to 0.25. However, there is a substantial drop in Nusselt number for high blockage ratio. Overall, the enhancement of heat transfer was significantly augmented by 58% through decreasing the gap ratio for small blockage ratio (i.e. when the cylinder is close to the wall). In contrast, for $\beta = 0.4$, the maximum heat transfer augmentation was more than twofold, which is found at $\gamma = 1$ (i.e. when the cylinder is placed furthest from the walls.) The efficiency index η_{eff} was greater than 1 or nearly 1 for all the cases teste, which demonstrates that the heat transfer enhancement for this flow is viable. The maximum gain in heat transfer generated by placing the cylinder in the channel near to the wall with that at the centerline was obtained at $\beta = 0.1$ as the cylinder is further approached the heated wall.

The magnitude of the local Nusselt number distribution increases proportionally with Reynolds number and blockage ratio. The position where the each distribution exhibits a maximum value is independent of Reynolds number for small blockage ratios at $\gamma = 0.5$ and 0.25. However, the position moves downstream with increasing Reynolds number for $\beta = 0.4$ at $\gamma = 1$.

Chapter 6

Optimal Transient Disturbances Leading to Vortex Shedding

This chapter presents the role of linear transient growth in the subcritical regime, below the onset of von Kármán vortex shedding, and its consequences on the transition to unsteady flow. More specifically, while the base flow is linearly stable, perturbations may exhibit significant transient growth before eventual decay .

The critical Reynolds number for the transition to unsteady flow, Re_c, in the presence of magnetic fields can be very large; an understanding of the non-normal growth properties of the flow may enable unsteady flow to be triggered at lower Reynolds numbers using only low level forcing. It is unknown how the addition of a cylinder into an MHD duct flow influences the transient response of the flow, and whether this may be exploited to further enhance heat transfer.

Firstly, a brief description of the geometry and boundary conditions together with details of the grid-resolution study is given in § 6.1. The Hartmann number dependence on the optimal growth is presented in § 6.2.1. In the following section, the structure and the evolution of the disturbance field are considered in § 6.2.3. The Reynolds number dependence on the optimal growth is given in § 6.2.6. Finally, the response of the flow to continuous upstream disturbances is presented in § 6.3.

Some of the results in this chapter have previously been published in Hussam *et al.* (2012).

6.1 Geometry and Boundary Conditions

The configuration of the system under investigation is a rectangular duct confining a circular cylinder placed at the centre of the duct parallel to the magnetic field and perpendicular to the flow direction, as presented previously in Fig. 4.1.

The boundary conditions are imposed on equations (3.62) and (3.61) as the same for the previous chapters. For the transient growth analysis, zero-velocity Dirichlet boundary conditions are imposed on the perturbation field on all boundaries during integration of the forward and adjoint equations as recommended by Blackburn *et al.* (2008a).

The computational domain is divided into a grid of elements. Elements are concentrated in areas of the domain that experience high velocity gradients. The meshes comprise between 1052 and 1484 elements, depending on blockage ratio, and details of meshes can be found in § 4.2.1. The upstream and downstream lengths x_u and x_d chosen for this study are 8 and 25, respectively, as determined by the domain size study below. The dependence of energy growth on upstream domain length is determined through the calculation of energy growth for a fixed time span of $\tau = 6$. Tables 6.1 and 6.2 show the effect of truncating the domain upstream length while keeping the downstream length and the inner portion of the mesh constant. For each blockage ratio, two Reynolds numbers are considered to ensure that the mesh chosen is adequate to resolve the solution in the subcritical range. For $\beta = 0.1$ and $Ha^{\star} = 50$, $Re = 200$ and 580 are considered, and for $\beta = 0.4$ and $Ha^{\star} = 50$, $Re = 400$ and 1160 are considered. It can be noted that the effect of truncating the upstream length from $32d$ to $8d$ results in less than a 3% difference in the growth rate prediction for the four cases in Tables 6.1 and 6.2. As might be expected higher Reynolds number increases the error, while increasing the Hartmann number decreases the error.

As before, a grid resolution study was undertaken to determine a suitably accurate element polynomial degree. The polynomial degree used for most simulations was $N_p = 7$. Convergence tests were performed on two cases, again chosen at the upper end of the parameter range of this study. The first case featured

	$\beta=0.1,\ Re=200$		$\beta=0.1,\ Re=580$	
x_u	$G(6)$	$\%Error$	$G(6)$	$\%Error$
4	8.9665E-02	5.912	1.4353E+03	21.6
8	8.5021E-02	0.427	1.2150E+03	2.93
16	8.4665E-02	0.0065	1.1858E+03	0.469
32	8.4660E-02	0.0000	1.1803E+03	0.000

Table 6.1: The effect of variation of domain upstream length on growth energy at $\tau = 6$ across blockage $\beta = 0.1$ for $Ha^\star = 50$ for different Reynolds number as indicated.

	$\beta=0.4,\ Re=400$		$\beta=0.4,\ Re=1160$	
x_u	$G(6)$	$\%Error$	$G(6)$	$\%Error$
4	6.4643E-04	0.145	3.3138E+04	0.606
8	6.4737E-04	0.0004	3.3140E+04	0.599
16	6.4737E-04	0.0000	3.3313E+04	0.0825
32	6.4737E-04	0.0000	3.3340E+04	0.0000

Table 6.2: The effect of variation of domain upstream length on growth energy at $\tau = 6$ across blockage $\beta = 0.4$ for $Ha^\star = 50$ and different Reynolds number as indicated.

$\beta = 0.1$, $Ha = 120$ and $Re = 1000$, and the second featured $\beta = 0.4$, $Ha^\star = 480$ and $Re = 2000$. The results of these tests are shown in Table 6.3, which show convergence of the normalized length of the recirculation zone behind the cylinder (measured downstream from the aft surface of the cylinder), and the growth rate of the leading eigenmode from a linear stability analysis described in § 3.5. This shows that the differences in both the recirculation zone length and growth rate for $N_p = 7$ relative to the most highly resolved case ($N_P = 9$) are less than 1%.

6.2 Transient Energy Growth

Firstly, the results as a function of τ and Ha for a fixed value of Re at different blockage ratios β are presented, and subsequently the dependence on Re is considered.

	$\beta = 0.1, Re = 1000$		$\beta = 0.4, Re = 2000$	
N_p	L_R/D	σ	L_R/D	σ
5	1.511	-0.04991	0.721	-0.1053
6	1.552	-0.07281	0.724	-0.1287
7	1.549	-0.09185	0.725	-0.1572
8	1.526	-0.09122	0.725	-0.1579
9	1.532	-0.09136	0.725	-0.1584

TABLE 6.3: Convergence of the normalized circulation length L_R/d and maximum growth rate σ across blockage ratio $\beta = 0.1$ and $\beta = 0.4$ for $Ha = 1200$ with increasing polynomial order.

6.2.1 Hartmann Number Dependence on Optimal Growth

Figs. 6.1 and 6.2 show the transient energy growth G of optimal disturbances as a function of time interval τ for the steady base flow at four different blockage ratios covering $0.1 \leq \beta \leq 0.4$ at different Hartmann numbers and $Re = 400$. It also makes sense to define the critical parameter ratio $C_{Re} = (Re - Re_c)/Re_c$, since transient growth is relevant to critical Reynolds number. For blockage ratios $0.1 \leq \beta \leq 0.4$ and $50 \leq Ha^\star \leq 120$, this ratio ranges between -0.82 to -0.43. The initial observation on these data is, though the chosen Re for the analysis is well below the critical Reynolds number for unsteady flow at the lowest Hartmann number $Ha^\star = 50$, there exist perturbations which grow in energy by sometimes more than a thousand times. In addition, the significant damping effect of Hartmann number is also revealed. For example, for $\beta = 0.1$ the peak energy growth is 60.93 and 2.72 at $Ha^\star = 50$ and $Ha^\star = 120$, respectively. For $\beta = 0.4$, there is growth of energy by a factor of 1.86×10^3 and 7.22, respectively. For all β, it is found that increasing $Ha^\star$ leads to a significant reduction of the energy amplification of the disturbances and to a shift of the peak growth towards smaller times. This is not surprising given that the Hartmann term acts as an extra damping in addition to viscous damping. However, for a fixed modified Hartmann number, the global maxima of energy growth also varies significantly with blockage ratio, being larger at higher β, and the maximum amplification occurs for larger times. This is probably a result of the increased acceleration of the flow in the neighborhood of the cylinder for higher blockage ratios, making the Reynolds number effectively higher for higher β, although increasing β also shortens the separation bubble length as well.

6.2.2 Structure of Optimal Disturbance Fields

Fig. 6.3 plots the vorticity field of the optimal initial perturbations for the four blockages considered in this study (as presented in Figs. 6.1 and 6.2) at Hartmann numbers $Ha^\star = 50$ and 120. In each, the optimal disturbance field is localized in the region of the boundary layer separation around the cylinder near the wake as also observed in the analysis of Hill (1992); Giannetti & Luchini (2007) and Abdessemed *et al.* (2009b) for the case without a magnetic field ($Ha^\star = 0$). Perhaps not surprisingly, the structure of the disturbance is consistent across these blockage ratios. The perturbation convects along the separation region being amplified to the peak growth state downstream of the recirculation bubble. In Fig. 6.4, the resulting time interval for maximum growth, $\tau_{\max}$, is plotted as a function of the circulation length at $Ha^\star = 50$. It is observed that $\tau_{\max}$ increases significantly as circulation length increases. This is commensurate with the amplifying nature of the separated shear layers in the wake, as the disturbance travels further and grows larger as it convects down the longer wake. This phenomenon is consistent with transient growth in several systems, including a plane channel (Reddy *et al.* 1998), rectangular duct (Zikanov 1996), and abrupt geometrical expansion flows (Blackburn *et al.* 2008a,b; Cantwell *et al.* 2010).

6.2.3 Evolution of Optimal Disturbance Fields

Fig. 6.5(a, c) shows the vorticity of the initial perturbation for $\beta = 0.1$ at $Re = 400$, and $Ha^\star = 50$ and 1200, for which $\tau_{\max} = 5.54$ and 1.72, respectively. It can be seen that independent of Hartmann number, the optimal perturbation field remain concentrated around the limiting streamline identifying the recirculation bubble.

In Fig. 6.5(b, d), the evolution from this optimal initial disturbance is plotted, i.e. the disturbance that linearly evolves from these disturbances at $t = 5.54$ and

(a) $\beta = 0.1$

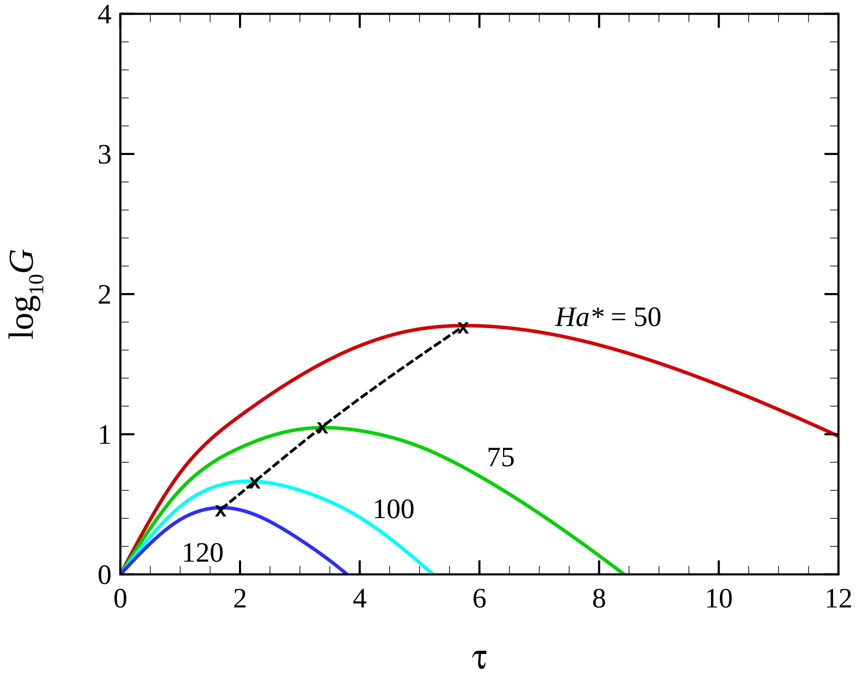

(b) $\beta = 0.2$

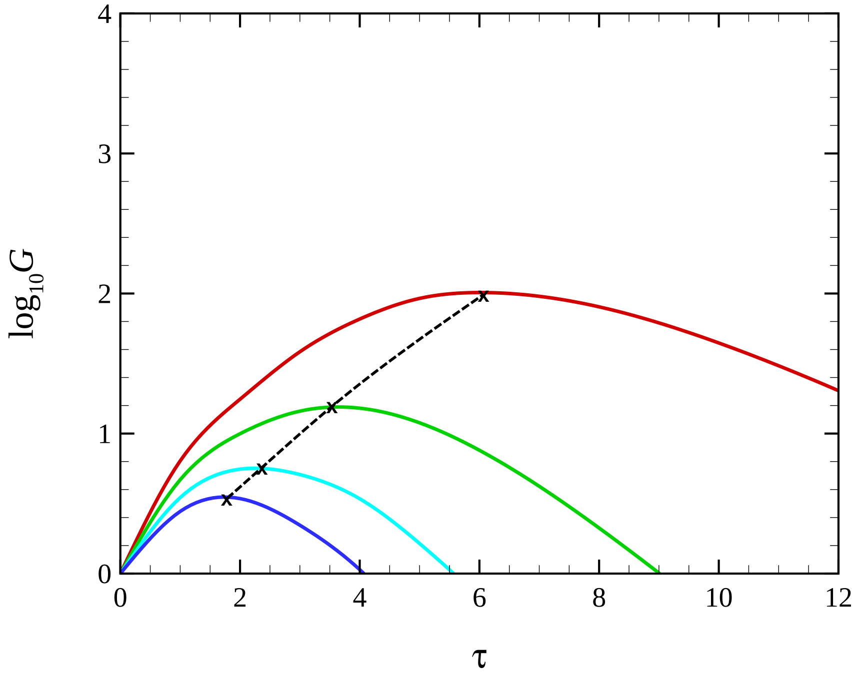

FIGURE 6.1: Plots of $\log_{10} G$ against τ, at blockage ratios 0.1 and 0.2 at different Hartmann numbers as shown for $Re = 400$. The dashed-line curves shows the locus of maximum growth as a function of τ.

(a) $\beta = 0.3$

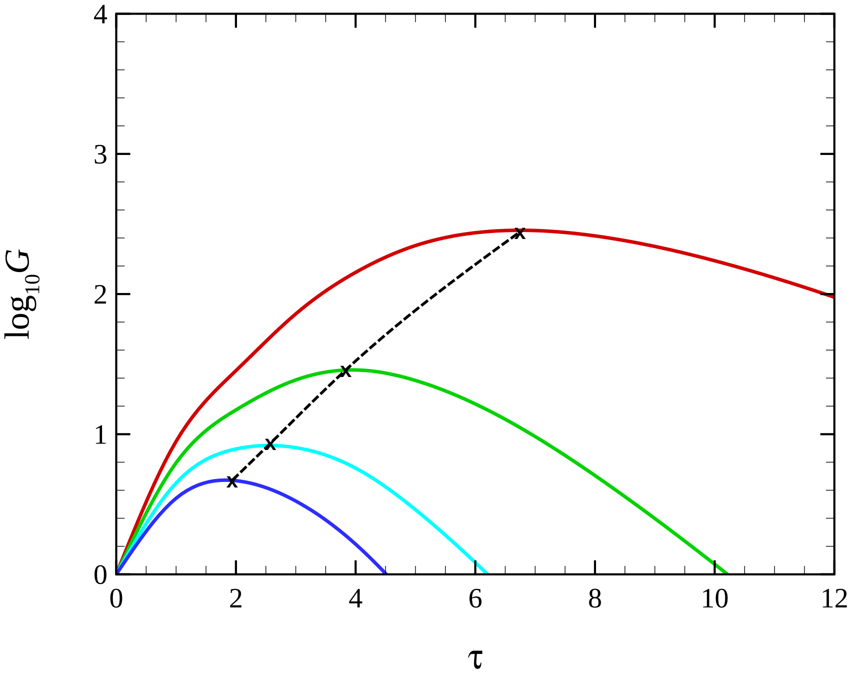

(b) $\beta = 0.4$

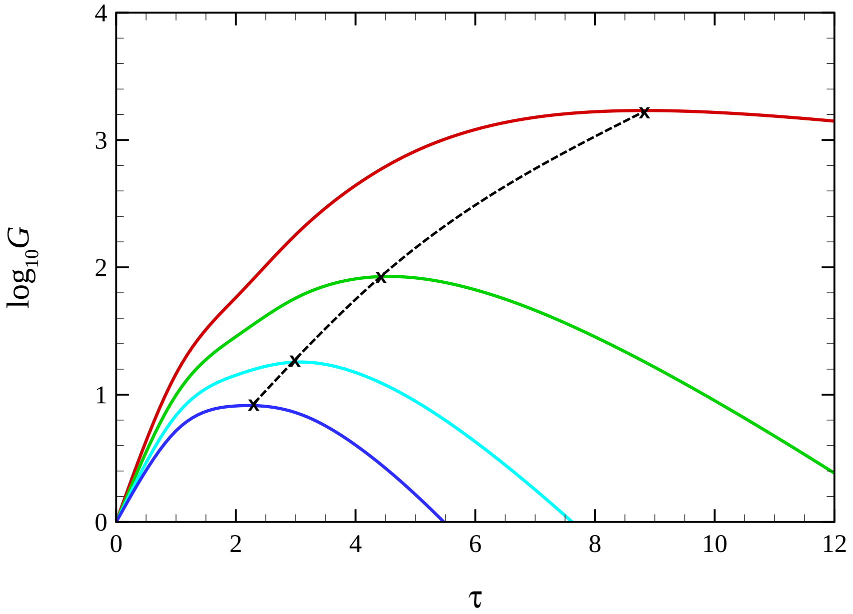

FIGURE 6.2: Plots of $\log_{10} G$ against τ, at blockage ratios 0.3 and 0.4 at and Hartmann numbers as shown for $Re = 400$. The dashed-line curves shows the locus of maximum growth as a function of τ.

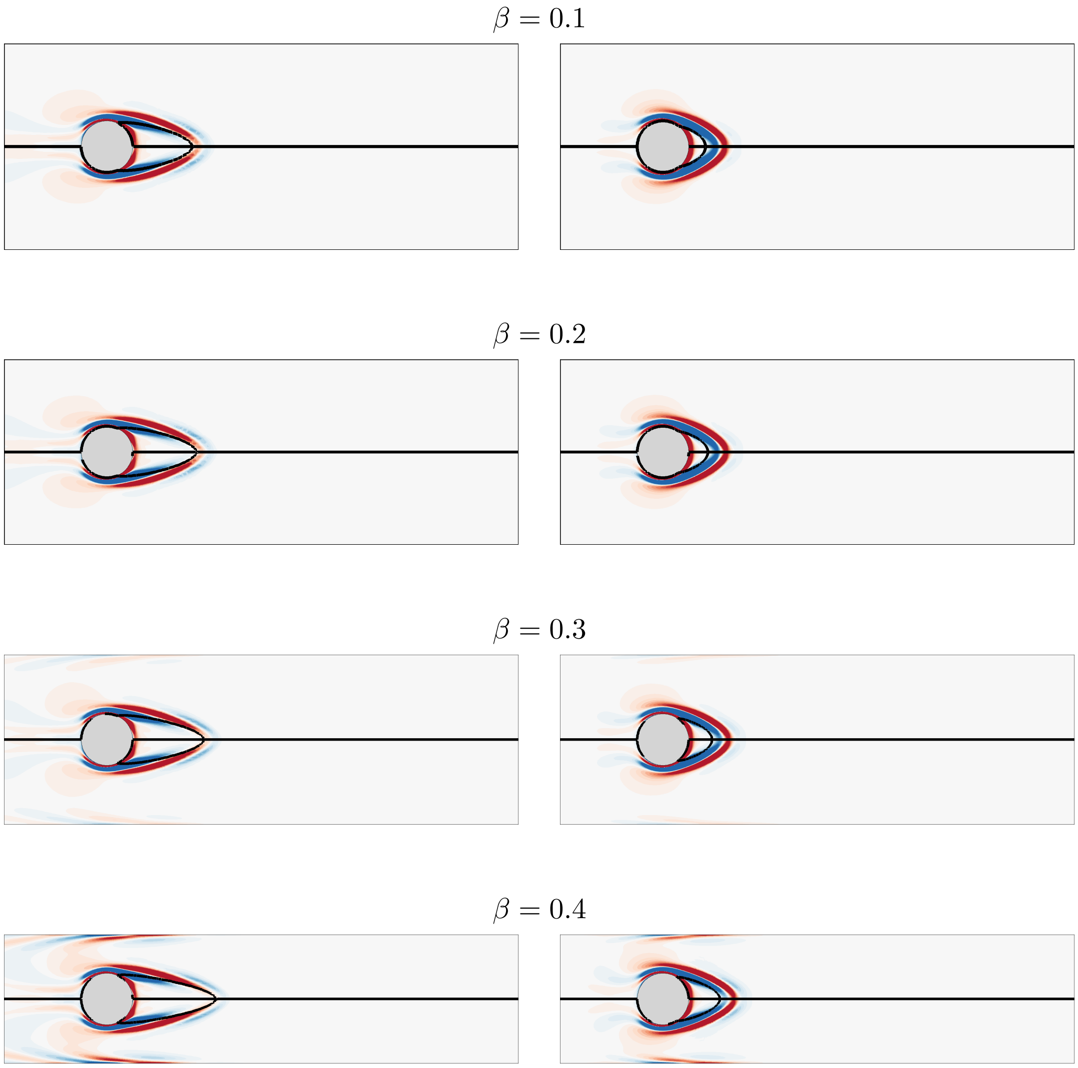

FIGURE 6.3: Plots of vorticity of the optimal initial perturbation at $\tau_{\max}$ and blockage ratios as labeled for $Re = 400$. Hartmann numbers $Ha^{\star} = 50$ (left) and 120 (right) are shown. The streamlines of the stable base flow is overlaid in each case.

$t = 1.72$. At the peak growth time, the disturbance flow structures present as a series of counter-rotating spanwise rollers. However, for $\beta = 0.4$, at $Ha = 500$ (see Fig. 6.6b), interaction with the channel wall boundary layers (the Shercliff layers) occurs downstream of the cylinder. Vorticity is drawn into the channel and interacts with the vorticity detached from the rear of the cylinder. The level of wall boundary layer disturbance was observed to increase significantly as the blockage ratio increased from $\beta = 0.1$ to 0.4. In fact, for $\beta \lesssim 0.2$ there were no strong perturbation structures observed along the walls.

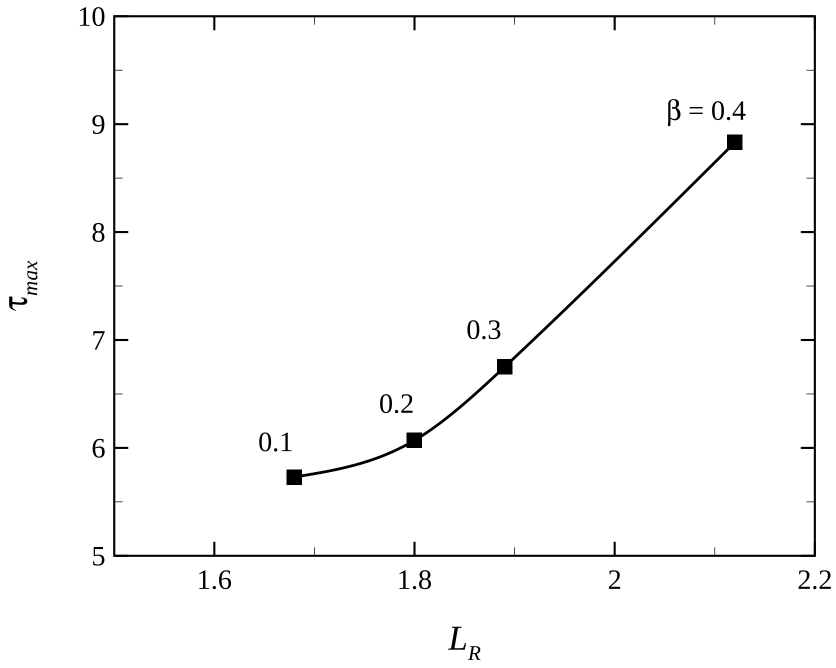

FIGURE 6.4: Maximum τ of the energy maxima at $Ha^\star = 50$ as a function of circulation length at different blockage ratios.

6.2.4 Characteristic of Optimal Perturbation Field

Consideration is now given to the time evolution of a predicted optimal disturbance from its initial condition, through to, and beyond, $\tau_{\max}$. Fig. 6.7 shows a sequence of perturbation vorticity contours that evolve from the optimal initial state at $\beta = 0.3$, $Re = 400$, $Ha^\star = 50$, and $\tau = 6.90$. At early times, the disturbance that passes through this region interacts with the boundary layer (the Shercliff layers) detached from the walls. Then, the wave packet is amplified while traveling downstream. The disturbances consist of a roller packet structure and the maximum rate of growth occurs at the beginning of the sequence when the perturbation passes through the separation bubble. This spatial pattern indicates that the energetic amplification of the perturbation is, at least initially, consistent with convective instability: the amplitude of maximum energy growth moves in a frame convecting with the disturbance, and the energy at the initial disturbance location decays as the disturbance convects away.

(a) $Ha^\star = 50$, $t = 0$

(b) $Ha^\star = 50$, $t = \tau_{\max} = 5.54$

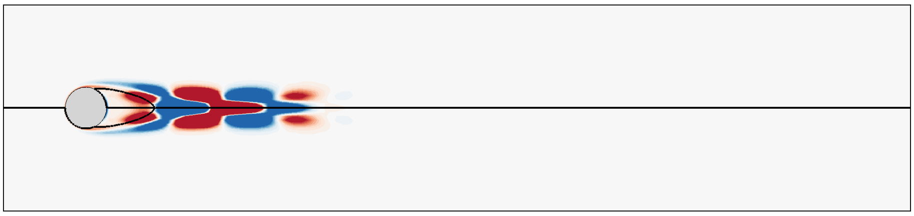

(c) $Ha^\star = 120$, $t = 0$

(d) $Ha^\star = 120$, $t = \tau_{\max} = 1.72$

FIGURE 6.5: Contours of spanwise vorticity for $\beta = 0.1$ and $Re = 400$. (a) and (c) show the optimal disturbance initial condition at $Ha^\star = 50$ and 120, respectively. (b) and (d) show the development of these linear disturbances to $t = \tau_{\max}$. Streamlines of the stable base flow are overlaid in each case. Vorticity contour levels of $|\omega| \leq 0.05$ are plotted in frames (a) and (c), and levels of $|\omega| \leq 0.5$ are plotted in frames (b) and (d).

(a) $Ha^\star = 50$, $t = 0$

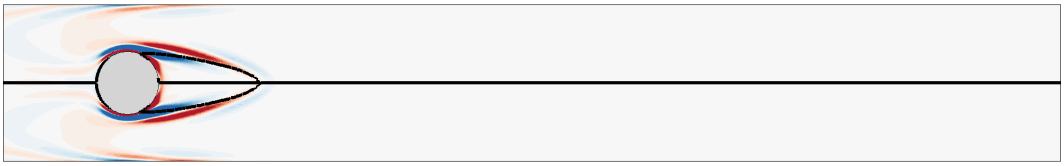

(b) $Ha^\star = 50$, $t = \tau_{\max} = 8.26$

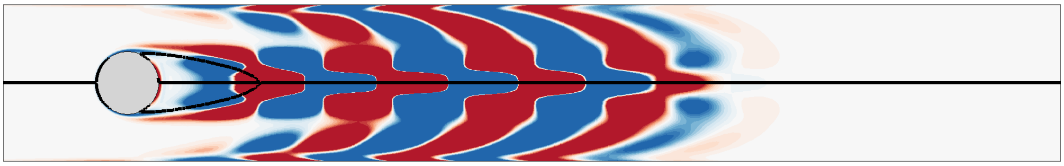

(c) $Ha^\star = 120$, $t = 0$

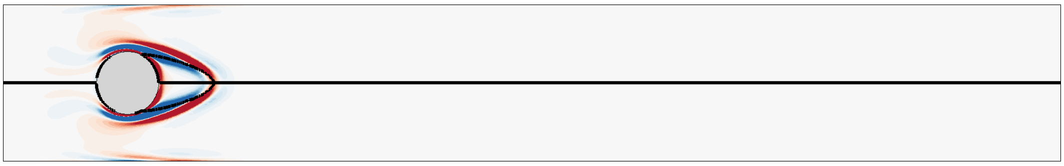

(d) $Ha^\star = 120$, $t = \tau_{\max} = 2.43$

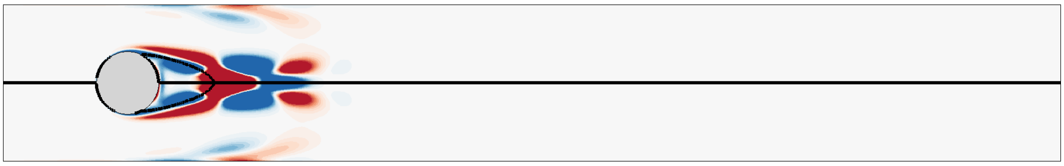

FIGURE 6.6: Contours of spanwise vorticity for $\beta = 0.4$ and $Re = 400$. (a) and (c) show the optimal disturbance initial condition at $Ha^\star = 50$ and 120, respectively. (b) and (d) show the development of these linear disturbances to $t = \tau_{\max}$. Contour levels are as per Fig. 6.5.

To illustrate this, Fig. 6.8 shows the profiles of the vertical velocity component that evolve from the optimal initial state for the case shown in Fig. 6.7. The vertical velocity component is extracted along the line $y = 0$. The profiles are normalized to have absolute maximum value of unity. Again the characteristic dynamics of convective instability are apparent. The initial disturbance decays as the disturbance convects away. The extremely sharp fluctuation in the optimal perturbation can be observed in the boundary layer separation near the wake. The average streamwise wavelength of the fluctuations of the vortical structures

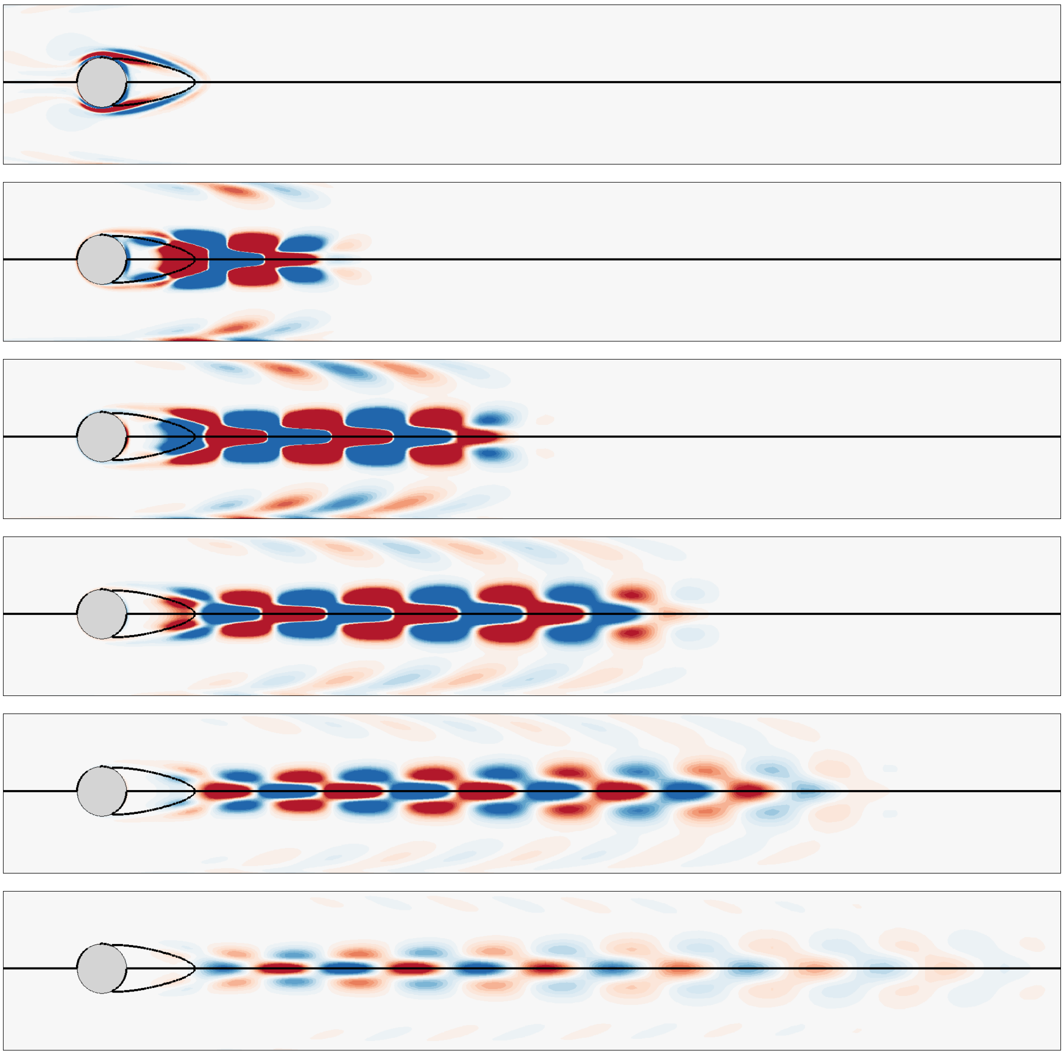

FIGURE 6.7: Time sequence of linear perturbation vorticity contours developed from the optimal disturbance initial condition for $\beta = 0.3$, $Re = 400$, and $Ha^{\star} = 50$ at $t = \tau_{\max}$. Flow from left to right. From top to bottom, frames show times $t = 0$, 4, 8, 12, 16 and 20. white and black representing positive and negative vorticity, respectively. Separation streamlines of the base flow are overlaid in each case.

leaving the circulation bubble at the optimal time estimated by zero-crossing analysis is $\lambda_x/d = 2.30$ and 2.59, at $Ha^{\star} = 50$ and 120, respectively. The characteristics of the optimal perturbation fields at the point of maximum growth for the case of $Ha^{\star} = 50$ and 120 at different blockage ratios are given in Table 6.4.

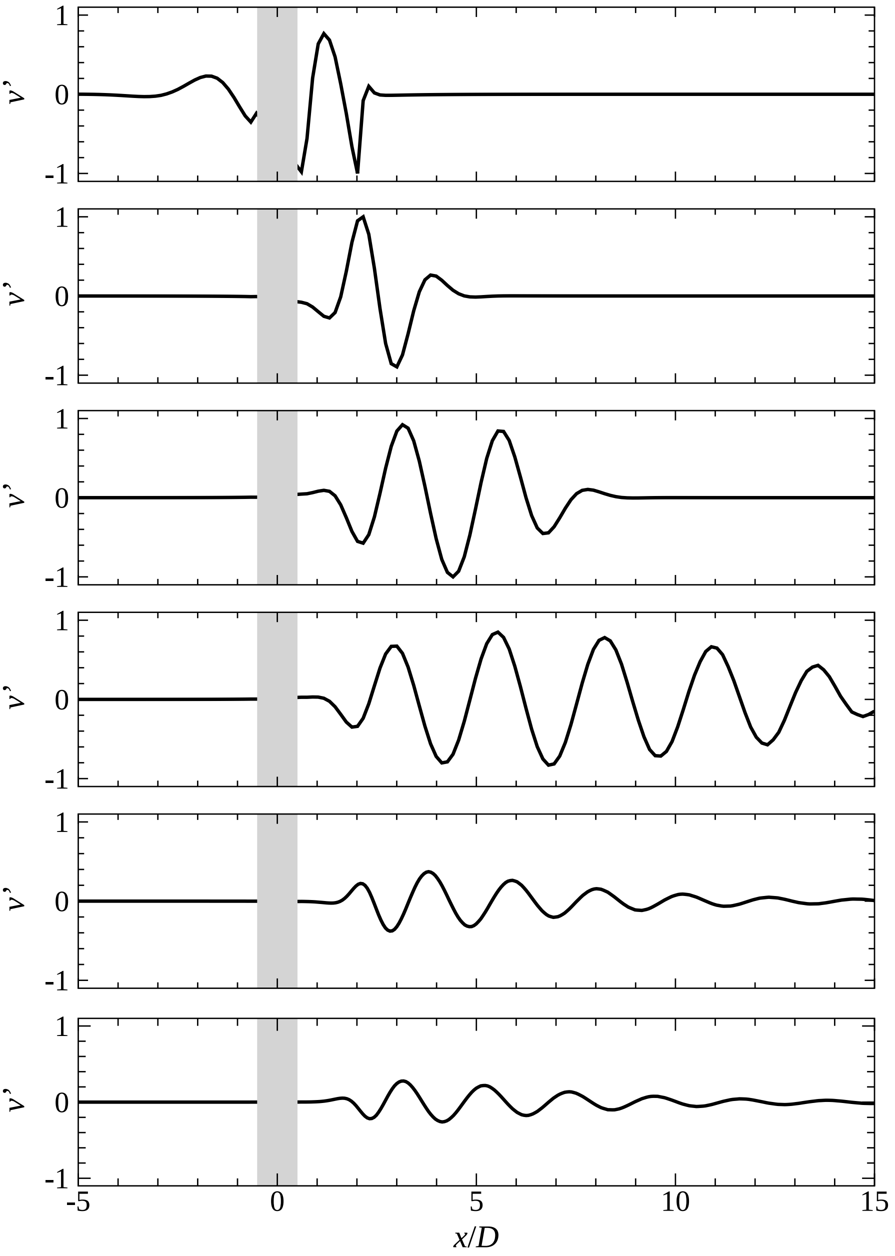

FIGURE 6.8: Time sequence of the vertical component of the perturbation velocity (v') profile along the channel centerline obtained at $\beta = 0.3$, $Re = 400$ and $Ha^{\star} = 50$. The sequence evolves from the optimal disturbance achieving peak energy growth, which had an evolution time $\tau_{\max} = 6.90$. From top to bottom, frames show times $t = 0$, 4, 8, 12, 16 and 20. The shaded region denotes the location of the cylinder.

6.2.5 Optimal Perturbation and Global Instability Mode

Fig. 6.9 presents a sequence of the base-10 logarithm of energy contours that evolved from the initial optimal disturbance obtained for $\beta = 0.3$, $Re = 1075$, $Ha^\star = 50$ and $\tau = 7.51$. The flow structures that give rise to these energy contours are a series of counter-rotating spanwise rollers. Initially the energies of the optimal disturbance are concentrated around the cylinder. Then, the disturbance energy convects downstream along the separated shear layer and is amplified until $t = \tau_{\max}$. For $t > \tau_{\max}$, there is no significant further downstream convection of the disturbance, which instead remains largely in place several diameters downstream of the cylinder, where it slowly decays away. The centroid location of the energy of the global linear instability mode (real eigenmode corresponding to a growth rate $\sigma = -0.0402$) lies at $x_c \approx 3.5$. For the optimal disturbance at $t = \tau_{\max}$ and $t > \tau_{\max}$, the centroid location of evolved perturbation energy are $x_c = 4.22$ and $x_c \approx 3.5$, respectively.

These properties imply that the action of the optimal disturbance is to perturb the leading global instability mode. This behaviour is consistent with the observation for a cylinder in a non-magnetohydrodynamic flow past a circular cylinder (Abdessemed *et al.* 2009a) That study further demonstrated that a flow seeded with the optimal disturbance beyond a transition Reynolds number experienced a far more rapid evolution of the instability than was obtained via the global instability mode (i.e. relying on exponential growth only). While the unstable regime is not considered in this study, a similar behaviour would be expected in this flow due to the consistent manner in which the optimal disturbances excite the global instability modes.

6.2.6 Reynolds Number Dependence

The Reynolds number dependence of the maximum growth and the associated disturbances are now considered. Figs. 6.10 and 6.11 show the predicted transient energy growth G of optimal perturbations as a function of evolution time τ for the steady base flows. For blockage ratios $0.1 \leq \beta \leq 0.4$, $50 \leq Ha^\star \leq 120$ and $300 \leq Re \leq 800$, the critical parameter ratio C_{Re} ranges between -0.87 and

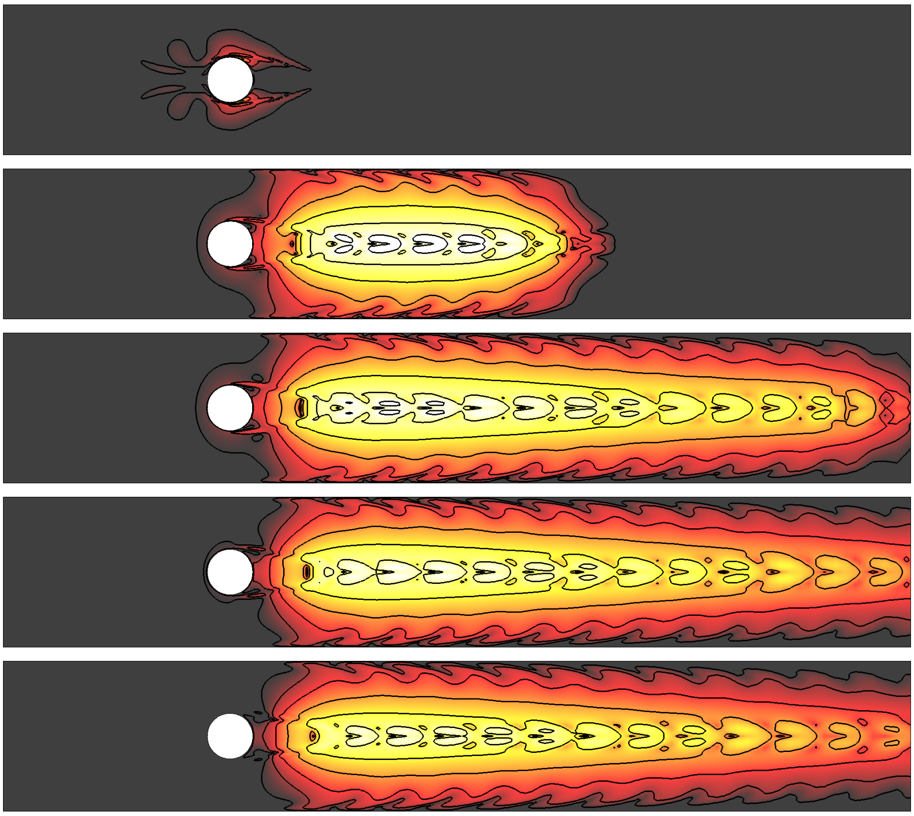

FIGURE 6.9: Contours of the base-10 logarithm of energy developed from the global optimum disturbance initial condition for $\beta = 0.3$, $Re = 1075$ and $Ha^{\star} = 50$. From top to bottom, frames show times $t = 0$, 4, 8, 16 and 32.

β	$Ha^{\star} = 50$				$Ha^{\star} = 120$			
	x_c	$\tau_{\max}$	λ_x	f	x_c	$\tau_{\max}$	λ_x	f
0.1	2.57	5.54	2.54	0.30	1.60	1.72	1.81	0.25
0.2	3.10	6.10	2.37	0.32	1.18	1.83	2.37	0.27
0.3	4.00	6.90	2.30	0.36	1.37	2.01	2.59	0.28
0.4	4.67	8.26	2.21	0.40	1.75	2.43	2.89	0.35

TABLE 6.4: Characteristics of the optimal perturbations at the time of maximum growth $\tau_{\max}$ for different blockage ratios at Hartman numbers as indicated and a Reynolds numbers $Re = 400$. Along with $\tau_{\max}$ the centroid location x_c of the evolved perturbation energy, the local axial wave length λ_x, and frequency f of the perturbation.

β	Re_{c1} $(Ha = 500)$	Re_{c1} $(Ha = 1200)$
0.1	248.53	283.43
0.2	164.49	275.78
0.3	157.46	263.37
0.4	140.69	241.55

TABLE 6.5: Critical Reynolds numbers for positive energy growth of optimal disturbances Re_{c1} for $Ha^\star = 50$ and 120 as indicated for different blockage ratios.

-0.40. For all β, while the chosen Reynolds numbers for the analysis are well below Re_c, there exists perturbations that grow in energy by factors of 3.81×10^2, 6.99×10^2, 2.0×10^3, and 1.89×10^4 at $\beta = 0.1$, 0.2, 0.3, and 0.4, respectively. For all Re at $Ha^\star = 120$, it is found that increasing β leads to a significant increase of the energy amplification and to a shift of the global maxima towards smaller evolution times. For $\beta \leq 0.2$, there is a substantial change in the $\tau_{\max}$ of the global maxima. However, this is less pronounced for $\beta \gtrsim 0.3$, where $\tau_{\max}$ occurs consistently at smaller τ.

6.2.7 Critical *Re* for Positive Energy Growth

The critical Reynolds number for positive energy growth of optimal disturbances, Re_{c1}, corresponds to the Reynolds number below which $G(\tau) \leq 1$ for all τ. By inspection of this data, this corresponds to the Reynolds number at which the gradient of G–τ data at $\tau = 0$ is zero, as for smaller Re, G decreases monotonically with τ. For each β, gradients were obtained for each Reynolds number using polynomial curve fitting. The resulting Re_{c1} at $Ha^\star = 50$ and 120 for different blockage ratios are presented in Table 6.5. These results demonstrate that it is possible to find disturbances which invoke positive energy growth around a circular cylinder. For all β (see Fig. 6.10), it can be seen that for $Re \geq Re_{c1}$ the optimal curve has a positive slope at $\tau = 0$ and there is a range of τ for which the energy of an optimal disturbance increases rather than decreases from its initial value.

(a) $\beta = 0.1$

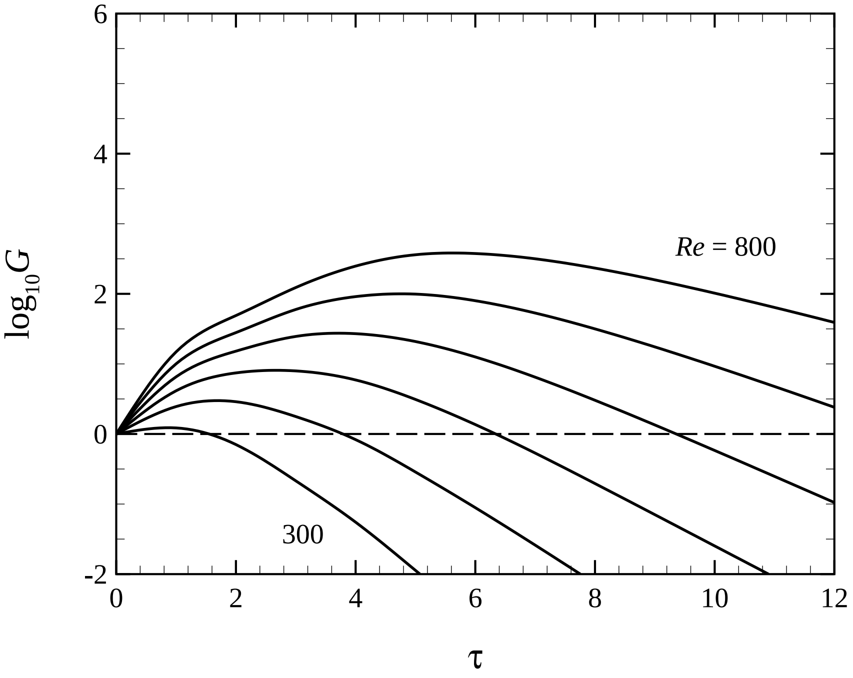

(b) $\beta = 0.2$

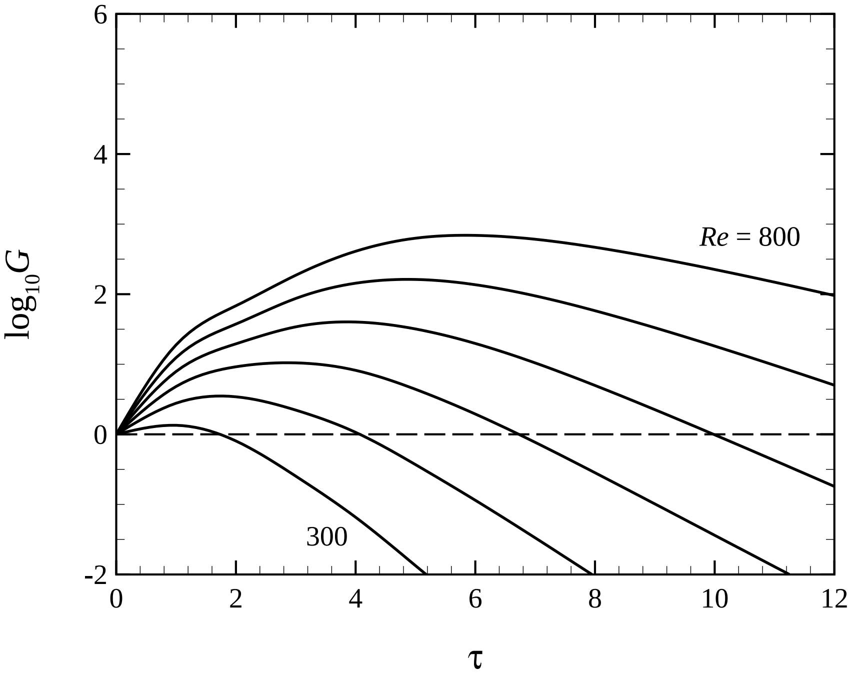

FIGURE 6.10: Plots of the transient energy growth, G, against τ, at different blockage ratio for Reynolds numbers from 300 to 800 in steps of 100 and $Ha^{\star} = 120$. In (a), the critical parameter ranges from $C_{Re} = -0.78$ to -0.40 over $300 \leq Re \leq 800$, while in (b) the critical parameter ranges from $C_{Re} = -0.82$ to -0.51.

(a) $\beta = 0.3$

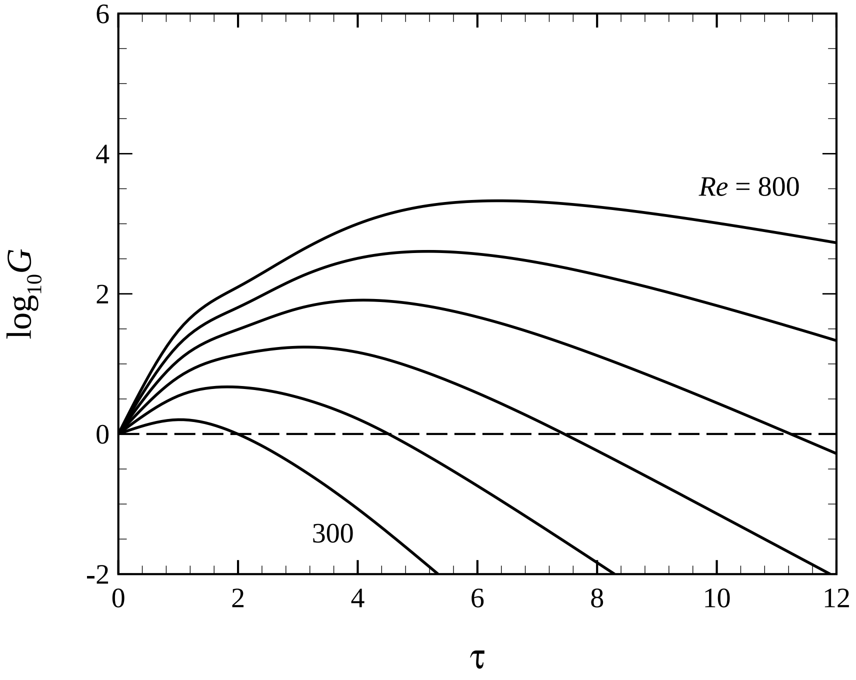

(b) $\beta = 0.4$

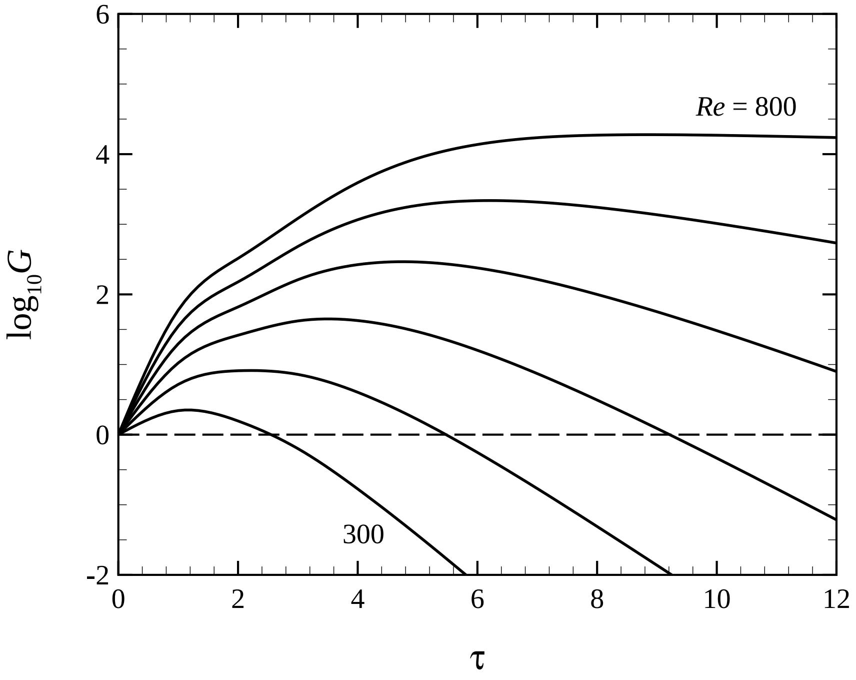

FIGURE 6.11: Plots of the transient energy growth, G, against τ, at different blockage ratio for Reynolds numbers from 300 to 800 in steps of 100 and $Ha^{\star} = 120$. In (a), the critical parameter ranges from $C_{Re} = -0.85$ to -0.60 over $300 \leq Re \leq 800$, while in (b) the critical parameter ranges from $C_{Re} = -0.87$ to -0.64.

6.2.8 The Variation of G_{max} and τ_{max} with $\boldsymbol{Re}$

Figs. 6.12(a, b) and 6.13(a, b) show the variations of $G_{\max}$ and $\tau_{\max}$ as functions of Re for different β at $Ha^\star = 50$ and 120, respectively. In addition, these data are also plotted against C_{Re} in Figs. 6.14(a, b) and 6.15(a, b). For all β, it is found that $G_{\max}$ grows exponentially or faster with Re and (C_{Re}) at $Ha^\star = 50$ and 120. For low Hartmann numbers the growth appears to be quadratic with Re and (C_{Re}), at least initially beyond the onset of positive amplification. At higher Reynolds numbers (higher critical parameter ratios) the variation appears to be linear. This is consistent with previous findings for non-magnetic bluff body flows (Blackburn *et al.* 2008a; Thompson 2011). At the higher Hartmann number the growth is much closer to linear from the point of positive amplification. In addition, for a given β, there is a significant change in the asymptotic slope of the curves as Hartmann number increases from $Ha^\star = 50$ to 120, decreasing by almost 40%. In the high Re linear regimes, the growth rates are 0.0091, 0.0096, 0.0117, and 0.0152 at $Ha^\star = 50$, and 0.0057, 0.0062, 0.0070 and 0.0089 at $Ha^\star = 120$ for $\beta = 0.1$, 0.2, 0.3, and 0.4, respectively. To quantify this further, $G_{\max}$ at $Ha^\star = 50$ increases by factor of approximately 8.13, 9.12, 14.7 and 33.1, and 3.72, 4.17, 5.01 and 7.76 for $Ha^\star = 120$ for each Re increment of 100, for $\beta = 0.1$, 0.2, 0.3, and 0.4, respectively.

When considering the data in the context of the critical parameter (figures 6.14 and 6.15), it is interesting to note that the effect of increasing blockage ratio becomes more pronounced. For instance, the case with $\beta = 0.4$ reaches $\log_{10} G_{\max} \approx 1.8$ at $C_{Re} \approx -0.8$, whereas at $\beta = 0.1$, this level of energy growth is only obtained at $C_{Re} \approx -0.43$, nearly twice as close to the transition Reynolds number in this flow. Therefore increasing blockage leads to an increased sensitivity to non-modal transient growth in this flow. When considering the predicted optimal perturbation fields displayed in figure 6.3, which are strongest immediately transverse to and downstream of the cylinder, this result supports the observation that an increased blockage ratio will increase the local velocities as the flow passes around the cylinder, leading to increased rates of shear and ultimately sensitivity to transient growth in the flow (Blackburn *et al.* 2008a,b).

For larger Reynolds numbers (high critical parameter ratios), a linear variation between $\tau_{\max}$ and Re is observed, corresponding to the higher Reynolds number linear regime observed for $\log G_{\max}$. From Fig. 6.12(b) and Fig. 6.13(b), at $Ha^\star = 50$, $\partial\tau_{\max}/\partial Re = 0.0238$, 0.0239, 0.0269 and 0.0362, and 0.0097, 0.0102, 0.0114 and 0.018 at $Ha^\star = 120$ for $\beta = 0.1$, 0.2, 0.3, and 0.4, respectively. It is noted that these gradients only display a very weak blockage ratio dependence compared to the $G_{\max}$ variation.

6.3 Response of the Flow to Continuous Upstream Disturbances

To demonstrate the relevance of linear growth computations to a real flow in the presence of inflow noise, direct numerical simulations (DNS) have been performed. The initial state is the steady flow at $Re = 1160$, $Ha^\star = 200$ and $\beta = 0.4$. This case has been chosen as it exhibits the maximum energy growth of all the cases investigated in the previous sections. For this purpose a random white noise with small amplitude is added to the velocity field at the inlet to the computational domain. Therefore, we aim to see strong evidence of disturbances growing to non-linear levels as the base flow is excited with noise.

In a non-magnetohydrodynamic flow, an injected disturbance decays only through the action of viscosity. However, in these flows Hartmann damping also acts to damp disturbances. The rate at which disturbance vorticity (ω) decays can be approximated using equation (4.7). Using this expression for these flow conditions gives $\frac{\mathrm{d}(\log_e \omega)}{\mathrm{d}t} \approx -0.344$. If it is assumed that inflow disturbances convect at approximately u_0, then by the time a disturbance reaches the cylinder, it will have decayed to just 7.5% of its original strength. This Hartmann damping would be even stronger at lower Reynolds numbers and higher Hartmann numbers. Ultimately, this means that upstream disturbances need to be significantly stronger in these magnetohydrodynamic flows than in comparable non-magnetohydrodynamic channel flows to facilitate amplification of the disturbances to non-linear levels.

Fig. 6.16 shows the vorticity in the disturbance invoked by the addition of

(a)

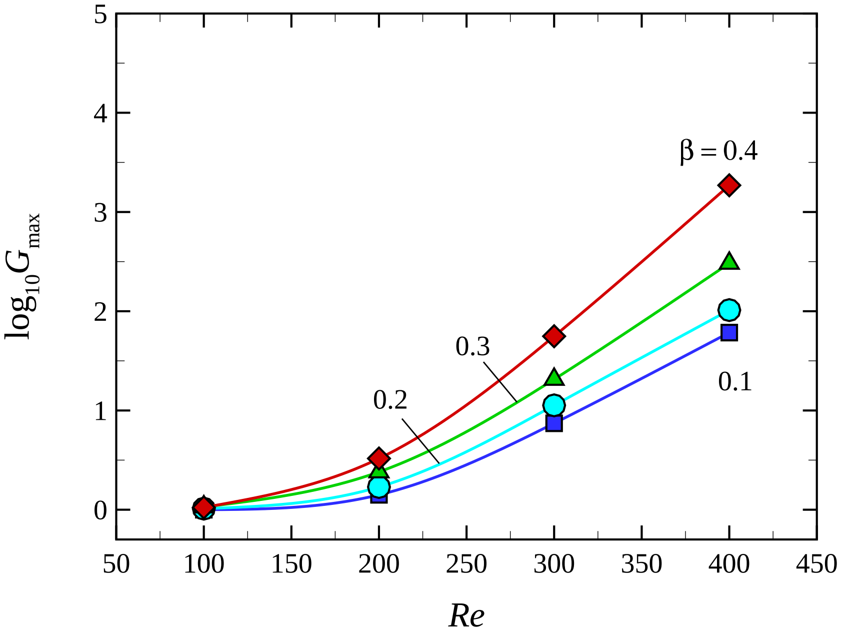

(b)

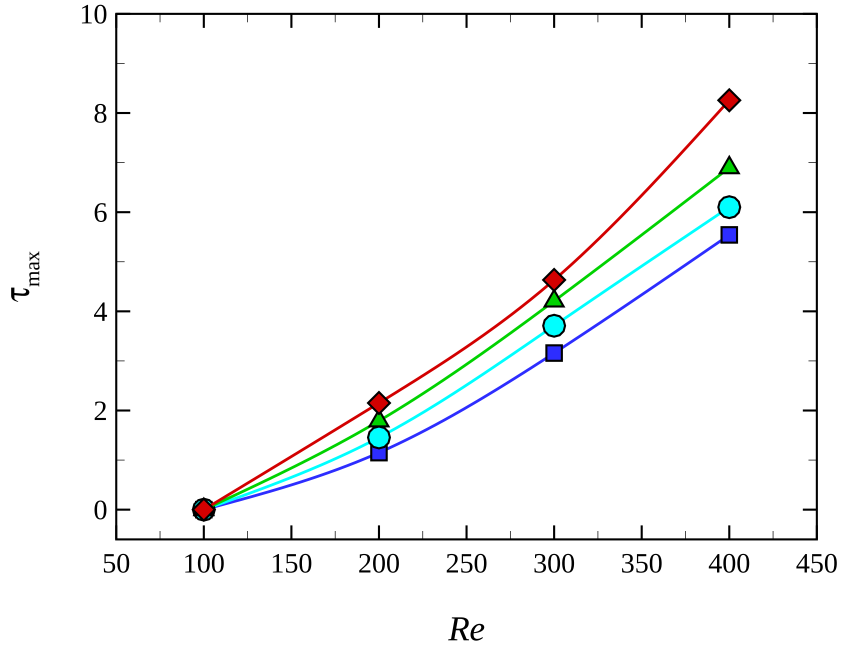

FIGURE 6.12: Maximum energy growth $G_{\max}$ (a) and time of maximum of the energy maximum (b) as a function of Reynolds number for different blockage ratios β at $Ha^{\star} = 50$. Linear trends in the data in (a) signifies an exponential relationship. The values of Re is below the critical Reynolds numbers Re_c. The asymptotic slopes of $\partial \log_{10} G_{\max})/\partial Re$ at $\beta = 0.1$, 0.2, 0.3, and 0.4 are 0.0091, 0.0096, 0.0117, and 0.0152, respectively.

(a)

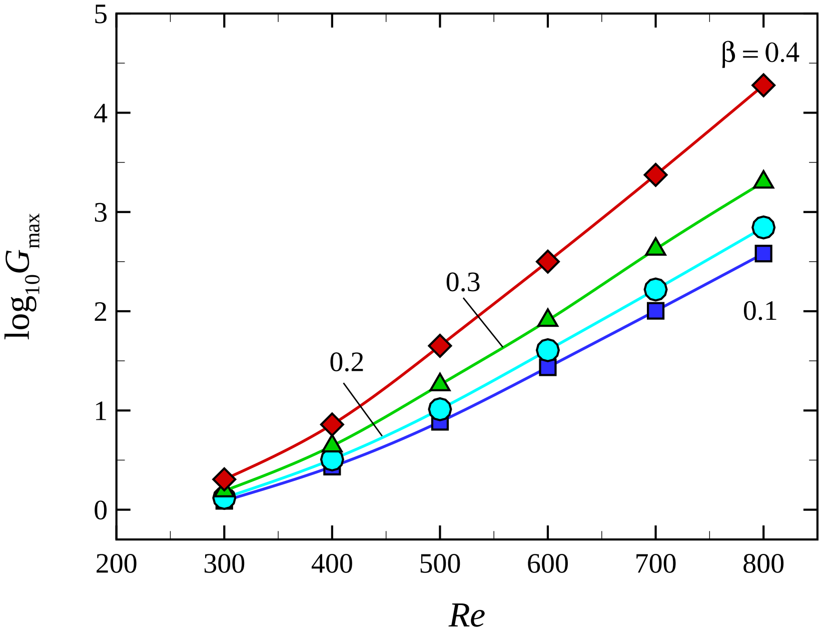

(b)

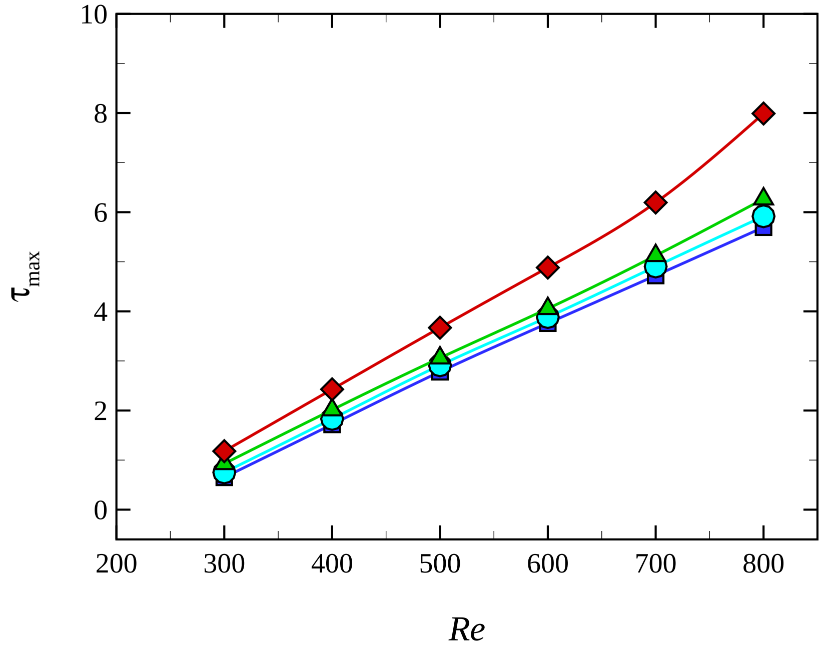

FIGURE 6.13: Maximum energy growth $G_{\max}$ (a) and time of maximum of the energy maximum (b) as a function of Reynolds number for different blockage ratios β at $Ha^{\star} = 120$. The values of Re is below the critical Reynolds numbers Re_c. The asymptotic slopes of $\partial \log_{10} G_{\max} / \partial Re$ at $\beta = 0.1$, 0.2, 0.3, and 0.4 are 0.0057, 0.0062, 0.007 and 0.0089 respectively.

(a)

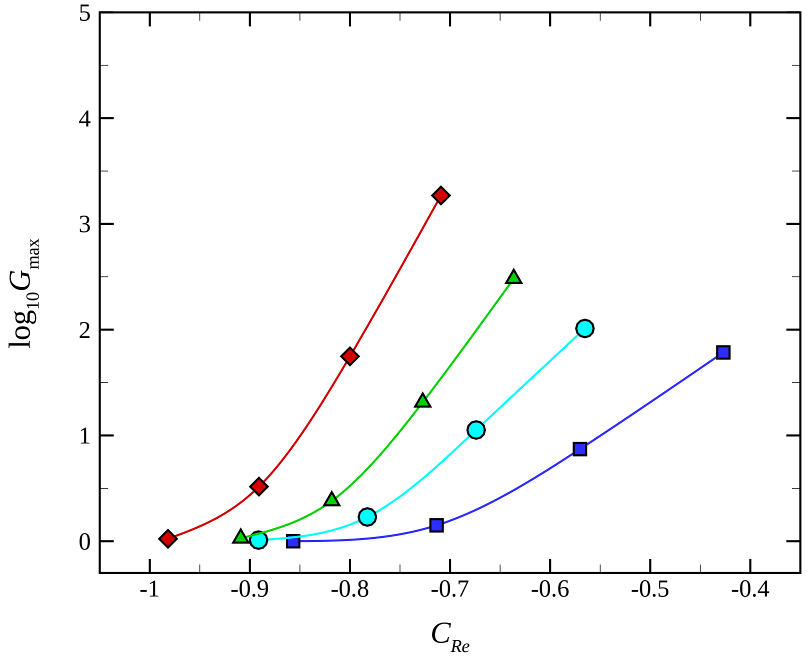

(b)

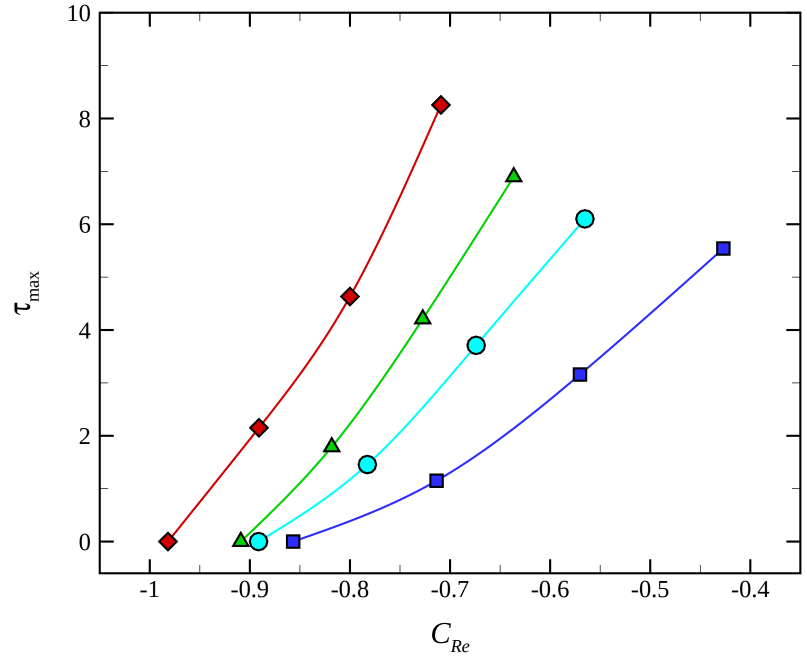

FIGURE 6.14: Maximum energy growth $G_{\max}$ (a) and time of maximum of the energy maximum (b) as a function of critical parameter ratio C_{Re} for different blockage ratios β at $Ha^\star = 50$. The minimum and maximum C_{Re} corresponding to $Re = 100 - 400$ are -0.92 and -0.43, respectively. Colours and symbols as per Fig. 6.12.

(a)

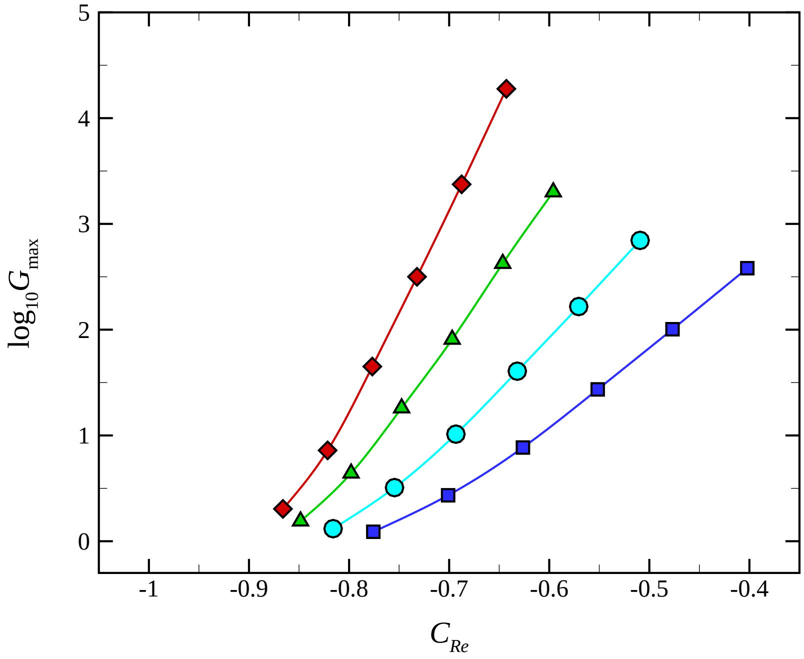

(b)

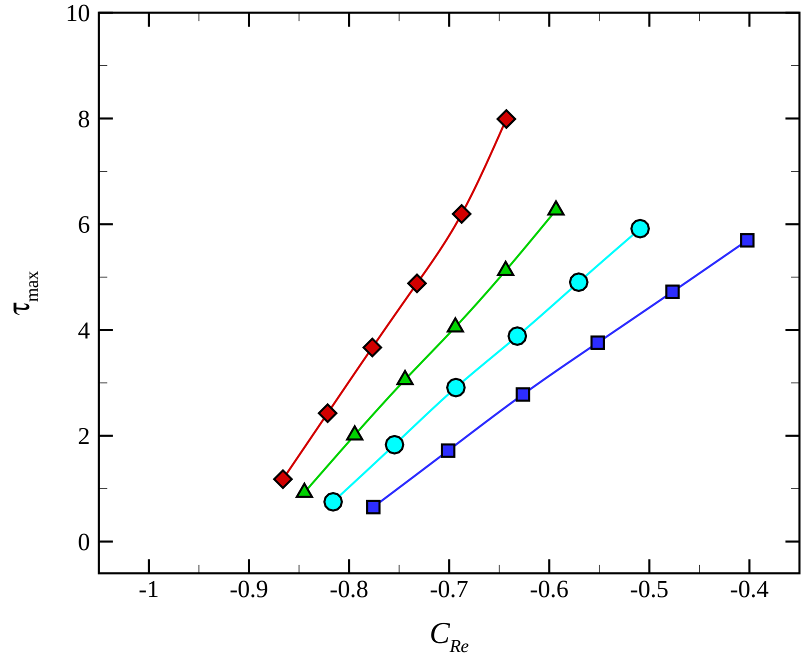

FIGURE 6.15: Maximum energy growth $G_{\max}$ (a) and time of maximum of the energy maximum (b) as a function of critical parameter ratio C_{Re} for different blockage ratios β at $Ha^{\star} = 120$. The minimum and maximum C_{Re} corresponding to $Re = 300 - 800$ are -0.87 and -0.40, respectively. Colours and symbols as per Fig. 6.13.

white noise to the inflow. Even for low levels of random noise (e.g. a disturbance envelope of $0.1u_0$), a distinct pattern of disturbance is observed behind the cylinder. This disturbance pattern appears in the vicinity of the separation of the flow from the sides of the cylinder, and is observed to propagate downstream along the separated shear layers in the wake, becoming broader. These flaring disturbance zones meet at the wake centerline, and further downstream a disturbance pattern is observed which is consistent with those observed to have evolved from the optimal initial disturbance leading to maximum energy growth for the given parameters.

Further analysis of the system with the inflow perturbed by white noise with an amplitude of $0.5u_0$ is elucidated in Fig. 6.17. In Fig. 6.17(a), a simulated dye visualization image is produced (Sheard *et al.* 2007; Sheard 2009) following injection of a high concentration of passive tracer particles into the flow from the vicinity of the surface of the cylinder. Particles are evolved using an implementation Neild *et al.* (2010) of the high-order particle transport algorithm of Coppola *et al.* (2001). This visualization approach reveals an instantaneous streakline pattern in the flow, which demonstrates that at these flow and perturbation conditions (which are below the critical Reynolds number for the onset of vortex shedding), the level of upstream disturbance is sufficient to invoke an observable wavy disturbance downstream of the wake recirculation bubble.

Fig. 6.17(b) plots vorticity in the flow, which exhibits the same wavy perturbation seen in Fig. 6.17(a). The flow is characterized by a pair of symmetric counter-rotating vortices on either side of the wake centerline. The bubble length of the wake is of particular interest when considering the behavior of transient disturbances in the flow, as separated shear layers appear to consistently act as an amplifier of disturbances. Note that the vorticity decays relatively quickly downstream of the wake recirculation bubble due to Hartmann damping, though waviness in the dye streak persists further downstream. This may have significant implications for efforts to enhance mixing across magnetohydrodynamic channel flows.

Attention is now directed to the disturbance field, which is generated by subtracting the unperturbed flow from the perturbed flow. In Fig. 6.17(c), vorticity in the disturbance field is plotted. In comparison to the strength of vorticity structures in the wake, very weak vorticity structures can be observed to the left of the cylinder. This demonstrates the significant degree by which disturbances have been amplified as they convect past and downstream of the cylinder. Included for comparison with this disturbance field are the corresponding optimal perturbation evolved to $\tau_{\max}$ and the leading global linear instability mode (Figs. 6.17(f) and 6.17(g), respectively). Downstream of the recirculation bubble a good agreement is observed across these three plots: alternating-sign vortex structures repeating at a consistent streamwise wavelength are observed, which decay further downstream of the cylinder. The notable point of difference is that the white-noise disturbance field also features diverging zones of disturbance vorticity convecting from the flow separation points either side of the cylinder and into the wake. Whereas the optimal disturbance at $\tau_{\max}$ and the global mode correspond to isolated disturbances in an otherwise unperturbed flow, the disturbance field is continuously fed by upstream disturbances. The visible disturbances in the separated shear layers appear as a result of this continuous injection of upstream disturbances, and reflect the amplifying nature of this region of the wake flow.

The energy field of the disturbance offers an added perspective on the perturbed flow, and is plotted in Fig. 6.17(d). Whereas the disturbance vorticity field compares favorably with that of the optimal growth mode evolved to time $t \approx \tau_{\max}$, the energy fields are notably different. Firstly, the disturbance energy field exhibits a clear asymmetry about the centreline downstream of the cylinder. This asymmetry demonstrates that the disturbance has evolved to levels well beyond the linear regime, and is consistent with the observed waviness in Figs. 6.17(a) and 6.17(b). Secondly, the disturbance energy field displays significant zones of energy either side of the cylinder, which is absent from the optimal disturbance energy plots in the vicinity of $\tau_{\max}$ (see Fig. 6.9). This feature bears a close similarity to the energy field of the optimal initial condition, which is shown in Fig. 6.17(e). The interpretation to be drawn from this is that the weak inflow

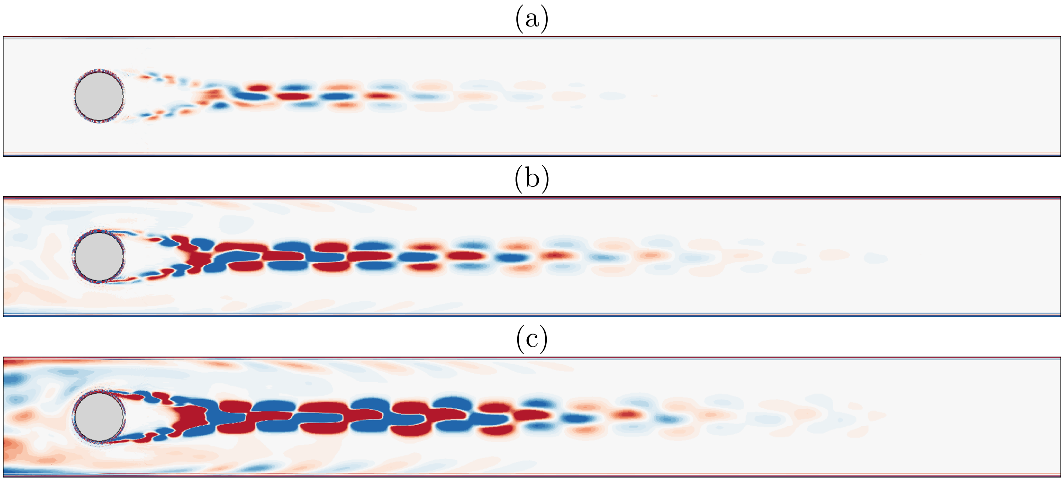

FIGURE 6.16: Disturbance vorticity contours obtained for $Re = 1160$, $Ha^{\star} = 200$ and $\beta = 0.4$. The disturbance velocity field was isolated by subtracting the unperturbed steady-state solution from a snapshot of the simulations perturbed by white noise. Shown are cases computed with envelopes of white noise amplitudes of (a) $0.1u_0$, (b) $0.3u_0$, and (c) $0.5u_0$.

disturbances supply energy to the optimal transient modes in the flow, which in turn lead to amplification of the disturbances as they convect aft of the cylinder and into the wake. As the optimal mode has been shown to act as an amplifier for the global linear instability mode (as also seen in Abdessemed *et al.* (2009a)), these disturbances therefore manifest in a fashion consistent with the instability mode effectively leading to a (weak) von Kármán vortex street.

6.4 Chapter Summary

In this chapter, an investigation has been carried out into the transient growth of optimal linear perturbations of a liquid metal magnetohydrodynamic flow past a confined cylinder in a duct under a strong axial magnetic field in the subcritical regime prior the onset of oscillations. Under these conditions, the flow is quasi two–dimensional and the modified Navier–Stokes equations are solved in a two–dimensional domain.

For all blockage ratios, for a given Reynolds number, very significant transient energy growth was found in this regime, which suggests a potential for the de-

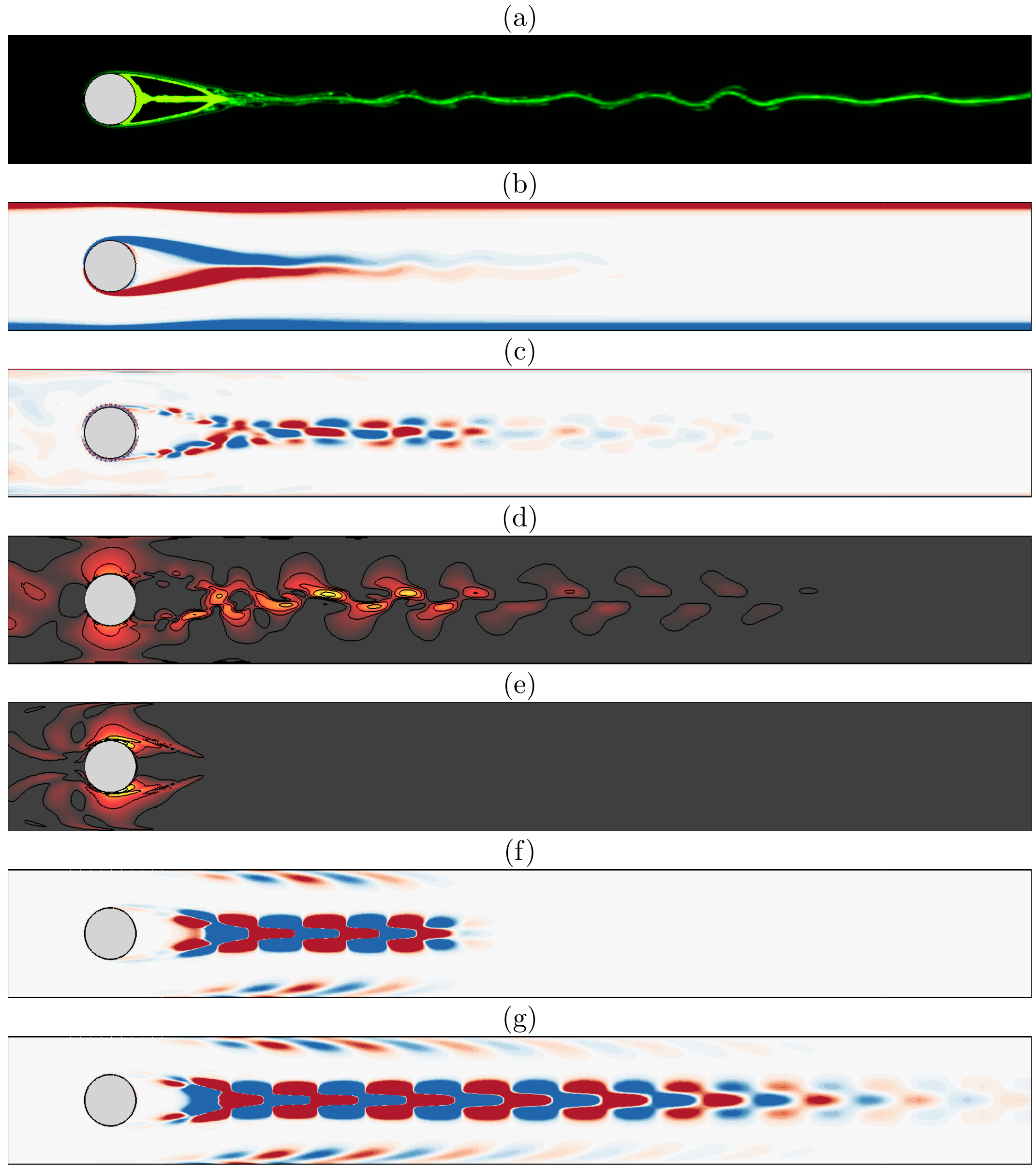

FIGURE 6.17: Plots visualizing a computation at $Re = 1160$, $Ha^{\star} = 200$ and $\beta = 0.4$ perturbed by a random disturbance at the inflow with an amplitude of up to $0.5u_0$. Frames show (a) simulated dye visualization of the disturbed flow; (b) the vorticity field of the disturbed flow; (c) the isolated disturbance vorticity as per Fig. 6.16; (d) the base-10 logarithm of the energy in the disturbance field shown in (c); (e) the base-10 logarithm of the energy of the optimal initial disturbance computed for evolution time $\tau_{\max}$ for the unperturbed flow; (f) vorticity field of the linear optimal initial disturbance evolved to time $t = \tau_{\max}$; and (g) vorticity in the leading global instability mode for the unperturbed flow obtained from a linear stability analysis. In each frame, arbitrary contour levels are plotted to elucidate the key features of the flow in each frame.

sign of actuation mechanisms to promote vortex shedding and thus enhance heat transfer in these ducts. The energy amplification of the disturbances was found to decrease significantly with increasing Hartmann number, where the maximum growth peaks at shorter time intervals. This is due to the reduction of perturbation kinetic energy by Hartmann damping. The global maxima of energy was found to vary significantly with blockage ratio, being longer at higher β. The structure of the disturbance was found to be consistent across all blockage ratios being tested.

The optimal disturbance was maximal in the region of the boundary layer separation around the cylinder near the wake. The perturbation convects along the separating region being amplified to the peak growth state downstream of the recirculation bubble. The $\tau_{\max}$ was found to increase significantly as recirculation length increases which demonstrates the amplifying nature of the separated shear layers in the wake.

For all Re at high Hartmann number, it was found that increasing β leads to a significant increase of the energy amplification and to shift the global maxima towards smaller times. For $\beta \leq 0.2$, there was a substantial change in the $\tau_{\max}$ of the global maxima. However, it changed very slightly for $\beta \geq 0.3$.

The critical Reynolds number for positive energy growth of the optimal disturbance, Re_{c1}, was found to increase significantly with increasing blockage ratio and Hartmann number. The optimal disturbances at $Re \leq Re_{c1}$ monotonically decreased with τ, while for $Re \geq Re_{c1}$ the energy of an optimal disturbance increases rather than decreases from its initial value. For all β, it is found that $G_{\max}$ grows exponentially with Re at low and high Hartmann numbers.

Direct numerical simulation in which the inflow was perturbed by white noise demonstrated that the optimal transient growth properties of the flow could be activated by continuous upstream random perturbations, which results in a significant amplification of the disturbances as they pass around the cylinder. This was sufficient to partially destabilize the wake through the global instability responsible for producing the von Kármán wake, despite the simulation being run at conditions below the critical Reynolds number for vortex shedding.

Chapter 7

Heat Transfer Enhancement Induced by a Torsionally Oscillating Cylinder

The results presented in chapter 6 demonstrated that very significant transient energy growth was found in the subcritical regime below the onset of Kármán vortex shedding. The results show that the optimal disturbance fields are strongest near the cylinder and that they are consistent with an asymmetrical disturbance with respect to the horizontal centreline of the system. This suggests a potential for the design of actuation mechanisms to invoke unsteady flow at low Reynolds numbers and thus enhancing the heat transfer from the heated surface in ducts using a perturbation introduced through the cylinder. Examples could be either a transverse or torsional oscillation tuned to the frequency of the evolving optimal disturbance.

In this chapter, a mechanism for enhancement of heat transfer from the heated duct wall is explored, based on a torsional cylinder oscillation intended to excite vortex shedding in the normally steady-state flow regime. This is significant due to the natural damping of vortex shedding that occurs at high Hartmann number, which in turn limits the efficiency of heat transfer. To this end, the fluid structure and heat transfer characteristics of the flow of a liquid metal past a circular cylinder undergoing torsional oscillation and confined in a duct in the presence of a strong magnetic field will be investigated. The effects of the angular torsional oscillation velocity amplitude A and oscillation frequency f_e on the heat transfer and flow characteristics are examined for a test case with a constant blockage ratio $\beta = 0.3$ and Hartmann number $Ha^\star = 50$.

7.1 Motivation of this Study

As stated, the work contained in this chapter was motivated by the findings of chapter 6. The rationale for investigating this proposed heat transfer enhancement mechanism is outlined here. Vorticity and energy contours of the optimal disturbance field for $\beta = 0.3$, $Ha^\star = 50$ and $Re = 1075$ are presented in Fig. 7.1. The initial disturbance vorticity field is concentrated in the vicinity of the cylinder around the recirculation bubble as shown in Fig. 7.1(a). Fig. 7.1(b) presents the base-10 logarithm of energy contours of the initial disturbance, which further indicates that the energies of initial optimal disturbance are localized and concentrated around the cylinder. The work presented in Chapter 6 demonstrated that the optimal disturbance excites the global instability mode associated with vortex shedding, and that vortex shedding will enhance heat transfer through the duct wall when compared to the Hartmann-damped steady-state flow at higher Hartmann numbers. The proximity of optimal perturbation structures to the cylinder motivates the pursuit of a mechanism for perturbation of the flow that is invoked at or near the surface of the cylinder.

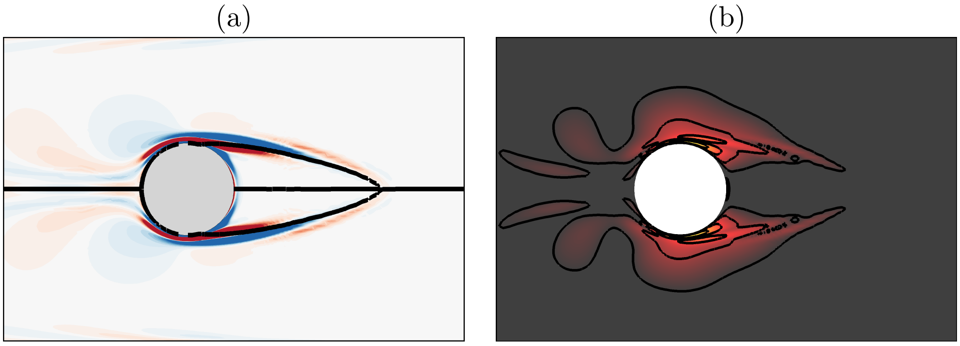

FIGURE 7.1: Vorticity and energy contours of the optimal initial disturbance at $Re = 1075$, $Ha^\star = 50$ and $\beta = 0.3$, acuired for $\tau = 7.51$. Frames show (a) the vorticity field of the optimal initial disturbance, and (b) the base-10 logarithm of energy in the initial disturbance. Contours level are arbitrary chosen, and in (a) the solid lines show the separating streamlines for the underlying flow.

The perturbation vorticity field in Fig. 7.1(a) has reflective symmetry about the wake centreline. Thus, the underlying velocity field cannot possess reflective symmetry about the wake centreline. This implies that a perturbation mechanism that acts to break symmetry about the wake centreline will be preferred for inciting instability. To further illustrate the asymmetry of the flow that is introduced by the evolving optimal perturbation, Fig. 7.2 shows time histories of vertical and axial velocity components that are generated from perturbing the flow with the optimal initial condition. The velocity components are recorded at locations immediately above and below the cylinder. The amplitude of oscillations decrease over time as the disturbance convects downstream. Notice that both the vertical and horizontal velocity components measured above and below the cylinder have identical time histories. This reiterates that the optimal perturbation breaks the reflective symmetry of the wake. Possible perturbation mechanisms that could feed energy into the separating shear layers could include imposing a transverse oscillation on the cylinder (Leontini *et al.* 2007; B.Celik & Beskok 2009; Celik *et al.* 2010), or a torsional oscillation (Baek & Sung 1998; Mahfouz & Badr 2000). Working within the constraints of the present numerical algorithm, though the remainder of this chapter a mechanism featuring torsional oscillation of the cylinder will be explored for its potential to enhance the heat transfer from the heated wall.

7.2 Geometry and Boundary Conditions

As before, the configuration of the physical system to be considered is shown in Fig. 7.3 where a circular cylinder of diameter d is placed at the centre of a duct parallel to the magnetic field and perpendicular to the flow direction. In this case a torsional oscillation is imposed on the cylinder about its own axis. The duct walls and the cylinder are assumed to be electrically insulated. A uniform homogeneous axial magnetic field with a strength B is imposed parallel to cylinder axis. One of the walls oriented parallel to the magnetic field is heated to a constant wall temperature T_w whereas the other wall and the inflow have temperature T_0. The cylinder is located at $8d$ and $25d$ from the inlet and outlet, respectively, which

(a) $\mathbf{x}/d = (0, 0.6)$

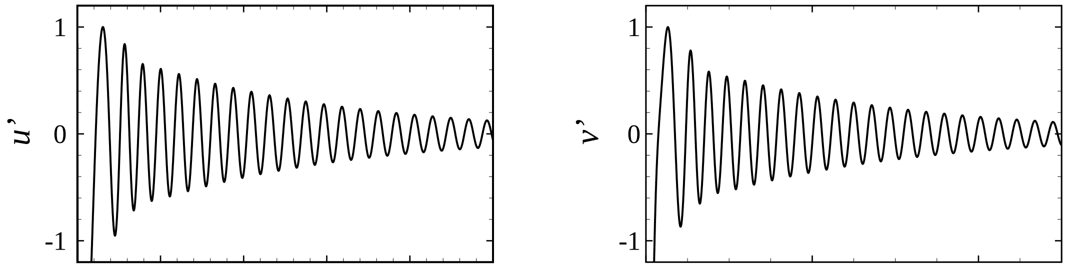

(b) $\mathbf{x}/d = (0, -0.6)$

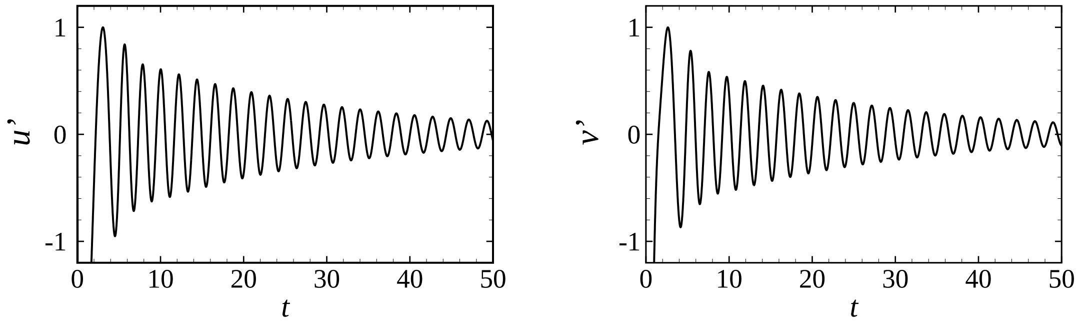

FIGURE 7.2: The time histories of u' and v' velocities recorded at locations (a) above and (b) below the cylinder for $Re = 1075$, $Ha^\star = 50$ and $\beta = 0.3$, for linearized evolution of the optimal perturbation ($\tau = 7.51$). x and y are measured from the centre of the cylinder. These velocities are normalized to have an absolute maximum value of unity.

are sufficient to obtain domain independent results as demonstrated previously in § 4.2.1.

The boundary conditions imposed here are identical to those used for the symmetrical flow geometry, with the exception of the imposed cylinder rotation. On the cylinder wall, a periodic torsional oscillation condition is applied. Since the cylinder is rotated sinusoidally in time at a forcing frequency f_e, the angular velocity of the cylinder is expressed as

$$\dot{\boldsymbol{\theta}}_{\text{cyl}} = A \sin(2\pi f_e t). \tag{7.1}$$

The maximum tangential surface speed of the cylinder is therefore given by $A(d/2)$, and the angular amplitude of displacement of the oscillation is given

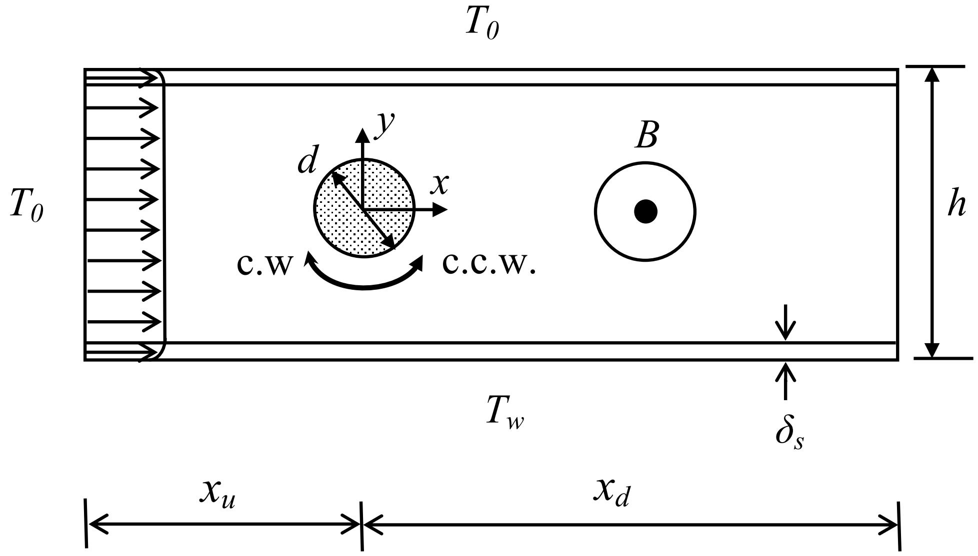

FIGURE 7.3: The physical model of the torsionally oscillating cylinder system under investigation. The magnetic field B acts in the out-of-plane direction, parallel to the cylinder axis. δ_S is the thickness of the Shercliff layer, and h and d are the duct width and cylinder diameter, respectively. The blockage ratio $\beta = d/h = 0.3$. The upstream and downstream lengths are $x_u = 8d$ and $x_d = 25d$, respectively.

by $A/(2\pi f_e)$. Hereafter, A is taken to have been non-dimensionlized by u_0/d and frequency results are reported based on the dimensionless Strouhal number defined in equation (3.76), $St_e = \dfrac{f_e d}{u_0}$. The cylinder is thermally insulated, and a zero normal temperature gradient is imposed at its surface.

In this chapter, the blockage ratio and Hartmann number are kept constant at $\beta = 0.3$ and $Ha^\star = 50$, and the control parameters St_e and A are varied. The mesh representing the elemental discretization of the computational domain is shown in Fig. 7.4.

Again, a convergence study for spatial resolution has been performed by varying the element polynomial degree from 4 to 9, while keeping the macro-element distribution around the cylinder unchanged unchanged. However, it is true that cylinder rotation reduces the boundary layer thickness at the cylinder surface so

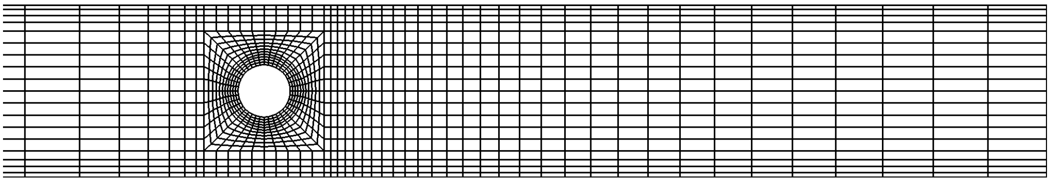

FIGURE 7.4: Spectral element mesh of the confined symmetrical cylinder employed for the torsional oscillation study. The mesh extends $8d$ upstream and $25d$ downstream of the cylinder. Collection points within elements are not shown.

N_p	$C_{L,\mathbf{max}}$	$C_{M,\mathbf{max}}$	$\boldsymbol{Nu}$
4	4.7330	0.6693	2.5451
5	4.6408	0.6788	2.5494
6	4.6608	0.6732	2.5553
7	4.6766	0.6736	2.5617
8	4.6768	0.6738	2.5616
9	4.6768	0.6740	2.5615

TABLE 7.1: Peak lift coefficient amplitude $C_{L,\max}$ and average Nusselt number along the heated wall Nu with varying polynomial order for a torsional oscillating cylinder at $Ha^\star = 50$, $Re = 1075$, $A = 3$, $St_e = 0.2$ and $\beta = 0.3$.

that higher interpolation order is needed to obtain the same accuracy as for the previous studies, as is shown by the p-refinement resolution study. This has been conducted to gain an understanding as to whether the addition of cylinder rotation affects the spatial convergence of the simulations. The maximum lift coefficient $C_{L,\max}$, maximum moment coefficient $C_{M,\max}$ and the time-averaged Nussult number along the heated wall Nu were monitored. Convergence tests were performed for an oscillation amplitude $A = 3$, $St_e = 0.2$, $Re = 1075$, $Ha^\star = 50$ and $\beta = 0.3$. This case has been chosen as it exhibits high energy growth compared to other case at small blockage ratios. The results are presented in Table 7.1. It is found that the results differ by less than 0.5% of the most resolved case when $N_p = 7$, which is hereafter used for the remaining simulations reported in this chapter.

7.3 Effects of Oscillation Frequency and Amplitude on Heat Transfer

In this chapter, a wide range of velocity amplitudes A and forcing frequencies St_e are investigated. The velocity amplitude is varied over the range $0 \leq A \leq 3$, while the forcing frequency is varied over $0 \leq St_e \leq 10$. This range of parameters is consistent with the range employed in previous studies which have considered the torsional oscillation of a cylinder in a free stream flow (e.g. Mahfouz & Badr (2000)). However, to focus on important results, vorticity and temperature contours are presented only for cases where the maximum heat transfer occurred.

The time-averaged Nusselt number for a broad range of forcing frequency St_e is shown in Fig. 7.5 for a selection of oscillation ampliudes. Note that without cylinder rotation, the flow remains steady for this combination of parameters. The critical Reynolds number for the onset of vortex shedding at this β and Ha is $Re_c = 1100$. The figure shows that there is a significant enhancement in heat transfer obtained for high angular velocity amplitudes. It is also interesting to observe that as the oscillation amplitude increases, the frequency producing peak heat transfer decrease, and a wider range of frequencies produce heat transfer enhancement. For comparison, frequencies associated with both the dominant linear instability and the optimal disturbance are each included in the plot. It can be seen that increasing A shifts the frequency for peak heat transfer enhancement away from these frequencies, presumably as a result of non-linearity of the imposed perturbation.

In Fig. 7.6, the peak heat transfer coefficient at each angular velocity amplitude, $Nu_{\max}$, is plotted against A. It can be observed that $Nu_{\max}$ increases significantly as A increased. This may be attributed to the fact that stronger vortices are generated behind the cylinder when it oscillates with larger amplitude thanks to the higher shear between the moving cylinder surface and the flow during the part of the cycle where the cylinder is moves against the flow. It is noted that the most rapid increases are formed for smaller A. hence there is a diminishing benefit in terms of heat transfer enhancement when the amplitude is

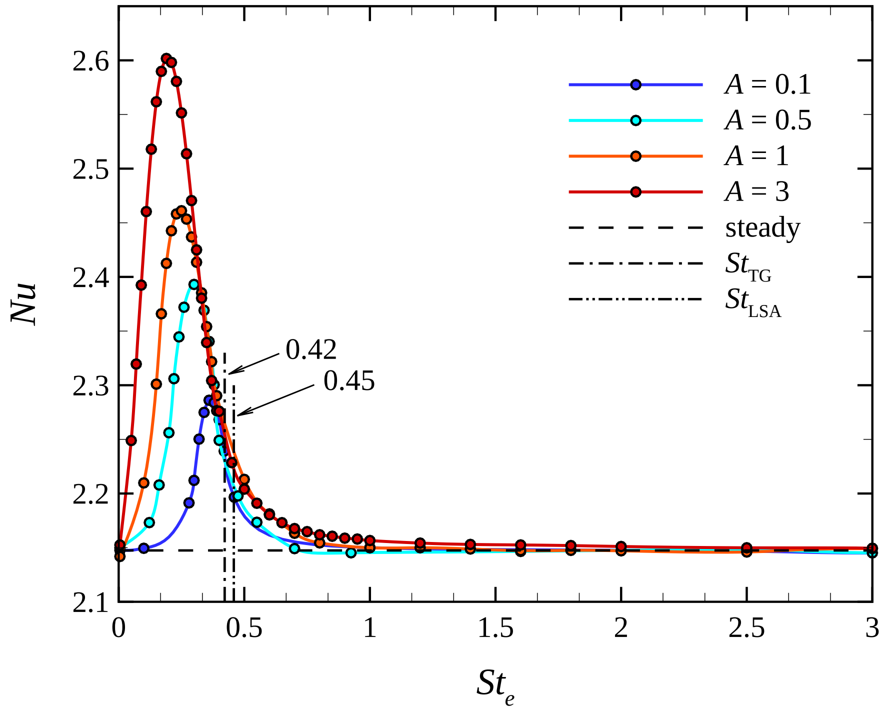

FIGURE 7.5: The distribution of time-averaged Nusselt number over the heated surface of the side wall with excitation frequency of the cylinder at different amplitudes for $Re = 1075$ and $Ha^{\star} = 50$. For reference, Nusselt number for the case of steady flow without oscillation ($St_e = 0$) is shown by the horizontal dashed line.

progressively increases.

The percentage increments to the overall heat transfer are approximately 6.5%, 11.5%, 15%, and 22% for $A = 0.1$, 0.5, 1.0, and 3.0, respectively, over that obtained for steady flow. The effect of increasing the amplitude on heat transfer enhancement is further clarified in Fig. 7.7. However, again it is noted that the change in heat transfer per unit increase in A decreases with increasing A. This indicates there is a practical limit to the benefit of this heat transfer enhancement mechanism, whereby the benefit of enhancing heat transfer may be outweighed by the cost of increasing A.

To illustrate the role of oscillation and perturbation frequencies on the flow, Fig. 7.8(a) shows the variation of forcing frequency for maximum heat transfer $St_{e,\max}$ with oscillation amplitude. The figure suggests that as $A \to 0$, the optimal

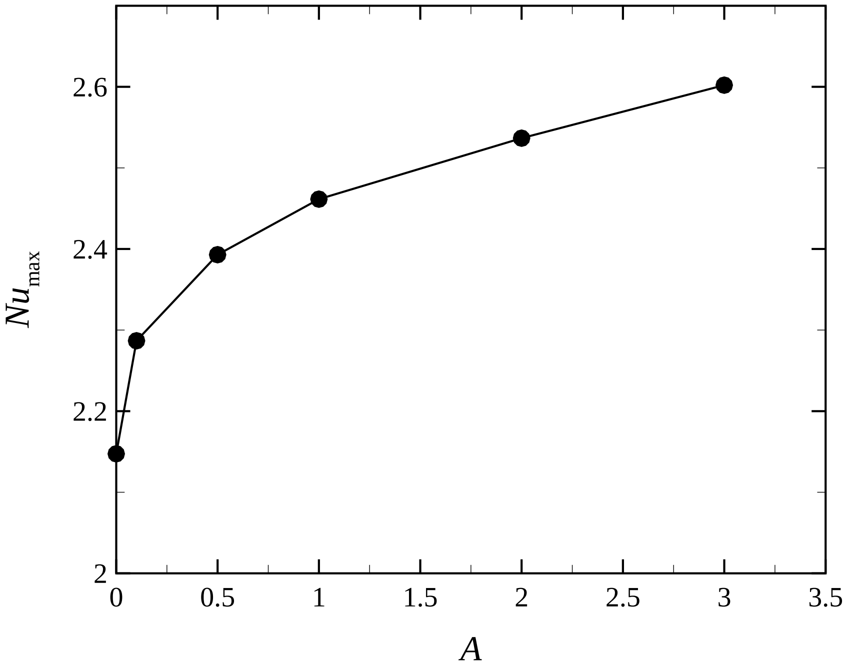

FIGURE 7.6: The variation of peak time-averaged $Nu_{\max}$ over the heated surface with velocity amplitude of the cylinder for $Re = 1075$ and $Ha^\star = 50$.

excitation frequency approaches the frequency of the global mode predicted from linear stability analysis. Fig. 7.8(b) presents the frequency predicted by linear stability analysis (LSA), transient growth (TG) analysis and DNS as a function of Reynolds number. Relatively higher frequencies are observed prior to the onset of vortex shedding. The preferred wake frequency is observed to decrease as the non-linear regime is entered (either through increasing the Reynolds number or by imposing a higher-amplitude forcing through oscillation of the cylinder), which also creates large-scale oscillations in the wake. In addition, it is worth mentioning that frequencies predicted by LSA and those by TG are very close, and they intersect near the unsteady transition Reynolds number. This confirms a conclusion of chapter 6 that heat transfer enhancement is viable, and is consistent with the position that the optimal perturbation excites and feeds energy into the global wake mode.

In order to determine the range of driving frequencies where appeciable heat transfer enhancement is generated, a full width at half maximum (FWHM) anal-

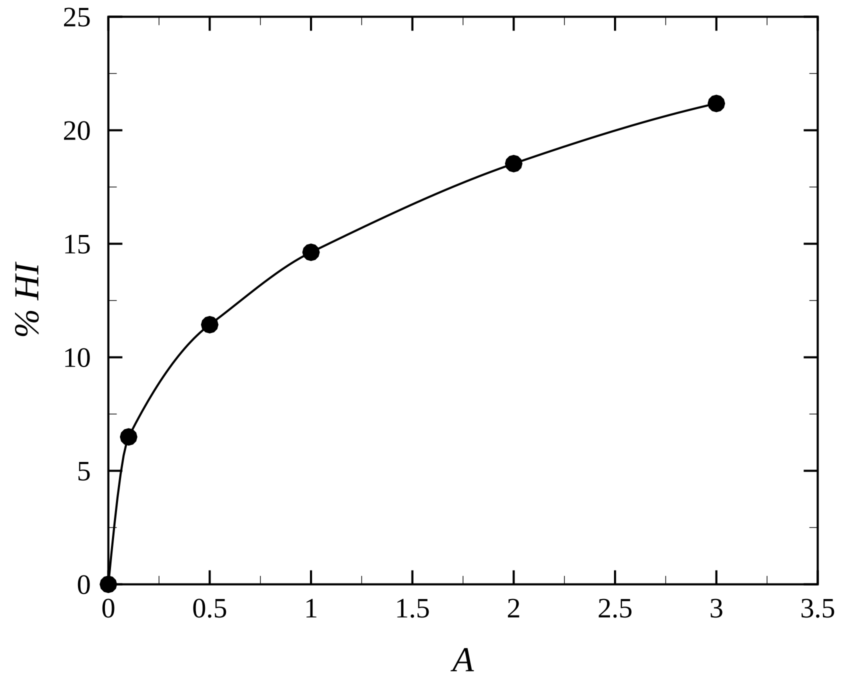

FIGURE 7.7: The percentage increase to the heat transfer generated by oscillating a cylinder in the duct as a function of velocity amplitude of the cylinder for $Re = 1075$ and $Ha^{\star} = 50$.

ysis is applied. The full width at half maximum is a parameter usually used to describe the width of a peak of a function (Smith 2003). It is given by the frequency range at which the function reaches half its maximum value as indicated in Fig. 7.9. A smaller FWHM corresponds to a narrower frequency bandwidth and vice versa for larger FWHM. The details of FWHM obtained at different amplitudes are listed in Table 7.2. These are represented relative to the zero-oscillation baseline $Nu_s = 2.15$. The results show that FWHM almost doubles as the forcing frequency is increased from 0.1 to 3. Thus at large amplitude, the range of forcing frequencies that produce significant heat transfer improvement is higher than for small amplitudes.

7.4 Flow Structure and Heat Transfer

In this section, the effect of a torsional cylinder oscillation on the flow structure and heat transfer are examined. Vorticity contours for different frequency

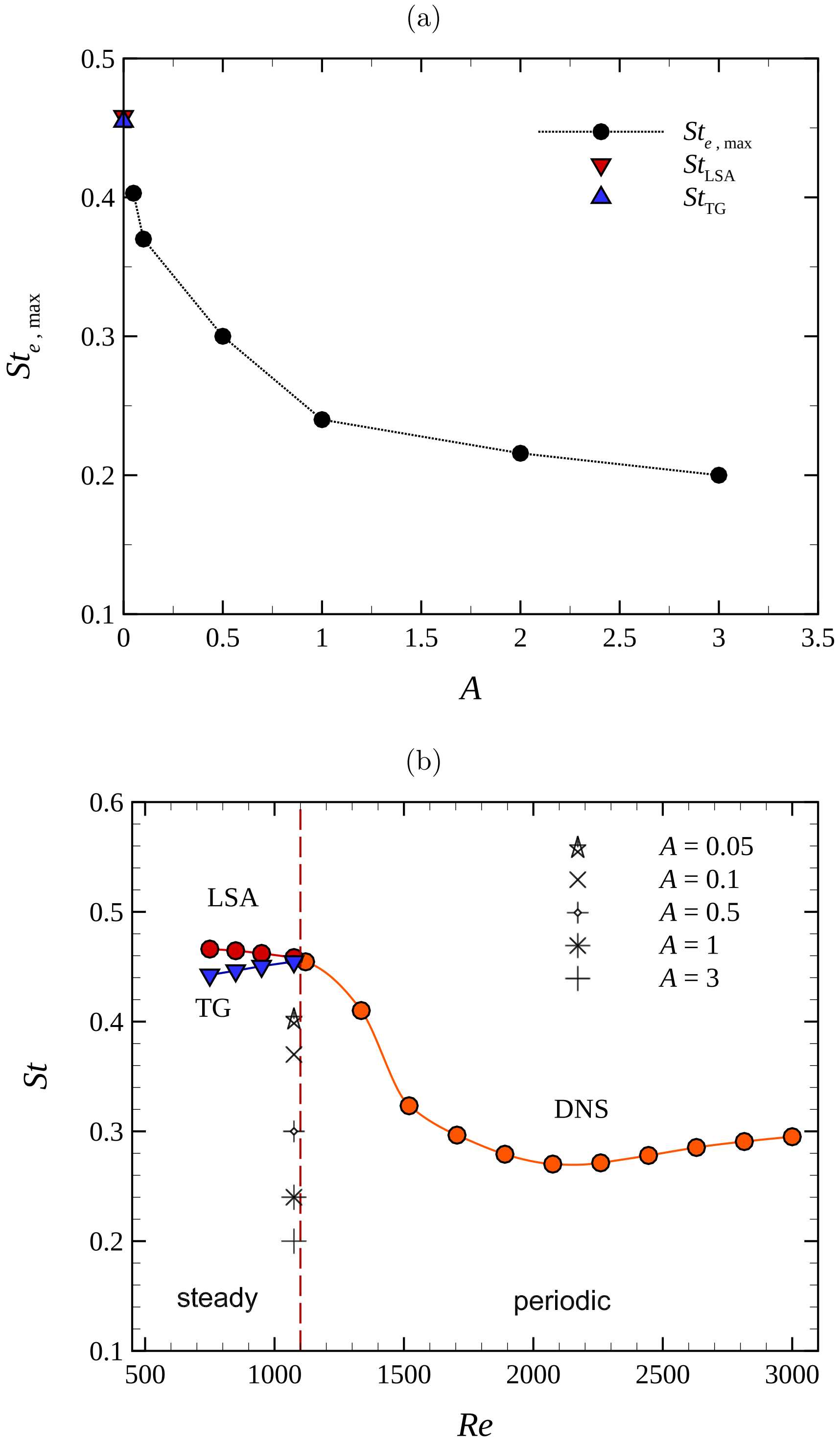

FIGURE 7.8: (a) A plot of oscillation frequency for maximum Nusselt number ($St_{e,\max}$) as a function of angular velocity amplitude of the cylinder. (b) A plot of shedding frequency St against Re showing the natural frequency predicted by linear stability, DNS and transient growth analyses, as labelled. The data from (a) is included at $Re = 1075$ for comparison.

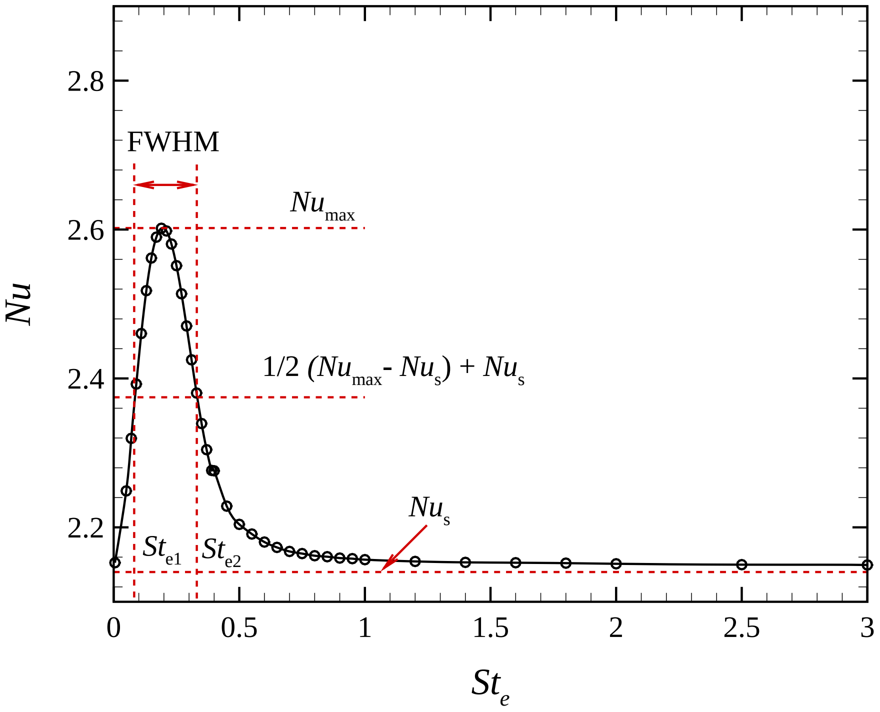

FIGURE 7.9: Estimation of full width at half maximum FWHM of frequencies at $A = 3$ for $Re = 1075$ and $Ha^{\star} = 50$.

amplitudes at the frequency of maximum heat transfer augmentation are shown in Figs. 7.10-7.13 (parts $\mathrm{b_i} - \mathrm{e_i}$). Each set of figures show results for a different amplitude A, compared to those for a stationary cylinder. Snapshots are provided at each quarter of an oscillation cycle. For stationary case, the flow is characterized by a pair of a symmetric counter-rotating vortices on the either side of the wake centerline. The temperature field is time-independent, and steady structures observed in the thermal boundary layer.

A	Half max.$\boldsymbol{Nu_{\mathbf{max}}}$	$\boldsymbol{St}_{e1}$	$\boldsymbol{St}_{e2}$	FWHM
0.1	2.2171	0.3016	0.4287	0.1271
0.5	2.2702	0.2038	0.3896	0.1858
1.0	2.3044	0.1501	0.3798	0.2298
3.0	2.3747	0.0865	0.3358	0.2493

TABLE 7.2: Calculated full width at half maximum FWHM Strouhal number ranges at different oscillation amplitudes for $Re = 1075$ and $Ha^{\star} = 50$.

At the lowest amplitude of oscillation ($A = 0.1$), a pattern of wake shedding is produced that closely resembles natural vortex shedding in an unperturbed flow above the critical Reynolds number. Note in particular that successive alternately shed vortices align approximately in a single row. These advecting vortices weakly interact with the wall boundary layers as they travel downstream (note the visible variation in wall boundary layer thickness between approximately 1 and $5d$ downstream of the cylinder). Considering Fig. 7.11, as the cylinder oscillation amplitude is increased to $A = 0.5$, the vortex formation length shortens and the vortices move closer to channel side walls as as they convect downstream. In addition, the intensity of vortices increases. The wall shear layers start to entrain inwards to interact with the vortices shed from the cylinder. This effect is further pronounced at $A = 1$ (Fig. 7.12), whereas by $A = 3$ (Fig. 7.13) the wall shear layers roll up into opposite-sign vortices that pair with wake vortices. These counter-rotating vortex pairs then self-propel inwards from the walls, explaining the increasing heat transfer enhancement with increasing A. It can also be speculated that the reason for the diminishing heat transfer enhancement at larger A may be because this mechanism for inciting advection of the fluid away from the heated wall has a limited capacity for enhancement, and has likely been likely exhausted by $A = 3$.

In order to better characterize the effect of the vortex patterns on the wall heat transfer, corresponding temperature contours are presented in Figs. 7.10-7.11 (parts $\mathrm{b_{ii}} - \mathrm{e_{ii}}$). The wavy structures observed in the thermal boundary layers are due to the cross-stream mixing induced by the presence of advecting vortices. The net effect is for low-temperature fluid to be transported toward the hot region of the channel and the high-temperature fluid near the heated wall to be convected away to mix with the low-temperature fluid. This process enhances the mixing between the heated surface and the cold fluid, and as a result the heat transfer is significantly enhanced compared to the stationary cylinder.

Fig. 7.14 presents the distribution of the local Nuselt number Nu_w along the heated surface as a function of stream-wise coordinate x for different oscillation amplitudes. It is found that the effect of oscillation amplitude on the distribution

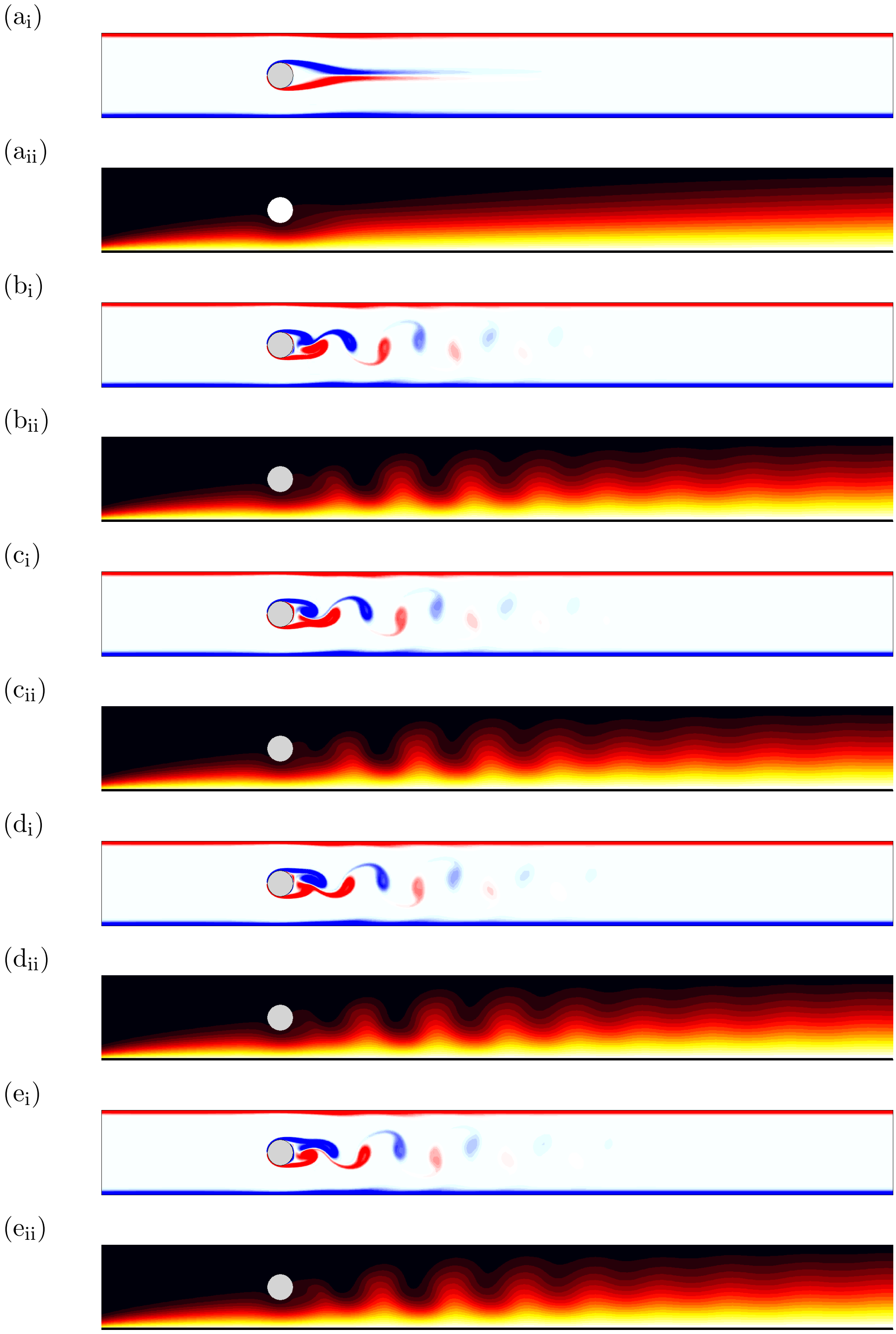

FIGURE 7.10: Vorticity and temperature contours plots for fixed and torsional oscillating in a channel for $Re = 1075$, $Ha^{\star} = 50$ and $\beta = 0.3$. Fixed cylinder (a$_{\rm i}$,a$_{\rm ii}$). Rotating oscillating cylinder for one oscillating cycle at $A = 0.1$ for maximum frequency: (b$_{\rm i}$,b$_{\rm ii}$) $t = t_0 + T_e/4$, (c$_{\rm i}$,c$_{\rm ii}$) $t = t_0 + 2T_e/4$, (d$_{\rm i}$,d$_{\rm ii}$) $t = t_0 + 3T_e/4$ and (e$_{\rm i}$,e$_{\rm ii}$) $t = t_0 + T_e$. In the vorticity plots, red and blue contours show positive and negative vorticity, and in the temperature plots, yellow is hot and black is cold fluid, respectively.

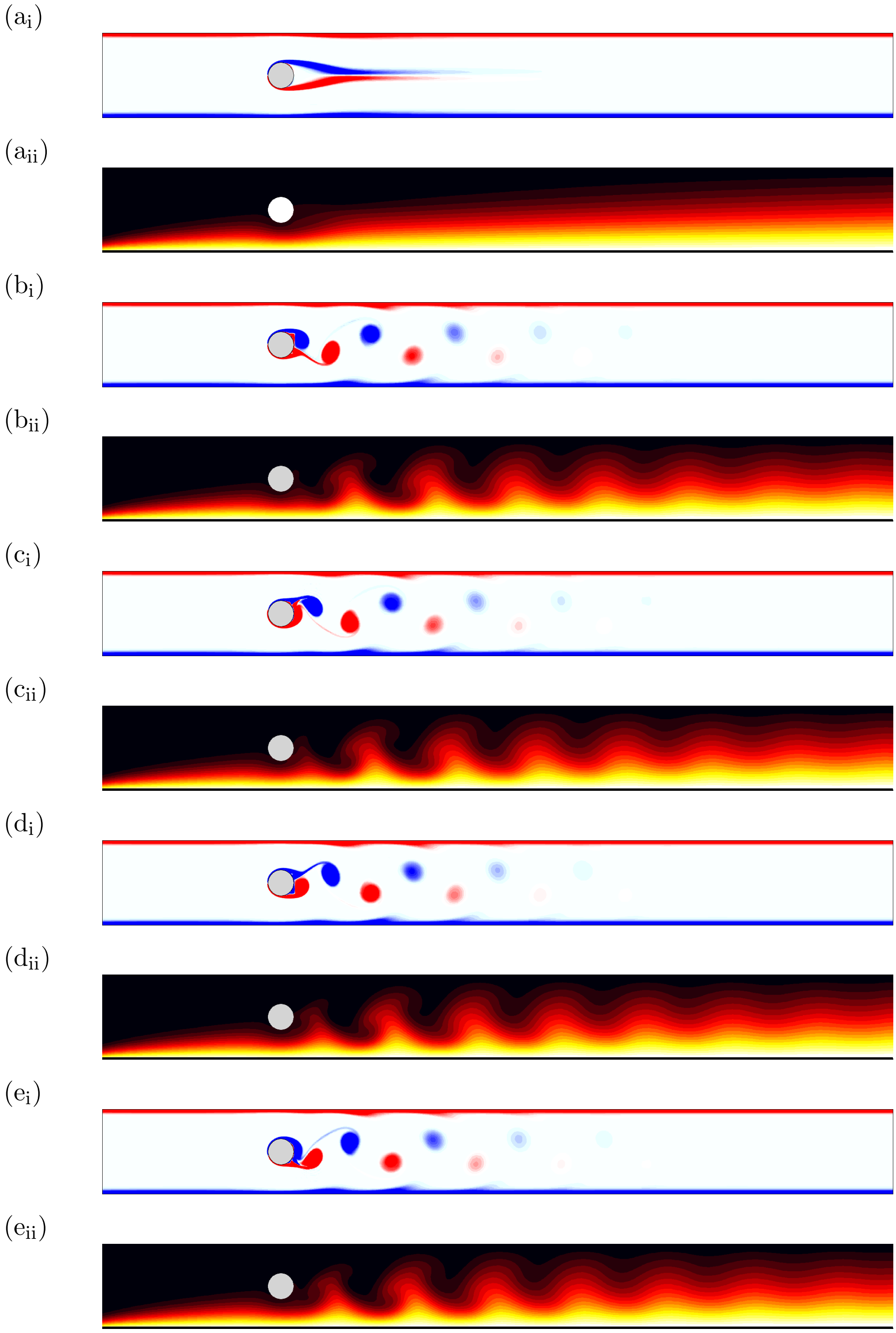

FIGURE 7.11: Vorticity and temperature contours plots for fixed and torsional oscillating in a channel for $Re = 1075$, $Ha^\star = 50$ and $\beta = 0.3$. Fixed cylinder (a_i,a_{ii}). Rotating oscillating cylinder for one oscillating cycle at $A = 0.5$ for maximum frequency: (b_i,b_{ii}) $t = t_0 + T_e/4$, (c_i,c_{ii}) $t = t_0 + 2T_e/4$, (d_i,d_{ii}) $t = t_0 + 3T_e/4$ and (e_i,e_{ii}) $t = t_0 + T_e$. Contours and shading are as per Fig. 7.10.

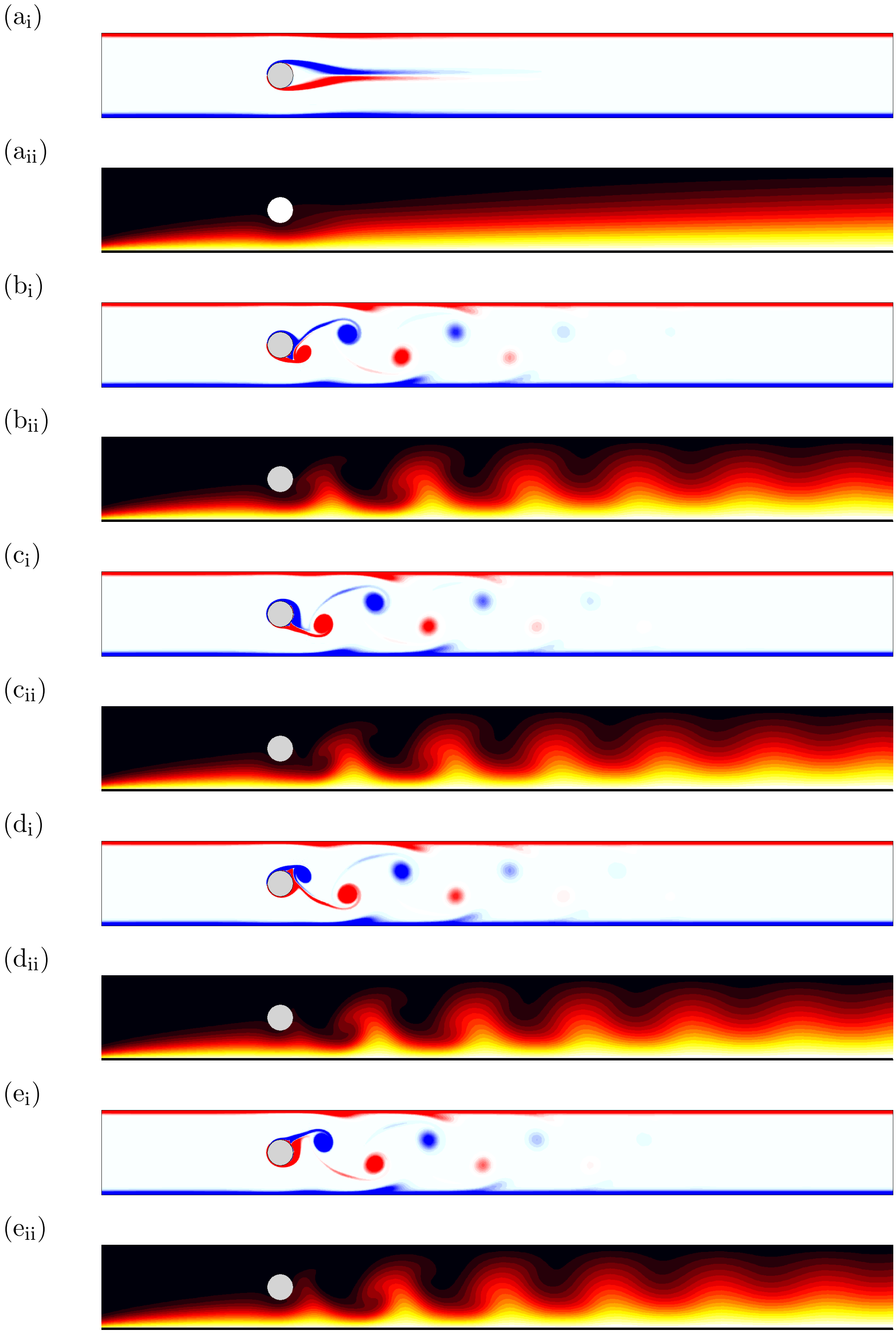

FIGURE 7.12: Vorticity and temperature contours plots for fixed and torsional oscillating in a channel for $Re = 1075$, $Ha^\star = 50$ and $\beta = 0.3$. Fixed cylinder (a$_\mathrm{i}$,a$_\mathrm{ii}$). Rotating oscillating cylinder for one oscillating cycle at $A = 1$ for maximum frequency: (b$_\mathrm{i}$,b$_\mathrm{ii}$) $t = t_0 + T_e/4$, (c$_\mathrm{i}$,c$_\mathrm{ii}$) $t = t_0 + 2T_e/4$, (d$_\mathrm{i}$,d$_\mathrm{ii}$) $t = t_0 + 3T_e/4$ and (e$_\mathrm{i}$,e$_\mathrm{ii}$) $t = t_0 + T_e$. Contours and shading are as per Fig. 7.10.

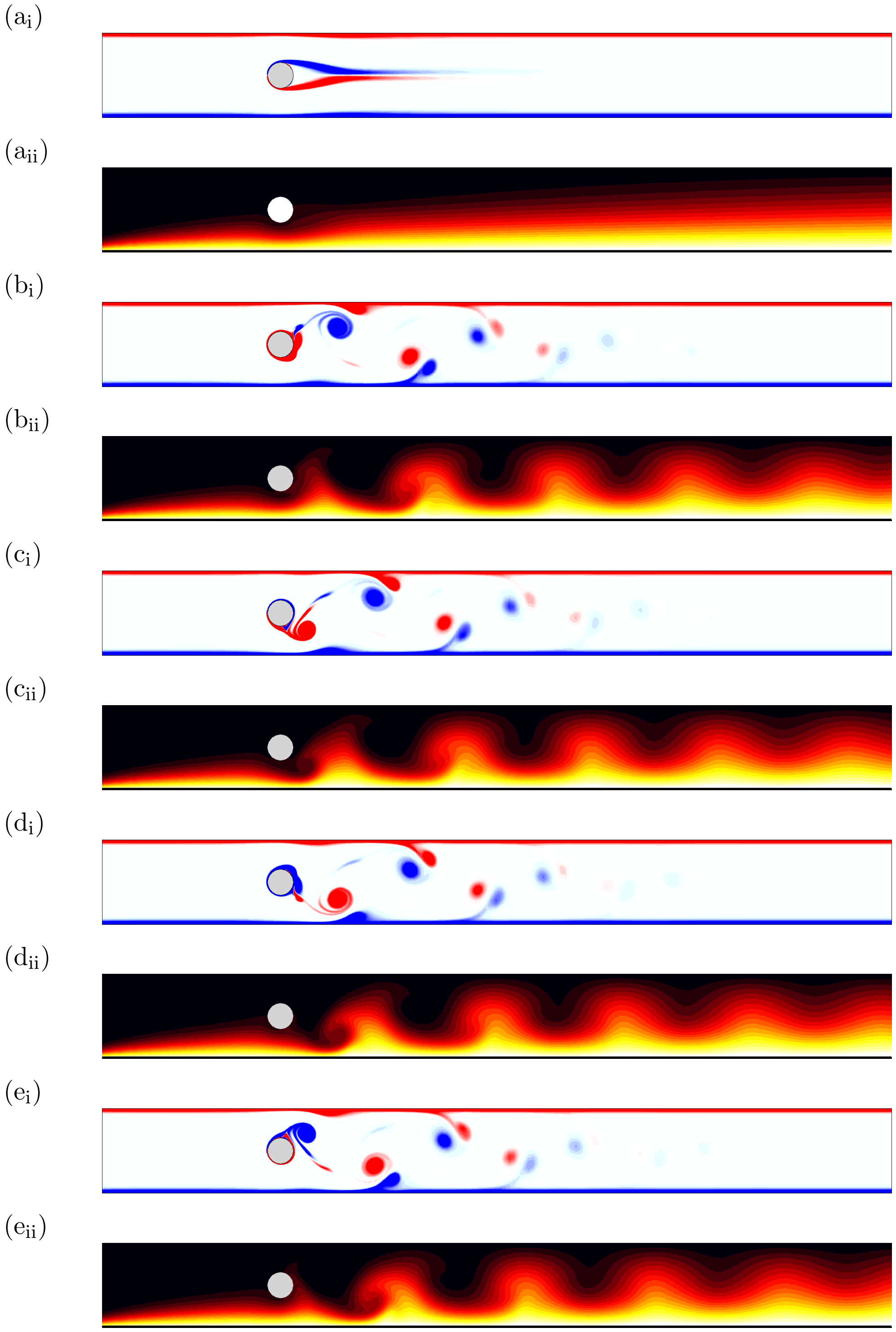

FIGURE 7.13: Vorticity and temperature contours plots for fixed and torsional oscillating in a channel for $Re = 1075$, $Ha^\star = 50$ and $\beta = 0.3$. Fixed cylinder (a$_\mathrm{i}$,a$_\mathrm{ii}$). Rotating oscillating cylinder for one oscillating cycle at $A = 3$ for maximum frequency: (b$_\mathrm{i}$,b$_\mathrm{ii}$) $t = t_0 + T_e/4$, (c$_\mathrm{i}$,c$_\mathrm{ii}$) $t = t_0 + 2T_e/4$, (d$_\mathrm{i}$,d$_\mathrm{ii}$) $t = t_0 + 3T_e/4$ and (e$_\mathrm{i}$,e$_\mathrm{ii}$) $t = t_0 + T_e$. Contours and shading are as per Fig. 7.10.

of Nusselt number along the heated wall is significant. The figure shows that as A is increased, there is a progressive increase in Nu_w over a region extending from the cylinder to a distance downstream of the cylinder. It can also be seen that the duct wall region over which the local Nusselt number is increased (compared to the $A = 0$) moves upstream. i.e. As A is increased over 0.1, 0.5 and 1, the point of maximum increase in local Nusselt number advances upstream from approximately $x/d = 10$ to 5 (see Fig. 7.14b). The large oscillation velocity amplitude ($A = 3$) also produces maximum increase in Nu_w at approximately $x/d = 5$, but it is also notable that unlike the lower oscillation velocity amplitudes, $A = 3$ shows significantly increased local Nusselt number near to the cylinder (i.e. $1 \lesssim x/d \lesssim 2.5$). An explanation for this can be deduced from the vorticity plots shown in Figs. 7.10-7.13. These figures show that for $A = 3$, the wake vortices are cast to the side walls much nearer to the cylinder than for the smaller amplitudes. As a result, the highest local Nusselt number is observed for the $A = 3$ case. On the other hand, the local Nusselt number measurements upstream of the cylinder are coincident for all velocity amplitudes, where the flow and heat transfer characteristics are very similar. This demonstrates that the heat transfer enhancement benefit is only felt downstream of the cylinder, and this is also reflected in Figs. 7.10-7.13, where no visible differences are apparent in the vorticity and temperature fields upstream of the cylinder.

A notable observation from Fig. 7.14 is that the enhancement to heat transfer is higher in the near wake region, where the wake vortices are strongest. Further downstream these vortices decrease in strength rapidly due to Hartmann damping, and the local Nusselt number again approaches that for the steady wake case. The predicted enhancement to the time-averaged Nusselt number was based on using the entire computational domain length to calculate the spatial average; however, perhaps a more physically based averaging length would be the active wake region. In practice, there would be no reason to just use a single cylinder to enhance heat transfer, i.e. more cylinders could be positioned along the duct centreline to regenerate the wake.

Figs. 7.10-7.13, show that the wake vortices are clearly discernible for only

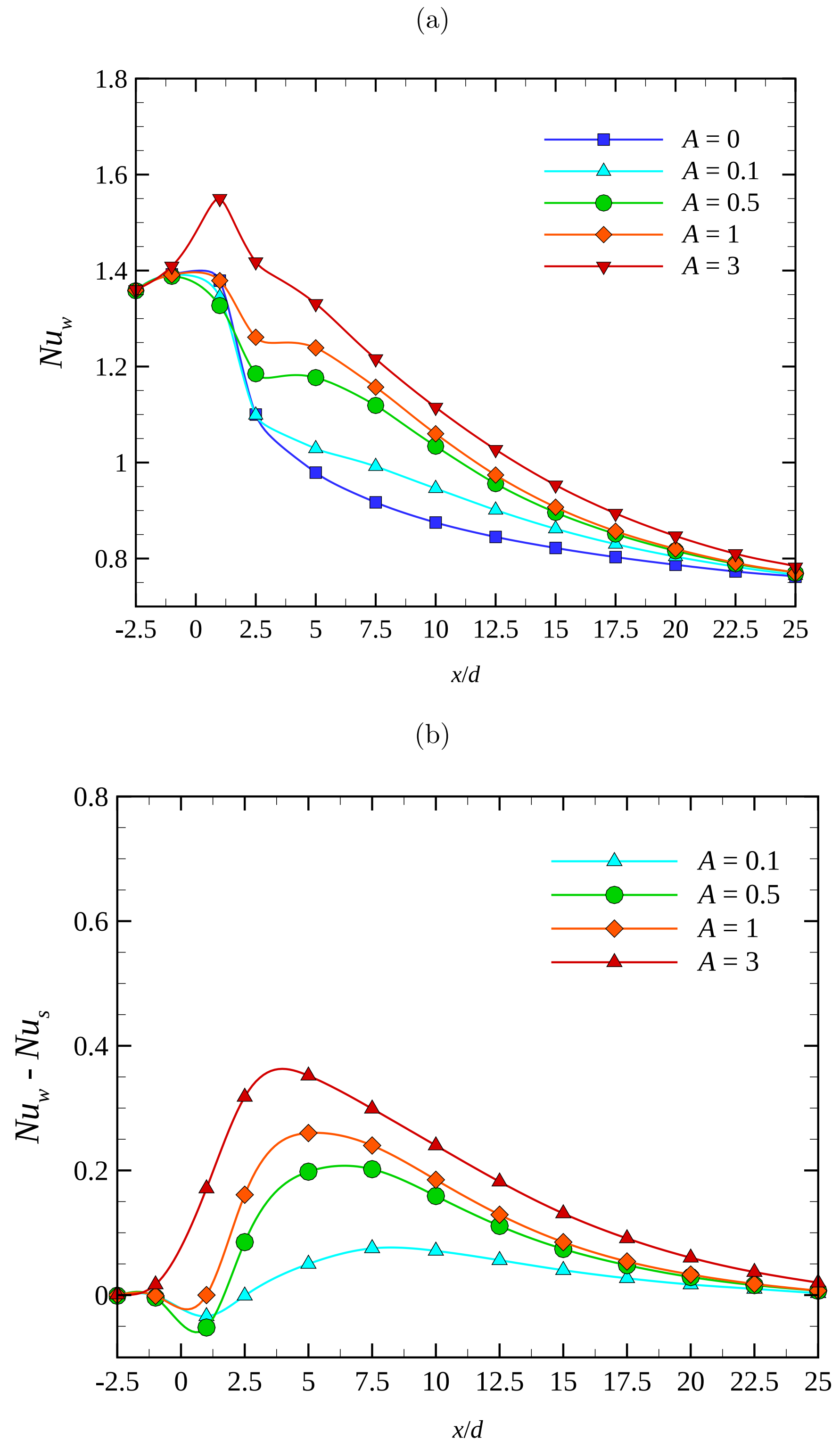

FIGURE 7.14: (a) Local Nusselt number over the heated surface of the side wall and (b) the difference $Nu_w - Nu_s$ as a function of x/d at different oscillation amplitudes for maximum frequency at $Re = 1075$ and $Ha^{\star} = 50$.

approximately 10 cylinder diameters downstream. For example, for small and large velocity amplitudes ($A = 0.1$ and $A = 3$), the ratio between the vorticity at 10 cylinder diameters to that of maximum vorticity $\omega_{x=10d}/\omega_{\max} \approx 0.1$ and 0.04, respectively. Reducing the spatial averaging length to just the $10d$ immediately downstream of the cylinder increases the heat transfer enhancement over the base case from 22% to 33% for $A = 3$. For the other rotation speeds the enhancement is also approximately 50% more.

7.5 Power Requirements

Consideration is now given to the mechanical power required to oscillate the cylinder about its axis. The moment of inertia of the cylinder, friction in bearings and other mechanical losses are not considered. Only the power required to overcome the moment exerted by the flow on the cylinder is considered. Mathematically, this can be determined from the dot product of the moment exerted by the fluid on the cylinder and its angular velocity vector as

$$P(t) = -\mathbf{M}(t) \cdot \dot{\boldsymbol{\theta}}_{\mathrm{cyl}}(t), \tag{7.2}$$

where the negative sign appearing in equation (7.2) indicates that the power is added to the system to drive the cylinder. Here both $\mathbf{M}$ and $\dot{\boldsymbol{\theta}}_{\mathrm{cyl}}$ are defined as counterclockwise positive. The time-averaged power is obtained by integrating the instantaneous power over a time using

$$P_{\mathrm{avg}} = \frac{-1}{t} \int_0^t \mathbf{M} \cdot \dot{\boldsymbol{\theta}}_{\mathrm{cyl}} \, \mathrm{d}t. \tag{7.3}$$

The time variation of the moment and mechanical power required to drive the cylinder for different velocity amplitudes at maximum frequency is presented in Fig. 7.15 for different velocity amplitudes at the maximum frequency. From Fig. 7.15(a), a significant phase-shift in the moment is observed as A increases. Therefore, it is expected that the power required to oscillate the cylinder grows substantially as A increases. The time variation of power in Fig. 7.15(b) indicates that the minimal power requirement occurs for $A = 0.5$. This is likely related to the fact that the forcing frequency at small amplitude approaches the frequency of global mode (see Fig. 7.8), resulting in the flow resembling that of stationary confined cylinder above the shedding transition.

To quantify the magnitude of oscillations in the moment time history, which are not necessarily perfectly sinusoidal, a root mean square (RMS) measure of the moment is employed, defined as

$$M_{\text{RMS}} = \sqrt{\frac{1}{t}\int_0^t [m(t)]^2 dt}. \tag{7.4}$$

It is found that M_{RMS} increases almost 321%, 682% and 1986% as A changes from 0.1 to 0.5, 1 and 3, respectively. The variation of M_{RMS} with A is shown in Fig. 7.16(a), which follows a power law relationship that is given by

$$M_{\text{RMS}} = 0.045\ A^{0.89}. \tag{7.5}$$

The variation in the time-averaged and maximum power are predicted in Fig. 7.16. The figure reveals that the averaged and maximum powers increases significantly with increasing A, and they depend on approximately the 1.9^{th} power. The relation between the power and amplitude is found to be

$$P_{\text{max}} = 0.055\ A^{1.88}, \tag{7.6}$$

$$P_{\text{avg}} = 0.023\ A^{1.89}. \tag{7.7}$$

Interestingly, $P \propto A^{1.9}$ and $M \propto A^{0.9}$. In the other words, $P \propto M \times A$, which follows from equation (7.1) , as A is a measure of the angular velocity appearing in equation (7.2).

To quantify the power required to torsionally oscillate the cylinder against the flow, a comparison is made to the power required to pump the fluid through the channel. The time-averaged pumping power is calculated using the pressure drop across the channel for the fixed and torsionally oscillated cylinder. The pumping power $P_{\Delta p}$, listed in Table 7.3, increases with increasing velocity amplitude of the cylinder. Not suprisingly, the larger velocity amplitude ($A = 3$), results in only 3.5% increase in the pumping power compared to that for a stationary cylinder, and the power required to oscillate the cylinder is about two order of magnitudes lower than for the pumping power. Using the data given in Table 7.3, the increase

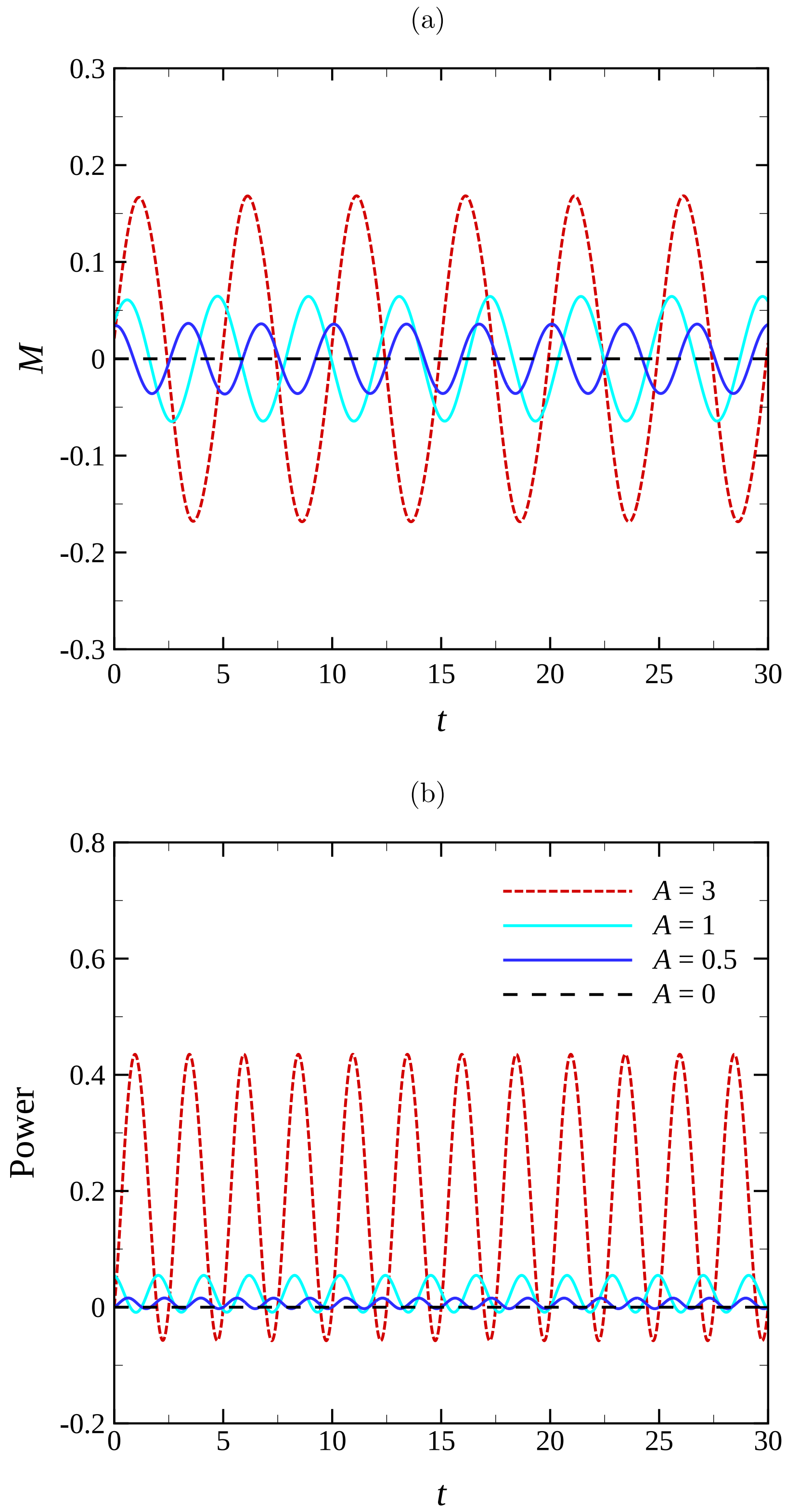

FIGURE 7.15: Time variation of (a) the moment and (b) the power required to drive the cylinder for $A = 0.5$, 1 and 3 at the optimal frequency.

(a)

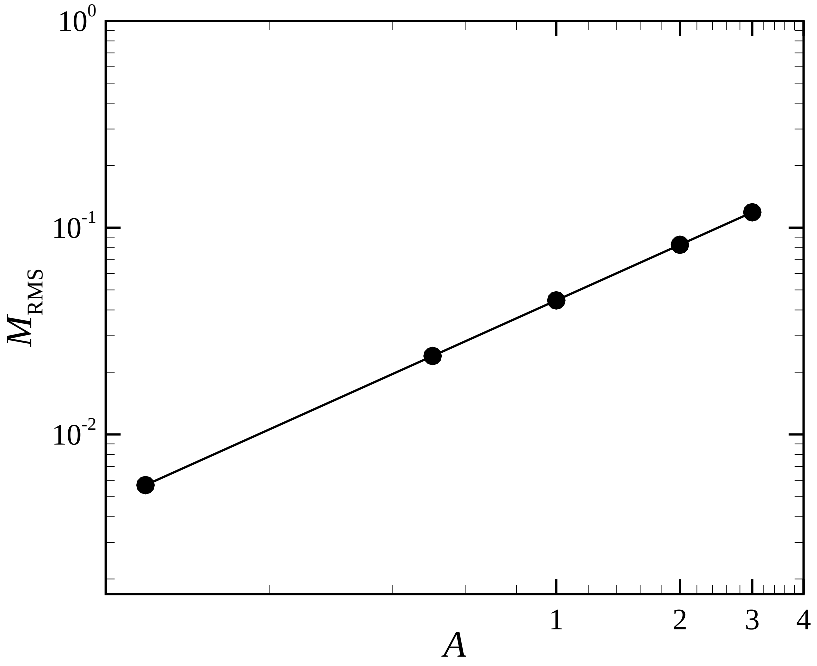

(b)

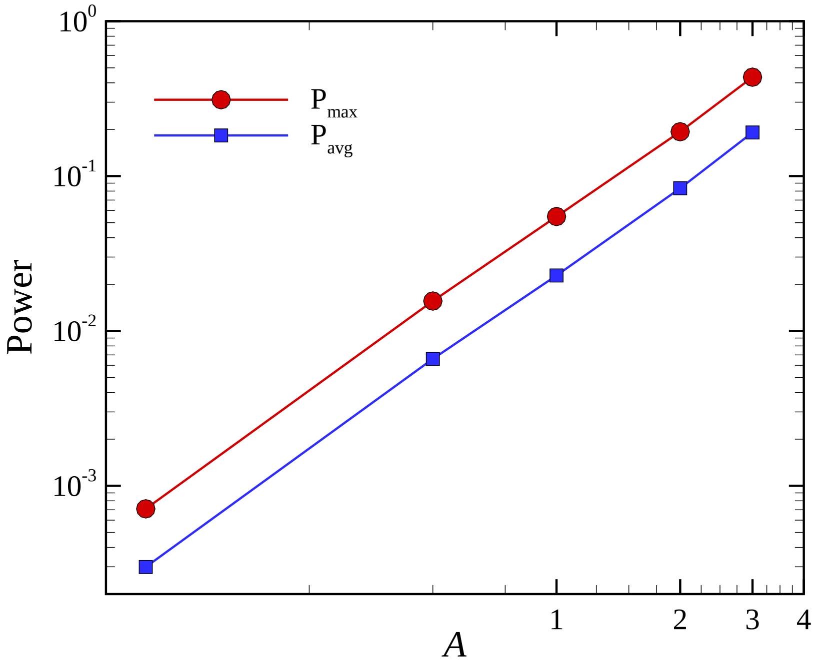

FIGURE 7.16: (a) The root mean square of the moment M_{RMS}, (b) time-averaged and maximum power required to drive the cylinder, both plotted on logarithmic scales against A.

A	$P_{\Delta p}$	P_{avg}
0.0	1.93	0.0
0.1	1.94	2.99×10^{-4}
0.5	1.96	6.60×10^{-3}
1.0	1.97	2.28×10^{-2}
3.0	2.01	1.91×10^{-1}

TABLE 7.3: Pumping power required to drive fluid in the channel ($P_{\Delta P}$) and the time-averaged power required to oscillate the cylinder, for $Re = 1075$ and $Ha^{\star} = 50$.

in power compared with the stationary case are approximately 3% and 13% for $A = 1$ and 3, respectively. For $A \leq 0.5$, the increase is almost negligible.

7.6 Chapter Summary

In this chapter, a mechanism for heat transfer enhancement in the steady flow regime due to damping at high Hartmann number involving rotational oscillation of a cylinder placed in a duct is proposed and investigated over a wide range of oscillation amplitudes and forcing frequencies. The motivation for exploring this mechanism was inspired by the transient growth analysis performed in the previous chapter, which indicated that the optimal disturbances are localized near the cylinder and are characterised by an asymmetrical disturbance with respect to the wake centreline.

The results show that there is a considerable increase in heat transfer from the heated channel wall due to rotational oscillation of the cylinder, with maximum enhancement of almost 22% observed for the highest amplitude case examined over steady flow, increasing to more than 30% in a zone extending $10d$ downstream of the cylinder. The range of St_e for effective enhancement was widened, and the frequency at which the peak Nusselt number occurred was shifted slightly to the lower frequency, as A was increased. It was found that as the amplitude was reduced, the optimal forcing frequency approached the frequency of the global mode. FWHM analysis showed that for the largest amplitude case the range of forcing frequencies that produced higher augmentation in heat transfer was approximately 100% larger than for the smallest amplitude case.

The wake vorticity and temperature contours were found to be closely related. As the amplitude was increased, the formation of strong discrete wake vortices induced the wall boundary layers to be drawn away from the walls enhancing heat transfer. The effect of oscillation amplitude on the distribution of local Nusselt number Nu_w along the heated wall was significant. For small A, the distribution was found to be similar to that for a fixed cylinder (i.e. $A = 0$). However, for large A, significant enhancement occurred in the cylinder near the wake before dropping away further downstream.

Calculations of the power required to oscillate the cylinder indicated that the demands of time-averaged and maximum power significantly increased as the velocity amplitude of oscillation increased from $A = 0.1$ to 3, and they depend on 1.89^{th} and 1.88^{th} power, respectively. For the largest amplitude, an increase in the pumping power was predicted compared to that for the stationary cylinder, the pumping power was increased 3.5%. The power required to oscillate the cylinder was about two order of magnitudes lower than that for pumping power.

Given that the improvement in heat transfer enhancement diminished with increasing A, and the that the power requirements increases more steeply with increasing A, it is apparent that there will certainly be a practical limit to the available benefit of implementing a mechanism such that proposed here. However, further exploration of these matters is beyond the scope of the present study.

Chapter 8

Conclusions and Recommendations for Future Work

A numerical study on the investigation of magnetohydrodynamic flows and heat transfer past a circular cylinder in a duct under a strong magnetic field parallel to the cylinder axis has been conducted using a spectral-element method. Under these conditions, the flow is quasi-two-dimensional and the modified Navier–Stokes equations are solved in a two–dimensional domain. The numerical simulations have been performed over a range of parameters including Reynolds numbers $50 \leq Re \leq 3000$, modified Hartmann number $50 \leq Ha^\star \lesssim 500$, and blockage ratios $0.1 \leq \beta \leq 0.5$. The few studies which have investigated similar flow systems in the past have presented either the vortex dynamics or the heat transfer enhancement at constant small blockage ratio. The present study provides a detailed investigation of the magnetohydrodynamic flows and heat transfer enhancement as well as the transient response of the flow over a wider range of blockage ratios. The major conclusions from this study are outlined below, along with some suggestions for future work.

8.1 Conclusions

The critical Reynolds number for the transition from steady to unsteady flow at different Hartmann numbers and blockage ratios was determined. It was found that it increases with increasing Hartmann number and blockage ratio. The increment in Re_c was more pronounced at high $Ha^\star$ and β.

In the steady flow regime, the effect of Hartmann number on the recirculation bubble was found to be more significant at high blockage ratio. For $\beta = 0.1$, the recirculation bubble is visible up to $Ha^\star = 120$, while it is suppressed completely beyond $Ha^\star \approx 500$ for $\beta = 0.4$. This was due to the consequence of Lorentz force, which produces a force opposing the flow resulting in a decrease of the wake length. The variation in the wake recirculation length is determined as a function of Reynolds number, Hartmann number and blockage ratio, and a universal scaling law is proposed as $L_R/d + 0.709 \propto Re^{0.844} Ha^{\star -0.711} \beta^{0.166}$.

In the unsteady flow regime, for small blockage ratio (i.e. $\beta \leq 0.2$) at $Ha^\star = 50$ and $Ha^\star = 120$, the structure of the vortex street was found to resemble vortex shedding behind a circular cylinder in open non-MHD flows, where regular positive and negative vortices shed alternately from the shear layer either side of the cylinder. For $\beta = 0.3$ and $Ha^\star = 50$, boundary layer entrainment of the Shercliff layers from the duct side walls occurs downstream of the cylinder, which was observed to increase gradually as the blockage ratio increases through 0.4 and 0.5. At these blockage ratios, the interaction between the Kármán vortex street and vortices detached from duct side walls creates an obstacle that impeded its downstream advection.

For $\beta \geq 0.3$ and $Ha^\star = 120$, the vortex street was observed to be completely suppressed. The recirculation regions had almost constant length and separation angle, and their shape changed little for $\beta = 0.4$ and 0.5.

For all β, it is found that the drag coefficient C_D firstly decreases and then increases as Reynolds number increases. The drag coefficient was dominated by the pressure contribution. This is a result of the effect of Hartman friction and the confinement of the wall which delay the transitions of the flow to a higher Reynolds number. Therefore, the viscous contribution is much smaller than that of the pressure. For all blockage ratio, it was also found that at each blockage ratio the data collapse onto universal curves at lower values of $Re/Ha^{\star 0.8}$.

The heat transfer from the heated wall was significantly dependent on the Hartmann number and blockage ratio. It was found that it increased substantially as blockage ratio was increased at $Ha^\star = 50$ while it increased gradually for $Ha^\star = 120$. Downstream cross-stream mixing induced by the cylinder wake was found to increase heat transfer from the heated wall by more than a factor of two in some cases when compared to the steady-state duct flow.

The distribution of local Nusselt number along the heated wall of the duct, Nu_w, was found to be independent on Hartamnn number for small blockage ratios (i.e. $\beta \leq 0.2$) while for high blockages, the change in Nu_w was remarkable with changing Hartmann number. The results also demonstrated that the curves of Nu_w collapse to a single curve at high Hartmann number and small blockage ratio.

The proximity of the cylinder to the heated wall has significant effects on both the flow and heat transfer. For $\beta = 0.1$, a two-row vortex street is formed with clockwise negative and counter-clockwise positive vortices shed from the top and the bottom shear layers of the cylinder, respectively. For $\beta \geq 0.2$, the structure of the vortex shedding changes dramatically on further decreases of gap ratio. The vortex street drifts farther away from the wall and is convects along over the entire downstream region. For high blockage ratio at $\gamma \geq 0.5$, the shear layer along the lower side of the cylinder and the shear layer along the wall merge and roll up together downstream. At the smallest gap ratio, the wake vorticity on the upper side of the cylinder elongates farther downstream.

The heat transfer enhancement depends strongly on the proximity of the cylinder to the heated wall. This is due to interaction of the lower wall shear layer with that on the cylinder surface. For small blockage ratio, it increases significantly as the gap ratio decreases from 1 to 0.25. However, there is a substantial drop in heat transfer for high blockage ratio. Overall, the enhancement of heat transfer was significantly augmented by 58%, 79% and 85%, respectively, by decreasing the gap ratio for blockage ratios $\beta \leq 0.2$. In contrast, for $\beta = 0.4$, the maximum heat transfer augmentation was more than a factor of two (128%) at $\gamma = 1$ (i.e. when the cylinder is far from the wall). Therefore, placing the cylinder in the channel near the heated wall will not lead to a large pressure drop, but the action of vortex shedding near the heated wall will improve the heat transfer.

For all blockage ratios, a very significant transient energy growth was found in the subcritical regime below the onset of the Kármán vortex shedding. The optimal disturbance field is consistently concentrated near the cylinder around the limiting streamline identifying the recirculation bubble, and is consistent with an asymmetrical disturbance with respect to the horizontal centreline of the system. This suggests a potential for the design of actuation mechanisms to invoke vortex shedding at low Reynolds numbers and thus enhance the heat transfer from the heated surface in ducts using a perturbation introduced through the cylinder.

The energy amplification of the disturbances was found to decrease significantly with increasing Hartmann number and led to a shift of the peak growth towards smaller times. This is due to the reduction of perturbation kinetic energy by Hartmann damping. Conversely, the global maximum of energy was found to increase significantly with increasing blockage ratio. This is due to the increased acceleration of the flow in the neighborhood of the cylinder for higher blockage ratios, making the Reynolds number effectively higher for higher β, although increasing β also shortens the separation bubble length as well. The structure of the disturbance was found to be consistent across all blockage ratios being tested. The perturbation convects along the separating region being amplified to the peak growth state downstream of the recirculation bubble. The resulting time interval for maximum growth $\tau_{\max}$ was found to increase significantly as recirculation length increases which demonstrates the amplifying nature of the separated shear layers in the wake. This phenomenon is consistent with transient growth in several systems for non MHD flows.

The critical Reynolds number for positive energy growth of the optimal disturbance Re_{c1} was found to increase significantly with increasing blockage ratio and Hartmann number. The optimal disturbances at $Re \leq Re_{c1}$ monotonically decreased with τ, while for $Re \geq Re_{c1}$ the energy of an optimal disturbance increases rather than decreases from its initial value. For all β, it is found that $G_{\max}$ grows exponentially with Re at low and high Harmann numbers.

Direct numerical simulation in which the inflow was perturbed by white noise demonstrated that the optimal transient growth properties of the flow could be activated by continuous upstream random perturbations, which result in a significant amplification of the disturbances as they pass around the cylinder. This is sufficient to destabilize the wake through the global instability mode responsible for producing the von Kármán wake, despite the simulation being run at conditions below the critical Reynolds number for vortex shedding.

A mechanism for heat transfer enhancement from the heated surface in ducts in the Hartmann-damped steady flow regime involving rotational oscillation of the cylinder is proposed to invoke unsteady flow at low Reynolds numbers, and thus enhance the heat transfer using a perturbation introduced through the cylinder. The motivation for choosing this mechanism was inspired from the transient growth analysis reported in this thesis, which indicated that the optimal disturbances are localized near the cylinder and are characterized by an asymmetrical disturbance with respect to the wake centreline.

It was found that there was a considerable increase in heat transfer from the heated channel wall due to rotational oscillation of the cylinder, with maximum enhancement of $\simeq 30\%$ observed at higher amplitude than that of steady flow if only the section of the wall adjacent to the vortex rollers in the wake is considered.

It is found that as the angular velocity of oscillation A increases, the forcing frequency range for effective enhancement and the frequency at which the peak of Nusselt number occurs is shifted slightly to a lower frequency. The frequencies predicted by linear stability analysis and those by transient growth analysis are very close, and they intersect near the transition, which confirms the fact concluded by transient growth analysis that heat transfer enhancement is viable, the optimal perturbation excites and feeds energy into the global mode.

8.2 Future Work

It is hoped that the present investigation has provided some understanding of the dynamics and heat transfer of a magnetohydrodynamic flow past a circular cylinder confined in a duct under a strong magnetic field. However, it has in turn raised a number of questions that present potential avenues for further study. These include:

- Investigations should performed on the flow past a cylinder with square or triangular cross-sections at different angles of attack to compare the dynamics of the flow and level of heat transfer augmentation obtained to that of a circular cylinder.

- For small blockage ratios, the effect of placing two or more tandem cylinders near the heated wall on the flow and heat transfer characteristics will be important as the length of ducts used for these flows is long. This may reveal other states of shedding of fundamental interest.

- The effect of varying duct aspect ratio may affect the flow transitions and heat transfer characteristics.

- A fully three–dimensional study is required to investigate the influence of the weak three-dimensionality in the Shercliff layers for certain values of Re, $Ha^\star$ and β. A three–dimensional linear stability analysis is desirable for a condition of high blockage and offset ratio to verify whether the base flow is genuinely two–dimensional.

References

ABDESSEMED, N., SHARMA, A. S., SHERWIN, S. J. & THEOFILIS, V. 2009a Transient growth analysis of the flow past a circular cylinder. *Phys. Fluids* **21** (4), 044103.

ABDESSEMED, N., SHERWIN, S. J. & THEOFILIS, V. 2009b Linear instability analysis of low-pressure turbine flows. *J. Fluid Mech.* **628**, 57–83.

ACRIVOS, A., LEAL, L. G., D.SNOWDEN, D. & PAN, F. 1968 Further experiments on steady separated flows past bluff objects. *J. Fluid Mech.* **34**, 25–48.

AIRIAU, C. & CASTETS, M. 2004 On the amplification of small disturbances in a channel flow with a normal magnetic field. *Phys. Fluids* **16** (8), 2991–3005.

ALBARÈDE, P. & MONKEWITZ, P. 1992 A model for the formation of oblique shedding and chevron patterns in cylinder wakes. *Phys. Fluids A* **4**, 744–756.

ANAGNOSTOPOULOS, P., ILIADIS, G. & RICHARDSON, S. 1996 Numerical study of the blockage effects on viscous flow past a circular cylinder. *Int. J. Numer. Meth. Fl.* **22** (11), 1061–1074.

ANDREEV, O. V. & KOLESNIKOV, Y. 1993 Possibilities of heat transfer intensification to the MHD problems of liquid metal fusion blankets. In *The Seventh International Beer Sheva Seminar on MHD Flows and Turbulence*. Jerusalem, Israel.

ANDREEV, O. V. & KOLESNIKOV, Y. 1997a Experimental flow around a conducting cylinder in an axial homogeneous magnetic field. *Magnetohydrodynamics* **34**, 286–293.

ANDREEV, O. V. & KOLESNIKOV, Y. 1997b MHD instabilities at transverse flow around a circular cylinder in an axial magnetic field. In *Transfer Phenomena in Magnetohydrodynamic and Electroconducting Flows: Selected Papers of the PAMIR Conference held in Aussois, France, 22-26 September, 1997* (ed.

A. Alemany, P. Marty & J. P. Thibault), *Fluid Mechanics and its Applications*, vol. 51, pp. 205–210. Aussois, France: Kluwer Academic Publishers, ISBN: 978-3-642-03085-7.

Baek, S.-J. & Sung, H. 1998 Numerical simulation of the flow behind a rotary oscillating circular cylinder. *Phys. Fluids* **10**, 869–876.

Barkley, C., Blackburn, H. & Sherwin, S. 2008a Direct optimal growth analysis for timesteppers. *Int. J. Numer. Meth. Fl.* **57**, 1435–1458.

Barkley, D., Blackburn, H. M. & Sherwin, S. J. 2008b Direct optimal growth analysis for timesteppers. *Int. J. Numer. Meth. Fl.* **57**, 1435–1458.

Barkley, D. & Henderson, R. D. 1996 Three-dimensional Floquet stability analysis of the wake of a circular cylinder. *J. Fluid Mech.* **322**, 215–241.

Barleon, L., Burr, U., Mack, K. & Stieglitz, R. 2001 Magnetohydrodynamic heat transfer research related to the design of fusion blankets. *Fusion Techn.* **39**, 127–156.

Barleon, L., Burr, U., MacK, K.-J. & Stieglitz, R. 2000 Heat transfer in liquid metal cooled fusion blankets. *Fusion Eng. Des.* **51-52**, 723–733.

Barleon, L., Mack, K. J., Kirchner, R. & Stieglitz, R. 1995 Heat transfer in MHD-flow at high Hartmann numbers and improvement by turbulence promotions. *Magnetohydrodynamics* **31**, 328–337.

B.Celik & Beskok, A. 2009 Mixing induced by a transversely oscillating circular cylinder in a straight channel. *Phys. Fluids* **21**, 073601.

Bearman, P. W. & Zdravkovich, M. M. 1978 Flow around a circular cylinder near a plane boundary. *J. Fluid Mech.* **89** (01), 33–47.

Behr, M., Hastreiter, D., Mittal, S. & Tezduyar, T. E. 1995 Incompressible flow past a circular cylinder: Dependence of the computed flow field on the location of the lateral boundaries. *Comp. Meth. Appl. Mech. Eng.* **123** (1-4), 309–316.

Beskok, A. & Warburton, T. C. 2001 An unstructured hp finite-element scheme for fluid flow and heat transfer in moving domains. *J. Comput. Phys.* **174**, 492–509.

Biau, D., Soueid, H. & Bottaro, A. 2008 Transition to turbulence in duct flow. *J. Fluid Mech.* **596**, 133–142.

Blackburn, H. M., Barkley, D. & Sherwin, S. J. 2008a Convective instability and transient growth in flow over a backward-facing step. *J. Fluid Mech.* **603**, 271–304.

Blackburn, H. M. & Lopez, J. 2003 On three-dimensional quasiperiodic floquet instabilities of two-dimensional bluff body wakes. *Physics of Fluids* **15**, L57–L60.

Blackburn, H. M., Marques, F. & Lopez, J. M. 2005 Symmetry breaking of two-dimensional time-periodic wakes. *J. Fluid Mech.* **522**, 395–411.

Blackburn, H. M. & Sheard, G. J. 2010 On quasi-periodic and subharmonic Floquet wake instabilities. *Phys. Fluids* **22** (3), 031701.

Blackburn, H. M., Sherwin, S. J. & Barkley, D. 2008b Convective instability and transient growth in steady and pulsatile stenotic flows. *J. Fluid Mech.* **607**, 267–277.

Bloor, M. S. 1964 The transition to turbulence in the wake of a circular cylinder. *J. Fluid Mech.* **19**, 290–304.

Boeck, T., Krasnov, D., Rossi, M. & Zikanov, O. 2009 Transient growth in MHD duct flow. In *Advances in Turbulence XII* (ed. B. Eckhardt), *Springer Proceedings Physics*, vol. 132, pp. 829–832. Springer Berlin Heidelberg.

Branover, R. H. H. 1978 *Magnetohydrodynamic Flow in Ducts*. Halsted.

Bühler, L. 1996 Instabilities in quasi-two-dimensional magnetohydrodynamic flows. *J. Fluid Mech.* **326**, 125–150.

Burr, U., Barleon, L., Müller, U. & Tsinober, A. 2000 Turbulent transport of momentum and heat in magnetohydrodynamic rectangular duct flow with strong sidewall jets. *J. Fluid Mech.* **406**, 247–279.

Camarri, S. & Giannetti, F. 2010 Effect of confinement on three-dimensional stability in the wake of a circular cylinder. *J. Fluid Mech.* **642**, 477–487.

Cantwell, C. D. & Barkley, D. 2010 Computational study of subcritical response in flow past a circular cylinder. *Phys. Rev. E* **82** (2), 026315.

Cantwell, C. D., Barkley, D. & Blackburn, H. M. 2010 Transient growth analysis of flow through a sudden expansion in a circular pipe. *Phys. Fluids* **22** (3), 1–15.

Celik, B., Akdag, U., Gunes, S. & Beskok, A. 2008 Flow past an oscillating circular cylinder in a channel with an upstream splitter plate. *Phys. Fluids* **20**, 103603.

Celik, B., Raisee, M. & Beskok, A. 2010 Heat transfer enhancement in a slot channel via a transversely oscillating adiabatic circular cylinder. *Int. J. Heat Mass Trans.* **53**, 626–634.

Chakraborty, J., Verma, N. & Chhabra, R. P. 2004 Wall effects in flow past a circular cylinder in a plane channel: A numerical study. *Chem. Eng. Proc.* **43** (12), 1529–1537.

Chen, J. H., Pritchard, W. G. & Tavener, S. J. 1995 Bifurcation for flow past a cylinder between parallel planes. *J. Fluid Mech.* **284**, 23–41.

Chew, Y. T., Cheng, M. & Luo, S. C. 1995 A numerical study of flow past a rotating circular cylinder using a hybrid vortex scheme. *J. Fluid Mech.* **299**, 35–71.

Chomaz, J. M. 2005 Global instabilities in spatially developing flows: Non-normality and nonlinearity. *Annu. Rev. Fluid Mech.* **37** (1), 357–392.

Collins, W. M. & Dennis, S. C. R. 1973 Flow past an impulsively started circular cylinder. *J. Fluid Mech.* **60**, 105–127.

Coppola, G., Sherwin, S. J. & Peiró, J. 2001 Nonlinear particle tracking for high-order elements. *J. Comput. Phys.* **172**, 356–386.

Couder, Y. B. C. 1986 Experimental and numerical study of vortex couples in two-dimensional flows. *J. Fluid Mech.* **173**, 225–251.

Coutanceau, M. & Bouard, R. 1977a Experimental determination of the main features of the viscous flow in the wake of a circular cylinder in uniform translation. part 1. steady flow. *J. Fluid Mech.* **79**, 231–256.

Coutanceau, M. & Bouard, R. 1977b Experimental determination of the main features of the viscous flow in the wake of a circular cylinder in uniform translation. part 2. unsteady flow. *J. Fluid Mech.* **79**, 257–272.

Cuevas, S., Smolentsev, S. & Abdou, M. A. 2006 On the flow past a magnetic obstacle. *J. Fluid Mech.* **553**, 227–252.

Davidson, P. A. 1995 Magnetic damping of jets and vortices. *J. Fluid Mech.* **299**, 153–186.

Davidson, P. A. 1997 The role of angular momentum in the magnetic damping of turbulence. *J. Fluid Mech.* **336**, 123–150.

Davidson, P. A. 2001 *An Introduction to Magnetohydrodynamics*. Cambridge University Press.

Dennis, S. C. R. & Chang, G.-Z. 1970 Numerical solutions for steady flow past a circular cylinder at reynolds numbers up to 100. *J. Fluid Mech.* **42**, 471–489.

Dousset, V. & Pothérat, A. 2008 Numerical simulations of a cylinder wake under a strong axial magnetic field. *Phys. Fluids* **20** (1), 017104.

Dušek, J., Le, G. P. & Philippe, F. 1994 A numerical and theoretical study of the first hopf bifurcation in a cylinder wake. *J. Fluid Mech.* **264**, 59–80.

Farhadi, M., Sedighi, K. & Korayem, A. M. 2010 Effect of wall proximity on forced convection in a plane channel with a built-in triangular cylinder. *Int. J. Thermal Sci.* **49**, 1010–1018.

Frank, M., Barleon, L. & Müller, U. 2001 Visual analysis of two-dimensional magnetohydrodynamics. *Phys. Fluids* **13** (8), 2287–2295.

Fu, W.-S. & Tong, B.-H. 2004 Numerical investigation of heat transfer characteristics of the heated blocks in the channel with a transversely oscillating cylinder. *Int. J. Heat Mass Trans.* **47**, 341–351.

Gaster, M. 1971 Vortex shedding from circular cylinder at low reynolds numbers. *J. Fluid Mech.* **46**, 749–756.

Gerard-Varet, D. 2002 Amplification of small perturbations in a Hartmann layer. *Phys. Fluids* **14** (4), 1458–1467.

Gerrard, J. H. 1978 The wakes of cylindrical bluff bodies at low reynolds number. *Phil. Trans. Royal Soc. London A, Math. Phys. Sci.* **288** (1354), 351–382.

Giannetti, F. & Luchini, P. 2007 Structural sensitivity of the first instability of the cylinder wake. *J. Fluid Mech.* **581**, 167–197.

Gottlieb, D. & Orszag, S. A. 1977 *Numerical analysis of spectral methods: Theory and Applications*, , vol. 2. SIAM.

Griffith, M. D., Leontini, J., Thompson, M. & Hourigan, K. 2011 Vortex shedding and three-dimensional behaviour of flow past a cylinder confined in a channel. *J. Fluids Struct.* **615**, 221–252.

Grigoriadis, D. G. E., Sarris, I. E. & Kassinos, S. C. 2010 MHD flow past a circular cylinder using the immersed boundary method. *Comput. Fluids* **39** (2), 345–358.

Grove, A. S., shair, F. H., Petersen, E. E. & Acrivos, A. 1964 An experimental investigation of the steady separated flow past a circular cylinder. *J. Fluid Mech.* **19**, 60–80.

Hammache, M. & Gharib, M. 1991 An experimental study of the parallel and oblique vortex shedding from circular cylinders. *J. Fluid Mech.* **232**, 567–590.

Hartmann, J. 1937 Theory of the laminar flow of an electrically conductive liquid in a homogeneous magnetic field. *K. Dan. Vidensk. Selsk. Mat. Fys. Medd.* **15** (6), 1–28.

Hartmann, J. & Lazarus, F. 1937 Experimental investigations on the flow of mercury in a homogeneous magnetic field. *K. Dan. Vidensk. Selsk. Mat. Fys. Medd.* **15** (7), 1–45.

Henderson, R. D. 1997 Nonlinear dynamics and pattern formation in turbulent wake transition. *J. Fluid Mech.* **352**, 65–112.

Hill, D. C. 1992 A theoretical approach for analyzing the restabilization of wakes. In *30th AIAA Aero. Sci. Meeting and Exhibit*. Reno, NV, USA: National Aeronautics and Space Administration, Ames Research Center, National Technical Information Service, Moffett Field, CA, USA, AIAA Paper No 92-0067.

Hossain, M. A. 1992 Viscous and Joule heating effects on MHD-free convection flow with variable plate temperature. *Int. J. Heat Mass Trans.* **35**, 3485–3487.

Hsieh, T.-C. & Chen, J.-H. 2006 Emergence of attached recirculating eddy for flow around a circular cylinder asymmetrically placed in a channel. *J. Marine Sci. Techn.* **14**, 147–154.

Hunt, J. C. R. & Stewartson, K. 1965 Magnetohydrodynamic flow in rectangular ducts. II. *J. Fluid Mech.* **23**, 563–581.

Hussam, W. K., Thompson, M. C. & Sheard, G. J. 2011 Dynamics and heat transfer in a quasi-two-dimensional MHD flow past a circular cylinder in a duct at high Hartmann number. *Int. J. Heat Mass Trans.* **54** (5), 1091–1100.

Hussam, W. K., Thompson, M. C. & Sheard, G. J. 2012 Optimal transient disturbances behind a circular cylinder in a quasi-two-dimensional magnetohydrodynamic duct flow. *Phys. Fluids* **24** (2), 024150.

Incropera, F. P., Dewitt, D. P., Bergman, T. L. & Lavine, A. S. 2011 *Fundamentals of heat and mass transfer*. John Wiley.

Jackson, C. P. 1987 A finite-element study of the onset of vortex shedding in flow past variously shaped bodies. *J. Fluid Mech.* **182**, 23–45.

Josserand, J., Marty, P. & Alemany, A. 1993 Pressure and drag measurements on a cylinder in a liquid metal flow with an aligned magnetic field. *Fluid Dyn. Res.* **11** (3), 107–117.

Karniadakis, G. E., Israeli, M. & Orszag, S. A. 1991 High-order splitting methods for the incompressible Navier–Stokes equations. *J. Comput. Phys.* **97** (2), 414–443.

Karniadakis, G. E. & Sherwin, S. J. 2005 *Spectral/hp Element Methods for Computational Fluid Dynamics*. Oxford University Press.

Khan, W. A., Yovanovich, J. R. & Culham, M. M. 2004 Fluid flow and heat transfer from a cylinder between parallel planes. *J. Thermophys. Heat Tfr.* **18** (3), 395–403.

Kirillov, I. R., Reed, C. B., Barleon, L. & Miyazaki, K. 1995 Present understanding of MHD and heat transfer phenomena for liquid metal blankets. *Fusion Eng. Des.* **27**, 553–569.

Kit, L., Turntaev, S. & Tsinober, A. B. 1970 Investigation with a conducting anemeter of the effect of magnetic field on disturbances in the wake of a cylinder. *Magnetohydrodynamics* **6** (3), 331–335.

Kit, L. G., Kolesnikov, Y. B., Tsinober, A. B. & Shtern, P. G. 1969 Use of a conduction anemometer in investigating the MHD wake behind a body. *magnetohydrodynamics* **5**, 46–50.

Kolesnikov, Y. B. & Andreev, O. V. 1997 Heat-transfer intensification promoted by vortical structures in closed channel under magnetic field. *Exptl Thermal Fl. Sci.* **15**, 82–90.

Kolesnikov, Y. B. & Tsinober, A. B. 1971 Three-dimensional magnetohydrodynamic flow past a cylinder of finite length. *Magnetohydrodynamics* **7**, 271–273.

Kolesnikov, Y. B. & Tsinober, A. B. 1972a Two-dimensional turbulent flow behind a circular cylinder. *Magnetohydrodynamics* **8** (3), 300–307.

Kolesnikov, Y. B. & Tsinober, A. B. 1972b Two-dimensional turbulent flow in a channel with inhomogeneous electrical conductivity of the walls. *Magnetohydrodynamics* **8** (3), 23–31.

Kolesnikov, Y. B. & Tsinober, A. B. 1976 Experimental investigation of two-dimensional turbulence behind a grid. *Fluid Dyn.* **9**, 621–624.

Krasnov, D., Zikanov, O., Rossi, M. & Boeck, T. 2010 Optimal linear growth in magnetohydrodynamic duct flow. *J. Fluid Mech.* **653**, 273–299.

Krasnov, D. S., Zienicke, E., Zikanov, O., Boeck, T. & Thess, A. 2004 Numerical study of the instability of the Hartmann layer. *J. Fluid Mech.* **504**, 183–211.

Lahjomri, J., Capéran, P. & Alemany, A. 1993 The cylinder wake in a magnetic field aligned with the velocity. *J. Fluid Mech.* **253**, 421–448.

Landau, L. D. & Lifshitz, E. M. 1976 *Mechanics*. Pergamon Press.

Lei, C., Cheng, L., Armfield, S. W. & Kavanagh, K. 2000 Vortex shedding suppression for flow over a circular cylinder near a plane boundary. *Ocean Eng.* **27** (10), 1109–1127.

Lei, C., Cheng, L. & Kavanagh, K. 1999 Re-examination of the effect of a plane boundary on force and vortex shedding of a circular cylinder. *J. Wimd Eng. Industial. Aerodyn* **80** (3), 263–286.

Leontini, J., Thompson, M. & Hourigan, K. 2007 Three-dimensional transition in the wake of a transversely oscillating cylinder. *J. Fluid Mech.* **577**, 79–104.

Leweke, T. & Provansal, M. 1995 The flow behind rings bluff body wakes without end effects. *J. Fluid Mech.* **288**, 256–310.

Lielausis, O. 1975 Liquid-metal magnetohydrodynamics. *Atomic Energy Rev.* **13**, 527–581.

Liou, T.-M., Chen, C.-C. & Tsai, T.-W. 2000 Heat transfer and fluid flow in a square duct with 12 different shaped vortex generators. *J. Heat Trans.* **122**, 327–335.

Mahfouz, F. M. & Badr, H. M. 2000 Forced convection from a rotationally oscillating cylinder placed in a uniform stream. *Int. J. Heat Mass Trans.* **43**, 3093–3104.

Marais, C., Godoy-Diana, R., Barkley, D. & Wesfreid, J. 2011 Convective instability in inhomogeneous media impulse response in the subcritical cylinder wake. *Phys. Fluids* **23**, 014104.

Marquet, O., Sipp, D. & Jacquin, L. 2008 Sensitivity analysis and passive control of cylinder flow. *J. Fluid Mech.* **615**, 221–252.

Massey, B. S. 2005 *Mechanics of fluid*. Taylor & Francis.

McCracken, G. & Stott, P. 2005 *Fusion: The Energy of The Universe*. Elsevier Academic Press.

Mettu, S., Verma, N. & Chhabra, R. 2006 Momentum and heat transfer from an asymmetrically confined circular cylinder in a plane channel. *Heat Mass Transf.* **42** (11), 1037–1048.

Moffatt, H. K. 1967 On the suppression of turbulence by a uniform magnetic field. *J. Fluid Mech.* **28**, 571–592.

Molokov, S., Moreau, R. & Moffatt, H. K. 2007 *Magnetohydrodynamics: Historical Evolution and Trends*. Springer.

Monkewitz, P. A. 1988 The absolute and convective nature of instability in two-dimensional wakes at low reynolds numbers. *Phys. Fluids* **5**, 999–1006.

Monkewitz, P. A. 1996 Modeling of self-excited wake oscillations by amplitude equations. *Exptl Thermal Fl. Sci.* **12**, 175–183.

Moreau, J. & Sommeria, R. 1988 Electrically driven vortices in a strong magnetic field. *J. Fluid Mech.* **189**, 553–569.

MOREAU, R. J. 1990 *Magnetohydrodynamics*. Dordrecht; Boston: Kluwer Academic Publishers.

MORZYŃSKI, M., AFANASIEV, K. & THIELE, F. 1999 Solution of the eigenvalue problems resulting from global non-parallel flow stability analysis. *Comput. Methods Appl. Mech. Eng.* **169**, 161–176.

MUCK, B., GUNTHER, C., MÜLLER, U. & BÜHLER, L. 2000 Three-dimensional MHD flows in rectangular ducts with internal obstacles. *J. Fluid Mech.* **418**, 265–295.

MÜLLER, U. & BÜHLER, L. 2001 *Magnetohydrodynamics in Channels and Containers*. Springer.

MÜNEVVER, S. 1987 Magnetohydrodynamic flow in a rectangular duct. *Int. J. Numer. Meth. Fl.* **7** (7), 697–718.

MUTSCHKE, G., GERBETH, G., SHATROV, V. & TOMBOULIDES, A. 1997 Two- and three-dimensional instabilities of the cylinder wake in an aligned magnetic field. *Phys. Fluids* **9** (11), 3114–3116.

MUTSCHKE, G., GERBETH, G., SHATROV, V. & TOMBOULIDES, A. 2001 The scenario of three-dimensional instabilities of the cylinder wake in an external magnetic field: A linear stability analysis. *Phys. Fluids* **13** (3), 723–734.

MUTSCHKE, G., SHATROV, V. & GERBETH, G. 1998 Cylinder wake control by magnetic fields in liquid metal flows. *Exptl Thermal Fl. Sci.* **16**, 92–99.

NEILD, A., NG, T. W., SHEARD, G. J., POWERS, M. & OBERTI, S. 2010 Swirl mixing at microfluidic junctions due to low frequency side channel fluidic perturbations. *Sens. Act. B: Chem.* **150**, 811–818.

NOACK, B. & ECKELMANN, H. 1994 A low-dimensional galerkin method for the three-dimensional flow around a circular cylinder. *Phys. Fluids* **6**, 124–143.

NORBERG, C. 1994 An experimental investigation of the flow around a circular cylinder: influence of aspect ratio. *J. Fluid Mech.* **258**, 287–316.

OYAKAWA, K., KOUROGI, Y., YAGA, M. & MIYAFUJI, Y. 2005 Heat transfer enhancement in duct with blunt body inserted close to its wall. *Heat Transf. - Asian Res.* **34**, 336–349.

Oyakawa, K. & Mabuchi, I. 1981 Fluid flow and heat transfer in a parallel plate duct containing a cylinder. *Bulletin JSME* **24**, 1795–1802.

Pothérat, A., Sommeria, J. & Moreau, R. 2000 An effective two-dimensional model for MHD flows with transverse magnetic field. *J. Fluid Mech.* **424**, 75–100.

Pothérat, A., Sommeria, J. & Moreau, R. 2005 Numerical simulations of an effective two-dimensional model for flows with a transverse magnetic field. *J. Fluid Mech.* **534**, 115–143.

Prasad, A. & Williamson, C. H. K. 1997 he instability of the shear layer separating from a bluff body. *J. Fluid Mech.* **333**, 375–402.

Price, S. J., Sumner, D., Smith, J. G., Leong, K. & Païdoussis, M. P. 2002 Flow visulization around a circular cylinder near to a plane wall. *J. Fluids Struct.* **16**, 175 – 191.

Provansal, M., Mathis, C. & Boyer, L. 1987 Bénard-von Kármán instability: Transient and forced regimes. *J. Fluid Mech.* **182**, 1–22.

Reddy, S. C., Schmid, P. J., Baggett, J. S. & Henningson, D. S. 1998 On stability of streamwise streaks and transition thresholds in plane channel flows. *J. Fluid Mech.* **365**, 269–303.

Rehimi, F. & Aloui, F. 2011 Synchronized analysis of an unsteady laminar flow downstream of a circular cylinder centred between two parallel walls using piv and mass transfer probes. *Exp. Fluids* **51**, 1–22.

Rehimi, F., Aloui, F., Nasrallah, S. B., Doubliez, L. & Legrand, J. 2008 Experimental investigation of a confined flow downstream of a circular cylinder centred between two parallel walls. *J. Fluids Struct.* **24**, 855–882.

Reichl, P., Hourigan, K. & M.C.Thompson 2005 Flow past a cylinder close to a free surface. *J. Fluid Mech.* **533**, 269–296.

Roberts, P. H. 1967 *An Introduction to Magnetohydrodynamics*. American Elsevier Pub. Co.

Roshko, A. 1954 On the development of turbulent wakes from vortex street. NASA Rep. 1191.

Roshko, A. 1993 The vortex-shedding process behind two-dimensional bluff bodies. *J. Wimd Eng. Industial. Aerodyn* **49**, 79–100.

Ryan, K., Thompson, M. C. & Hourigan, K. 2005 Three-dimensional transition in the wake of bluff elongated cylinders. *J. Fluid Mech.* **538**, 1–29.

Sahin, M. & Owens, R. G. 2004 A numerical investigation of wall effects up to high blockage ratios on two-dimensional flow past a confined circular cylinder. *Phys. Fluids* **16** (5), 1305–1320.

Schmid, P. J. & Henningson, D. S. 2001 *Stability and Transition in Shear Flows*. New York: Springer.

Sekhar, T., Sivakumar, R., Kumar, H. & kumar, T. R. 2005 Drag and pressure fields for the mhd flow around a circular cylinder at intermediate reynolds numbers. *J. Appl. Math.* **3**, 183 – 203.

Sekhar, T. V. S., Sivakumar, R., Kumar, H. & Ravi kumar, T. V. R. 2007 Effect of aligned magnetic field on the steady viscous flow past a circular cylinder. *Appl. Math. Model.* **31** (1), 130–139.

Shatrov, V., Mutschke, G. & Gerbeth, G. 1997 numerical simulation of two dimensional *mhd* flow around a circular cylinder. *magnetohydrodynamics* **33** (3).

Sheard, G. J. 2009 Flow dynamics and wall shear-stress variation in a fusiform aneurysm. *J. Eng. Math.* **64**, 379–390.

Sheard, G. J., Fitzgerald, M. J. & Ryan, K. 2009 Cylinders with square cross-section: Wake instabilities with incidence angle variation. *J. Fluid Mech.* **630**, 43–69.

Sheard, G. J. & King, M. P. 2011 The influence of height ratio on Rayleigh-number scaling and stability of horizontal convection. *Appl. Math. Mod.* **35**, 1647–1655.

Sheard, G. J., Leweke, T., Thompson, M. C. & Hourigan, K. 2007 Flow around an impulsively arrested circular cylinder. *Phys. Fluids* **19** (8), 083601.

Sheard, G. J., Thompson, M. C. & Hourigan, K. 2003 From spheres to circular cylinders: the stability and flow structures of bluff ring wakes. *J. Fluid Mech.* **492**, 147–180.

SHERCLIFF, J. A. 1953 Steady motion of conducting fluids in pipes under transverse magnetic fields. *Math. Proce. Cambridge Philosophical Soc.* **49** (1), 136–144.

SHERCLIFF, J. A. 1975 Some duct flow problems at high Hartmann number. *Zeitschrift für Angewandte Mathematik und Physik (ZAMP)* **26** (5), 537–548.

SMITH, S. W. 2003 *Digital signal processing: a practical guide for engineers and scientists*. Newnes.

SMOLENTSEV, S., VETCHA, N. & MOREAU, R. 2012 Study of instabilities and transitions for a family of quasi-two-dimensional magnetohydrodynamic flows based on a parametrical model. *Phys. Fluids* **24**, 024101.

SMOLENTSEV, S. Y. & DAZHI, D. A. 1996 The effect of a conducting inclusion on the heat transfer in a fully developed MHD flow in a rectangular channel. *Magnetohydrodynamics* **32**, 331–335.

SOMMERIA, J. & MOREAU, R. 1982 Why, how, and when, MHD turbulence becomes two-dimensional. *J. Fluid Mech.* **118**, 507–518.

TAKAMI, H. & KELLER, H. 1969 Steady two-dimensional viscous flow of an incompressible fluid past a circular cylinder. *Phys. Fluids* **12**, II51–II56.

TANEDA, S. 1956 Experimental investigation of the wakes behind cylinders and plates at low reynolds numbers. *J. Phys. Soc. Jpn.* **11** (6), 302–307.

TANEDA, S. 1963 The stability of two-dimensional laminar wakes at low reynolds numbers. *J. Phys. Soc. Jpn.* **18**, 288–307.

TANEDA, S. 1965 Experimental investigation of vortex streets. *J. Phys. Soc. Jpn.* **20** (9), 1714–1721.

TANIGUCHI, S. & MIYAKOSHI, K. 1990 Fluctuating fluid forces acting on a circular cylinder and interference with a plane wall - effects of boundary layer thickness. *Exp. Fluids* **9**, 197–204.

THOMPSON, M. C. 2011 Effective transition of steady flow over a square leading-edge plate. *J. Fluid Mech.* **under review**.

TRIANTAFYLLOU, G. 1992 Three-dimensional flow patterns in two-dimensional wakes. *J. Fluids Eng. Trans. ASME* **114**, 356–361.

Triantafyllou, G. S. & Dimas, A. A. 1989 Interaction of two-dimensional separated flows with a free surface at low froude numbers. *Phys. Fluids A* **1**, 1813–1821.

Tritton, D. J. 1959 Experiments on the flow past a circular cylinder at low reynolds numbers. *J. Fluid Mech.* **6**, 547–567.

Tritton, D. J. 1971 A note on vortex streets behind circular cylinders at low reynolds numbers. *J. Fluid Mech.* **45**, 203–208.

Tsui, Y.-Y., Leu, S.-W., Lin, C.-C. & Wu, P.-W. 2000 Heat transfer enhancement by multilobe vortex generators: Effects of lobe parameters. *Numer. Heat Transf.* **37**, 653–672.

Ueno, K., Saito, K. & Kamiyama, S. 2001 Three-dimensional simulation of mhd flow with turbulence. *JSME Intl. J. Series B* **44** (1), 38–44.

Unal, M. F. & Rockwell, D. 1988 On vortex formation from a cylinder. part 1. the initial instability. *J. Fluid Mech.* **190**, 491–512.

Valencia, A. 1995 Heat transfer enhancement in a channel with a built-in rectangular cylinder. *Heat Mass Transf.* **30**, 423–427.

Valencia, A. 1998 Numerical study of self-sustained oscillatory flows and heat transfer in channels with a tandem of transverse vortex generators. *Heat Mass Transf.* **33**, 465–470.

Van Dyke, M. 1982 *An album of fluid motion.* Parabolic Press.

Voropayev, S. I., Afanasyev, Y. D. & Filippov, I. A. 1991 Horizontal jets and vortex dipoles in a stratified fluid. *J. Fluid Mech.* **227**, 543–566.

Vos, P. 2011 From h to p efficiency: Optimising the implementation of spectral/hp element methods. PhD thesis, Imperial College London.

Wang, X. & Tan, S. 2008 Near-wake flow characteristics of a circular cylinder close to a wall. *J. Fluids Struct.* **24**, 605 – 627.

Williamson, C. H. K. 1988 The existence of two stages in the transition to three-dimensionality of a cylinder wake. *Phys. Fluids* **31** (11), 3165–3168.

Williamson, C. H. K. 1989 The existence of two stages in the transition to three-dimensionality of a cylinder wake. *J. Fluid Mech.* **206**, 206–627.

Williamson, C. H. K. 1996 Vortex dynamics in the cylinder wake. *Annu. Rev. Fluid Mech.* **28**, 477–539.

Williamson, C. H. K. & Miller, G. 1994 Control of three-dimensional phase dynamics in a cylinder wake. *Exp. Fluids* **18**, 26–35.

Wu, H.-W. & Perng, S.-W. 1999 Effect of an oblique plate on the heat transfer enhancement of mixed convection over heated blocks in a horizontal channel. *Int. J. Heat Mass Trans.* **42** (7), 1217 – 1235.

Yang, S.-J. 2003 Numerical study of heat transfer enhancement in a channel flow using an oscillating vortex generator. *Heat Mass Transf.* **39**, 257–265.

Yao, M., Nakatani, M. & Suzuki, K. 1995 Flow visualization and heat transfer experiments in a turbulent channel flow obstructed with an inserted square rod. *Int. J. Heat Fluid Flow* **16**, 389–397.

Yoon, H. S., Chun, H. H., Ha, M. Y. & Lee, H. G. 2004 A numerical study on the fluid flow and heat transfer around a circular cylinder in an aligned magnetic field. *Int. J. Heat Mass Trans.* **47** (19–20), 4075–4087.

Zavala Sansón, L., van Heijst, G. J. F. & N. A. Backx 2001 Ekman decay of a dipolar vortex in a rotating fluid. *Phys. Fluids* **13** (2), 440–451.

Zdravkovich, M. M. 1997 *Flow Around Circular Cylinders: A Comprehensive Guide Through Flow Phenomena, Experiments, Applications, Mathematical Models, and Computer Simulations*. Oxford University Press.

Zdravkovich, M. M. 2003 *Flow Around Circular Cylinders: A Comprehensive Guide Through Flow Phenomena, Experiments, Applications, Mathematical Models, and Computer Simulations*. Oxford University Press.

Zielinska, B. & Wesfreid, J. 1995 On the spatial structure of global modes in wake flow. *Phys. Fluids* **7** (6), 1418–1424.

Zikanov, O. Y. 1996 On the instability of pipe Poiseuille flow. *Phys. Fluids* **8** (11), 2923–2932.

Zovatto, L. & Pedrizzetti, G. 2001 Flow about a circular cylinder between parallel walls. *J. Fluid Mech.* **440**, 1–25.